A MONTE CARLO STUDY OF DOSE DISTRIBUTIONS AND ENERGY IMPARTED IN COMPUTED TOMOGRAPHY DOSIMETRY PHANTOMS

BY

JAMES VINCENT ATHERTON

A DISSERTATION PRESENTED TO THE GRADUATE SCHOOL
OF THE UNIVERSITY OF FLORIDA IN PARTIAL FULFILLMENT
OF THE REQUIREMENTS FOR THE DEGREE OF
DOCTOR OF PHILOSOPHY

UNIVERSITY OF FLORIDA

1993

ACKNOWLEDGMENTS

The author wishes to extend copious and sincere thanks to his committee chairman, Dr. William Properzio, for his many efforts on the author's behalf. The author also wishes to extend his thanks to his advisor and cochair, Dr. Libby Brateman, for her hard work, support and advice in the development of this project. Many thanks also go to the other committee members, Drs. Hintenlang, Honeyman, and Roessler, for their encouragement and assistance. Additional recognition is due Drs. Roessler and Brateman for rearranging their travel schedules to accommodate the author. The author also wishes to extend his sincere thanks to Dr. Walter Huda for his suggestions and advice. Also, thanks go to the staff of The CancerCare Center and particularly Dr. Eric Rost for the use of the computers and office equipment located there. The author would like to acknowledge the support he received from the CDRH through the assistance of Drs. Orhan Suleiman and Marvin Rosenstein.

The author wishes to extend his great thanks to his family for their continued love and encouragement. Finally, the author wishes to extend his most sincere thanks to his wife for her love and support during the course of this project.

TABLE OF CONTENTS

ACKNOWLEDGMENTS ii

LIST OF TABLES vi

LIST OF FIGURES ix

ABSTRACT xiii

CHAPTERS

1. INTRODUCTION 1

2. SURVEY OF COMMON CT SCANNER CHARACTERISTICS 13

Introduction 13

Basic Operational Principles 13

Differences Among CT Scanners from Various Manufacturers 15

Summary 27

3. THE MONTE CARLO TECHNIQUE 30

Introduction 30

Sampling Methods 32

Random Number Generation 37

Data Analysis 38

4. THE EGS MONTE CARLO SYSTEM 41

Introduction 41

EGS Components 43

Summary 65

5. VERIFICATION OF THE MONTE CARLO MODEL 67
Conservation of Energy 67
In Air Dose Calculation 69
Primary X Ray Transmission Through a Cylinder 71
6. DOSE DISTRIBUTIONS AND RELATED DOSIMETRIC QUANTITIES 74
Introduction 74
Dose Profiles 75
Integration of Dose Profiles 79
Photon Energy Variation 89
Beam Filter Variation 95
Slice Thickness Variation 98
Phantom Size Variation 100
Phantom Material Variation 100
SAD Variation 102
Summary 104
7. ENERGY IMPARTED RESULTS 106
Introduction 106
Photon Energy Variation 106
Beam Filter Variation 112
Slice Thickness Variation 115
Phantom Size Variation 115
Phantom Material Variation 115
SAD Variation 119
Phantom Composition and Shape Variation 120
Summary 128
8. DISCUSSION AND CONCLUSIONS 130

APPENDICES

A. CT MANUFACTURER SURVEY FORM 141

B. PRIMARY X RAY TRANSMISSION THROUGH A CYLINDER 145

C. DESCRIPTION OF MACRO $ELLCYL 148

D. LISTING OF PERMON1.MOR 156

REFERENCES 186

BIOGRAPHICAL SKETCH 194

LIST OF TABLES

Table 1-1 Comparison of effective dose equivalents for standard exams for three common CT scanners. 6

Table 1-2: Ratios of the effective dose equivalent to the energy imparted for different exams and scanners..... 9

Table 1-3. The range of parameters examined in this work..... 12

Table 2-1: Half value layers for the GE 9800 scanner as function of detector and kVp..... 19

Table 2-2: Comparison of head CTDI values [mrad./mAs]..... 28

Table 2-3: Comparison of body CTDI values [mrad/mAs]..... 29

Table 5-1: Illustration of conservation of energy for four separate Monte Carlo runs with an acrylic phantom and no filter with a 65 cm SAD..... 68

Table 5-2: Comparison of CTDI values per incident fluence for various energies and acrylic rod diameters..... 70

Table 5-3: Comparison of percentage transmission of primary radiation through acrylic cylinders of various diameters as calculated analytically and with the EGS code..... 72

Table 6-1: $\mathfrak{C}(r,\ell)$ as a function of integration limits ℓ and radial position r in a head phantom at 50 keV..... 83

Table 6-2: Summary of spectra data..... 92

Table 6-3: Comparison of $CTDI_{air}$ values for the three beam filters used..... 92

Table 7-1: Energy dispositions for an 8 cm acrylic phantom with no beam filter and a 5 mm slice thicknesses..... 107

Table 7-2: Energy dispositions for a 16 cm acrylic phantom with no beam filter and a 5 mm slice thickness..... 108

Table 7-3: Energy dispositions for an 8 cm acrylic phantom with no beam filter and 5 mm slice thickness for four spectra..... 109

Table 7-4: Percentage energy dispositions for an 8 cm acrylic phantom with no beam filter and 5 mm slice thickness for four spectra..... 109

Table 7-5: Energy dispositions in an 16 cm acrylic phantom with no beam filter and 5 mm slice thickness for four spectra..... 110

Table 7-6: Percentage energy disposition for four spectra in a 16 cm radius acrylic phantom with no beam filter..... 110

Table 7-7: Energy dispositions at 50 keV for 8 cm and 16 cm radii acrylic phantoms for a 5 mm slice thickness, for three filter configurations..... 113

Table 7-8: Percentage energy dispositions at 50 keV for 8 cm and 16 cm radii acrylic phantoms for a 5 mm slice thickness, for three filter configurations..... 113

Table 7-9: Comparison of energy disposition categories of monoenergetic beams with two typical CT spectra on a 16 cm acrylic phantom with the GE beam filter..... 114

Table 7-10: Percentage comparison of energy disposition categories of monoenergetic beams with two typical CT spectra on a 16 cm acrylic phantom with the GE beam filter..... 114

Table 7-11: Effect of slice thickness on energy dispositions for 50 keV incident photons on an 8 cm radius acrylic phantom with no filter..... 116

Table 7-12: Energy dispositions for acrylic phantoms with indicated radii for 50 keV incident photons and 5 mm slice thickness..... 116

Table 7-13: Variations of the energy dispositions with phantom material in an 8 cm radius phantom..... 117

Table 7-14: Variations of energy dispositions with phantom material in a 16 cm radius phantom..... 118

Table 7-15: Variation of energy dispositions with change in the SAD for 50 keV incident photons and a 5 mm slice thickness..... 120

Table 7-16: Energy dispositions in the anthropomorphic head phantom for the indicated incident energies with no beam filter..... 122

Table 7-17: Energy dispositions in the anthropomorphic head phantom with the GE filter for the indicated incident energies..... 123

Table 7-18: Energy dispositions in the anthropomorphic body phantom for the indicated incident energies and no beam filter..... 124

Table 7-19: Energy dispositions in the anthropomorphic body phantom for the indicated incident energies with the GE filter..... 125

Table 7-20: Energy dispositions for four x-ray spectra on anthropomorphic-type phantoms with no filter..... 127

Table 7-21: Percentage energy disposition for four x-ray spectra incident on anthropomorphic-type phantoms..... 127

Table 8-1: Comparison of the arithmetic average of the central value and 1 cm depth value of the normalized $C(r,L/2)$ ("average") and the normalized mean CTDI ($\overline{C}$) for monoenergies and spectra, calculated with no beam filter..... 132

LIST OF FIGURES

Figure 1-1: Schematic drawing of CT scanner geometry..... 1

Figure 3-1: Discrete probability density function..... 34

Figure 3-2: Discrete cumulative probability distribution..... 34

Figure 3-3: *top:* Continuous probability distribution; *bottom:* cumulative distribution functions..... 35

Figure 3-4: An illustration of the Rejection Method. Only the random pairs that fall under the curve are accepted..... 37

Figure 4-1: Flow control diagram of the EGS system..... 54

Figure 4-2 Illustration of the geometry described by subroutine HOWFAR in the user code CTMONO with five radial zones and five planar zones..... 58

Figure 4-3. Source and phantom configuration for cylindrical phantom..... 60

Figure 4-4(a): Head Phantom..... 64

Figure 4-4(b): Body Phantom..... 65

Figure 5-1: CTDI in air per incident fluence for acrylic rods of various sizes..... 71

Figure 6-1: Central portion of dose profiles in a 5 mm diameter acrylic rod for a 3 mm slice thickness for the indicated incident photon energies..... 76

Figure 6-2: Dose profiles along the central 5 mm in a 5 mm diameter acrylic rod for 80 keV photons and the indicated slice thicknesses..... 77

Figure 6-3: Normalized dose profiles at the center and at 1 cm depth in an 8 cm radius acrylic phantom for 80 keV incident photons and a 5 mm slice thickness... 77

Figure 6-4: Normalized dose profiles at the center and at 1 cm depth in a 16 cm radius acrylic phantom for 80 keV incident photons and a 5 mm slice thickness... 78

Figure 6-5: Portion of the dose profile along the positive *z*-axis at the center of a 16 cm radius acrylic phantom for 80 keV photons and 5 mm slice thickness..... 78

Figure 6-6: $\mathfrak{C}(r,\ell)$, normalized to the $CTDI_{air}$ value, as a function of the integration limit l in an 8 cm radius acrylic phantom at 50 keV for a 10 mm slice thickness..... 82

Figure 6-7: $\mathfrak{C}(r,\ell)$, normalized to the $CTDI_{air}$ value, as a function of the integration limit ℓ in an 8 cm radius acrylic phantom at 50 keV for a 5 mm slice thickness..... 82

Figure 6-8: $\mathfrak{C}(r,\ell)$, normalized to the $CTDI_{air}$ value, as a function of the integration limit ℓ in an 8 cm radius acrylic phantom at 50 keV for a 1 mm slice thickness..... 83

Figure 6-9: $\mathfrak{C}(r,\ell)$ values, normalized to the $CTDI_{air}$ value, as a function of the integration limit ℓ in an 8 cm radius acrylic phantom at 50 keV for a 5 mm slice thickness in a 140 cm long phantom..... 86

Figure 6-10: $\mathfrak{C}(r,\ell)$, normalized to the $CTDI_{air}$ value, as a function of the integration limit ℓ in an 8 cm radius acrylic phantom for a 120 kVp spectrum with 5.4 mm HVL, for a 10 mm slice thickness..... 86

Figure 6-11: $\mathfrak{C}(r,\ell)$, normalized to the $CTDI_{air}$ value, as a function of the integration limit ℓ in an 16 cm radius acrylic phantom at 50 keV for a 5 mm slice thickness..... 88

Figure 6-12: $\mathfrak{C}(r,\ell)$, normalized to the $CTDI_{air}$ value, as a function of the integration limit ℓ in a 16 cm radius acrylic phantom for a 120 kVp spectrum with 5.4 mm HVL, for a 10 mm slice thickness..... 88

Figure 6-13: $\mathfrak{C}(r,L/2)$ as a function of radial location in the 8 cm radius phantom, normalized to the $CTDI_{air}$ at the same energy, for a 5 mm slice thickness and various incident energies..... 90

Figure 6-14: $\mathfrak{C}(r,L/2)$ as a function of radial location in the 16 cm radius phantom, normalized to the $CTDI_{air}$ at the same energy, for a 5 mm slice thickness and various incident energies..... 90

Figure 6-15: Plots of the four spectra used in this work..... 92

Figure 6-16: $\mathfrak{C}(r,L/2)$ as a function of radial location for four spectra for 5 mm slices in an 8 cm radius acrylic phantom..... 94

Figure 6-17: $\mathfrak{C}(r,L/2)$ as a function of radial location for four spectra for 5 mm slices in a 16 cm radius acrylic phantom..... 94

Figure 6-18: $\mathfrak{C}(r,L/2)$ as a function of radial location in the acrylic 8 cm radius phantom at 50 keV for a 5 mm slice thickness, and the indicated beam filter..... 96

Figure 6-19: $\mathfrak{C}(r,L/2)$ as a function of radial location in the acrylic 16 cm radius phantom at 50 keV for a 5 mm slice thickness and the indicated beam filter..... 96

Figure 6-20: $\mathfrak{C}(r,L/2)$ as a function of radial location for the GE filter in a 16 cm acrylic phantom at 63 cm SAD for the 5 mm slice thickness, and various incident beams..... 99

Figure 6-21: $\mathfrak{C}(r,L/2)$ as a function of slice thickness in a 8 cm radius acrylic phantom at 80 keV..... 99

Figure 6-22: $\mathfrak{C}(r,L/2)$ plotted against relative distance from the center of the phantom for various values of phantom radius R..... 101

Figure 6-23: $\mathfrak{C}(r,L/2)$ plotted against radial location for various phantom materials in a 8 cm radius phantom for 50 keV photons and 5 mm slice thickness 101

Figure 6-24: $\mathfrak{C}(r,L/2)$ plotted against radial location for various phantom material in an 16 cm radius phantom for 50 keV photons and 5 mm slice thickness..... 103

Figure 6-25: $\mathfrak{C}(r,L/2)$ plotted against radial location for various SAD values for a 5 mm slice thickness and 50 keV photons..... 103

Figure 7-1: Percentage energy dispositions for an 8 cm acrylic phantom with no beam filter and a 5 mm slice thickness..... 107

Figure 7-2: Percentage energy dispositions for an 16 cm acrylic phantom with no beam filter and a 5 mm slice thickness..... 108

Figure 7-3: Percentage energy dispositions acrylic phantoms with indicated radii for 50 keV incident photons and 5 mm slice thickness..... 116

Figure 7-4: Percentage variations with phantom material. Data are for an 8 cm radius phantom and 5 mm slice thickness at 50 keV..... 117

Figure 7-5: Percentage variations with phantom material. Data are for a 16 cm radius phantom and 5 mm slice thickness at 50 keV..... 118

Figure 7-6: Percentage energy disposition for the anthropomorphic head phantom for a 5 mm slice and no beam filter..... 122

Figure 7-7: Percentage energy disposition for the anthropomorphic body phantom for a 5 mm slice and the GE beam filter..... 123

Figure 7-8: Percentage energy disposition for the anthropomorphic body phantom for a 5 mm slice and no beam filter..... 124

Figure 7-9: Percentage energy disposition for the anthropomorphic body phantom for a 5 mm slice and the GE beam filter..... 125

Figure B1: Source-phantom geometry..... 145

Figure C1: Geometry of intersection of a vector and an elliptical cylinder..... 148

Figure C2: Geometric possibilities of particle intersecting an elliptical cylinder.... 150

Figure C3: Geometry used to pick incident particle parameters..... 151

Abstract of Dissertation Presented to the Graduate School
of the University of Florida in Partial Fulfillment of the
Requirements for the Degree of Doctor of Philosophy

A MONTE CARLO STUDY OF DOSE DISTRIBUTIONS AND ENERGY IMPARTED IN COMPUTED TOMOGRAPHY DOSIMETRY PHANTOMS

by James Vincent Atherton

August 1993

Chairman: William Properzio, Ph.D.
Cochairman: Libby Brateman, Ph.D.
Major Department: Nuclear Engineering Sciences

The EGS4 Monte Carlo system was used to study the factors that affect dose distributions and the energy imparted to dosimetry phantoms in computed tomography (CT). The energy imparted is a useful quantity since it is directly correlated with the stochastic risk to the patient. Also, since the energy imparted per slice is independent of both the precise anatomic location of the scanned slice and the total number of slices imaged, the total energy imparted from an exam can be easily found.

The parameters that were investigated were incident energy, beam shaping filter, slice thickness, phantom size, phantom composition, and source-to-axis-distance (SAD). These parameters were evaluated for irradiation by both monoenergetic x-ray beams and typical x-ray spectra incident upon acrylic cylinders modeled on standardized Computed Tomography Dose Index (CTDI) phantoms. In addition, two phantoms similar to the anthropomorphic phantoms used in previous Monte Carlo investigations of patient dosimetry were studied, and the results obtained from these phantoms were compared to those obtained from the CTDI phantoms. In all cases the results obtained were normalized to the dose to acrylic determined "in-air" at the isocenter of the scanner in the absence of any other phantom. The results quantitatively demonstrate the effects of modifying key CT parameters on energy deposition patterns in CT dosimetry phantoms.

Also, a method is presented that allows estimation of the total energy imparted per slice to a CTDI phantom.

In general, the factors most affecting the quantitative values of energy deposited in CT dosimetry phantoms are beam filtration, the size and composition of the object being scanned, and the incident energy. The results also suggest that the energy imparted is only moderately dependent on the characteristics of the incident x-ray spectrum.

The results of this work may be used as a basis for estimating the energy imparted to a phantom or a patient for non-standard or newly developed CT exams or scanners. The values of the energy imparted may also be used to estimate other quantities such as the effective dose. These estimates may then be used as indices of stochastic risk for comparisons between scanners or imaging modalities, exam optimization, or for population-based studies of radiation detriment.

CHAPTER 1

INTRODUCTION

Computerized tomography (CT) is unlike any other radiological imaging method in that an x-ray beam, tightly collimated in one dimension, is revolved about an object and produces a complex three-dimensional pattern of energy deposition. The energy distribution is a function of the x-ray spectrum, the x-ray beam filtration, collimation, and the nature of the object scanned. A schematic drawing of the basic geometry of CT scanners is shown in Fig. 1-1.

Since the clinical introduction of CT in the early 1970s, dosimetric investigations have generally followed one of two tracks. One track has been the specification of radiation doses to exact locations in patients and phantoms. The other track has been the evaluation of total radiation risk to the patient from CT exams. The risk has generally been assessed in one of two ways: organ-by-organ dose determination; or by estimation of the total energy imparted to the patient.

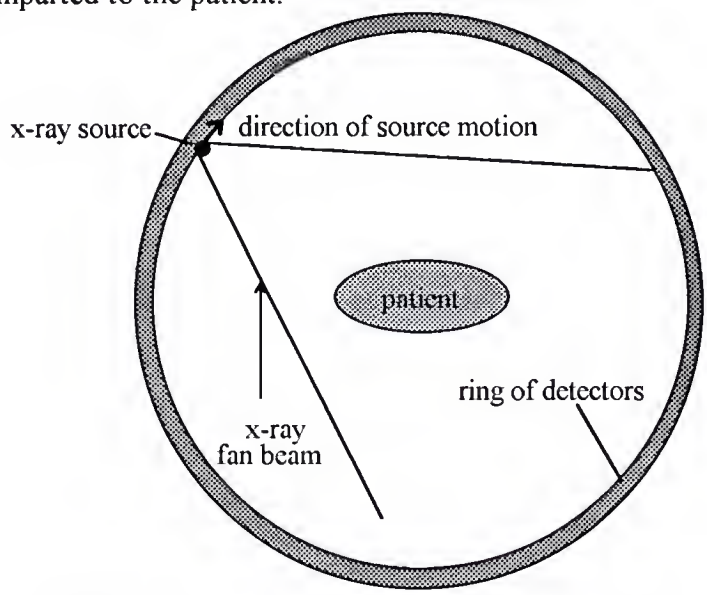

Figure 1-1: Schematic drawing of CT geometry.

Initial investigations of radiation dose in CT followed the first track, reporting doses to specific points or groups of points in phantoms. Horsley and Peters (1976) reported on the dose to the skull from multiple scans from an EMI scanner as measured in a Rando phantom. Dixon and Eckstrand (1978) used a film dosimetry system to measure surface dose in a 19 cm diameter water phantom for both single and multiple slices. McCullough and Payne (1978) used thermoluminescent dosimeters (TLD) to measure surface dose for single and multiple scans in circular and elliptical acrylic phantoms. Shope *et al.* (1982) used TLD to measure point doses for single and multiple scans in both cylindrical and anthropomorphic phantoms in scanners from ten manufacturers. They presented surface and center doses for the cylindrical phantom and the maximum dose measured in the anthropomorphic phantom. Fearon and Vucich (1985) measured surface doses in pediatric patients for several standard exams and compared the results to in-phantom measured values. Storrs and Byrd (1988) measured the dose to the lens of the eye for pediatric patients. There have been several studies of fetal or intrauterine dose from CT (Wagner, *et al.* 1986, Guidozzi *et al.* 1987, Felmlee *et al.* 1990).

In 1981 Shope *et al.* proposed the Computed Tomography Dose Index (CTDI) as a dose descriptor in CT. The CTDI is measured in cylindrical acrylic phantoms that are intended to approximate the size and shape of a patient's head and body. The CTDI, as defined by the United States Food and Drug Administration (FDA), is given by:

$$CTDI = \frac{1}{nT}\int_{-7T}^{+7T} D(z)\,dz \qquad (1\text{-}1)$$

where n is the number of scans per slice, $D(z)$ is the dose profile for a single scan along a line perpendicular to the scanned slice, and T is the nominal slice thickness (FDA 1985). The CTDI is given in units of absorbed dose to acrylic for a specific depth in one of the two cylindrical phantoms. The CTDI is meant to approximate the dose at the depth of measurement for a point in middle of fourteen contiguous scans. The CTDI is measured the center of the phantom and at one centimeter depth from the surface. The FDA has

mandated that CT manufacturers supply users with CTDI values for a particular CT scanner model for the range of tube potentials, tube currents, scan times, slice thicknesses, and gantry angles likely to be used clinically. The FDA requirement has had the effect of making the CTDI a standardized dose descriptor. Apart from its use as a dose estimator, the CTDI can be employed for intercomparisons among scanners, and as an acceptance testing and quality control check.

The CTDI is specified by the FDA to be given for two depths and with integration limits that are a function of the nominal slice thickness.[1] It should be noted that the FDA specifies only a *minimum* phantom length of 14 cm for CTDI measurements, and the phantoms commercially available are 16 cm long.[2] Note that the line integral of the dose can be calculated at *any* depth in the phantom and with *any* integration limits (up to the size of the phantom, of course). Viewed in this light, the CTDI as specified by the FDA is a special case of a "family" of CTDI's. Part of this work investigates these different classes of CTDI's and their relationship to the FDA's definition. A new, more generalized dose index is defined, and its relation to the total energy deposited is demonstrated.

The second main track of dosimetric investigations in CT have endeavored to evaluate the total radiation risk to the patient undergoing an examination. For doses of less than 1 Gy, the total risk to the patient is considered to be the sum of the risks associated with the individual irradiated organs (ICRP 1977). In diagnostic radiology the main concern is with stochastic effects, e.g., carcinogenesis, genetic injury, and conceptus injury (ICRP 1986). Although doses from CT scans are greater than in conventional radiography, the doses are below the threshold for deterministic effects such as lens opacification or skin erythema (ICRP 1990). The method of estimating risk by using the weighted sum of the doses to individual organs is the basis of the Effective Dose Equivalent H_E (ICRP 1977) and the Effective Dose E (ICRP 1990) quantities. The

[1] Spokas (1982) has pointed out a weakness with the definition of the CTDI in that it combines a dose measurement with an imaging parameter that is not measured. He suggested an alternate descriptor of CT performance, the effective width w, but the CTDI remains to be the most widely used CT dose descriptor.
[2] Nuclear Associates, Carle Place, NY 11514

weighting values used in calculation of E were intended to take into account the risk of fatal cancer induction, the risk and the severity of non-fatal cancer induction, the probability of severe hereditary effects, and the relative length of life lost for general populations. The effective dose E is given by

$$E = \sum_{T} w_T H_T$$

where H_T is the equivalent dose in organ or tissue T and w_T is the weighting factor for tissue T. The tissue weighting factor represents the relative contribution from tissue or organ T to the overall stochastic effects from uniform irradiation of the whole body. To ensure that a uniform equivalent dose is numerically equal to a uniform equivalent dose over the whole body, the sum of tissue weighting factors is one (ICRP 1990). The values of E and H_E are given in units of Sv and are numerically equal to the absorbed dose in Gy, because the radiation weighting factor w_R (formerly the quality factor Q) is unity for photons.[3] The calculation of H_E is similar to that for E, but different risk estimates (hence different weighting factors) and fewer organs are used in the calculation. The risk estimates used in the determination of the weighting factors for the effective dose equivalent are based on an occupationally exposed population.

The effective dose equivalent and its successor the effective dose are both intended as a method to assess non-uniform irradiations for use in radiation protection. The weighting factors used in the calculation of H_E are based on radiation risk estimates for radiation workers, but the factors used in the calculation of E are based on risk estimates for whole populations (ICRP 1990). The effective dose equivalent (and to some extent the effective dose) have been used as a gauge in establishing radiation risks to patients in diagnostic radiology. In the case of the effective dose equivalent, the patient population has different demographics and presumably different risk factors than do radiation

---

[3] As given in ICRP 60, $H_T = \sum_{R} w_R D_{T,R}$ where $D_{T,R}$ is the absorbed dose averaged over organ or tissue T from radiation R, and w_R is the radiation weighting factor.

workers. In spite of this limitation, the effective dose equivalent continues to be used as a yardstick in comparing patient doses in diagnostic radiology (Shrimpton *et al.* 1991, Jones *et al.* 1991, Le Heron 1992). The use of the effective dose equivalent as an absolute indicator of patient risk may not be as appropriate as the use of the effective dose, but it does provide an objective method of comparison of differing irradiation conditions. One aim of this project is the development of a method allowing estimation of H_E or E in CT, based on the estimation of energy imparted values.

Organ dose assessment in CT has generally followed two approaches: measurement in anthropomorphic phantoms, and Monte Carlo-based calculations in idealized mathematical phantoms. In general, physical measurement in an anthropomorphic phantom has the advantage using of a realistic phantom but tends to be a very labor-intensive process. Monte Carlo simulation can be used to study a wide range of irradiation configurations, but it has the disadvantage of being computationally demanding and time intensive.

Huda and Sandison (1985) used TLD to measure organ dose from an EMI scanner in a Rando phantom and presented risk estimates for standard exams, based on the ICRP risk estimates for radiation workers. Huda and Sandison (1986) also published effective dose equivalents based on the EMI scanner measurements. Fearon and Vucich (1985) measured organ doses in a pediatric anthropomorphic phantom, although they presented neither H_E values nor risk estimates. In 1989 Huda *et al.* extrapolated the EMI measurements to other models of CT scanners and presented H_E values for standard exams. Nishizawa *et al.* (1991) measured organ doses in a Rando phantom for a wide range of CT scanners used in Japan. They similarly determined the effective dose equivalents for standard exams for selected CT scanners.

There have been two significant studies using mathematical modeling for organ dose assessment. In 1985 Drexler *et al.* published organ dose tables calculated by using Monte Carlo simulation for standardized CT exams. These tables provide doses to a number of organs in mathematically modeled male and female phantoms. The CT geometry was

based on that of a Siemens Somatom scanner. Faulkner and Moores (1987) used the Drexler data to provide organ dose estimates for three different types of CT scanners. Panzer *et al.* (1989) have also used the Drexler data to estimate organ doses, based on a survey of 122 facilities in the former West Germany. Neither Faulkner and Moores nor Panzer *et al.* presented effective dose equivalent values for standard exams. Recently, Shrimpton *et al.* (1991) and Jones *et al.* (1991) of the National Radiation Protection Board (NRPB) in the United Kingdom published organ dose tables for a range of CT scanners and standard exams. The NRPB results were obtained using Monte Carlo simulation on a mathematical anthropomorphic phantom. Values of H_E and E were included with the organ dose values presented.

Comparison of results from the organ-dose studies listed above shows a wide variation in the results, even when comparing the same type of scanner for the same type of exam. A comparison of findings from various authors is given in Table 1-1, which lists effective dose equivalent values for four standard exams for the scanners which the studies had in common. It is seen that the values of the effective dose equivalent for the same exam and the same machine can vary by more than a factor of two. These variations seem to be mainly due to three reasons: differences in the clinical protocol of "standard" exams; differences in the treatment of the non-specified "remainder" tissues; and the

Table 1-1: Comparison of effective dose equivalents for standard exams for three common CT scanners.

Effective dose equivalent in mSv by scanner								
Scanner:	**GE 9800**			**Siemens DRH**		**Siemens DRG**		
	——— *study** ———							
Exam	***A***	***B***	***C***	***A***	***C***	***B*-(male)**	***B*-(female)**	***C***
Head	1.9	—	4.3	2.3	2.5	—	—	2.6
Chest	15.7	7.7	9.0	16.0	5.8	6.5	6.5	5.3
Abdomen	6.3	—	10.3	9.5	8.1	2.6	2.7	7.0
Pelvis	6.7	—	11.0	13.4	7.9	6.2	12.5	5.5

* Data are from Huda *et al.* (1989) abbreviated *A*; Nishizawa *et al.* (1991) abbreviated *B*; and Shrimpton *et al.* (1991) abbreviated *C*.

differences between TLD measurements in physical phantoms and mathematical modeling. Thus, even with standardized measurement techniques and standard phantoms, estimation of organ dose and patient risk provides inconsistent and widely varying results. Furthermore, organ dose assessment is difficult to perform. One must either use a large number of small dosimeters placed in an anthropomorphic phantom, or one must employ a mathematical model which must be constructed and tested for accuracy. Moreover, in order to study different examinations and exposure geometries, multiple measurements must be performed. Organ dose studies therefore tend to be labor and time intensive and usually provide results for only a limited number of examination types or exposure geometries.

Another method of assessing the radiation risk to the patient has been through estimation of the total energy deposited or imparted to the patient from an exam. As the studies cited below indicate, the energy imparted to the patient (formerly "integral dose") has been shown to be a useful estimator of stochastic risk in diagnostic radiology. The use of the energy imparted to a patient as a risk estimator assumes a homogeneous mix of radiosensitive and radioresistant tissues within the body (Wall *et al.* 1988). This method is both simpler and cruder than organ dose estimation, and several arguments can be made for its use. The energy imparted is a physical quantity and is independent of organ-weighting factors. These weighting factors are based on risk estimates which in turn are subjectively-judged and subject to change following developments in the knowledge of radiobiology (Greening 1986). They are subjective values and are not a physical quantity. Also, organ dose determinations, as demonstrated above, vary widely in their results and ignore inter-patient variations in organ dimensions and positioning (Harrison 1983). Concerning the efficacy of using energy imparted as a risk indicator, Wall *et al.* (1988, p. 8) state:

> ...the distribution of sensitive organs within the trunk may in many circumstances be sufficiently uniform for the errors involved in this approach to be no greater than those associated with using a suitable

> combination of specific organ doses and weighting factors to express the overall risk.

They conclude (p.55):

> The reasonable degree of correlation that is evident between energy imparted and health detriment for a wide range of x-ray examinations suggests that in *appropriate circumstances* it [the energy imparted] can represent a useful practical quantity for estimating the risk to patients.

The studies below show that the energy imparted can be used outright as an indicator of patient risk, or it can be used to estimate other risk indicators.

Bengtsson *et al.* (1978) used the energy imparted as a basis for risk estimates for conventional radiographic examinations. They based their estimates on the risk coefficient 1.65×10^{-2} Sv^{-1} for radiation workers (ICRP 1977) and identified a risk of 2.0×10^{-4} J^{-1}, which corresponds to a ratio of 12.1 mSv/J. Southon (1980) reported values for energy imparted in comparisons of six different CT scanners but did not present any explicit risk estimates corresponding to the energy imparted values. Shrimpton (1985) studied the relationship between the energy imparted and the effective dose equivalent in common radiographic examinations and found a linear relationship (within a factor of two) between the two of 13.8 mSv/J. Le Heron (1992) claimed "good agreement" between the energy imparted and the effective dose in conventional radiography, although he did not present any values. He based his work on the NRPB organ dose data (Jones and Wall 1986).

Alm Carlsson and Carlsson (1986) discussed the merits of using a quantity called the *mean absorbed dose* $\overline{D}$, given as $\overline{D} = \varepsilon/M$, where ε is the total energy imparted and M is the mass of the patient. In a homogeneous whole-body exposure, the ratio of $H_E/\overline{D}$ would be 1.0 Sv/Gy, which corresponds to a H_E/ε ratio of 14.3 mSv/J for a 70 kg patient or phantom. The authors analyzed studies of patient dose in radiology (Laws and Rosenstein 1978, Rosenstein 1982, Huda 1984, and Stentström *et al.* 1986) and concluded that in *all cases*, the ratios $H_E/\overline{D}$ were in the range of 0.44 Sv/Gy to 2.8 Sv/Gy with a mean near 1.0 Sv/Gy. For a 70 kg patient or phantom, these values represent H_E/ε

Table 1-2: Ratios of the effective dose equivalent to the energy imparted for different exams and scanners.

	H_E/ε ratios in mSv/J		
Exam type	**EMI 5005**	**GE 9800**	**Siemens DRH**
Head	10.5	16.9	16.5
Chest	28.1	19.5	21.5
Abdomen	14.2	23.5	21.5
Pelvis	17.8	29.4	24.1

The values shown for the EMI scanner are based on data from Huda (1984) and Huda and Sandison (1986). The data for the GE and Siemens scanners are from a private communication from Dr. P.C. Shrimpton of the NRPB.

ratios of 6.3 mSv/J to 40 mSv/J with a mean near 14.3 mSv/J. The radiological studies included in this assessment all involved examinations of the head and trunk.

In the specific area of CT imaging, Huda (1984) investigated the relationship between energy imparted and risk for four standard exams in CT. The risk estimates were based on those of the ICRP (ICRP 1977). He based his conclusions on measurements made in an anthropomorphic phantom scanned in an EMI 5005 scanner. The results were also used to calculate H_E values for the exams (Huda and Sandison 1986). The ratios of H_E/ε based on these two works are shown in Table 1-2. Also included in Table 1-2 are values of H_E/ε for the GE9800 and Siemens DRH, obtained from Dr. P.C. Shrimpton of the NRPB Medical Dosimetry Group in the United Kingdom. The GE and Siemens data are based on the NRPB CT organ dose study (Shrimpton *et al.* 1991 and Jones *et al.* 1991). The values for the GE and Siemens units are based on the same scan protocols (mAs, slice width, number of slices) as used in the EMI exams.

The values of H_E/ε shown in Table 1-2 are in the range of H_E/ε values derived from the Alm Carlsson and Carlsson data, although somewhat larger. The data for the two more modern scanners are quite consistent. These data show how energy imparted values may be employed to estimate the effective dose equivalent for given irradiation conditions. By combining the data in Table 1-2 with values of the energy imparted in the different

anatomic regions, it should be possible to make estimates of the effective dose equivalent for a wide variety of possible exposure conditions.

The overall goal of this project is provision of the fundamental knowledge necessary for the development of a method allowing a simple and convenient way of estimating the energy imparted per CT slice. Values of the energy imparted may then be used as an index of stochastic risk. The organ dose studies cited above provide data for only a limited number of exam types and scanner types. A more generalized method, employable by clinical medical physicists without access to specialized and costly dosimetry systems, would provide a way of estimating a risk-based index for non-standard or newly established exams or CT scanners. The energy imparted per CT slice has the advantage of being independent of both the number of slices and the exact anatomic location of each slice. Energy imparted values and subsequent risk estimates can be used for exam optimization, intercomparisons between different imaging modalities, and population-based studies of detriment.

The basis of this project is the assumption that the energy imparted can be used as an index of the stochastic risk to a patient. This assumption is clearly justified on the basis of the works cited above. Furthermore, Carlsson and Alm Carlsson (1990) have stated that, for risk estimates, only crude dosimetry is necessary. The wide availability and use of CTDI phantoms make them an attractive object to study. However, the question of how closely CTDI phantoms model actual patients or anthropomorphic phantoms has not yet been determined. This work therefore studies the factors that determine how much energy is deposited in both CTDI and anthropomorphic phantoms and the patterns of that energy deposition. Quantified estimates of the energy imparted to anthropomorphic phantoms are compared to the energy deposited in CTDI phantoms.

This study uses the EGS Monte Carlo system to investigate patterns of energy deposition in phantoms (Nelson *et al.* 1985). The influence of beam energy, beam

filtration, phantom size, phantom composition, source-to-axis distance (SAD), and slice thickness on the pattern of energy distribution is systematically determined.

The variables studied are listed in Table 1-3. Each of the parameters was varied over the stated range with the remaining variables held constant at their default value. For each run (i.e., a series of Monte Carlo simulations with identical initial parameters), the energy deposition pattern is found as a function of radial and longitudinal position within the phantom. The dose to each position is calculated, as are line integrals of the dose. The doses as well as the energies deposited in regions of the phantom are normalized to the dose measured in a small acrylic rod placed at the isocenter of the hypothetical scanner. In addition, the Monte Carlo method allows labeling of photons so as to differentiate between scattered and primary contributions to any quantity of interest, therefore allowing identification of scattered and primary components of the energy deposited and of the energy exiting the phantom. Calculations performed in this manner allow the study of the nature of the dose distributions in a way that is not practical by physical measurement. The CTDI is investigated as a function of radius and as a function of the integration limits. The relationship between the CTDI and the energy imparted is studied for the range of irradiation conditions considered.

The first step in this project was to determine the ranges of variation of the important characteristics of CT scanners. Although this study uses a simplified model of CT scanners, it is desirable to base the mathematical model on realistic geometries and characteristics. Results from the study are then more pertinent to clinical situations. To accomplish this goal, a survey form was mailed to several CT manufacturers that asked for descriptions of their scanners. The results provided a good overview of the characteristics of common CT scanners in clinical use. The results from the survey were used in determining both the range of values and the default values of the important scanner characteristics in the Monte Carlo calculations.

Table 1-3: The range of parameters examined in this work.

Parameter	*default*	*Range investigated*
Beam Energy	50 keV	40, 50, 60, 80, 100, 120, 140 keV, typical spectra
Beam Filter	none	none, perfect[4], GE9800
Slice Thickness	5 mm	1, 2, 3, 5, 10 mm
Phantom Material	acrylic	acrylic, water, bone, fat, lung, muscle[5]
Phantom Radius	8, 16 cm	6, 8, 10, 12, 14, 16, 20 cm
SAD	65 cm	50, 65, 80 cm
Phantom Type	CTDI	CTDI, anthropomorphic-analog

This dissertation is organized in the following way. The results from the CT manufacturer survey are presented in Chapter 2. Chapter 3 provides a background of the past uses of Monte Carlo simulation in diagnostic radiological physics and describes the basic techniques of Monte Carlo simulation. The EGS system, along with the details of the models used in this work, are presented in Chapter 4. The accuracy of the Monte Carlo model is verified in Chapter 5. Chapter 6 introduces a new quantity, the Generalized CTDI (GCTDI), and presents the results concerning dose deposition patterns, the relationship of the energy imparted to the GCTDI, and the variation of the GCTDI as a function of the variables in Table 1-2. The results concerning the energy imparted to phantoms are presented in Chapter 7. Chapter 8 discusses the results and presents conclusions concerning the entire study.

---

[4] A perfect filter is constructed such that the total path length for any ray emerging from the x-ray source within the fan beam is constant. For a right cylindrical cylinder of radius R with long axis normal to the scan plane, the filter thickness t is found from $2R = t + L$ where L is the path length through the cylinder.

[5] In this category the phantoms are assumed to be of the same dimensions as the CTDI phantoms but comprised of the different materials listed. The material data were obtained from ICRU Report No. 44 (ICRU 1989).

CHAPTER 2

SURVEY OF COMMON CT SCANNER CHARACTERISTICS

Introduction

The first step in this project was to determine the ranges of variation of the characteristics of CT scanners. This study uses a simplified mathematical model of CT scanners which is based on realistic geometries and characteristics. A survey form was mailed to several CT manufacturers which asked for descriptions of their scanners. The results provided a good overview of the characteristics of common CT scanners in clinical use. The results from the survey were used in determining the both the range of values studied and the default values of the scanner characteristics.

Basic Operational Principles

Computed tomography was introduced to the radiology community in the early 1970s. The modality's explosive growth is illustrated by the fact that approximately 2.2 million CT studies were performed in hospitals in 1980, only seven to eight years after the first commercial CT units became available (Bunge and Herman 1987). CT is now considered an essential element in radiological imaging.

In a computed tomography examination, the patient is exposed to a highly collimated beam of x rays at a number of angular increments. The transmitted x rays are absorbed by a series of detectors, and the data from these projections are used to create a two-dimensional map of linear attenuation coefficients, i.e., an image.

The configuration of x-ray tube, x-ray detectors, and the manner in which these elements are moved, has changed through several so-called "generations." The first CT scanner, introduced by Hounsfield (1973), had a single detector and a pencil x-ray beam, which moved in a translate-rotate manner, i.e., the detector and x-ray tube translated along a line parallel to the image plane acquiring data. The tube and detector were then rotated one degree, and the process repeated. To overcome the problems of slow scan times and poor resolution, a second generation was devised with multiple detectors and a small fan-shaped x-ray beam. The second generation retained the original translate-rotate motion.

In the third generation of CT scanners, the translate motion of the tube and detectors was replaced with a rotate-only motion. A broad fan-shaped x-ray beam is used with several hundred detectors, and the entire tube-detector system rotates around the machine's isocenter. The fourth generation CT scanner has stationary detectors, and only the x-ray tube rotates around the patient.

Recently a new type of CT scanner has been developed by Imatron.[1] In these scanners, the patient lies on a large evacuated chamber. An electron beam is scanned across a series of small tungsten targets lining the interior of the evacuated chamber. These targets act like the anode in a standard x-ray tube and produce x rays which are collimated, transverse the patient, and are detected by an array of detectors. Both the tungsten targets and the array of detectors cover an arc of 210°. These machines have the advantage of fast (50 - 100 ms) scan times but have slightly poorer image quality than conventional CT scanners.

The following manufacturers provided information regarding their scanners: Elscint[2], Picker[3], Siemens[4], and General Electric[5] (GE). Elscint supplied data concerning four of their scanners, all third generation. Picker provided information on four of their

---

[1] Imatron, Inc., San Francisco CA 94080.
[2] Elscint Ltd., Haifa, Israel
[3] Picker International Inc., Highland Heights, OH 44143
[4] Siemens Medical Systems Inc., Iselin, NJ 08830
[5] GE Medical Systems, Milwaukee, WI 53201

fourth generation models. Siemens supplied data for three of their scanners, which are all third generation. GE provided data for two versions of the same model scanner.

Differences Among CT Scanners From Various Manufacturers

This section outlines the differences and similarities among scanners from different manufacturers. A questionnaire was designed to allow comparisons among scanners in physical construction, radiologic technique factors available, and reported CTDI. A copy of this questionnaire is presented in Appendix A. The questionnaire was sent to the major manufacturers of CT scanners. This questionnaire is the primary source of the information presented in this chapter; however, not all manufacturers complied with the request for complete information. The data provided are given in this section. One manufacturer did not return the questionnaire; and one supplied the data requested, with the exception of a description of their beam-shaping filter. These missing data are described below.

The sections below describe the features of the various CT scanners provided by the manufacturers. Two tables summarize the CTDI data at the end of the section. (Note that the electrical potential across the x-ray tube is abbreviated as "kVp", the current through the x-ray tube is represented by "mA", and the product of the exposure time and the tube current is abbreviated as "mAs".)

ELSCINT EXEL 2400 Elite/2400E

Radiologic technique factors available: Four peak tube potentials are available: (100, 120, 130, and 140 kVp); however, Elscint recommends that only 120 and 140 kVp be used routinely. The tube currents available are 50, 100, 120, 150, and 200 mA, and the scan times available are 0.5, 1, 2, 4, and 8 s, with 1 to 4 s routinely used. The generator is 3-phase with continuously-supplied voltage.

Tube characteristics: There are two focal spots of nominal sizes 1.5 mm x 1.4 mm and 0.8 mm x 1.4 mm. The manufacturer specified neither the criteria used for focal spot

size selection nor the orientation of focal spot sizes with respect to the anode-cathode axis. The anode angle is 7°, and the anode is constructed of tungsten-on-graphite composite.

Geometry: The four slice thicknesses available (1.2, 2.5, 5, and 10 mm) are specified at the isocenter. The fan beam arc is 22°. The source-to-isocenter distance is 63 cm, and the isocenter-to-detector distance is 46 cm. The scanner is third-generation with three scan angles (202°, 360°, 382°) available, although 360° and 382° are routinely used. The beam is oriented such that heel effect intensity variation is not present in the scan plane. The gantry tilt angles were not supplied.

Filtration: The inherent filtration is equivalent to 1.1 mm Al equivalent at 100 kVp. The unit has both a flat, fixed, added filter and a shaped compensating filter, the details of which are proprietary. The couch attenuation is equivalent to 1.4 mm Al (the kVp was not specified).

CTDI: The CTDI for the head phantom using the recommended head technique (120 kVp, 300 mAs, 10 mm) is 3.9 cGy (13.0 mrad/mAs) in the center and 4.6 cGy (15.3 mrad/mAs) in the 12 o'clock (maximum value) position. For the body phantom and technique, the CTDI is 1.7 cGy (5.4 mrad/mAs) in the center and 3.6 cGy (11.4 mrad/mAs) at 12 o'clock (140 kVp, 315 mAs, 10 mm). Elscint has provided CTDI slice-width and voltage dependence data. The maximum deviation from the specified CTDI values is ±20%.

ELSCINT 2400

Radiologic technique factors available: Four peak tube potentials are available (100, 120, 130, and 140 kVp); however, Elscint recommends that only 120 and 140 kVp be used routinely. The tube currents available are 50, 100, 120, 150, and 200 mA, and the scan times available are 0.5, 1, 2, 4, and 8 seconds, with 1 to 4 s routinely used. The generator is 3-phase with continuously-supplied voltage.

Tube characteristics: There are two focal spots of nominal sizes 1.5 mm x 1.7 mm and 0.8 mm x 1.7 mm. The anode angle is presently 10° (although it will be changed to 7° in the near future, according to the manufacturer), and the anode is constructed of tungsten on graphite composite. Again, neither the orientation of the focal spots nor the criteria used for focal spot size selection were specified.

Geometry: The four slice thicknesses available (1.2, 2.5, 5 and 10 mm) are specified at the isocenter. The fan beam arc is 22°. The source-to-isocenter distance is 63 cm, and the isocenter-to-detector distance is 46 cm. The scanner is third-generation with three scan angles (202°, 360°, 382°) available, although 360° and 382° are routinely used. The beam is oriented such that heel effect intensity variation is not present in the scan plane. The gantry tilt angles were not supplied.

Filtration: The inherent filtration is 1.1 mm Al equivalent at 100 kVp. The unit has both a flat, fixed, added filter and a shaped compensating filter, the details of which are proprietary. The couch attenuation is 1.4 mm Al equivalent (at an unspecified kVp).

CTDI: The CTDI for the head phantom using the recommended head technique (120 kVp, 300 mAs, 10 mm) is 3.8 cGy (12.7 mrad/mAs) in the center and 4.5 cGy (15 mrad/mAs) in the 12 o'clock (maximum value) position. For the body phantom and technique (140 kVp, 310 mAs, 10 mm), the CTDI is 1.6 cGy (5.2 mrad/mAs) in the center and 3.5 cGy (11.3 mrad/mAs) at 12 o'clock. Elscint has provided CTDI slice-width and voltage dependence data. The maximum deviation from the specified CTDI values is ±20%.

ELSCINT 1800

Radiologic technique factors available: Four peak tube potentials are available (100, 120, 130, and 140 kVp); however, Elscint recommends that only 120 and 140 kVp be used routinely. The tube currents available are 50, 100, 120, 150, and 200 mA, and the

scan times available are 0.5, 1, 2, 4, and 8 s, with 1 to 4 s routinely used. The generator is 3-phase with continuously-supplied voltage.

Tube characteristics: The nominal focal spot size is 1.5 mm x 17 mm. The anode angle is 10°, and the anode is constructed of tungsten-on-graphite composite.

Geometry: The three slice thicknesses available (2, 5, and 10 mm) are all specified at the isocenter. The fan beam arc is 22°. The source-to-isocenter distance is 63 cm, and the isocenter to-detector-distance is 46 cm. The scanner is third-generation, with three scan angles (202°, 360°, 382°) available, although 360° and 382° are routinely used. The beam is oriented such that heel effect intensity variation is not present in the scan plane. The gantry tilt angles were not supplied.

Filtration: The inherent filtration is equivalent to 1.1 mm Al at 100 kVp. The unit has both a flat, fixed, added filter and a shaped compensating filter, the details of which are proprietary. The couch attenuation is 1.4 mm Al equivalent at an unspecified kVp.

CTDI: The CTDI for the head phantom using the recommended head technique (120 kVp, 300 mAs, 10 mm) is 3.1 cGy (10.3 mrad/mAs) in the center and 3.6 cGy (12.0 mrad/mAs) in the 12 o'clock (maximum value) position. For the body phantom and technique (140 kVp, 310 mAs, 10 mm), the CTDI is 1.3 (4.2 mrad/mAs) cGy in the center and 3.1 cGy (10 mrad/mAs) at 12 o'clock. Elscint has provided CTDI slice-width and voltage dependence data. The maximum deviation from the specified CTDI values is ±20%.

GENERAL ELECTRIC 9800

The GE 9800 CT scanner is available with two different detector systems. The older version, with xenon detectors, has several different characteristics from the newer version, with "HiLight®" (solid state) detectors. These differences are noted where appropriate.

Three peak tube potentials available (80, 120, and 140 kVp); GE recommends 120 kVp for routine use. The tube currents available are 10, 20, 40, 70, 100, 120, 170, 200, 240, and 300 mA, and the scan times available are 2, 3, 4, and 8 s. The generator is 3-phase with continuously-supplied voltage.

Tube characteristics: The nominal focal spot size is 0.9 mm x 0.7 mm. The anode angle is 7°, and the anode is constructed of tungsten and rhenium on a titanium-zirconium-molybdenum substrate.

Geometry: The 9800 series are third generation scanners. The four slice thicknesses available are 1.5, 3, 5, and 10 mm, all specified at the isocenter. The fan beam arc is 45°. The beam is oriented such that heel effect intensity variation is not present in the scan plane. The source-to-isocenter distance is 63 cm, and the isocenter-to-detector distance is 47 cm. The gantry can tilt ±20°.

Filtration: The inherent filtration of the x ray tubes were not explicitly listed. However, the values of the half-value layers of the central rays are listed in Table 2-1 below.

CTDI: The CTDI of the 9800 varies with the type of detector. Solid State: The CTDI for the head phantom using the recommended head technique (120 kVp, 340 mAs, 10 mm) is 4.0 cGy (11.8 mrad/mAs) in the center and also 4.0 cGy (11.8 mrad/mAs) at 1 cm depth. For the body phantom and technique (120 kVp, 340 mAs, 10 mm), the CTDI is 1.1 cGy (3.2 mrad/mAs) in the center and 2.0 cGy (5.9 mrad/mAs) at 1 cm depth. Xenon: The CTDI for the head phantom using the recommended head technique (120 kVp, 340 mAs, 10 mm) is 5.0 cGy (14.7 mrad/mAs) in the center and 4.8 cGy (14.1 mrad/mAs) at 1 cm depth. For the body phantom and technique (120 kVp, 340 mAs, 10

Table 2-1: Half value layers for the GE 9800 scanner as function of detector and kVp.

Detectors	*80 kVp [mm Al]*	*120 kVp [mm Al]*	*140 kVp [mm Al]*
Solid State	3.9	6.2	7.1
Xenon	3.6	5.0	6.0

mm), the CTDI is 1.4 cGy (4.1 mrad/mAs) in the center and 2.5 cGy (7.4 mrad/mAs) at 1 cm depth. GE provided CTDI slice-width and voltage dependence data, although the maximum variation of the CTDI values were not provided.

PICKER 1200 SX

Radiologic technique factors available: The peak tube potentials available cover the range from 100 to 140 kVp in 5 kVp steps. The tube currents range from 5 to 200 mA in 15 mA increments, and the scan times available are 1 to 20 s. The generator waveform is high-frequency; the frequency was not provided.

Tube characteristics: The two nominal focal spot sizes are 0.5 mm x 1.65 mm and 0.9 mm x 2.4 mm. The orientations of the focal spots with respect to the scan plane were not indicated. The anode angle is 12°, and the anode is constructed of a tungsten-rhenium track on molybdenum.

Geometry: The slice thicknesses available range from 1 to 10 mm in 1 mm increments at the isocenter. The fan beam arc is 24° for head scans and 48° for body scans. The source-to-isocenter distance is 64 cm, and the isocenter-to-detector distance is 85 cm. The scanner is fourth-generation with three scan angles (220°, 360°, 398°) available, although only 360° is routinely used. The beam is oriented such that heel effect intensity variation is not present in the scan plane. The gantry can tilt ±20°.

Filtration: The inherent filtration is 3 mm Al equivalent at 100 kVp. The unit has both a flat, fixed, added filter and a shaped compensating filter, the details of which are proprietary and not disclosed. The couch attenuation is 0.8 mm Al equivalent at an unspecified kVp.

CTDI: The CTDI for the head phantom using the recommended head technique (130 kVp, 240 mAs, 10 mm) is 3.7 cGy (15.4 mrad/mAs) in the center position and 4.1 cGy (17.1 mrad/mAs) at 1 cm depth. For the body phantom and technique (130 kVp, 240 mAs, 10 mm), the CTDI is 1.5 cGy (6.3 mrad/mAs) in the center and 4.2 cGy (17.5

mrad/mAs) at 1 cm. Picker has provided CTDI slice-width, voltage dependence, slice thickness, added filtration and scan angle dependence data. The maximum deviation from the specified CTDI values is ±15%.

PICKER IQ Premier

Radiologic technique factors available: The only peak tube potential available is 130 kVp. The tube currents available are 20, 45, 65, 85, 105, and 125 mA, and the scan times available are 2 and 4 s. The solid-state, high-frequency generator is mounted on a rotating frame.

Tube characteristics: The nominal focal spot size is 0.9 mm x 2.0 mm. The anode angle is 12°, and the anode is constructed with a tungsten-rhenium track on molybdenum.

Geometry: The slice thicknesses available are: 2, 5, and 10 mm, all specified at the isocenter. The fan beam arc is 48°. The source-to-isocenter distance is 64 cm, and the isocenter-to-detector distance is 85 cm. The scanner is fourth-generation with two scan angles (360° and 379°) available, although 360° is routinely used. The beam is oriented such that heel effect intensity variation is not present in the scan plane. The gantry can tilt ±30°.

Filtration: The inherent filtration was specified to be 3 to 4 mm Al equivalent at 130 kVp. The unit has both a flat, fixed, added filter and a shaped compensating filter, the details of which are proprietary and not disclosed. The couch attenuation is 0.8 mm Al equivalent at an unspecified kVp.

CTDI: The CTDI for the head phantom using the recommended head technique (130 kVp, 260 mAs, 10 mm) is 4.2 cGy (16.2 mrad/mAs) in the center position and 3.9 cGy (15.0 mrad/mAs) in the 12 o'clock position. For the body phantom and technique (130 kVp, 260 mAs, 10 mm) the CTDI is 1.6 cGy (6.2 mrad/mAs) in the center and 3.5 cGy (13.5 mrad/mAs) at 12 o'clock. Picker has provided CTDI slice-width, voltage

dependence, slice thickness, added filtration and scan angle dependence data. The maximum deviation from the specified CTDI values is ±15%.

PICKER IQ and IQ T/C

Radiologic technique factors available: The only peak tube potential available is 130 kVp. The tube currents are 20, 45, 65, 85, 105, and 125 mA, and the scan times available are 2 and 4 s. The solid-state, high-frequency generator is mounted on a rotating frame.

Tube characteristics: The nominal focal spot size is 0.9 mm x 2.0 mm. The anode angle is 13.5°, and the anode is constructed with a tungsten-rhenium track on molybdenum.

Geometry: The slice thicknesses available are 2, 5, and 10 mm, all specified at the isocenter. The fan beam arc is 48°. The source-to-isocenter distance is 64 cm, and the isocenter-to-detector distance is 85 cm. The scanner is fourth-generation with two scan angles (360° and 379°) available, although 360° is routinely used. The beam is oriented such that heel effect intensity variation is not present in the scan plane. The gantry can tilt ±30°.

Filtration: The inherent filtration was specified as 3 to 4 mm Al equivalent at 130 kVp. The unit has both a flat, fixed, added filter and a shaped compensating filter, the details of which are proprietary and were not disclosed. The couch attenuation is 0.8 mm Al equivalent at an unspecified kVp.

CTDI: The CTDI for the head phantom using the recommended head technique (130 kVp, 260 mAs, 10 mm) is 4.7 cGy (18.1 mrad/mAs) in the center position and 4.4 cGy (16.9 mrad/mAs) in the 12 o'clock position. For the body phantom and technique (130 kVp, 260 mAs, 10 mm), the CTDI is 1.7 cGy (6.5 mrad/mAs) in the center and 3.9 cGy (15.0 mrad/mAs) at 9 o'clock. Picker provides CTDI slice-width, voltage dependence, slice thickness, added filtration and scan angle dependence data. The maximum deviation from the specified CTDI values is ±15%.

PICKER PQ-2000

Radiologic technique factors available: The peak tube potentials available are 80, 100, 120, 130, and 140 kVp. The tube currents are 30, 50, 65, 100, 125, 150, 175 and 200 mA, and the scan times available are 1, 1.5, 2, 3, and 4 s. The solid-state, high-frequency generator is mounted on a rotating frame.

Tube characteristics: There two nominal focal spot sizes are 0.9 mm x 2.4 mm and 0.6 mm x 1.65 mm. The anode angle is 12.5°, and the anode is constructed with a tungsten-rhenium track on molybdenum.

Geometry: The slice thicknesses available are 1.5, 2, 3, 4, 5, 8, and 10 mm, at the isocenter. The fan beam arc is 44°. The source-to-isocenter distance is 64 cm, and the isocenter-to-detector distance is 85 cm. The scanner is fourth-generation with a scan angle of 360°. The beam is oriented such that heel effect intensity variation is not present in the scan plane. The gantry can tilt ±30°.

Filtration: The inherent filtration is 3 mm Al equivalent at 100 kVp. The unit has both a flat, fixed, added filter and a shaped compensating filter, the details of which are proprietary and were not disclosed. The couch attenuation is 0.8 mm Al equivalent at an unspecified kVp.

CTDI: Picker has indicated that the CTDI report for the PQ-2000 is not complete but that the CTDI values can be expected to be similar to those for the IQ. The CTDI for the head phantom using the recommended head technique (130 kVp, 250 mAs, 10 mm) is 4.7 cGy (18.8 mrad/mAs) in the center position and 4.4 cGy (17.6 mrad/mAs) in the 12 o'clock position. For the body phantom and technique (130 kVp, 250 mAs, 10 mm), the CTDI is 1.7 cGy (6.8 mrad/mAs) in the center and 3.9 cGy (15.6 mrad/mAs) at 9 o'clock. Picker has provided CTDI slice-width, voltage dependence, slice thickness, added filtration and scan angle dependence data. The maximum deviation from the specified CTDI values is ±15%.

SIEMENS Somatom PLUS

Radiologic technique factors available: The peak tube potentials available are 80, 120, and 137 kVp. The tube currents available are 70 to 300 mA (the increments were not specified), and the scan times available are 0.7, 1, 2, 3, 4, 5, and 6 s. The generator has a high-frequency waveform.

Tube characteristics: The nominal focal spot size is 1.1 mm x 1.8 mm. The anode angle is 10°, and the anode is tungsten-on-graphite.

Geometry: The slice thicknesses available are 1 through 10 mm in 1 mm increments, specified at the isocenter. The fan beam arc is 42°. The source-to-isocenter distance is 70 cm, and the isocenter-to-detector distance was not supplied. The scanner is third-generation with two scan angles (360° and 240°) available, although 360° is routinely used. The beam is oriented such that heel effect intensity variation is not present in the scan plane. The gantry can tilt ±25°.

Filtration: The inherent filtration is 2.5 mm Al equivalent at 120 kVp. The unit has only a flat, fixed, added filter, which is 0.2 mm Cu. The couch attenuation is 1.2 mm Al equivalent at an unspecified kVp.

CTDI: The CTDI for the head phantom using the recommended head technique (120 kVp, 500 mAs, 10 mm) is 3.9 cGy (7.7 mrad/mAs) in the center position and 5.0 cGy (9.9 mrad/mAs) at the 1 cm-depth position. For the body phantom and technique (120 kVp, 290 mAs, 10 mm), the CTDI is 1.2 cGy (4.1 mrad/mAs) in the center and 2.8 cGy (9.6 mrad/mAs) at 1 cm depth. Siemens provides CTDI slice-width, voltage dependence, slice thickness, and scan angle dependence data. The expected variations in CTDI values are given as ±15%.

SIEMENS Somatom HiQ

Radiologic technique factors available: The peak tube potentials available are 85, and 133 kVp. The tube currents are 70 to 225 mA (the increment was not specified), and

the scan times available are 1.3, 2, 2.7, 4, and 8 s. The generator has a high-frequency waveform.

Tube characteristics: The nominal focal spot size is 1.8 mm x 1.8 mm. The anode angle is 10°, and the anode is tungsten-on-graphite.

Geometry: The slice thicknesses available are 1 through 10 mm (the increment was not specified) at the isocenter. The fan beam arc is 42°. The source-to-isocenter distance is 70 cm, and the isocenter-to-detector distance was not supplied. The scanner is third-generation with two scan angles (360° and 240°) available, although 360° is routinely used. The beam is oriented such that heel effect intensity variation is not present in the scan plane. The gantry can tilt ±25°.

Filtration: inherent filtration is 2.5 mm Al equivalent at 120 kVp. The unit has only a flat, fixed, added filter, which is 0.1 mm Cu. The couch attenuation is 1.2 mm Al equivalent at an unspecified kVp.

CTDI: The CTDI for the head phantom using the recommended head technique (133 kVp, 350 mAs, 5 mm) is 4.1 cGy (11.7 mrad/mAs) in the center position and 5.3 cGy (15.1 mrad/mAs) at the 1 cm-depth position. For the body phantom and technique (133 kVp, 225 mAs, 10 mm), the CTDI is 1.2 cGy (5.2 mrad/mAs) in the center and 2.4 cGy (10.7 mrad/mAs) at 1 cm depth. Siemens provides CTDI slice-width, voltage dependence, slice thickness, and scan angle dependence data. The expected variations in CTDI values are given as ±15%.

SIEMENS Somatom CRX

Radiologic technique factors available: The only peak tube potential available is 125 kVp. Neither the tube currents nor the scan times were provided. The high-frequency generator pulses the tube potential at a frequency of 360 pulses per second.

Tube characteristics: The nominal focal spot size is: 1.6 mm x 1.6 mm. The anode angle is 10°, and the anode is tungsten-on-graphite.

Geometry: The slice thicknesses available are 2, 4, and 8 mm, specified at the isocenter. The fan beam arc is 32°. The source-to-isocenter distance is 70 cm, and the isocenter-to-detector distance was not supplied. The scanner is third-generation with a scan angle of 360°. The beam is oriented such that heel effect intensity variation is not present in the scan plane. The gantry can tilt ±25°.

Filtration: The inherent filtration is 2.2 mm Al equivalent at 125 kVp. The unit has only a flat, fixed, added filter, which is 0.2 mm Cu. The couch attenuation is 1.2 mm Al equivalent at an unspecified kVp.

CTDI: Only the surface CTDI values were supplied by Siemens. The CTDI for the standard head technique (125 kVp, 550 mAs, 8 mm) is 4.7 cGy (8.6 mrad/mAs). The CTDI for body scans is 2.6 cGy (8.0 mrad/mAs) using the standard technique (125 kVp, 330 mAs, 8 mm).

Data Not Obtained

Below is the list of data not provided by the manufacturers.

PHILIPS: All Models

Philips has not returned the questionnaire.

PICKER: All Models

Picker has returned the questionnaire but has refused to provide the construction details of their shaped compensating filter(s).

SIEMENS: Somatom CRX

Neither the available tube currents nor scan times were supplied.

Summary

The CT system information above may be summarized as follows. According to the manufacturers' recommendations, most scanners use 360° rotation of the tube, continuous voltage supply, and very similar peak tube voltages. In addition, the source-to-isocenter distances are similar (between 63 and 70 cm) as well; this indicates the x-ray output for different scanners (specified at a given distance) would depend primarily on the filtration present. The major difference among the scanners is the type of x-ray beam filtration, i.e., the presence or absence of a beam-shaping filter. The presence of a shaped compensating filter is expected to produce a more homogeneous depth-dose distribution pattern in the phantom than the use of a flat filter because of the preferential filtering of the beam near the periphery of the phantom. The variation in depth dose distributions can be seen from inspection of the ratios of the CTDI at the central position to the CTDI at the 1 cm depth position. Table 2-2 below lists the CTDI for typical exams as a function of mrad per mAs for the head exam in the center of the phantom and at 1 cm depth.[6] Table 2-3 lists the CTDI for body exams as function of mrad per mAs as measured in the center and at 1 cm depth. Note that the mrad/mAs values are listed for the manufacturer-recommended technique.

The head-CTDI data in Table 2-2 show that the Picker units, all fourth generation scanners, produce larger CTDI values than do the other units which are all third generation scanners. Also, the effects of the shapes and materials of the beam-shaping filters are readily observed. The Siemens units have only a fixed, flat filter, and the ratios of the central-to-peripheral CTDI values are smaller than for any other manufacturer's scanner. This situation is contrasted with the GE 9800-series — the ratio of the CTDI values is almost unity. The ratios for the Picker units are also close to one with the exception of the 1200SX. The 1200SX presumably has a beam-shaping filter of a

[6] The unit mrad/mAs, while a non-SI unit, is commonly used in clinical medical physics and for convenience will be used here.

different design than do the other Picker units. The Elscint units have ratios between the values of the Siemens units and the GE and Picker units, demonstrating the effects of differences in the filter designs.

The body-CTDI data in Table 2-3 show that the fourth generation Picker scanners also produce larger CTDI values than do the third generation scanners. In general, the effect of the beam-shaping filter is reduced. All of the units, including the Siemens scanners with no beam-shaping filter, have central-to-peripheral CTDI ratios of approximately 0.35 to 0.55. The Picker 1200SX has smaller ratio than the other Picker units do, again illustrating a probable difference in beam-filtration.

Table 2-2: Comparison of head CTDI values [mrad/mAs]. Values are derived from the manufacturer's recommended technique.

Manufacturer/Model	**Center**	**1 cm**	**Ratio‡**
Elscint			
Exel 2400 Elite/E	13.0	15.3	0.85
2400	12.7	15.0	0.85
1800	10.3	12.0	0.86
General Electric			
9800 - Xenon	14.7	14.1	1.04
9800 - Hilight	11.8	11.8	1.00
Picker			
1200SX	15.4	17.1	0.90
IQ Premier	16.2	15.0	1.08
IQ, IQ T/C	18.1	16.9	1.07
PQ2000	18.8	17.6	1.07
Siemens			
Somatom Plus	7.7	9.9	0.78 *
Somatom HiQ	11.7	15.1	0.78 *
Somatom CRX	**	8.6	

‡ CTDI at center ÷ CTDI at 1 cm depth

* 5 mm slice thickness

** not supplied

Table 2-3: Comparison of body CTDI values [mrad/mAs]. Values are derived from the manufacturer's recommended technique.

Manufacturer/Model	**Center**	**1 cm**	**Ratio‡**
Elscint			
Exel 2400 Elite/E	5.4	11.4	0.47
2400	5.2	11.3	0.46
1800	4.2	10.0	0.42
General Electric			
9800 - Xenon	4.1	7.4	0.55
9800 - Hilight	3.2	5.9	0.54
Picker			
1200SX	6.3	17.5	0.36
IQ Premier	6.2	13.5	0.46
IQ, IQ T/C	6.5	15.0	0.43
PQ2000	6.8	15.0	0.45
Siemens			
Somatom Plus	4.1	9.6	0.43
Somatom HiQ	5.2	10.7	0.49
Somatom CRX	**	8.0	

‡ CTDI at center ÷ CTDI at 1 cm depth
** not supplied

CHAPTER 3

THE MONTE CARLO TECHNIQUE

Introduction

The Monte Carlo method is a calculational technique that utilizes random sampling to solve problems numerically that may be difficult or impossible to solve analytically. Radiation transport is simulated in the Monte Carlo technique by following individual particles on a "random walk" through given geometries and media. The term particle, as used here, refers to either photons or electrons. Random numbers are used to sample the probability distributions that describe particle behavior. By recording events of interest that occur during a large number of these random histories, one may accumulate average values for the events or quantities of interest (Cashwell and Everett 1959). In contrast to analytic methods, Monte Carlo simulation can use realistic cross sections, model realistic beam conditions, and model complex geometries (Chilton *et al.* 1984). The price paid for using the method is lengthy calculational times. Monte Carlo simulation can also assess quantities that cannot be physically measured, e.g., the percentage of dose contributed by Compton interaction recoil electrons (Ito 1988).

The Monte Carlo method has been used in the studies of nuclear medicine physics, radiation oncology physics, diagnostic radiological physics, and in radiation protection. Use of the method has increased greatly with the advent of small, powerful computers and the availability of several general-purpose Monte Carlo codes to the medical physics community (Andreo 1991). As an illustration of the explosive growth the method has seen in the field of radiological physics, consider the following. A review of uses of the

method by Raeside in 1976 had 86 references. In 1991 Andreo reviewed work in the field since the Raeside paper and had 299 references in a list ten pages long (!).

In the field of diagnostic radiological physics the Monte Carlo method has been used to study both dosimetry and imaging. Dosimetry studies have investigated dose deposition in individual organs from specific radiographic examinations and in anthropomorphic phantoms. The absorbed dose from chest radiography was estimated using Monte Carlo methods by Koblinger and Zaràndi (1973). Doi and Chan (1980) used the method to evaluate absorbed dose in film/screen mammography. Morin produced a Monte Carlo model of a CT scanner in 1980 to investigate artifact removal but did not consider patient dose. Dance (1984) used the method to calculate integral dose (energy imparted) in xeromammography. Patient dose from dental radiography was estimated by Gibbs *et al.* (1984) using a method described by Pujol and Gibbs (1982). In 1983 Beck *et al.* published a work describing a Monte Carlo model for estimating integral dose in CT examinations. The method used by Beck *et al.* was based on a simple elliptical, homogeneous phantom and estimated integral dose to large volumes of the phantom. They did not, however, do any direct measurements in a phantom to verify their calculation, and did not take into account fan beam intensity variations.

Several investigations have used Monte Carlo methods to estimate organ doses in anthropomorphic phantoms from a wide range of diagnostic radiological procedures. Rosenstein (1976) reported on the use of the Medical Internal Radiation Dose (MIRD) phantom to calculate organ doses from simple radiographic exams. The phantom used simple mathematical expressions to model the shapes and sizes of various internal organs. In 1985 Jones and Wall of the NRPB in the United Kingdom published a study that was similar to Rosenstein's in method. They used the MIRD phantom with modifications suggested by Christy (1980), e.g., breasts were incorporated. The results of the study were similar to Rosenstein's, although some differences occurred and were attributed to differences in x-ray spectra and phantom geometry. Kramer *et al.* (1982) at the

Gesellschaft für Strahlen-und Umweltforschung (GSF) in Germany produced patient organ dose data based on Monte Carlo simulations with male and female anthropomorphic phantoms (ADAM and EVA), similar to the MIRD phantom. In 1985 Drexler *et al.* produced a set of tables which allow estimation of organ dose based on calculations with the ADAM and EVA phantoms. The results for simple radiographic exams are similar to those of Rosenstein's and Jones and Wall. In addition, organ dose data for CT were included for pelvis, liver, lung, and head exams. These data were described in Chapter 1. The NRPB study (Jones *et al.* 1990, Shrimpton *et al.* 1990) of CT organ doses lists organ doses for a range of standard examinations and CT scanners.

Sampling Methods

In the Monte Carlo method of numerical analysis, statistical results are obtained by sampling appropriate probability distributions. The general methods with which probability distributions are sampled are described in this chapter. The next chapter describes the specific probability distributions and the sampling methods used in the EGS Monte Carlo system, which is a general purpose, public domain code. The following treatment is based on that of Carter and Cashwell (1975) and Chan (1981).

Monte Carlo simulation constructs a set of random samples $\{x_i\}$ based on a set of random numbers $\{r_i\}$ that are uniformly distributed on the unit interval. The samples $\{x_i\}$ are distributed according to a *probability density function,* or PDF, $p(x)$ such that:

$p(x)\,dx$ = the probability that any x_i will lie between x and $x+dx$.

We may also define the *cumulative distribution function,* or CDF, $P(x)$ in terms of $p(x)$:

$$P(x) = \int_{-\infty}^{x} p(y)dy \qquad (3\text{-}1)$$

which is the sum of probabilities of x_i falling inside each infinitesimal interval between -∞ and x. Because the probabilities of mutually exclusive events are additive, $P(x)$ is interpreted as the probability that any given x_i is less than x. The function $P(x)$ is non-

decreasing in x, because $p(x) \geq 0$ for all x. The probability integrated along all possible outcomes is unity.

The properties of probability distribution functions and cumulative distribution functions are used in the three sampling methods described below.

Inversion Method of Sampling

Assume that a given series of events $E_1, E_2, \ldots, E_n$ are mutually exclusive and have probabilities $p_1, p_2, \ldots, p_n$ such that $\Sigma p_i = 1$. Such a series of events may be the type of interaction a photon undergoes — the occurrence of a photoelectric absorption, for instance, precludes the occurrence of any other type of interaction. If a random number ζ, uniformly distributed on the unit interval, is selected such that

$$p_1 + p_2 + \cdots + p_{i-1} \leq \zeta < p_1 + \cdots + p_i$$

then the random number ζ uniquely determines the event E_i. Next, a probability density function $p(x)$ can be constructed such that $p(x) = p_i$, with the understanding that x is mapped on the interval $0 \leq x \leq n$ to the events $E_1 \ldots E_n$, and that event E_i is determined from $(i-1) \leq x < i$. The function $p(x)$ is a step function such as that depicted in Fig. 3-1. If the PDF is normalized, the sum of the rectangular areas must be unity. We next define a cumulative distribution function $P(x)$ which is written as

$$P(x) \equiv \int_0^x p(x')\,dx' \qquad (0 \leq x \leq n) \tag{3-2}$$

and shown in Fig. 3-2. Obviously $P(0) = 0$ and $P(n) = 1$. Also, since $P(i) = p_1 + \ldots + p_i$, the term $P(x)$ can be interpreted as $\Pr\{\hat{x} < x\}$, i.e., the probability that any randomly selected value of x is less than a given x. Furthermore, if a random number $\zeta \in [0,1]$ is selected and the equation

$$\zeta = P(x) = \int_0^x p(y)dy \tag{3-3}$$

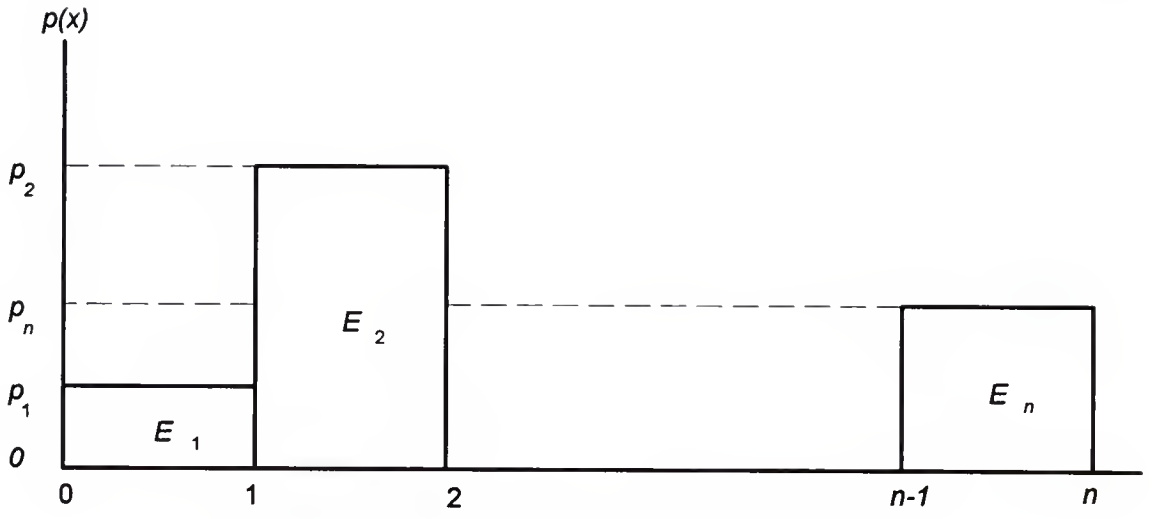

Figure 3-1: Discrete probability density function.

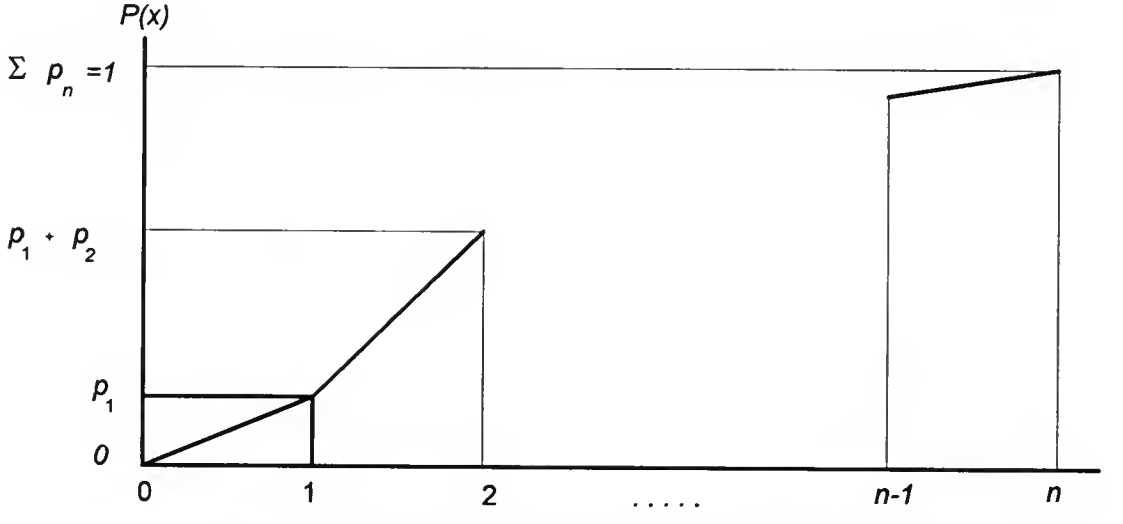

Figure 3-2: Discrete cumulative probability distribution.

is solved for x, x will fall on the interval $(i-1) \le x < i$ with frequency p_i, thereby determining a value for i and thus determining event E_i.

The discrete case can be extended to the continuous case (see Figure 3-3) by making the step size of $p(x)$ arbitrarily small. If Δx is an infinitesimally small increment of x, and x is given in the range $[x,x+\Delta x]$, then the CDF is given by definition. That is, as Δx approaches zero, the probability that x falls between x and $x+\Delta x$ is approximated by

$$\begin{aligned} P(x+\Delta x) - P(x) &= \frac{dP(x)}{dx}\Delta x \\ &= p(x)\Delta x. \end{aligned} \tag{3-4}$$

If ζ is a random number and if $p(x)$ is defined over the interval $a \le x < b$, then

$$\zeta = P(x) = \int_a^x p(y)dy \tag{3-5}$$

determines x as a function of ζ, x representing a random sample of the function $p(x)$.

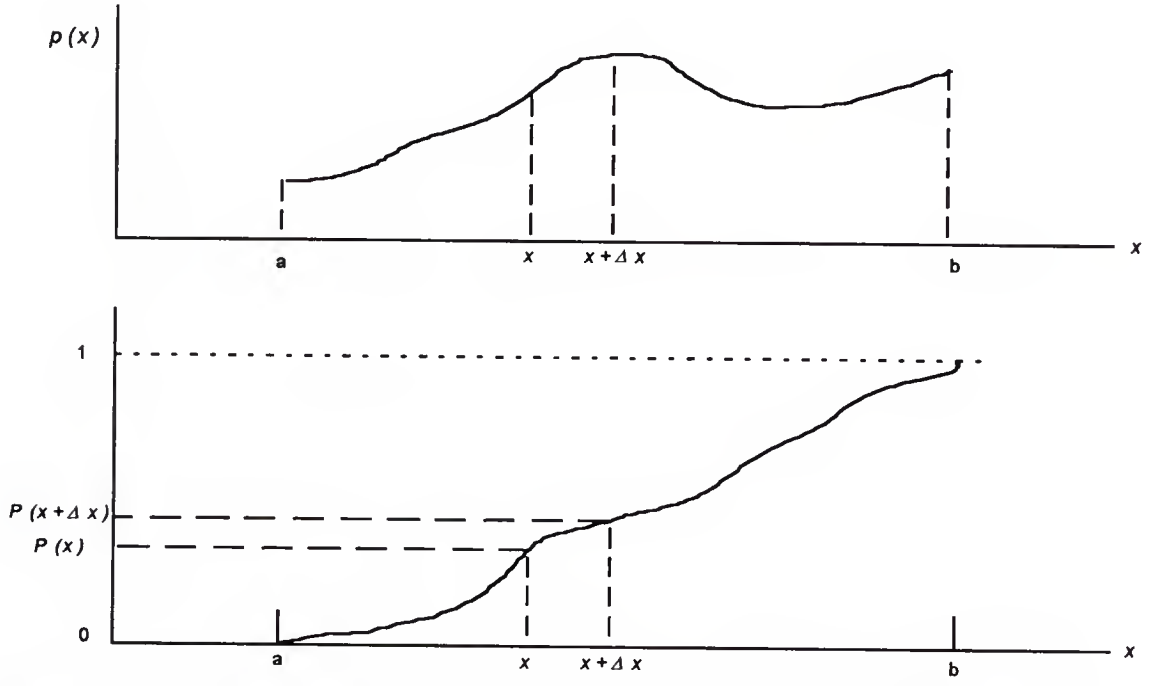

Figure 3-3: *top:* Continuous probability distribution; *bottom:* cumulative distribution functions.

Rejection Method of Sampling

The rejection method was first described by Kahn (1950). The method is used in situations in which the probability distribution function $p(x)$ is bounded and calculable. If $p(x)$ is defined on an interval $[a,b]$ and M is the maximum value of $f(x)$ on the interval $[a,b]$, then the function $p^*(x)$ can be defined such that

$$p^*(x) = p(x)/M. \tag{3-6}$$

Next, two random numbers, ζ_1 and ζ_2 are generated, and x^*, a possible value for x, is computed from $x^* = a + \zeta_1(b - a)$. If $\zeta_2 \leq p^*(x^*)$, then the value of x^* is accepted; if not the process is repeated. A rigorous proof of the rejection method is given by Spanier and Gelbard (1969).

The efficiency of the method is defined as the probability that a given set of random numbers is not rejected. The efficiency E is simply the ratio of the area under the curve $p(x)$ to the area under the circumscribing rectangle and is given by

$$E = \frac{p(x)}{M(b-a)}. \tag{3-7}$$

Clearly PDFs that are "spiked" are not efficiently sampled using the rejection method. Such PDFs may be sampled using the composition method, described below. The rejection method is illustrated graphically in Figure 3-4.

Composition Method of Sampling

The composition method has been described by Carter and Cashwell (1975), Nelson *et al.* (1985), and Williamson (1988). If a PDF $p(x)$ can be put in the form of

$$p(x) = \sum_{i=1}^{n} \alpha_i f_i(x) g_i(x) \tag{3-8}$$

where $f_i(x)$ and $g_i(x)$ are PDFs, $g_i(x) \in [0,1]$, and α_i are positive real numbers, then $p(x)$ can be sampled as follows. A random number ζ_1 is chosen and i is found such that

$$\sum_{j=1}^{i-1}\alpha_j < \zeta_1 \sum_{j=1}^{n}\alpha_j \le \sum_{j=1}^{n}\alpha_j \ . \tag{3-9}$$

Next, a sampled value x^* from $f_i(x)$ is selected. For example, if $f_i(x)$ is sampled using the direct method described above, then x^* is found from

$$\zeta_2 = \int_{-\infty}^{x^*} f_i(x)\,dx \tag{3-10}$$

where ζ_2 is a random number. Finally, another random number ζ_3 is chosen. If $\zeta_3 < g_i(x^*)$, then x^* is accepted; if not, the process is started again.

Random Number Generation

The basis of all Monte Carlo simulations is the availability of a long sequence of numbers such that the occurrence of each number in the sequence is unpredictable and the

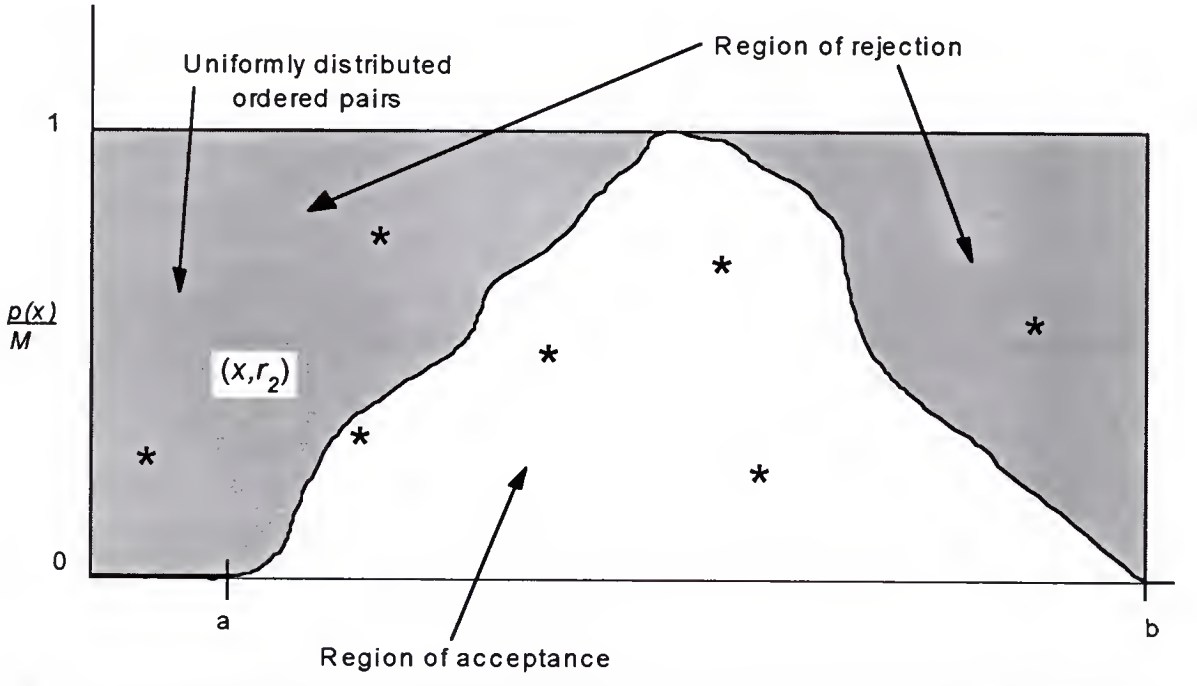

Figure 3-4: An illustration of the Rejection Method. Only the random pairs that fall under the curve are accepted.

sequence of numbers will pass statistical tests designed to detect departures from randomness (Hammersley And Handscomb 1964). Series of random numbers are available from published tables (Tippett 1927, Rand Corporation 1955), physical sources (James And Arnason 1973), and algorithms (Knuth 1969).

Sequences of numbers obtained from an algorithm are called *pseudorandom* numbers to reflect their deterministic origin and are routinely used in modern Monte Carlo simulation (Morin *et al.* 1988). The algorithm used to produce random numbers in the EGS system is called the multiplicative-linear-congruential method (Lehmer 1951). Random integers I are generated according to

$$I_i = (aI_{i-1} + c) \bmod 2^k \tag{3-11}$$

where I_i is the i^{th} random integer in the sequence, a is multiplier, c is the increment, and k is the number of bits in the integers of the computer. In the EGS system, and on a 32-bit computer, the following values are used:

$a = 663608941$,

$c = 0$, And

$k = 32$.

The actual random number used in sampling any given distribution is

$$\zeta_i = \frac{I_i}{2^k} \tag{3-12}$$

The first number I_0 used to start the sequence is called the "seed number". In the EGS system the default seed number is 987654321, and $\zeta_I \in [0,1]$. The cycle length, which is the length of the random number sequence before it starts repeating itself is approximately 10^9 (Ehrman 1981).

Data Analysis

Monte Carlo simulation is a statistical method; therefore, an estimate of statistical uncertainty must be determined. The following method of uncertainty estimation is

described by Rogers and Bielajew (1990). The total number of histories for a particular run is broken up into N_B equal batches, and an estimate of the quantity of interest x_i (e.g., energy deposited in a region) is obtained for each batch. The final estimate of the quantity x is $\langle x \rangle$, the mean of the x_i values. The estimate of the variance of the mean, s^2, is then

$$s^2_{\langle x \rangle} = \frac{1}{N_B(N_B - 1)} \sum_{i=1}^{N_B} (x_i - \langle x \rangle)^2 . \tag{3-13}$$

Because x_i values are assumed to be drawn from a normal distribution, it can be assumed that the interval $(\langle x \rangle - s, \langle x \rangle + s)$ contains the true mean in about 68% of all cases, and the interval $(\langle x \rangle - 2s, \langle x \rangle + 2s)$ contains the true mean in about 95% of the cases.[1] In this work, results are presented $\pm 1s$, and N_B is 10 for all cases.

For each run the following data are recorded:

- kinetic energy of the incident beam
- phantom material
- source-to-axis-distance (SAD)
- phantom radius (or semi-axis lengths)
- slice width in cm
- number of histories.

The following data categories are scored for each run:

- total energy incident on the phantom
- scattered energy absorbed
- primary energy absorbed

---

[1] Given n independent, identically distributed, random variables $x_1, x_2, \ldots x_n$ with mean m and variance σ^2, the Central Limit Theorem is written as

$$P\left\{ a \le \frac{X_n - m}{\sigma / \sqrt{n}} \le b \right\} = \frac{1}{\sqrt{2\pi}} \int_a^b e^{-t^2/2} dt,$$

where $X_n = \frac{1}{n} \sum_{i=1}^{n} x_i$ from which it follows that the distribution of the sum of n independent, identically distributed, random variables approaches a normal distribution.

- total energy absorbed
- scattered energy emerging from phantom
- primary energy emerging from phantom
- total energy emerging from phantom
- GCTDI (for circular phantoms)[2]
- dose (z,r) (for circular phantoms).

The mean value and the estimate of the variance s of each quantity are calculated in all cases.

[2] The Generalized Computed Tomography Dose Index, which is defined in Chapter 6.

CHAPTER 4

THE EGS MONTE CARLO SYSTEM

Introduction

The Electron-Gamma-Shower version-4 (EGS) Monte Carlo system is used in this work. The EGS system is a general-purpose Monte Carlo code that simulates coupled electron-photon transport over an energy range from several keV to several TeV (Nelson *et al.* 1985). The simulation may be carried out in any material and in any geometry specified by the user. EGS takes into account the predominant photon interactions in the diagnostic energy range: coherent scattering, Compton scattering, and photoelectric absorption. EGS can also simulate electron transport; however in this work all electrons are assumed to be locally absorbed because of their short range and negligible bremsstrahlung production . The continuous-slowing-down-approximation (CSDA) range of electrons is <0.2 mm in acrylic at 100 keV (Berger and Seltzer 1983), and the radiation yield (the fraction of energy radiated away) for a 100 keV electron is 0.0005 in acrylic and 0.001 in cortical bone (Johns and Cunningham 1983).

The original EGS system was designed to simulate and study the interaction of high energy electromagnetic cascades with matter. In 1985, version 4 of the EGS system was published (Nelson *et al.* 1985), the system having been expanded and the dynamic range extended down to 1 keV for photons and tens of keV for charged particles.

The EGS system is written in the computer language Mortran3, which is a high-level, structured language similar to FORTRAN (Cook, 1983). Mortran3 uses a macro-processor facility for string replacement. Included in the EGS system is a translator that

converts the Mortran3 code into ANSI standard FORTRAN77. The problem-specific code written by the user is combined with the standard EGS files to produce a large program that is then translated into FORTRAN for compilation and execution. This modularity makes for ease in programming and debugging. (See Appendix D for an example of a Mortran3 user code, which was written to simulate radiation transport in and around a right circular cylinder irradiated by a fan beam with a perfectly compensating bow-tie filter.)

The EGS system has been used by numerous investigators in the area of medical physics. Rogers and Bielajew (1990) have provided an extensive list of the ways the system has been benchmarked, and EGS has been shown to provide accurate results over a wide range of medical physics problems. Examples include the work of Rogers (1982), who modeled photon detector response functions with EGS and showed excellent (<1%) agreement with measured values. The EGS system was used to calculate depth dose curves in water for ^{60}Co beams and also showed excellent agreement with measurements, including the buildup region (Rogers *et al.* 1985). Mohan *et al.* (1986) used the EGS system to calculate dose distributions for 20 MV photon beams as well as for ^{60}Co beams. The calculated and measured data presented by Mohan *et al.* are virtually identical. The system has also reproduced absolute dose measurements based on a monoenergetic 7-MeV photon beam (Mach and Rogers 1984). The beam was produced in van de Graaff accelerator using the $^{19}F(p,\alpha\gamma)^{16}O$ reaction, and the fluence was known to within ±1.1%. EGS calculated the dose per unit fluence to within the experimental measurement error of ±1.6% as measured with a Baldwin-Farmer chamber and the AAPM TG21 protocol (AAPM 1983). Herbold *et al.* (1988) used EGS to calculate buildup factors for photons in the 15-100 keV range. Dose distributions around ^{125}I seeds have been calculated using EGS by Scarbrough *et al.* (1990) and by Cygler *et al.* (1990).

EGS Components

There are four major components of a Monte Carlo code (Rogers and Bielajew 1990):

(A) algorithms for sampling the physical processes,
(B) material data for the media of interest (e.g., cross section data),
(C) geometry description and methods for scoring quantities of interest, and,
(D) data analysis.

The manner by which EGS handles each of these components is described below, as well as the specific code and subroutines written for this project. In general, the sampling algorithms used and the material data are already programmed, and the EGS-user need not be concerned with the inner details of the code. The user must however write subroutines which describe the media to be used, the geometry in which the simulation is to be conducted, the quantities to be scored or recorded, and the manner in which the resulting data is to be handled. The method of data analysis used in this work was discussed in the preceding chapter.

Algorithms

The EGS Monte Carlo system as used in this work is an analog Monte Carlo system.[1] That is, one particle is followed at a time, and physical processes are simulated as closely as possible. The particle is observed as it undergoes discrete events. The results of these discrete events are accessible to the user and, depending on the problem at hand, can be stored for later analysis. The code simulates these events by sampling the probability distributions which govern the following physical processes:

1. the distance traveled by the particle between interaction sites,
2. the type of interaction that occurs at each site,

---

[1] Several variance reduction methods are used in quantity scoring; however particle transport is strictly analog. This is in contrast to another method, used by Rosenstein (1976) in which photoelectric cross sections are excluded, and particles are assigned statistical weights based on their probability of having survived photoelectric interactions at any point in their history. Energy deposition events are recorded as the product of the energy of the particle and the weight of the particle.

3. the energy and/or direction of the particle(s) emerging from an interaction site, and
4. determination of particle trajectories in the reference cartesian coordinate system.

Particles being transported are described by a series of variables. The particle properties stored are its current location in cartesian coordinates, direction cosines, energy, charge, statistical weight, and the geometric region. (Geometric regions are defined in the geometry subroutine HOWFAR, as explained below.) Particle properties are stored on a last-in-first-out (LIFO) stack. The particle on the top of the stack is transported until an interaction takes place, until its energy drops below a pre-set energy threshold, or until the particle leaves the geometry of interest. If the particle leaves the geometry or if the energy drops below the cutoff, the particle is discarded (after some bookkeeping) and the simulation continues with the new top-most particle. The term bookkeeping refers to the records kept and actions taken when a particle is discarded, which in turn depend on the quantities of interest in the problem. Recording the location and energy of a particle when it leaves the geometry of interest is an example of bookkeeping. When an interaction occurs and more than one particle emerges (e.g., a Compton-scattered photon and an electron), the particle with the lowest energy is put on the top of the stack to prevent an overflow of particles. When the stack is empty, the initial particle's history is complete and another history may commence.

Random Path Length Sampling

As listed above, the program must determine how far a particle travels from its present location before it interacts with the medium. EGS uses inversion sampling to determine the distance to the next interaction. In this case, the PDF is the probability that a particle will not interact in the distance x and is given by

$$f(x) = \frac{\exp(-x/\lambda)}{\lambda}, \tag{4-1}$$

where λ is the mean free path. The CDF is found from

$$F(x_i) = \frac{1}{\lambda}\int_0^{x_i} \exp(-x'/\lambda)\, dx' = \zeta_i \ , \tag{4-2}$$

where ζ_i is a random number on the unit interval. Solving for x_i, (the randomly-sampled path length), we obtain the expression

$$x_i = -\lambda \ln(1-\zeta_i) = -\lambda \ln \zeta_i \tag{4-3}$$

because if ζ_i is uniformly distributed over the interval [0,1], then [1 - ζ_i] is also uniformly distributed on the same interval. This result applies only if the medium is homogeneous, of constant density, and infinitely large in size. In the more usual case for which the photon is traveling through a finite-sized volume composed of different regions and materials, a slightly more complicated sampling scheme is used. The procedure used in EGS is as follows and is taken from SLAC-Report-265 (Nelson *et al.* 1985) which describes the system.

1. Compute λ at the present location.
2. Select a random number ζ and set $t_1 = \lambda N_\lambda = \lambda \ln \zeta$. ($N_\lambda$ is the randomly-sampled number of pathlengths.)
3. Calculate the distance d to the nearest boundary along the photon's present direction.
4. Set t_2 = the smaller of t_1 and d; transport t_2.
5. Subtract t_2/λ from N_λ; if the result is zero, then the photon has not left the present region, and an interaction will occur: Leave this loop.
6. This step is reached if $t_1 > d$ and a boundary is reached. If the new region is the same material, go to step 2; otherwise, go to step 1.

Using this technique a photon may be transported through any type of heterogeneous media.

Interaction Selection

Once the interaction point has been selected, the type of interaction that is to occur must be sampled. EGS can account for the three main interactions that photons undergo in the diagnostic range, i.e., Compton scatter, coherent scatter, and photoelectric interactions. The probability of a given interaction occurring is proportional to its cross

section (Williamson 1988). If the possible interactions are numbered 1,2,...n, then the *branching ratio* $F(i)$ is defined to be

$$F(i) = \frac{\sum_{j=1}^{i} \sigma_j}{\sigma_t}, \tag{4-4}$$

where σ_j is the cross section for the j^{th} type interaction and σ_t is the total cross section, given by

$$\sigma_t = \sum_{j=1}^{n} \sigma_j \quad . \tag{4-5}$$

The number i of the interaction to occur is selected by choosing a random number ζ and finding i such that

$$F(i-1) \le \zeta < F(i). \tag{4-6}$$

As a simple example, suppose that there is a 80% chance of a photoelectric interaction and a 20% chance of a Compton interaction for a given photon. If ζ is less than 0.8, then the photoelectric interaction is chosen; if not, the Compton interaction is chosen.

Once the point of interaction and the type of interaction has been sampled, the interaction itself must be simulated in order to determine the energy and direction of the particle(s) leaving the interaction point. The PDF of an interaction is the differential cross section of that interaction (Williamson 1988).

Photoelectric Interactions. A photoelectric interaction occurs when a photon interacts with an atomic electron. The photon is absorbed and an electron is ejected from the atom with a kinetic energy equal to the difference between the photon energy and the electron binding energy. Also, either a fluorescent x ray or an Auger electron is emitted upon filling the vacancy in the inner shell (Evans 1955). If a photoelectric interaction has been chosen, one of two possibilities occurs. If the photon energy k is less than the K-edge energy E_K, then the photon is discarded, and the energy k is simply deposited at the

location of the interaction. If $k \geq E_K$, a photoelectron is created with kinetic energy E where

$$E = k - E_K \,, \tag{4-6}$$

and a photon of energy E_K is created and forcibly discarded (i.e., absorbed) at the point of interaction. The photoelectron can then be transported until it drops below an energy cutoff, at which point local deposition occurs. In this work, the electron energy cutoff is 500 keV, so all electrons are absorbed at the point of interaction. Thus in any case the final result of a photoelectric interaction is the deposition of the total energy of the photon at the point of the interaction.

Rayleigh Scattering. Coherent, or Rayleigh, scattering occurs when an incident photon interacts with the electron cloud of an atom. The atom is neither ionized nor is it excited; the only result of the interaction is a photon with the incident energy scattered through a small angle from the initial trajectory (Johns and Cunningham 1983). For Rayleigh scattering in a medium, EGS calculates total cross sections which are based on the weighted sum of the cross sections of the atoms in the medium, the weight being the proportion of atoms of a given type. The differential cross section for Rayleigh scattering is given by (using the notation of Nelson *et al.*, 1985):

$$\frac{d\sigma_R(\theta)}{d\Omega} = \frac{r_e^2}{2}\left(1+\cos^2\theta\right)\left[F_T(q)\right]^2 \tag{4-7}$$

where r_e is the classical electron radius (2.8×10^{-13} cm^2), θ is the polar scattering angle, $F_T(q)$ is the atomic form factor, q is the momentum transfer parameter, $q = 2k\sin(\theta/2)$, and k is the photon energy. The assumption of independent atoms is also used in calculating the form factor for the medium, i.e., the atomic form factors are combined in a weighted sum. This procedure is known to produce inaccuracies because molecular structure can affect coherent scatter (Johns and Yaffe 1983). However, for photons in the diagnostic energy range in water, the maximum discrepancy between cross sections is less than 10%. The magnitude of the effect is not known for acrylic or other tissue-like materials;

however, the discrepancies are considered small enough to be ignored. The differential cross section can be written, using the substitutions $\mu = \cos\theta$, $d\Omega = 2\pi d\mu$, and $q^2 = 2k^2(1-\mu)$, as

$$\frac{d\sigma_R(q^2)}{dq^2} = \frac{\pi r_e^2}{k^2}\left(\frac{1+\mu^2}{2}\right)\left[F_T(q)\right]^2 . \tag{4-9}$$

Next $A(q')$ is defined as

$$A(q') \equiv \int_0^{q'} \left[F_T(q)\right]^2 d(q^2) , \tag{4-10}$$

and the cross section may be written as

$$\frac{d\sigma_R(q^2)}{dq^2} = \frac{\pi r_e^2}{k^2} A(q^2_{\max})\left(\frac{1+\mu^2}{2}\right)\frac{\left[F_T(q)\right]^2}{A(q^2_{\max})} . \tag{4-11}$$

The term $q_{\max}$ is the maximum value that q can take, i.e., when $\mu = -1$. When expressed in this form, $\left[F_T(q)\right]^2 / A(q^2_{\max})$ can be used as a PDF (i.e., the $f_i(x)$ function in the composition method), and $(1+\mu^2)/2$ can be used as the rejection function (i.e., the $g_i(x)$ function). The PDF is sampled by generating the random number ζ_1 and finding q^2 from

$$\zeta_1 = \frac{A(q^2)}{A(q^2_{\max})} . \tag{4-12}$$

The corresponding μ value is found from $\mu^* = 1 - q^2/2k^2$. A new random number ζ_2 is generated, and the value of μ^* is accepted if

$$\zeta_2 \le \frac{1+\mu^{*2}}{2} . \tag{4-13}$$

If μ^* is not accepted the procedure is repeated until a suitable value is found. To increase calculational efficiency the EGS system sets up look-up tables for the form factors $F(q)$ which are based on the values given by Hubbell and Overbø (1979). Once the polar scattering angle has been determined, the azimuthal angle is randomly sampled from the 2 π distribution and is found from $2\pi\zeta$, where ζ is a random number on the unit interval.

Compton Scattering. A Compton scattering event occurs when a photon strikes an atomic electron. The electron emerges from the collision with an energy T and at an angle φ with respect to the incident photon's direction of motion. This process is fully described by Evans (1955). As discussed above, the electron energy is assumed to be absorbed at the site of the interaction; thus its direction following the interaction is not considered. The relationship between the electron energy and the photon energy is found through conservation of energy:

$$k_0 = k + T, \tag{4-14}$$

where k_0 is the incident photon energy, and k is the scattered photon energy. The relationship of the scattered photon energy and direction to the incident photon is described below.

Compton interactions are sampled using the composition method. For sampling purposes, the Compton differential cross section can be written (Butcher and Messel 1960) as

$$\frac{d\Sigma_{compt}}{d\varepsilon} \propto \frac{1}{k_0}\left[\frac{1}{\varepsilon}+\varepsilon\right]\left[1-\frac{\varepsilon \sin^2\theta}{1+\varepsilon^2}\right], \tag{4-15}$$

where $\varepsilon = k/k_0$, and θ is the angle between the initial and scattered photon trajectories. The relationship between k and θ is given by

$$k = \frac{k_0}{1+(1-\cos\theta)k_0/m} \tag{4-16}$$

where m is the electron rest energy. The differential cross section is thus in the form $f(\varepsilon)g(\varepsilon)$ where $f(\varepsilon) = [\varepsilon + 1/\varepsilon]$ and

$$g(\varepsilon) = \left[1-\frac{\varepsilon \sin^2\theta}{1+\varepsilon^2}\right]. \tag{4-17}$$

The function $f(\varepsilon)$ may be factored as

$$f(\varepsilon)=\frac{1}{\varepsilon}+\varepsilon=\sum_{i=1}^{2}\alpha_i f_i(\varepsilon) \tag{4-18}$$

where

$$\alpha_1=\ln\left(\frac{1}{\varepsilon_0}\right), \qquad f_1(\varepsilon)=\frac{1}{\ln(1/\varepsilon_0)}\left(\frac{1}{\varepsilon_0}\right), \tag{4-19}$$

$$\alpha_2=\frac{(1-\varepsilon_0^2)}{2}, \qquad f_2(\varepsilon)=\frac{2\varepsilon}{(1-\varepsilon_0^2)}, \tag{4-20}$$

and $\varepsilon_0=1/(1+2k_0/m)$. The function f_1 is sampled by generating a random number ζ and finding $\varepsilon=\varepsilon_0\exp(\alpha_1\zeta)$. Next the function f_2 is changed via the change of variable

$$\varepsilon'=\frac{\varepsilon-\varepsilon_0}{1-\varepsilon_0} \tag{4-21}$$

to the function

$$f_2'(\varepsilon')=\alpha_1' f_1''(\varepsilon')+\alpha_2' f_2''(\varepsilon') \tag{4-22}$$

where $\alpha_1'=\frac{k_0'}{k_0'+1}$, $\alpha_2'=\frac{1}{k_0'+1}$, $f_1''(\varepsilon')=2\varepsilon'$, and $f_2''(\varepsilon')=1$. The rejection function is calculated by finding t, where

$$t=\frac{m(1-\varepsilon)}{k_0\varepsilon}, \tag{4-23}$$

and the required value of $\sin^2\theta$ is found from

$$\sin^2\theta=t(2-t). \tag{4-24}$$

The algorithm that EGS uses for sampling the Compton differential cross section follows (random numbers on the interval [0,1] are designated by ζ_i):

1. Calculate k_0, ε_0, α_1, and α_2.
2. Calculate ε :

   If $\alpha_1 \geq (\alpha_1+\alpha_2)\zeta_1$, then calculate $\varepsilon=\varepsilon_0\exp(\alpha_1\zeta_2)$;

   otherwise use $\varepsilon=\varepsilon_0+(1-\varepsilon_0)\varepsilon'$,

where $\mathcal{E}'$ is the larger of ζ_3 and ζ_4 if $k_0' \geq (k_0'+1)\zeta_2$, and

$\mathcal{E}' = \zeta_3$ if $k_0' < (k_0'+1)\zeta_2$.

3. Calculate t and the function $g(\mathcal{E}) = \left[1 - \frac{\mathcal{E}\sin^2\theta}{1+\mathcal{E}^2}\right]$.

   If ζ_4 (or ζ_5) < g($\mathcal{E}$), then reject $\mathcal{E}$, and go back to step 2 above.

4. If $\mathcal{E}$ is accepted, the scattered electron energy is found from conservation of energy. The polar scattering angle θ is then found from

$$\cos\theta = \frac{(k_0+m)k - k_0 m}{k_0 k},$$

and the azimuthal angle φ is randomly selected.

Coordinate Rotation

This algorithm is used by EGS to determine particle trajectories following interactions. A particle's spatial location is described a vector $\boldsymbol{r} = (x,y,z)$ located in a cartesian coordinate system. The particle's direction is expressed by direction cosines. Direction cosines are the cosines of the angles the trajectory makes with the x, y, and z axes: α, β, and θ, respectively. The direction cosines may be expressed in terms spherical coordinates:

$$\begin{aligned} u &= \cos\alpha = \cos\varphi \sin\theta \\ v &= \cos\beta = \sin\varphi \sin\theta \\ w &= \cos\theta \end{aligned} \qquad (4\text{-}25)$$

where θ is the polar angle and φ is the azimuthal angle (Williamson 1988). A vector $\Omega = (u,v,w)$ may thus be defined. The advantage of using this system is that, under a translation S, the new spatial coordinate $\boldsymbol{r}' = (x',y',z')$ may be found from

$$\begin{aligned} x' &= x + uS \\ y' &= y + vS \\ z' &= z + wS \end{aligned} \qquad (4\text{-}26)$$

or in vector notation,

$$\boldsymbol{r}' = \boldsymbol{r} + \Omega S \,. \tag{4-27}$$

Selection of a scattering interaction will return a polar angle of deflection. This deflection is taken as that from the direction of the incident photon. When combined with a randomly selected azimuthal angle, the new direction cosines may be determined. Cashwell and Everett (1959) have described a method for determining the direction cosines (with respect to laboratory coordinates) of photons after multiple collisions. For systems for which θ is the polar angle and $w = \cos\theta$,

$$\begin{aligned} u' &= \frac{u^* uw}{p} - \frac{v^* v}{p} + w^* u \\ v' &= \frac{u^* wv}{p} + \frac{v^* u}{p} + w^* v \\ w' &= -u^* + w^* w \end{aligned} \tag{4-28}$$

where u', v', w' are the direction cosines of the deflected photon's line of flight; u, v, w are the direction cosines of the incident photon; u^*, v^*, w^*, are the direction cosines of the deflected photon's line of flight relative to u, v, w; and $p = \sqrt{1-u^2}$ for the unprimed, primed, and starred frames of reference.

Material Data

The discussion of sampling methods in the previous section indicates the need for a large amount of material data such as cross sections and branching ratios. Also, for calculational efficiency the data must be in a form that can be accessed quickly. In the EGS system a separate preprocessor code (PEGS — *P*reprocessor for *EGS*) is furnished to compute the physical quantities needed for the simulation by the EGS code. PEGS is usually run only once, and it establishes data sets for the materials and energy ranges to be used by the EGS user code.

PEGS constructs piecewise-linear fits over a large number of energy intervals of the branching ratio and cross section data (Nelson *et al.* 1985). The data sets are optimized to provide fast numerical manipulation. The materials used may be elements, compounds, or mixtures. For elements, the user can either utilize the default values for physical density and atomic weight or specify a value. This feature allows the use of different isotopes and the simulation of exact experimental conditions. When compounds are specified, the user must supply the number of elements in the compound, the density, the relative numbers of each type of atom in the compound, and the state of the compound. The characteristics of the compound (e.g., cross section) are based on the weighted sum of the component atoms; the weighting is determined by relative number of each type of atom in the compound. The information needed for the mixture option is the same as that for compounds, except, instead of the relative numbers of atoms, the relative weight of each type of atom present is specified.

It is also possible for the user to have Rayleigh scatter data included in the data set prepared by PEGS for any material. The inclusion of Rayleigh scatter in the simulation process is an option and must be specifically requested by the user, which is a feature that is most probably a remnant of the high-energy origins of the EGS code. Because of the nature of the narrow beams modeled, and because Rayleigh scatter usually only involves small angles, it was felt that exclusion of Rayleigh scatter might introduce errors into the results. Therefore, in order to make the EGS model as realistic as possible, Rayleigh scatter is included for all of the simulations reported in this work.

Geometry and Scoring Method

The user of the EGS system must write three Mortran3 routines to describe the problem at hand. These codes are called *User Codes* to emphasize their separate nature from the main EGS routines. The user must write:

1. MAIN - the driving program of the system,

2. HOWFAR - the subroutine in which the geometry of the problem is described, and,
3. AUSGAB - the subroutine which scores quantities of interest.

The EGS system is basically a series of subroutines which share data by COMMON blocks. Thus in writing MAIN, the user must follow a set of specific rules that dictates the order in which each subroutine must be called, which Mortran3 macros are to be used, and which subroutines are to be interconnected by which COMMON blocks. A simplified flow control diagram for the EGS system is shown in Fig. 4-1.

The MAIN routine dimensions and initializes the data arrays to be used in the simulation. It also sets COMMON variables which specify the cutoff energies, the units (e.g., cm) and the media names. MAIN then calls the HATCH subroutine to read in the media data created by PEGS. Once the preliminary initializations have been performed, MAIN calls the subroutine SHOWER, which initiates one history for each time it is called. The call to SHOWER specifies the parameters (e.g., location, energy, direction, region, electric charge, and statistical weight) of the initial particle in each history. Some of these

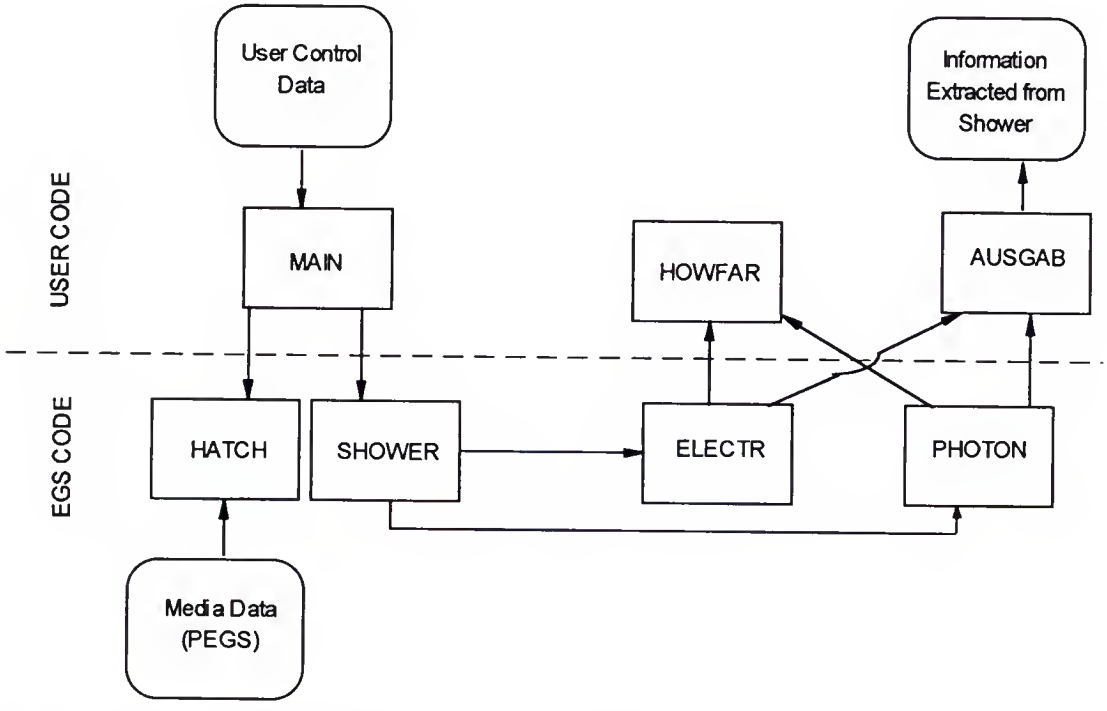

Figure 4-1: Flow control diagram of the EGS system

initial parameters may require sampling before the SHOWER call, such as finding a random trajectory within a CT-type fan beam, or sampling the incident spectrum for a photon energy. Finally, after the desired number of histories are simulated, the MAIN routine analyzes the results and outputs the desired data.

The purpose of the subroutine HOWFAR is to provide information to EGS about the nature of the geometry in which the Monte Carlo simulation is to be done. The user describes the shapes, sizes, and materials of objects in the geometry. Included in the EGS system are subprograms which are designed to aid the user in specifying geometric shapes in the subroutine HOWFAR (Nelson and Jenkins 1987). These subprograms simplify the specification of planes, spheres, cylinders, and cones; they determine the distance a particle must travel to intersect the surface of a given shape. (An example of such a subprogram that was written to define a right elliptical cylinder is listed in Appendix C.) Multiple elements using simple geometric shapes may be combined to form complicated structures. Different geometric regions within the geometry thus described are identified by region numbers. The user must then systematically examine (via IF...THEN...ELSE statements) all possible destinations of a particle exiting each region.

HOWFAR is called after a path length has been sampled from the exponential attenuation distribution. Given a particle region, position, and trajectory, HOWFAR calculates the distance to the nearest boundary of the region. If this distance is greater than the sampled distance to the next interaction, HOWFAR puts the particle on the boundary and sets the region number to that of the new region. The direction cosines are unchanged, and a new path length is sampled. Note that regions may or may not be of different materials.

The user can also tell HOWFAR to discard a particle if it enters into a region of no interest. For example, if the user is interested in dose deposition locations within a cylinder, particles that leave the cylinder can no longer deposit dose there. (In this work, the assumption is made that the particles leaving the geometry of interest cannot be

scattered back in.) Thus when HOWFAR determines that a certain particle has left the cylinder, it terminates the particle's history. Time and calculational effort are minimized, because particles that can not contribute to the final results are eliminated.

Three different geometries are simulated in this work: a circular cylindrical CTDI-type phantom, a small diameter acrylic rod, and an elliptical anthropomorphic-type phantom. The details of each are described below.

The purpose of the subroutine AUSGAB is to record or score quantities of interest. AUSGAB is called before a particle is discarded because it has fallen below the cutoff energy. The user can also specify that AUSGAB be called in other situations, such as before (or after) a specific interaction occurs. The user specifies the actions to take when AUSGAB is called. For example, the user may wish to record energy deposition in geometric regions. Energy deposition occurs when a photon or electron falls below the energy cutoff level and is absorbed at its present location. If, for example, a Compton electron is created, its kinetic energy is below the pre-set cutoff energy, and it will be discarded. AUSGAB is called, and the kinetic energy of the electron is added to the total energy deposited in the appropriate geometric location. The user can have AUSGAB record any of the characteristics of a particle, i.e., its energy, spatial coordinates, direction cosines, weight, charge, or current region.

Circular Cylindrical Phantom

The user code CTMONO was written by the author to simulate a CTDI-type phantom. The subroutine HOWFAR used in CTMONO was based on the version in DOSRZ, a code included in the EGS system. For this case, the subroutine HOWFAR specifies the geometry as follows. The isocenter of the scanner is taken to be at the origin of a cartesian coordinate system. A right cylindrical phantom is centered on the origin with the long axis coincident with the z-axis. The default material is acrylic. The cylinder is 16 cm long. The maximum radius is varied over a range of values, although most runs use either 8 cm or 16 cm. For dose-scoring purposes the phantom is divided into annular-

shaped regions. These dose-scoring regions are bounded by planes normal to the z-axis, and by concentric cylinders whose long axes are coincident with the *z*-axis. Figure 4-2 illustrates the general configuration of radial and planar zones. (Note that Fig. 4-2 is a schematic drawing and not an actual representation of the sizes of the zones used in this work.) Each annulus is defined by two planes and two cylinders. The regions between planes are assigned identifying numbers from 1 to NZ, with NZ being the total number of planar zones thus defined. Similarly, the zones or regions between cylinders are assigned identifying numbers from 1 (the central core) to NR, with NR total radial zones. The bounding-cylinders are also numbered 1 to NR, so each radial zone is associated with the larger of its bounding cylinders. (Radial region 1 is bounded by cylinder number 1, radial region 2 is bounded by cylinder number 2 on the outer surface and cylinder 1 on the inner surface. The outer cylinder defining region NR is the radius of the phantom.) Any point within the phantom is consequently located within a specific planar region (IZ), and a specific radial region (IX). The annuli are assigned region numbers, IRL. The region number of any location inside the phantom with known IX and IZ is found from

$$IRL = IZ + NZ(IX - 1) + 1 . \tag{4-29}$$

Given a region number IRL, the corresponding IX and IZ values are found from the expressions

$$IX = [(IRL - 2)/NZ] + 1 , \text{ and } IZ = IRL - 1 - NZ(IX - 1) . \tag{4-30}$$

The equations in (4-30) assume integer arithmetic and were obtained directly from the DOSRZ code.

The cylinders defining the radial zones are assigned radii of:

$0.25R$ - 0.5 cm,
$0.25R$ + 0.5 cm
$0.50R$ - 0.5 cm
$0.50R$ + 0.5 cm
$0.75R$ - 0.5 cm
$0.75R$ + 0.5 cm
R-1.0 cm, and
R, the radius of the phantom.

There are 60 planar zones. The thickness of the planar zones are as follows, with z given in cm:

$6 < |z| \leq 8$: 10 mm spacing

$2 < |z| \leq 6$: 5 mm spacing

$1 < |z| \leq 2$: 2.5 mm spacing

$0.6 < |z| \leq 1$: 2 mm spacing

$0.5 < |z| \leq 0.6$: 1 mm spacing

$0.1 < |z| \leq 0.5$: 0.5 mm spacing

$0 < |z| \leq 0.1$: 0.2 mm spacing

The smaller spacing of the planes near the center of the phantom was initially selected to provide good spatial resolution of the dose profile. It should be noted that integrals of the dose profile, which are discussed in Chapter 6, are calculated with all the planar zones collapsed into one large zone.

The geometry described in the subroutine HOWFAR was exploited for scoring efficiency by utilizing the cylindrical symmetry inherent in the problem. AUSGAB scored energy deposition in the annular regions described by a given IX and IZ. The total energy ε_{IRL} deposited in any given region IRL is used to calculate the absorbed dose D_{IRL} in that region from the expression

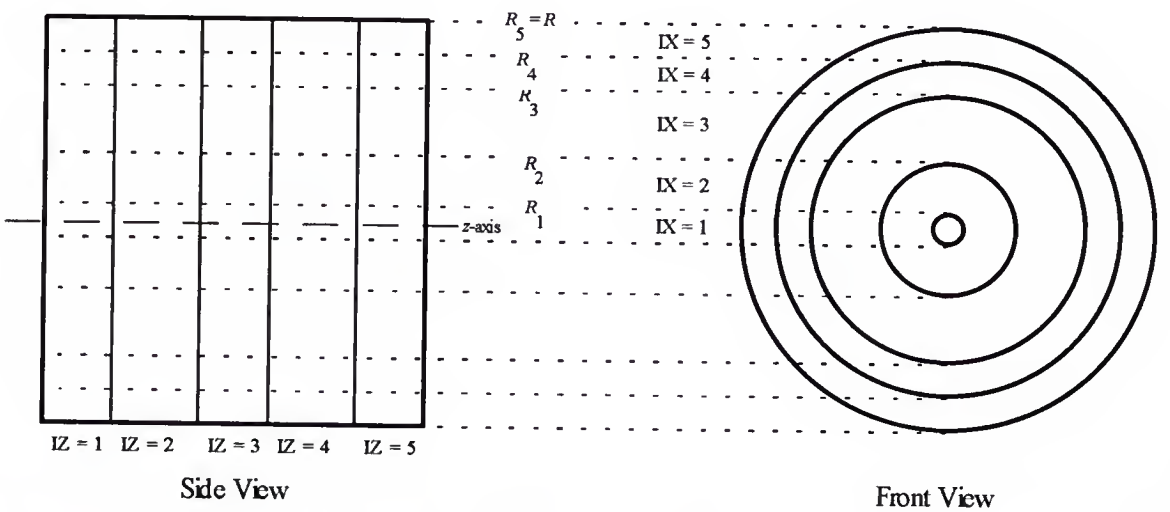

Figure 4-2 Illustration of the geometry described by subroutine HOWFAR in the user code CTMONO with five radial zones and five planar zones.

$$D_{\mathrm{IRL}} = \frac{\varepsilon_{\mathrm{IRL}}}{\rho V_{\mathrm{IRL}}} \tag{4-31}$$

where ρ is the medium density and V_{IRL} is the volume of the region. V_{IRL} is given by

$$V_{\mathrm{IRL}} = \pi (R_{\mathrm{IX}}^2 - R_{\mathrm{IX-1}}^2) T_{\mathrm{IZ}} , \tag{4-32}$$

where R_{IX} and $R_{\mathrm{IX-1}}$ are the radii of the indicated radial zones and T_{IZ} is the thickness of planar zone IZ.

The x-ray beam incident on the phantom is simulated as follows. With the phantom centered at the origin, a monoenergetic point source is located on the y-axis at a fixed distance from the origin. This distance is 65 cm by default. To ensure that all the photons emitted by the source strike the phantom, the initial direction for each photon is sampled using the "SELECT-POINT-IN-RECTANGLE" algorithm in the DOSRZ series of programs (see Fig. 4-3). This algorithm uses the fact that in the beam's-eye-view, the projected area of the beam intercepting the phantom is a rectangle. For each incident photon, the algorithm picks a random point within the rectangle, calculates the trajectory from the source to that point, and finds the point of intersection of the trajectory with the phantom. Once the location and trajectory of the incident photon is known, the radiation transport simulation commences.

The energy of the incident photon is determined before the call to subroutine SHOWER. For monoenergetic problems, the energy is simply a constant value. In cases for which the source is polyenergetic, the x-ray spectrum is treated as a PDF. The EGS system includes a source-handling subroutine, SRCRZ, that creates a CDF from a given spectrum. For problems involving x-ray spectra, the CDF is sampled prior to each photon history to assign the incident photon energy.

The CT-slice of thickness T is assumed to be centered about the origin. For a maximum phantom radius, R, the photons must be emitted so as to strike inside the rectangular box of dimensions $2R$ in the x-direction and T in the z-direction, centered at the origin and normal to the y-axis. In order to determine the points within the rectangle,

two random numbers ζ_1 and ζ_2 are selected, and the points in the box x_b and z_b are selected by:

$$\begin{aligned} x_b &= R(2\zeta_1 - 1) \\ y_b &= 0 \\ z_b &= (T/2)(2\zeta_2 - 1) \ . \end{aligned} \tag{4-33}$$

Once the two coordinates x_b and z_b are found, the direction cosines u, v, and w of the ray connecting the source point to the point in the box are determined, and from the cosines, the point of intersection with the phantom is found. The medium between the source point and the phantom surface is assumed provide negligible attenuation (e.g., air). Note that the cylindrical symmetry in the problem allows the use of only one source location.

Three beam filtration configurations were used in part of this investigation: no filter, and two beam-shaping, or bowtie, filters. One filter is a perfect or ideal filter. That is, for a given phantom size and material, the filter produces a beam for which the primary

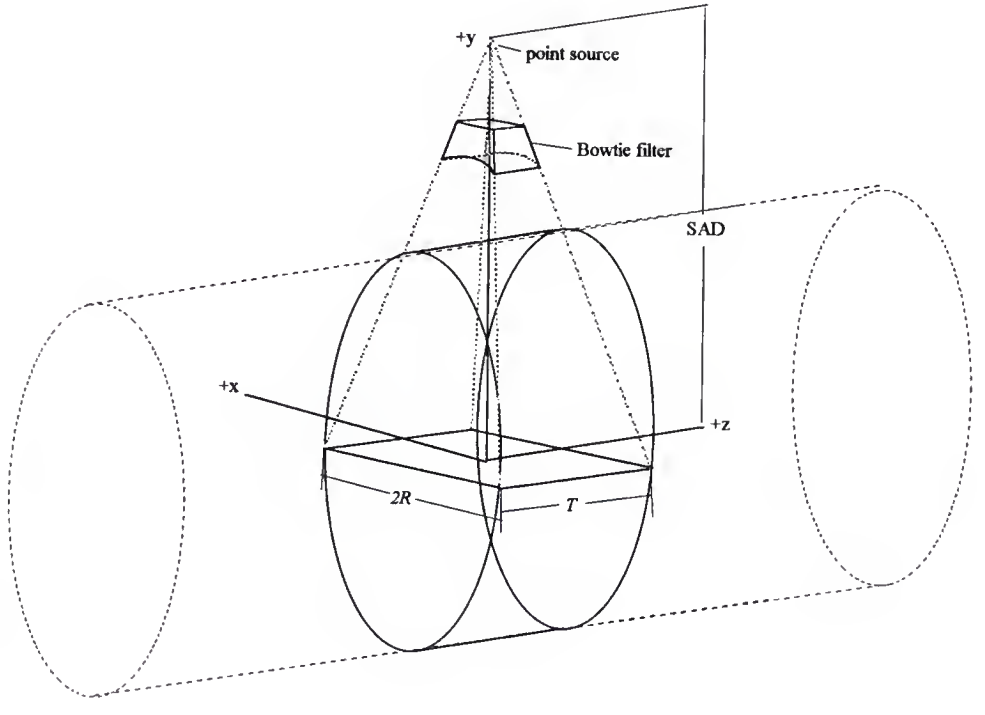

Figure 4-3: Source and phantom configuration for cylindrical phantom.

fluence exiting the phantom is independent of angle within the fan beam because the total path length is constant. The fan beam subtends angles over the range $[-\beta_{tot}/2, \beta_{tot}/2]$ with respect to the y-axis in the x-y plane. The trajectory of any photon in the fan beam can therefore be described by the absolute value of its angle with respect to the y-axis, β. At any angle within the fan beam the thickness of the filter is found from

$$t_f(\beta) + L(\beta) = 2R \tag{4-34}$$

where $t_f(\beta)$ is the thickness of the filter at angle β, $L(\beta)$ is the thickness through the phantom at angle β and R is the phantom radius. To ensure that the attenuation of the beam, and not just the path length, is constant for any angle within the fan beam, the filter is made from the same material as the phantom, i.e., acrylic.

The second beam-shaping filter is based on a real filter and modeled from data supplied by General Electric. The geometric configuration in this problem is modeled on the filter of a General Electric 9800-series CT scanner, the details of which were obtained from the manufacturer and are proprietary. The shape of the filter was digitized, and a fifth-order polynomial curve was fit to the data points. The distance through the filter as a function of angle in the fan beam was then calculated and tabulated in a lookup table, as was the linear attenuation coefficient for the filter material, Teflon (ICRU 1989).

For both filter types, a photon's initial trajectory angle within the fan beam is used to find the corresponding thickness of the filter. In a totally analog Monte Carlo simulation, the photon's random trajectory through the bowtie filter would be followed; however considerable computing would be spent following photons that never enter the phantom and thus are of no interest. In this study, a variance reduction method is used: a weight is assigned to each photon. The weight is simply the probability that the photon was transmitted through the filter, and is calculated by

$$W = \exp[-\mu(E)t(\beta)], \tag{4-35}$$

where W is the weight assigned, $\mu(E)$ is the linear attenuation coefficient of the filter material at energy E, and $t(\beta)$ is the thickness of the filter at angle β within the fan beam.

The weight of an incident photon is passed to all generations of its progeny. Jones and Shrimpton (1991) have shown that there is negligible difference between actually simulating transport in the filter and accounting only for attenuation effects as is done here.

The LATCH feature of the EGS system is used to differentiate between primary and scattered photons. LATCH is a variable that can be associated with each particle, along with energy, position, trajectory, charge, and weight. The value of LATCH can be passed to all succeeding generations of particles. The initial value of LATCH is zero for all photons and is changed if the photon undergoes an interaction. Subroutine AUSGAB is called if a scattering interaction is about to occur, and the LATCH value is checked. If the value was zero, it is then changed to ten, indicating a primary interaction. If the value was ten, it is changed to one, indicating a previously scattered photon. If the value was one, it is left as one. When a particle is to be deposited in a given region, the value of its LATCH is checked to determine into which category the energy is to be placed. The four possibilities are:

1. If the particle depositing the energy is a photon and LATCH is not equal to zero, then clearly it had been scattered at least once and the energy is deposited in the scatter category.
2. If the particle depositing has a LATCH of zero, then it must be either a photoelectron from a primary interaction, and it is scored in the primary bin, or a primary photon exiting the geometry.
3. If the particle depositing has a LATCH of ten, then it must be a Compton electron from a primary interaction and is scored in the primary bin.
4. If the particle has a LATCH of one, it must be is a multiply-scattered particle and so is placed in the scatter bin.

Another variance reduction technique, discard-within-a-zone (DWAZ), was used during the actual transport simulation. DWAZ dictates that when a particle does not have enough energy to reach a boundary, the energy may be assumed to be deposited in the zone in which it is being transported (Bielajew and Rogers 1988). The neglect of the range of electron travel is justified on the basis of the extremely small distances (~0.1 mm)

traveled by electrons at diagnostic energies in the materials considered here (Berger and Seltzer 1983), however the method also neglects any bremsstrahlung that may have been created. Fortunately the radiative yield of these electrons is so small (<0.1 %) that it is essentially zero in the materials used in this work (Johns and Cunningham 1983).

Small Acrylic Rod

The user code INAIR was written by the author to simulate an acrylic rod placed alone, i.e., "in-air" at the isocenter of a CT scanner. In the subroutine HOWFAR, a small right circular cylinder is described as centered at the origin of the coordinate system used, i.e., the isocenter. In this case, the same planar geometry as the larger cylinder is used, but only one radial zone is used because of the small sizes involved (from 1 mm to 10 mm in diameter; see the following chapter). The rod is specified to be made of acrylic and 16 cm long. This "in-air" rod was used for verification of the Monte Carlo model and also as a method of normalization, as described in the next chapter. The other user-written subroutines, MAIN and AUSGAB, used in INAIR were identical to those of CTMONO, and were described in the previous section.

Anthropomorphic Phantoms

In order to compare the results from the cylindrical CTDI-type phantom to those from an anthropomorphic-type phantom, a subprogram was written to simulate the radiation transport in and around an elliptical cylinder. Anthropomorphic phantoms are typically constructed (i.e., described mathematically) with elliptical bodies and heads (Christy 1980). The energy deposited in and absorbed doses in such phantoms are interpreted to be representative of these quantities in typical human subjects. The algorithm used for the description of the elliptical cylinder, and a listing of the Mortran3 code, are given in Appendix C. This code was used in the user codes BODYPHAN and HEADPHAN, which simulated anthropomorphic body and head phantoms, respectively.

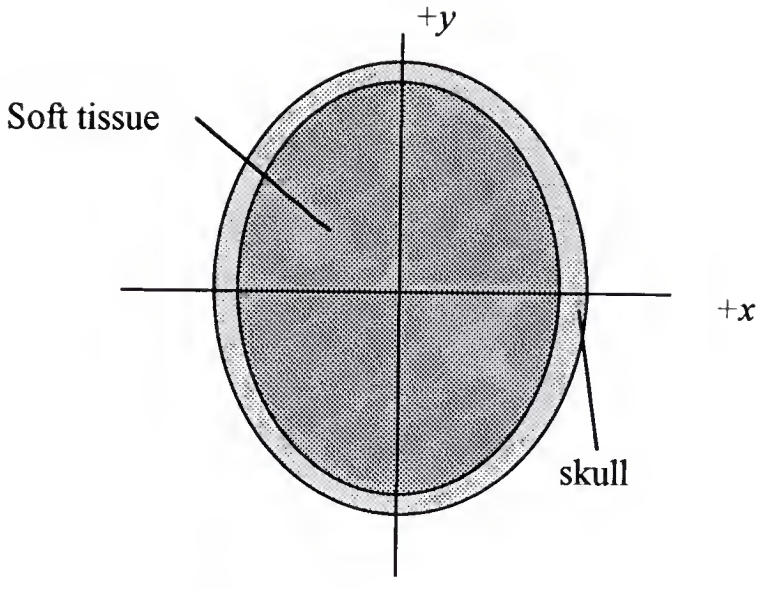

Figure 4-4(a): Head Phantom

Elliptical cylinders have at least two planes about which they are symmetric — in this case, three planes because the phantom is centered at the origin. Because of this symmetry, it is necessary to use source locations in only one quadrant in the x,y-plane. In the user codes BODYPHAN and HEADPHAN, the source location was randomly sampled from the range 0 to $\pi/2$. The source angle δ was defined as the angle between the ray connecting the source and the origin and the y-axis. The source angle was sampled by finding $\delta = (\pi/2)\zeta$, where ζ is a random number on the unit interval.

The anthropomorphic head phantom was constructed of skeletal tissue and adult soft tissue and was 24 cm long. A "skull" with semi-major and -minor axes of 10 cm and 8 cm, respectively, enclosed the soft tissue. The skull thickness was 9 mm throughout the phantom (Christy and Eckerman 1987), thus the ellipse defining the inner boundary of the skull had semi-major and semi minor axis of 9.1 cm and 7.1 cm, respectively. The head phantom is illustrated in Fig. 4-4(a).

The anthropomorphic body phantom used in this work is 70 cm long and had semi-major and semi-minor axes of 40 and 20 cm respectively. The phantom was constructed

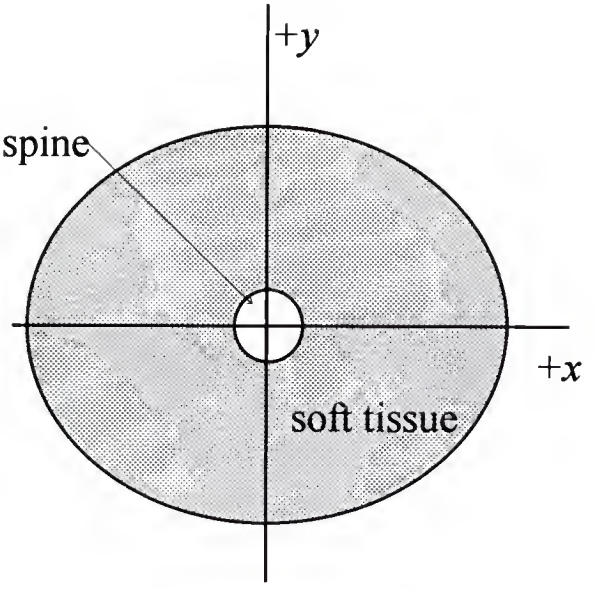

Figure 4-4b: Body phantom

of adult "soft tissue" as described by Christy and Eckerman (1987). A "spine" consisting of skeletal material was located inside the phantom along the *z*-axis. The skeletal tissue assumes a mix of cortical bone, trabecular bone, and red and yellow marrow (Christy and Eckerman 1987). The spine is an elliptical cylinder of with semi-major and semi-minor axes of 3.2 cm and 3.1 cm, respectively, as shown by Fig. 4-4(b) (Christy and Eckerman 1987).

The user codes BODYPHAN and HEADPHAN were tested by setting both semi-major axes to the same value (making circular cylinders), setting the media to be acrylic, and comparing values of the energy dispositions to previously computed results for the same configuration. In all cases the results were within the statistical uncertainty of the quantities examined.

Summary

This chapter has described the overall structure of the EGS system, as well as the specific methods and algorithms used therein for radiation transport simulation. The

details of the individual user codes specifically written to investigate energy deposition in phantoms from idealized CT scanners were also described.

The next chapter presents a comparison between data calculated with the EGS user codes described above and data calculated by analytic means, and is intended to validate the implementation of the EGS system. Chapters 6 and 7 present the results obtained with the system and the user codes described above.

All user codes mentioned in this work were run on Intel[2] 80386-based micro-computers equipped with Intel 80387 floating point co-processors. All these computers were run under the MS[3]-DOS 5.0 operating system, and used the Lahey[4] FORTRAN F77L EM/32-OS386 environment for running the execution code.

---

[2] Intel Corporation, Hillsboro OR 97124
[3] Microsoft Corporation, Redmond WA 98052
[4] Lahey Computer Systems, Incline Village NV 89450

CHAPTER 5

VERIFICATION OF THE MONTE CARLO MODEL

The references cited in the previous chapter demonstrate that the simulation of physical processes in the interaction of ionizing radiation with matter can be accurately modeled by EGS. Rogers and Bielajew (1989) state that, although the system has been shown capable of producing accurate results in a variety of situations, new code should not be trusted until some appropriate experimental or previously calculated data can be duplicated. The problem in comparing results is that high-quality experimental data are scarce. Simple, well-specified experimental setups are needed. In this work, mono-energetic photon beams in the diagnostic-energy range are incident on acrylic and other tissue-like phantoms. Because of a dearth of experimental results for this situation, comparisons were made between EGS results and theoretical relationships.

Conservation of Energy

The first method compares Monte Carlo results to those expected by applying the principle of conservation of energy. The quantity of energy absorbed in a volume can be written as

$$\bar{\varepsilon} = \bar{R}_{in} - \bar{R}_{out} + \overline{\Sigma Q}\,, \tag{5-1}$$

where $\bar{\varepsilon}$ is energy absorbed, $\bar{R}_{in}$ and $\bar{R}_{out}$ are radiant energies incident upon and escaping from the volume, and $\overline{\Sigma Q}$ is the change in rest mass (Carlsson and Alm Carlsson, 1990). The change in rest mass is assumed to be zero for interactions in the diagnostic energy range. Thus, the quantity of energy incident on a volume must be equal to the sum of that deposited and that escaping from the volume.

Table 5-1: Illustration of conservation of energy for four separate Monte Carlo runs with an acrylic phantom and no filter with a 65 cm SAD.

	Energy [keV]	80	80	80	120
	phantom radius [cm]	8	16	8	16
	slice width [mm]	5	5	10	5
	histories	2.0E6	5.0E6	5.0E6	5.0E6
	Energy disposition category	***Energy [keV]***			
1	*Total incident*	**1.6000E+08**	**4.0000E+08**	**4.0000E+08**	**6.0000E+08**
2	*Scattered imparted*	2.6312E+07	9.8485E+07	6.5857E+07	1.4813E+08
3	*Primary imparted*	2.3994E+07	7.5436E+07	5.9966E+07	1.1103E+08
4	*Total imparted*	**5.0306E+07**	**1.7392E+08**	**1.2582E+08**	**2.5917E+08**
5	*Scattered out*	9.3531E+07	2.1942E+08	2.3386E+08	3.2639E+08
6	*Primary out*	1.6163E+07	6.6584E+06	4.0315E+07	1.4437E+07
7	*Total out*	**1.0969E+08**	**2.2608E+08**	**2.7418E+08**	**3.4083E+08**
	sum of rows 2 and 3 *compare to row 4*	**5.0306E+07**	**1.7392E+08**	**1.2582E+08**	**2.5917E+08**
	sum of rows 5 and 6 *compare to row 7*	**1.0969E+08**	**2.2608E+08**	**2.7418E+08**	**3.4083E+08**
	sum of rows 4 and 7 *compare to row 1*	**1.6000E+08**	**4.0000E+08**	**4.0000E+08**	**6.0000E+08**

All of the user codes written for this project record in separate bins the amount of primary and scattered energy imparted to, and exiting from, the phantom. The total energy imparted and total exiting the phantom are recorded separately. Table 5-1 shows part of the raw EGS output from four different runs with different configurations. The photon energy, radius, slice width and number of histories are as listed. The energy disposition results have not been normalized and are in units of keV. The values in rows 1 through 7 are the raw, un-normalized data as output by EGS. The last three rows are the sums of the primary and scattered energies for the imparted and exiting-phantom categories. Note that the sum of these values is exactly the same as that calculated by EGS. The sum of the scattered and primary energies equals the total energy for both the energy imparted and energy exiting categories. The relationships between these quantities were checked for all runs and found to be correctly accounted for in all cases. This internal check shows that the user codes were written in a self-consistent manner.

In Air Dose Calculation

The next verification test compared the EGS results to an analytical calculation of absorbed dose in a small volume of tissue-like material. In general, the absorbed dose D to a small volume of material (assuming charged particle equilibrium) is given by:

$$D = E\frac{\mu_{en}}{\rho}(E)\Phi k, \tag{5-2}$$

where E is beam energy, $(\mu_{en}/\rho)(E)$ is the mass energy absorption coefficient of the medium for energy E, Φ is the photon fluence at the point of interest, and k is a constant that transforms units (Attix 1986). If dose is given in Gy, energy in keV, the mass energy absorption coefficient in cm^2/g, and the fluence in photons/cm^2 , then $k = 1.602\times10^{-13}$ Gy·g/keV. The use of this formula assumes that only primary radiation produces the dose in a small absorber and that any scattered radiation exits the volume of interest without further interaction.

Next, consider the small volume of tissue-like material to be located in the middle of a small (5 mm diameter) rod of such material, and the x-ray beam to be collimated so as to strike only the middle of the rod. The maximum dose is approximated by (5-2) because the small size of the rod produces negligible scatter and attenuation. Furthermore, if the dose is integrated along the length of the rod, a value for the $CTDI_{air}$ (i.e., the CTDI as measured in air) can be calculated. The integration limits in this calculation are not critical, because there is negligible dose deposition outside the primary-irradiated region. This $CTDI_{air}$ value should be the same as the mean dose in the directly irradiated region. Also, the $CTDI_{air}$ value should be independent of rod size (for sizes on the order of mm) because of the small amount of attenuation occurring, as shown below.

The user code INAIR was written to simulate acrylic rods with various diameters (1 to 10 mm) at a distance of 65 cm from a point source of monoenergetic x rays collimated to a narrow fan beam. In the interest of calculational efficiency, the size of the fan beam is

constrained to an angle that ensures that each photon strikes the rod, by using the "SELECT-POINT-IN-RECTANGLE" method described in the previous chapter. The photon fluence at the center of the rod is determined by the number of photon histories run. If N histories are run, with a slice thickness of t and rod diameter of r, then the incident fluence is $N/(tr)$ photons/cm^2 , and the dose D produced by the beam is calculated from (2) above. The dose was normalized to the incident fluence in units of photons per steradian.[1]

For each run, the dose profile was found. The dose profile was integrated and a value of $CTDI_{air}$ calculated. The results of the comparison between the analytic calculation and the EGS simulation are listed in Table 5-2. These data are shown graphically in Fig. 5-1. The values are listed for six energies and four rod diameters, and all values are in units of Gy/(photon/sr). The analytical calculations were performed using the attenuation data for acrylic from ICRU 44 (1989). The data in Table 5-2 show excellent agreement between the two methods of calculation. The largest discrepancies are seen at the lower energies: for the 5 mm rod, 2.6% at 40 keV, 2.5% at 60 keV, 1.6% at 80 keV, and 0.8% at 100 keV. These values are well within the uncertainty of the mass energy absorption coefficients, which are listed in ICRU 44 as in the range 3% to 10%.

Table 5-2: Comparison of CTDI values per incident fluence for various energies and acrylic rod diameters.

CTDI per fluence [Gy/(photon/sr)]						
	Photon energy [keV]					
diameter [mm]	**40**	**60**	**80**	**100**	**120**	**140**
analytic	6.82E-17	5.68E-17	6.94E-17	8.94E-17	1.13E-16	1.38E-16
1	6.94E-17	5.72E-17	6.97E-17	8.97E-17	1.13E-16	1.39E-16
3	6.92E-17	5.78E-17	7.06E-17	9.03E-17	1.14E-16	1.39E-16
5	7.00E-17	5.82E-17	7.05E-17	9.01E-17	1.14E-16	1.38E-16
10	7.07E-17	5.88E-17	7.11E-17	9.08E-17	1.14E-16	1.39E-16

[1] The solid angle Ω subtended by such a fan beam is given by $\Omega = tr/SAD^2$ where SAD is the source-to-axis-distance (Johns and Cunningham 1983).

The $CTDI_{air}$ values correspond to what would be measured in air if an appropriate dosimeter (e.g., a stack of small TLD chips in a holder) were placed at a CT scanner isocenter. This in-air measurement thus provides a convenient method of normalization between different exposure conditions (e.g., different phantom sizes and slice thicknesses). The 5 mm rod value is used for normalization because this size is the smallest one that can realistically be used in a clinical scanner (Shrimpton *et al.* 1991).

Primary X Ray Transmission Through a Cylinder

The third method of verification is the comparison between EGS and analytical results for transmission of primary photons in a tightly collimated fan beam through a cylinder of acrylic. If a mono-planar fan beam of x rays is incident on the cylinder in the plane normal to the long axis of the cylinder, the mean transmission $\overline{T}$ of the fan-beam through the cylinder is:

$$\overline{T} = \frac{1}{\varphi_{max}} \int_0^{\varphi_{max}} \exp[-\mu(E)L(\varphi)]d\varphi \ , \tag{5-3}$$

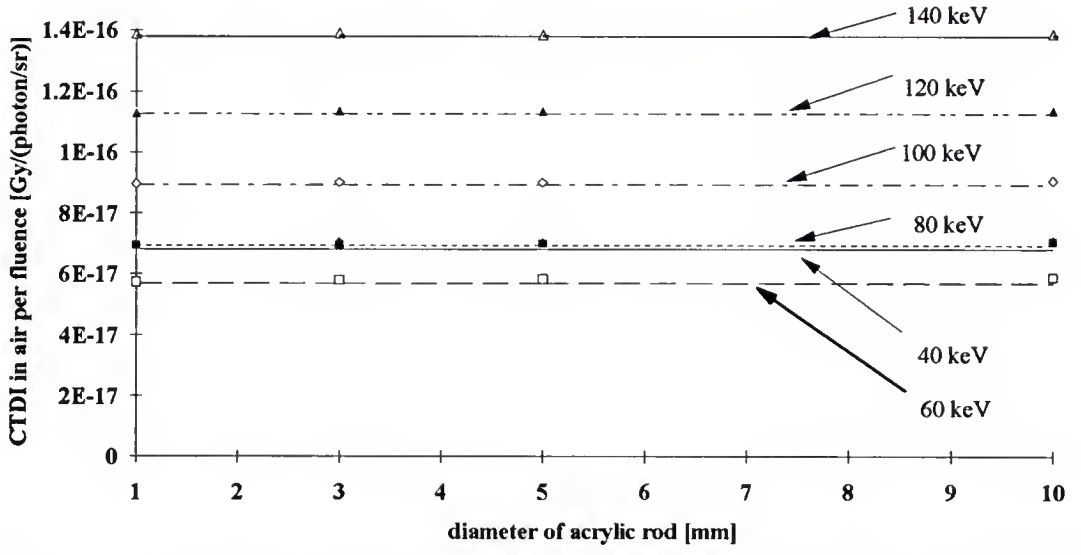

Figure 5-1: CTDI in air per incident fluence for acrylic rods of various sizes. Values from the analytic calculation are shown as lines.

where $\mu(E)$ is the linear attenuation coefficient of the phantom at energy E, φ is the angle within the fan beam, and $L(\varphi)$ is the distance through the phantom as a function of angle within the fan beam. It is shown in Appendix B that $L(\varphi)$ is given by

$$L(\varphi) = 2\left[R^2 - \frac{S^2 \tan^2 \varphi}{1+\tan^2 \varphi}\right]^{1/2} \tag{5-4}$$

where R is the radius of the cylinder, S is the distance from the source to the cylinder axis, and $\varphi_{max} = \tan^{-1}(R/S)$. Table 5-3 shows the results obtained with the EGS simulation and the analytical calculation.

There are minor discrepancies between the results: the analytic method gives slightly larger values at the lower energies and smaller phantom sizes, while the EGS values are slightly larger for the higher energies and larger phantoms. These differences are on the order of tenths of a percent. The largest discrepancies are in the 80 mm diameter phantom, over the 40 keV to 120 keV energy range, and are 1% to 3%. At 140 keV, the average discrepancy is approximately 5%, and this may be due to the interpolated value of the mass attenuation coefficient used in the analytic calculation. The overall uncertainties in the attenuation coefficients, as listed in ICRU Report 44 (ICRU 1989), are greater than 10% in the range 10 keV to 40 keV, 3% to 10% in the range 50 keV to 100 keV, and less than 3% at energies greater than 150 keV.

Table 5-3: Comparison of percentage transmission of primary radiation through acrylic cylinders of various diameters as calculated analytically and with the EGS code.

Percent transmission through acrylic cylinder								
energy	8 cm		16 cm		24 cm		32 cm	
[keV]	analytic	EGS	analytic	EGS	analytic	EGS	analytic	EGS
40	20.4	19.8	5.5	5.2	1.8	1.8	0.6	0.6
60	26.7	25.9	8.4	8.3	3.1	3.1	1.1	1.2
80	29.7	29.2	10.1	10.1	3.9	4.0	1.5	1.7
100	31.9	31.1	11.4	11.5	4.6	4.8	1.9	2.1
120	33.9	33.5	12.9	12.8	5.3	5.4	2.2	2.4
140	35.0	35.1	13.6	13.9	5.7	6.0	2.4	2.7

The discrepancies between the EGS and analytic results may be due to the uncertainties in the attenuation coefficients and differences between the monoplanar x-ray beam assumed in the analytic calculation and the finite-sized beam used in the Monte Carlo model. As a result of the small discrepancies noted, the agreement between the two methods may be considered to be excellent, indicating that the EGS user code was correctly configured.

The comparisons made above show that EGS can closely duplicate results calculated by the three analytic and independent means. The comparisons indicate that the user codes produced for this project were written and implemented correctly.

CHAPTER 6

DOSE DISTRIBUTIONS AND RELATED DOSIMETRIC QUANTITIES

Introduction

The user code MONOCT was written by the author to determine the energy deposition locations in a cylindrical phantom. The energy of the incident photons, the SAD, the phantom radius, the slice thickness, and the phantom material can all be changed over a range of values. In addition, two other user codes, PERFMON1 and GEMON1 were written to vary the type of beam filtration from none to a perfect filter to a GE9800 filter. A beam-shaping (or bow-tie) filter in a CT scanner is meant to reduce the dynamic range of the fluence of primary photons exiting the patient. The perfect filter represents an ideal situation that cannot be achieved in the clinical environment. The results using an actual bow-tie filter (the GE filter) may thus be compared to the ideal filter.

The sections below demonstrate the effects of varying different parameters on the dose distributions. These parameters are listed in Table 1-1 and include beam energy, beam filter, slice thickness, phantom material, phantom diameter, source-to-axis distance (SAD), and phantom type. First, dose profiles in air[1] are presented. Then, dose profiles are shown as a function of radial location r in standard CTDI phantoms. A new quantity the Generalized Computed Tomography Dose Index (GCTDI) is introduced, and the relationships among the dose profiles, the standardized CTDI and the GCTDI are shown. Next, a method of determining the energy imparted as a function of the GCTDI is

[1] As described in Chapter 5, the dose to a small acrylic rod placed at the isocenter of the hypothetical CT scanner.

outlined, and finally, the variations of GCTDI values as a function of both radial location and beam parameters are shown.

Dose Profiles

Energy deposition in each radial and planar location was found for each run of the user code, and the dose was calculated for each region. This dose calculation allowed the dose profiles along the longitudinal and radial axes to be examined. Also, the doses along longitudinal axes were integrated to find the CTDI as function of radius in the phantom.

The dose profiles *D(z)* calculated with a 5 mm diameter rod in air and for a 3 mm slice thickness are shown in Fig. 6-1 for the range of energies from 40 to 140 keV. The doses are normalized to the incident fluence in units of Gy/(photons/sr). The size of the symbol at each data point approximates the size of the error bars, indicating ±1 standard deviation. Figure 6-1 illustrates the small amount of dose deposition outside the directly irradiated region. The values of the doses in the directly irradiated region show the close agreement with the analytically derived doses shown in Table 5-2. Figure 6-1 shows how the mean value of the dose in the directly irradiated region is approximately equal to the $CTDI_{air}$. (The small variations in the dose as function of z in the directly irradiated region are due to the statistical fluctuations of the number of dose-deposition events occurring in each planar region.) The doses immediately adjacent to the central region (i.e., <1 mm) are approximately 2% of the mean dose in the central region. This percentage drops to tenths of a percent within several centimeters and to hundredths of a percent near the ends of the rod.

Figure 6-2 shows the comparison among the dose profiles for four slice thicknesses (1, 3, 5, and 10 mm) at 80 keV in the 5 mm diameter acrylic rod. This figure illustrates the independence of $CTDI_{air}$ values on the slice thickness, as anticipated. The area under the four curves are directly proportional to the slice thickness; when divided by the slice thickness, the integrated doses are the same.

Illustrative examples of dose profiles found in-phantom are shown in Figs. 6-3 through 6-5. The dose profiles for a 5 mm slice thickness in an 8 cm radius (the FDA "head" phantom) and 16 cm radius (the FDA "body" phantom) acrylic phantom are illustrated in Figs. 6-3 and 6-4, respectively. In both figures, the dose profile is shown for 80 keV photons and for two radial locations: at the center of the phantom and at 1 cm depth from the periphery of the phantom, which are the locations specified by the FDA for CTDI measurements. All dose values have been normalized to the $CTDI_{air}$ for the appropriate incident energy. In Fig. 6-3, the error bars for each data point are approximately the same size of the symbol at each point. This is also the case for the 1 cm depth dose data shown in Fig. 6-4. Figure 6-5 illustrates the uncertainties in the dose profile in the center of the CTDI body phantom for the 5 mm slice thickness and 80 keV

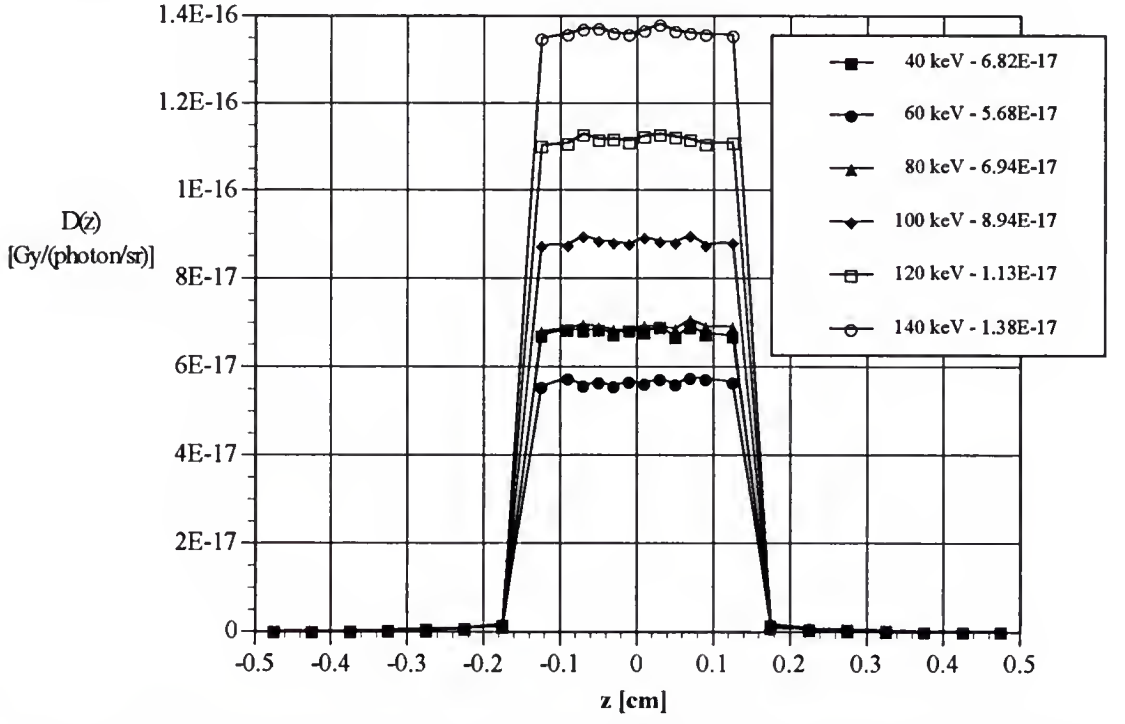

Figure 6-1: Central portion of dose profiles in a 5 mm diameter acrylic rod for a 3 mm slice thickness for the indicated incident photon energies. The analytically-derived values of $CTDI_{air}$ are shown in the legend for comparison. Error bars are approximately the size of the symbol at each data point.

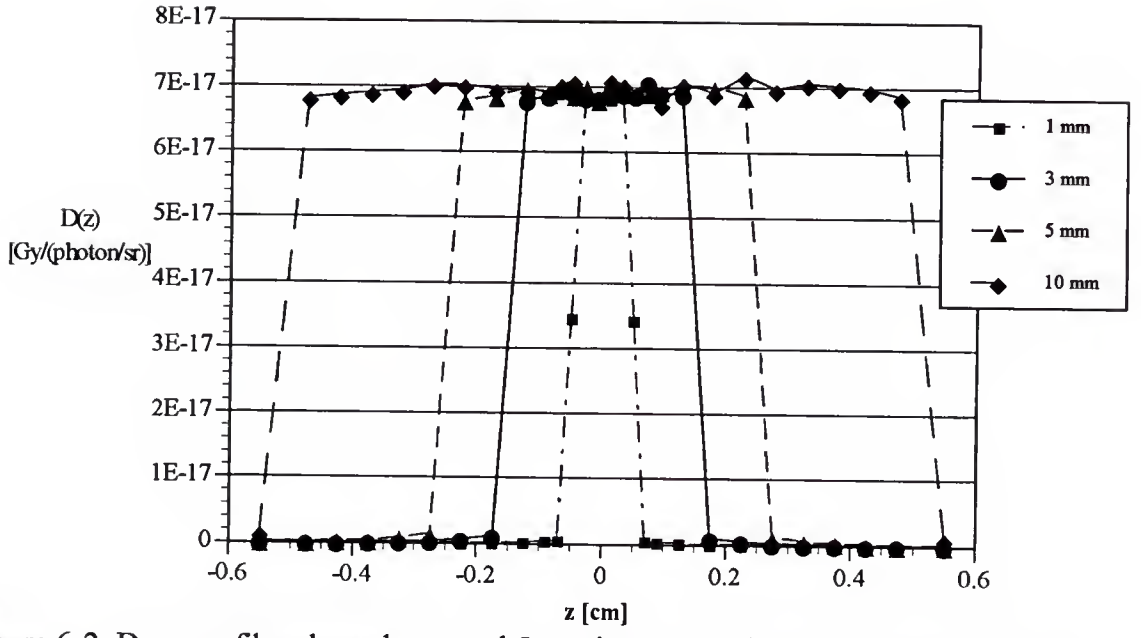

Figure 6-2: Dose profiles along the central 5 mm in a 5 mm diameter acrylic rod for 80 keV photons and the indicated slice thicknesses. Error bars are approximately the same size as the symbol at each data point.

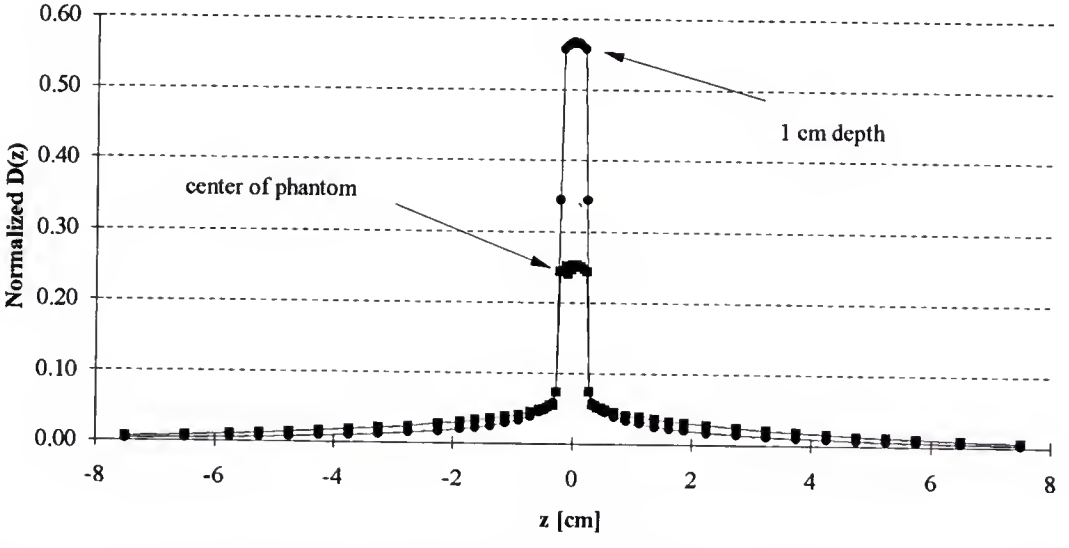

Figure 6-3: Normalized dose profiles at the center and at 1 cm depth in an 8 cm radius acrylic phantom for 80 keV incident photons and a 5 mm slice thickness. Error bars are approximately the size of the symbol at each data point.

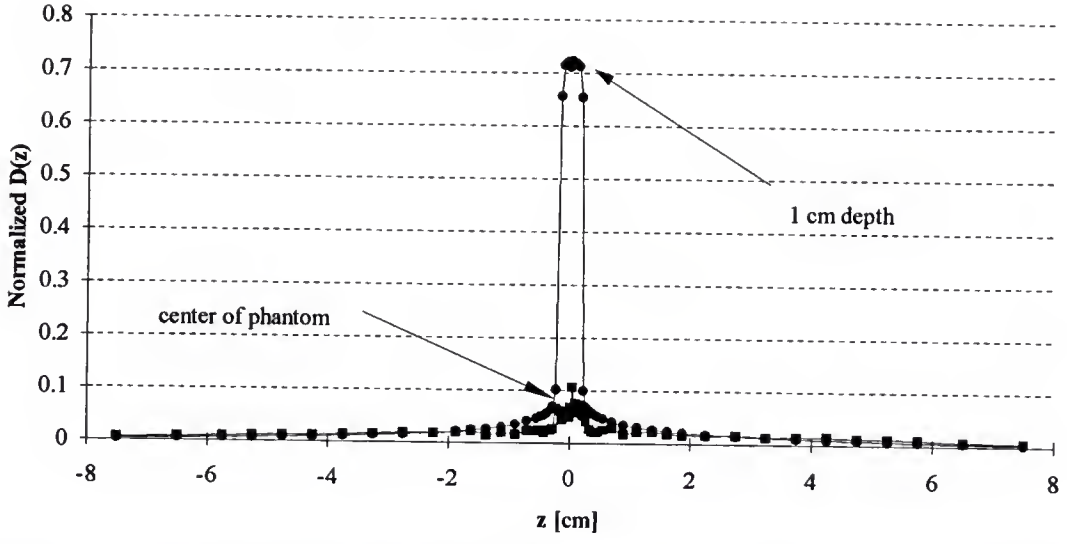

Figure 6-4: Normalized dose profiles at the center and at 1 cm depth in a 16 cm radius acrylic phantom for 80 keV incident photons and a 5 mm slice thickness. Error bars are approximately the size of the symbol at each data point for the 1 cm depth data. (Figure 6-5 shows error bars for the center of phantom data.)

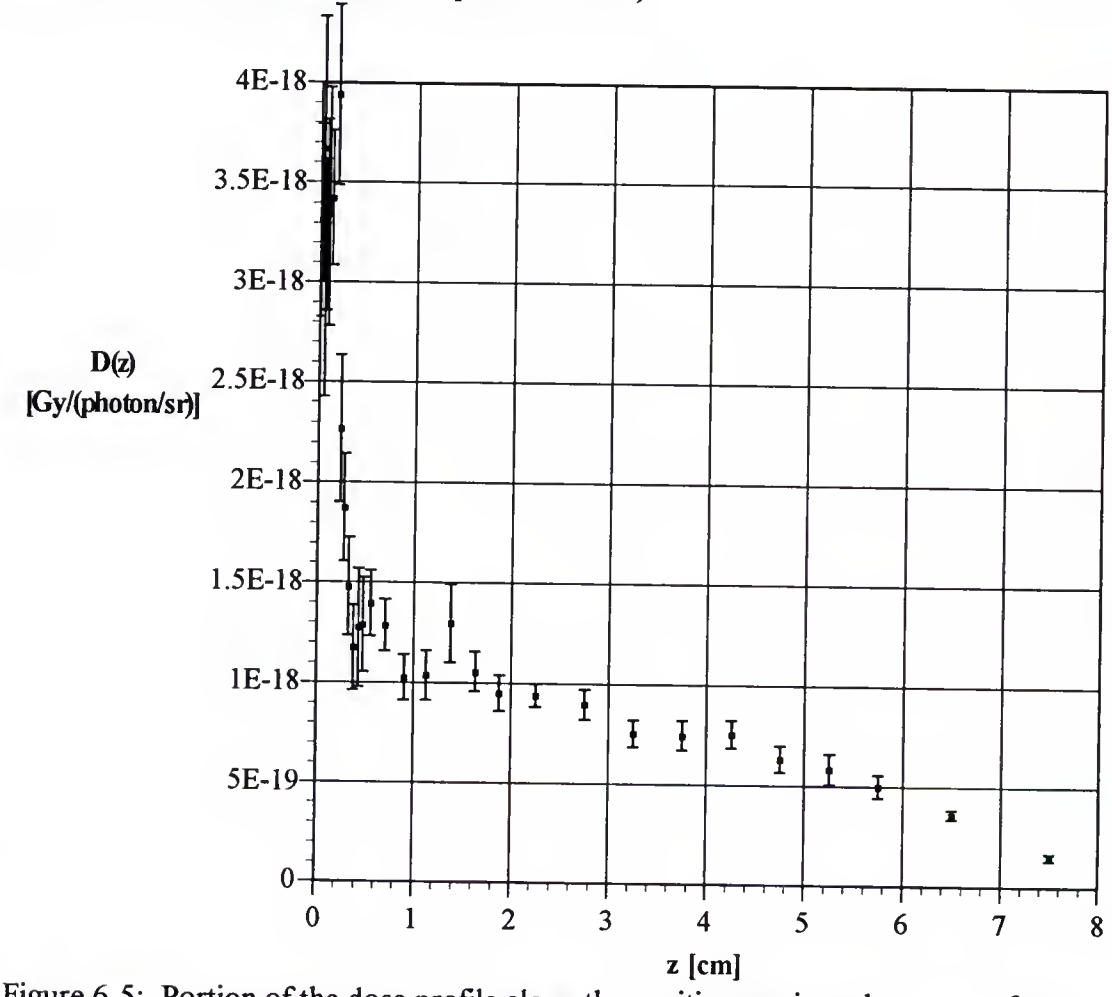

Figure 6-5: Portion of the dose profile along the positive z-axis at the center of a 16 cm radius acrylic phantom for 80 keV photons and 5 mm slice thickness. The error bars indicate ± 1 standard deviation.

incident photon energy. The error bars show ±1 standard deviation, and the doses are normalized to the incident photon fluence. The variability in the plot is a consequence of the small slab thicknesses used. Slab thicknesses two tenths of a millimeter were used in the center of the phantom to provide good spatial resolution of the dose. Not many dose deposition events occurred in these small volumes, producing larger uncertainties associated with the doses in those regions. These results are in good qualitative agreement with published dose profiles (Dixon and Ekstand 1978, McCullough and Payne, 1978, Southon 1981, Shope *et al.*, 1982, Fearon and Vucich, 1985, McCrohan *et al.*, 1987).

It is important to note that the data displayed in the following sections that concern line integrals of dose profiles are found by measuring the dose only in the cylindrical regions, i.e., the planar zones are collapsed into one large region. By accumulating the dose in the cylindrical shells, the uncertainties associated with the line integrals are reduced to less than 1% in all cases.

Integration of Dose Profiles

Dose distributions may be used to determine the total energy imparted to the phantom. For a homogeneous medium, total energy imparted ε can be found using the expression

$$\varepsilon = \int_M D\, dM = \rho \int_V D\, dV \ , \tag{6-1}$$

where ρ is the physical density of the medium (Carlsson and Alm Carlsson 1990). In a cylindrical phantom of length L and radius R centered on the origin of a cylindrical coordinate system, (6-1) can be written as

$$\varepsilon = \rho \int_{-L/2}^{+L/2} \int_0^{2\pi} \int_0^R D(z,\theta,r)\, r\, dr\, d\theta\, dz \ . \tag{6-2}$$

The result after the angular integration is

$$\varepsilon = \int_{0}^{R} \int_{-L/2}^{+L/2} D(z,r) 2\pi\rho r \, dr \, dz \ . \tag{6-3}$$

The definition of the CTDI for a single slice as specified by the FDA, presented in (1-1), is

$$CTDI = \frac{1}{T} \int_{-7T}^{+7T} D(z) dz,$$

where $D(z)$ is the dose profile for a single scan along a line perpendicular to the scanned slice, and T is the nominal slice thickness. Note that dose profiles can be integrated along *any* path length and at *any* radial location in the CTDI phantom. We can therefore define a Generalized Computed Tomography Dose Index, (GCTDI), with variable integration limits, and at any radial location within the phantom:

$$\mathfrak{C}(r,\ell) = \frac{1}{T} \int_{-\ell}^{+\ell} D(z,r) \, dz \ . \tag{6-4}$$

Here $D(z,r,)$ is the dose profile parallel to the z-axis for a single scan along a line perpendicular to the scanned slice, at radius r from the phantom center, and $\mathfrak{C}(r,\ell)$ represents the GCTDI at that radial location r and with integration limits $\pm\ell$. In the FDA definition, ℓ is $7T$ and r is defined at two places: at the center of the phantom and at a 1 cm depth from the phantom periphery.[2] If the integration in (6-4) is carried out along the total length of the phantom, the integration limits are $\pm L/2$. If (6-4) is substituted into (6-3), we obtain

$$\varepsilon = 2\pi\rho T \int_{0}^{R} \mathfrak{C}(r, L/2) r \, dr \ . \tag{6-5}$$

Because the integration limits have been fixed in the GCTDI (i.e., $L/2$), it can be assumed that the GCTDI is exclusively a function of radial location within the phantom.[3] With the

---

[2] The investigators who first proposed the quantity CTDI, (Shope *et al.*, 1981), stated that the CTDI is a good approximation of the dose at a location for a series consisting of more than 8 or 10 scans. The reason that the FDA specifies 14 scans is not in the literature to the author's knowledge.

[3] With the tacit assumption of fixed incident x-ray beam characteristics.

definition of a mean or effective value of the GCTDI, $\overline{\mathbb{C}}$, of constant value and independent of r, (6-5) can be rewritten as

$$\varepsilon = 2\pi\rho T\overline{\mathbb{C}}\int_0^R r\,dr = \pi R^2\rho T\overline{\mathbb{C}}\,, \tag{6-6}$$

which shows that the energy imparted is simply the product of the mass of the directly irradiated slice $\rho\pi R^2 T$ and the mean GCTDI.[4] Substituting (6-6) into (6-5) the explicit expression for the mean GCTDI is found:

$$\overline{\mathbb{C}} \equiv \frac{2}{R^2}\int_0^R \mathbb{C}(r, L/2) r\,dr\,. \tag{6-7}$$

Note that the use of the GCTDI implies integration over the entire length of the phantom.

The analysis above shows that the GCTDI is a useful parameter in calculating the total energy imparted to a CTDI phantom. Energy imparted can be used as an index of machine performance or of patient risk, as discussed in Chapter 1. A comparison between the energy deposition characteristics in CTDI phantoms and anthropomorphic-type phantoms is provided in the next chapter. The next two sections will show the relationships between the integration limits used, the slice thickness, and the incident x-ray beam energy for the CTDI head phantom and the CTDI body phantom.

CTDI Head Phantom

In order to investigate the differences between the GCTDI and the CTDI, data from several MONOCT runs with different slice thicknesses were analyzed. The resulting dose profiles were integrated over a range of limits from ±0.2 mm to ±8 cm for the 16 cm-long phantom. Figures 6-6 through 6-8 demonstrate the effect of changing the integration limits ℓ on the calculated value of the CTDI in a 8 cm radius acrylic phantom at 50 keV

[4] Here the term *directly irradiated slice* is taken to mean the volume $\pi R^2 T$. While this definition is not strictly true because of beam divergence, it is used here because the beam divergence is very small (<1°) for a 10 mm slice, and because of its use in calculating the energy imparted in CTDI phantoms.

for three slice thicknesses. Figure 6-6 shows the data for a 10 mm slice thickness, 6-7 for a 5 mm slice thickness, and 6-8 for a 1 mm slice thickness.

Data for fixed integration limits for the 8 cm radius phantom are summarized in Table 6-1. The integration limits chosen represent the total possible integration length for

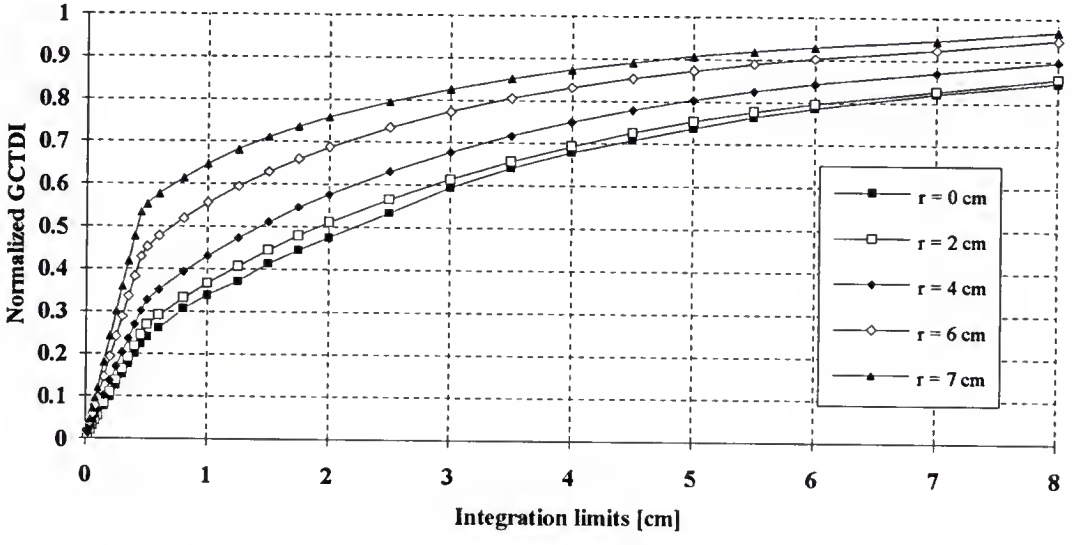

Figure 6-6: $\mathfrak{C}(r,\ell)$, normalized to the $CTDI_{air}$ value, as a function of the integration limit ℓ in an 8 cm radius acrylic phantom at 50 keV for a 10 mm slice thickness.

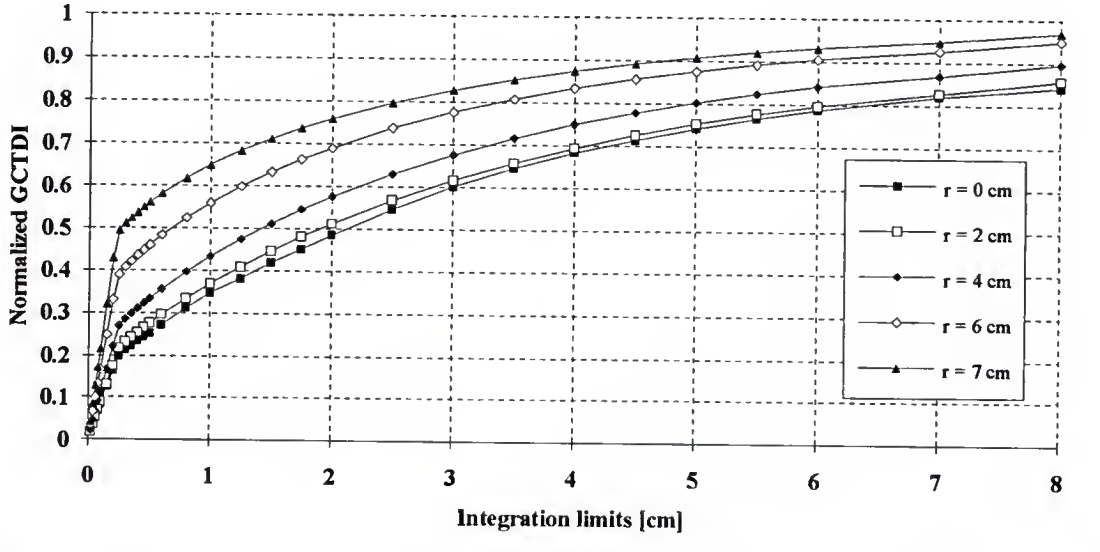

Figure 6-7: $\mathfrak{C}(r,\ell)$, normalized to the $CTDI_{air}$ value, as a function of the integration limit ℓ in an 8 cm radius acrylic phantom at 50 keV for a 5 mm slice thickness.

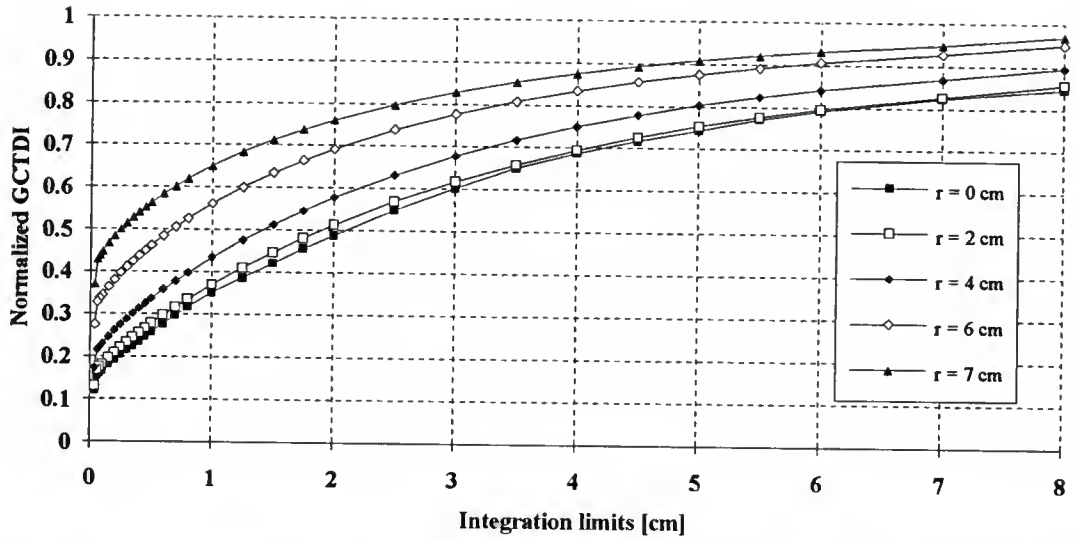

Figure 6-8: $\mathfrak{C}(r,\ell)$, normalized to the $CTDI_{air}$ value, as a function of the integration limit ℓ in an 8 cm radius acrylic phantom at 50 keV for a 1 mm slice thickness.

Table 6-1: $\mathfrak{C}(r,\ell)$ as a function of integration limits ℓ and radial position r in a head phantom at 50 keV. The results shown are the percentages of the values at each ℓ normalized to the value at ℓ=8.0 cm.

ℓ[cm]	r = 0 cm	r = 2 cm	r = 4 cm	r = 6 cm	r = 7 cm
10 mm slice thickness					
8.0	100.0	100.0	100.0	100.0	100.0
7.0	96.9	96.5	97.0	97.5	97.8
5.0	87.1	87.9	89.7	92.1	93.7
5 mm slice thickness					
8.0	100.0	100.0	100.0	100.0	100.0
5.0	88.1	87.9	89.6	92.1	93.6
3.5	76.8	76.8	79.9	85.0	87.9
1 mm slice thickness					
8.0	100.0	100.0	100.0	100.0	100.0
5.0	87.8	88.0	89.6	92.1	93.6
0.7	35.0	36.9	42.1	53.1	62.0

the 16 cm phantom (±8 cm), the integration length obtained with a typical pencil chamber used for CTDI measurements[5] (±5 cm), and the ±7T definition of the FDA.

The results indicate that, in the 1 cm slice thickness, integrating over the ±7 slice thicknesses produces CTDI and GCTDI values within 3% of each other at all radial positions. Measurement of the CTDI with a 10 cm pencil chamber underestimates $\mathbb{C}(r,L/2)$ by approximately 6% to 13%, depending on measurement location.

The 5 mm slice results show that the FDA definition of the CTDI produces dose estimates that are 12% to 23% less than the corresponding $\mathbb{C}(r,L/2)$ values, depending on measurement location. Use of a 10 cm pencil chamber underestimates $\mathbb{C}(r,L/2)$ by 7% to 12%, very similar to the results for the 1 cm slice.

The truncation effect is most obvious in the 1 mm slice data, where the FDA definition produces dose estimates that are 38% to 65% less than the corresponding $\mathbb{C}(r,L/2)$ values . The ±5 cm integration limit (i.e., the pencil chamber) underestimates $\mathbb{C}(r,L/2)$ by 6% to 12%.

The FDA-defined CTDI value can underestimate the actual point dose from a series of contiguous slices anywhere from 6% (at the 1 cm depth for 10 mm slices) to 65% (at the center position for 1 mm slices) at 50 keV. This finding is significant because CTDI values are routinely used as estimates of actual patient dose. The patient doses estimated from CTDI values are underestimates in any case because the CTDI is defined as dose to acrylic, not to tissue, and the f-factor is smaller for acrylic than for tissue.[6] Furthermore, if conventional CTDI measurements were used in place of the $\mathbb{C}(r,L/2)$ in the integration method described above, underestimation of the energy imparted to the phantom would

---

[5] Nuclear Associates, Carle Place NY 11514

[6] The f-factor is the ratio of absorbed dose in a medium to exposure in air, and is defined as

$$f_{\text{med}} = 0.873 \frac{(\bar{\mu}_{en}/\rho)_{\text{med}}}{(\bar{\mu}_{en}/\rho)_{\text{air}}},$$

(Attix, 1986). At energies less than 150 keV, the values of the mass energy absorption coefficients for water and for soft tissue are several percent larger than those for acrylic (ICRU 1989). The f-factors and absorbed doses for these materials are accordingly larger than that for acrylic.

result. The data in Table 6-1 can be used to calculate the energy imparted within the integration limits shown. When the $\pm 7T$ integration limit data are used to calculate $\overline{\mathbb{C}}$ with (6-7), the energy imparted is underestimated by 50% for 1 mm slices, 18% for 5 mm slices, and by 4% for 10 mm slices in the CTDI head phantom.

Another factor which can lead to underestimation of energy imparted to a patient is the physical size of the phantom — a phantom of a more realistic length would absorb more energy. (The anthropomorphic phantom described by Christy and Eckerman (1987) is 24 cm long.) The data shown in Figs. 6-6, 6-7 and 6-8 indicate that not all the scattered radiation is accounted for in the dose profile integrations. One would expect an asymptotic relationship between the GCTDI and the integration limits used. The user code LONGCT was written to determine the length of the phantom required to absorb all the radiation scattered out of the primary beam. LONGCT simulated 50 keV photons incident on a cylindrical acrylic phantom 140 cm in length, and of 8 cm radius. A 5 mm slice thickness was used. The results are shown in Fig. 6-9. The results indicate that, for circular phantoms 8 cm in radius, integration limits greater than approximately ±20 cm produce no significant (<1%) change in the GCTDI. Although not many patients would be expected to have 40 cm-long heads, these results indicate that CT exams of the head can deposit energy at locations relatively remote from the exam site. The data also indicate that if FDA's minimum phantom length of 14 cm was used, the energy imparted underestimate would be even greater.

The next investigation of the effects of varying integration limits in CTDI and GCTDI calculations uses spectra in place of monoenergetic incident x-ray beams. Figure 6-10 shows results obtained when a 120 kVp spectrum of 5.4 mm Al half-value layer (HVL) is incident on an 8 cm radius acrylic cylinder. The spectrum was obtained from Birch *et al.* (1979), and the data are shown for a 10 mm slice. For integration limits larger than the slice thickness, the effect of limiting the integration length is very similar to that exhibited by the monoenergetic x rays, which allows the conclusion that the CTDI/GCTDI

truncation effect in an 8 cm radius phantom is essentially energy independent in this model.

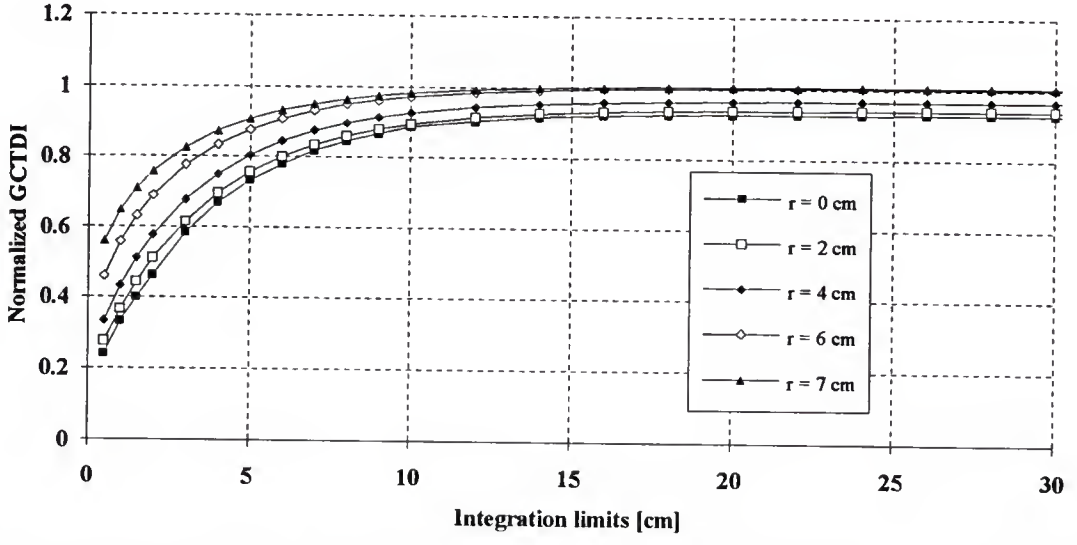

Figure 6-9: $\mathfrak{C}(r,\ell)$ values, normalized to the $CTDI_{air}$ value, as a function of the integration limit ℓ in an 8 cm radius acrylic phantom at 50 keV for a 5 mm slice thickness in a 140 cm long phantom.

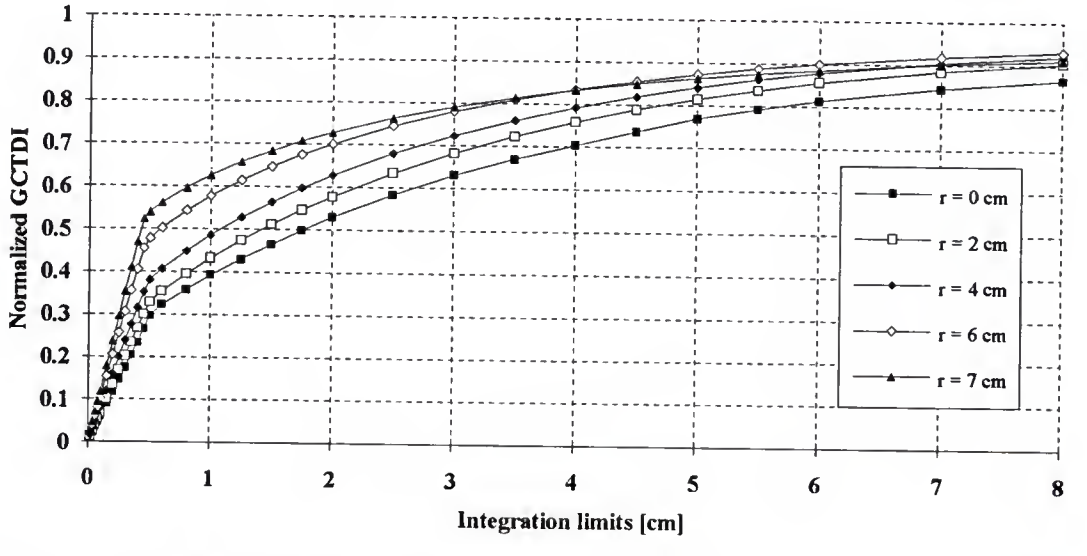

Figure 6-10: $\mathfrak{C}(r,\ell)$, normalized to the $CTDI_{air}$ value, as a function of the integration limit ℓ in an 8 cm radius acrylic phantom for a 120 kVp spectrum with 5.4 mm Al HVL, for a 10 mm slice thickness.

CTDI Body Phantom

The previous section presented GCTDI data concerning the CTDI head phantom. This section presents similar results found using the CTDI body phantom. The effects of integration limit variation using the 16 cm radius acrylic phantom are shown in Figs. 6-11 and 6-12.

Figure 6-11 demonstrates that the variation of $\mathbb{C}(r,\ell)$ has a much greater range in the body phantom at 50 keV than in the head phantom. The ±5 cm integration limits underestimates $\mathbb{C}(r,L/2)$ by 3% at the 1 cm depth position to 9% at the central position. The $\pm 7T$ limits underestimate $\mathbb{C}(r,L/2)$ by 5% at the periphery to 17% at the center.

Figure 6-12 presents data obtained with the 120 kVp 5.4 mm Al HVL spectrum incident on the 16 cm radius acrylic phantom with a 10 mm slice thickness. The spectrum data are similar to the 50 keV data, but are not identical. The ±5 cm integration limits underestimate $\mathbb{C}(r,L/2)$ by 5% at the 1 cm depth position to 19% at the central position. The $\pm 7T$ limits underestimate $\mathbb{C}(r,L/2)$ by 1% at the periphery to 19% at the center.

As in the head phantom, use of conventional CTDI measurements can underestimate both point dose and energy imparted values in the CTDI body phantom for thin slices. The $\mathbb{C}(r,L/2)$ data for the body phantom appears to be more energy dependent than the head phantom based on the results presented here.

The sections that follow present data showing the variation of $\mathbb{C}(r,L/2)$ with beam energy, beam filter, slice thickness, SAD, phantom material, and phantom radius. Mean values of the GCTDI are also given, and these values are calculated using the expression

$$\overline{\mathbb{C}} = \frac{\varepsilon}{\pi R^2 \rho T} \tag{6-8}$$

from the total energy imparted ε, which is known for each Monte Carlo run. A practical method of estimating the mean GCTDI is discussed in Chapter 7. Once the mean GCTDI value is known for a particular irradiation configuration, the energy imparted to the

phantom can be found using (6-6). Energy imparted values for various irradiation conditions are also discussed in the next chapter.

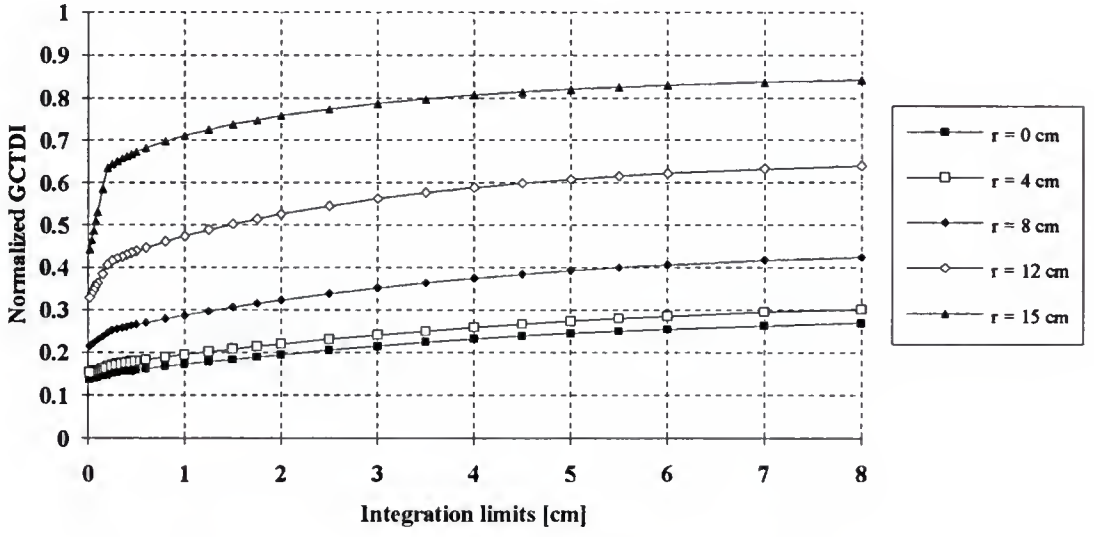

Figure 6-11: $\mathfrak{C}(r,\ell)$, normalized to the $CTDI_{air}$ value, as a function of the integration limit ℓ in an 16 cm radius acrylic phantom at 50 keV for a 5 mm slice thickness.

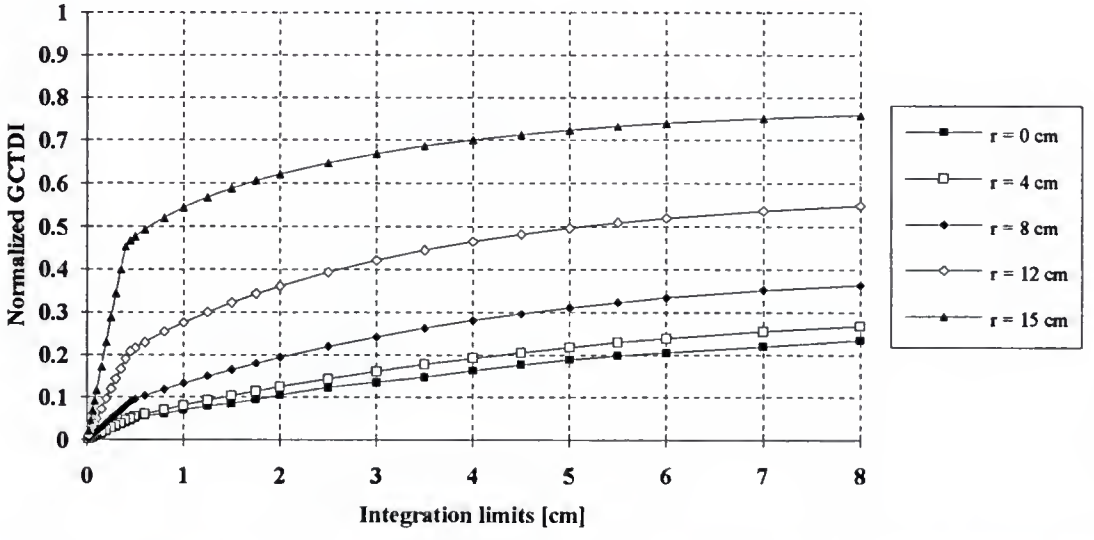

Figure 6-12: $\mathfrak{C}(r,\ell)$, normalized to the $CTDI_{air}$ value, as a function of the integration limit ℓ in an 16 cm radius acrylic phantom for a 120 kVp spectrum with 5.4 mm Al HVL, for a 10 mm slice thickness.

Photon Energy Variation

The values of $\mathfrak{C}(r,L/2)$, normalized to their respective $CTDI_{air}$ values, are shown in Figs. 6-13 and 6-14. Figure 6-13 plots $\mathfrak{C}(r,L/2)$ versus r in the CTDI head phantom for a 5 mm slice and a range of incident photon energies. Figure 6-14 shows the $\mathfrak{C}(r,L/2)$ values in the CTDI body phantom. For all points shown on both graphs, the statistical uncertainty associated with each point is less than 1%, and the error bars are smaller than the symbol at each point. Normalized $\overline{\mathfrak{C}}$ values are included in the legend for each energy.

It is apparent from inspection of Fig. 6-13 that, in the smaller phantom, the $\mathfrak{C}(r,L/2)$ values are similar for all energies above 40 keV. Because all values lie in the relatively narrow range between 0.75 and 0.95, it may be concluded that in the head phantom $\mathfrak{C}(r,L/2)$ values are nearly independent of both energy and radial location above 40 keV. In the body phantom, there is approximately a 50% reduction from the $\mathfrak{C}(15,L/2)$ (i.e., the peripheral) value to the $\mathfrak{C}(0,L/2)$ (i.e., the center) value. Although there is a significant variation with radial location in the larger phantom, there is relative energy independence of $\mathfrak{C}(r,L/2)$ above 50 keV. At the peripheral position, the values range from 0.75 to 0.85, and at the center, all the GCTDI values for energies above 50 keV are approximately 0.38.

The GCTDI results described above were found using monoenergetic incident x-ray beams. The characteristics of the GCTDI from x-ray spectra are shown next. The user code CTSPEC was written to simulate spectra incident on CTDI head and body phantoms. The spectra studied are plotted in Fig. 6-15. The spectrum labeled 120 kVp with a 4.5 mm Al HVL was measured by Fewell *et al.* (1981) and was obtained from a G.E. Maxiray x-ray tube with a 10° W anode angle and filtered with 2.8 mm of Al. The other spectra were obtained from Birch *et al.* (1979). The spectrum labeled 120 kVp with a 5.4 mm Al HVL was calculated with a 17° W anode angle and filtered with 4 mm of Al. The spectrum labeled as 120 kVp and 7.5 mm Al HVL was calculated for a 17° W anode angle and filtered with 0.25 mm of Cu. The spectrum identified as 125 kVp and 9.5 mm

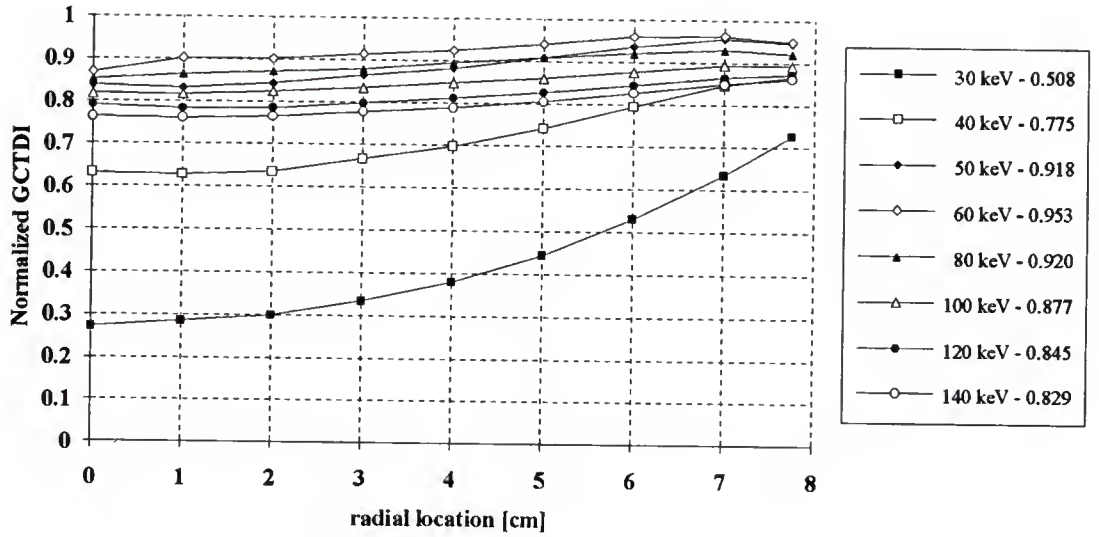

Figure 6-13: $\mathfrak{C}(r,L/2)$ as a function of radial location in the 8 cm radius phantom, normalized to the $CTDI_{air}$ at the same energy, for a 5 mm slice thickness and various incident energies. The normalized $\overline{\mathfrak{C}}$ for each energy is given in the legend.

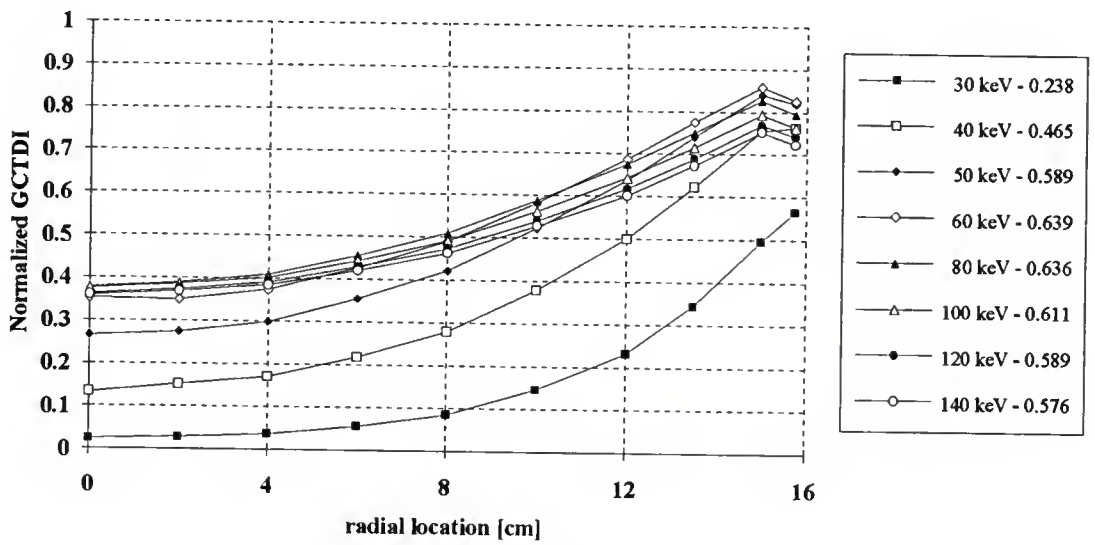

Figure 6-14: $\mathfrak{C}(r,L/2)$ as a function of radial location in the 16 cm radius phantom, normalized to the $CTDI_{air}$ at the same energy, for a 5 mm slice thickness and various incident energies. The normalized $\overline{\mathfrak{C}}$ for each energy is given in the legend.

Al HVL was calculated for a 24° W anode angle and filtered by 2.5 mm of Al and 0.4 of mm Cu. The mean photon energy $\overline{E}$ of a photon beam is calculated from the expression

$$\overline{E} = \frac{1}{N}\sum n_i E_i, \tag{6-9}$$

where n_i is the number of photons per energy interval, N is the total number of photons, and E_i is the energy of the interval (Birch *et al.*, 1979). The mean energies of the beams are found to be 50 keV for the 4.5 mm Al HVL beam, 52 keV for the 5.4 mm Al HVL beam, 61 keV for the 7.5 mm Al HVL beam, and 70 keV for the 9.5 mm Al HVL beam.

The GCTDI results found using these spectra, shown in Figs. 6-16 and 6-17, are normalized to the $CTDI_{air}$ values calculated for the spectra. The $CTDI_{air}$ values are calculated with the user code INAIRSPC, which is the code INAIR modified to use x-ray spectra instead of monoenergetic beams.

In order to determine the validity of these $CTDI_{air}$ values, an analytical calculation was performed, similar to that described in Chapter 5 using (5-2). For each spectrum, a mean mass energy absorption coefficient, $\overline{\mu}_{en}/\rho$, was found using the expression

$$\frac{\overline{\mu}_{en}}{\rho} = \frac{\int_0^{kVp}\left(\frac{\mu_{en}}{\rho}\right)\Psi(E)\,dE}{\int_0^{kVp}\Psi(E)\,dE}, \tag{6-10}$$

where $\Psi(E)$ is the energy fluence for energy E, and $\Psi(E) = E\Phi(E)$ (Attix, 1986). ICRU Report No. 44 (ICRU 1989) was used to obtain the mass energy absorption coefficients. The mean value of the energy absorption coefficient was used to calculate a dose in-air for each spectrum at a 65 cm SAD. Table 6-2 lists ($\overline{\mu}_{en}/\rho$, E_{corr} (the energy corresponding to that value of $\overline{\mu}_{en}/\rho$), $CTDI_{air}$ calculated analytically, and $CTDI_{air}$ found using EGS. The largest discrepancy between the two $CTDI_{air}$ values is approximately 9%, which is within the 10% uncertainty of the ICRU values (ICRU 1989).

Table 6-2: Summary of spectra data.

Spectrum		$\bar{\mu}_{en}/\rho$	E_{corr}	$CTDI_{air}$ [Gy/(photon/sr)]	
kVp	HVL [mm Al]	[cm²/g]	[keV]	analytical	EGS
120	4.5	0.0714	32	8.4×10^{-17}	7.7×10^{-17}
120	5.4	0.0574	36	7.8×10^{-17}	7.3×10^{-17}
120	7.5	0.0488	39	7.2×10^{-17}	6.9×10^{-17}
125	9.5	0.0421	42	6.7×10^{-17}	7.0×10^{-17}

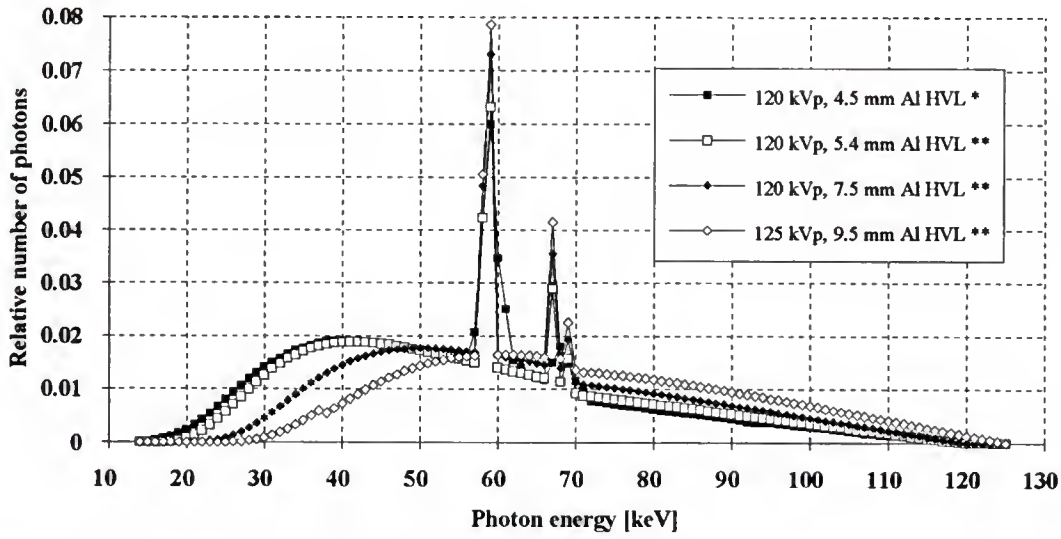

Figure 6-15: Plots of the four spectra used in this work.
* from Fewell *et al.* (1981).
** from Birch *et al.* (1979).

Table 6-3: Comparison of $CTDI_{air}$ values for the three beam filters used.

Energy	$CTDI_{air}$ [Gy/(photon/sr)]		
[keV]	No Filter	Perfect Filter	GE Filter
30	1.05×10^{-16}	1.04×10^{-16}	7.50×10^{-17}
40	7.00×10^{-17}	6.99×10^{-17}	5.58×10^{-17}
50	5.86×10^{-17}	5.86×10^{-17}	4.83×10^{-17}
60	5.82×10^{-17}	5.82×10^{-17}	4.91×10^{-17}
80	7.05×10^{-17}	7.05×10^{-17}	6.16×10^{-17}
100	9.01×10^{-17}	9.01×10^{-17}	7.94×10^{-17}

The GCTDI values shown in Figs. 6-16 and 6-17 are in the range expected from inspection of the monoenergetic data and reflect the differences in beam filtration and kVp. In the CTDI head phantom, all of the $\mathfrak{C}(r,L/2)$ curves for the spectra lie in the range near the 40 keV and 50 keV monoenergetic beam data, indicating a "mean" energy value less than that calculated with (6-9). In the CTDI body phantom, all the spectra curves lie between the 40 keV and 60 keV monoenergetic beam data. These data also indicate mean energies less than those calculated with (6-9). The most heavily filtered beams have similar characteristics and show the least attenuation through the phantom, as expected. Similarly, the greatest attenuation is seen in the 5.4 mm Al HVL spectrum, which results from a greater number of lower energy photons present in the beam.

The mean normalized $\overline{\mathfrak{C}}$ values of the spectra in the head phantom are: 0.749 for the 4.5 mm Al HVL beam, 0.800 for the 5.4 mm Al HVL beam, 0.839 for the 7.5 mm Al HVL beam, and 0.880 for the 9.5 mm Al HVL beam. As expected, these values of $\overline{\mathfrak{C}}$ for the spectra fall between the 40 keV and 50 keV monoenergetic values in the head phantom (0.775 at 40 keV and 0.918 at 50 keV).

In the body phantom the values of $\overline{\mathfrak{C}}$ are: 0.477 for the 4.5 mm Al HVL beam, 0.514 for the 5.4 mm Al HVL beam, 0.565 for the 7.5 mm Al HVL beam, and 0.599 for the 9.5 mm Al HVL beam. In the body phantom the $\overline{\mathfrak{C}}$ values are 0.465 at 40 keV, 0.589 at 50 keV, and 0.639 at 60 keV. Thus in the body phantom, all the spectra have $\overline{\mathfrak{C}}$ values either within the 40 keV and 50 keV monoenergetic data or very close to the 50 keV data.

The data show that the values of $\overline{\mathfrak{C}}$ are within 75% to 88% of $CTDI_{air}$ for the head phantom, and within 48% to 60% of $CTDI_{air}$ for the body phantom. These data are significant because they show that x-ray spectra with HVLs in the range used clinically all appear to behave similarly in terms of energy deposition.

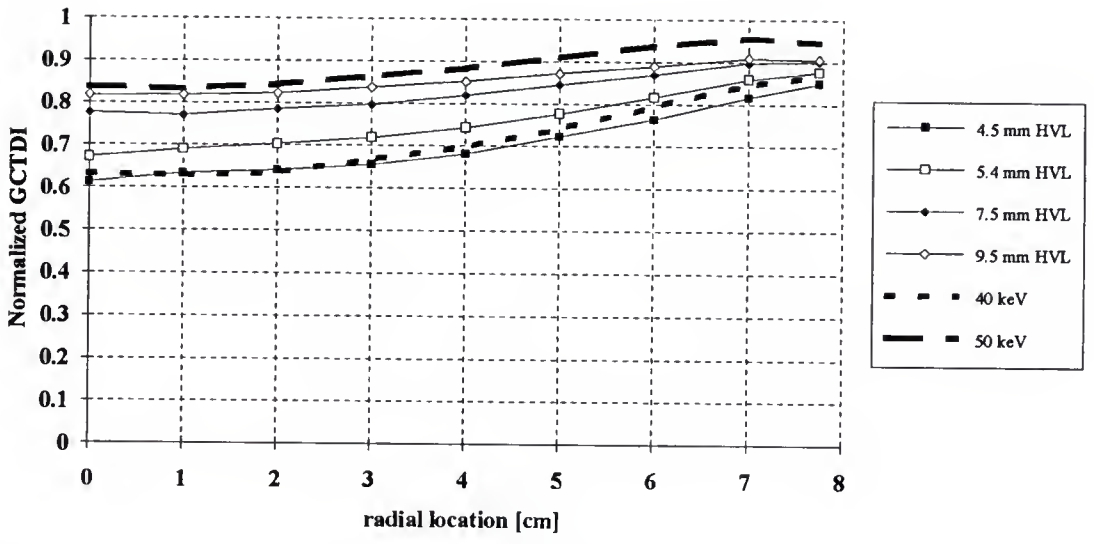

Figure 6-16: $\mathfrak{C}(r,L/2)$ as a function of radial location for four spectra for 5 mm slices in an 8 cm radius acrylic phantom. The data have been normalized to the $CTDI_{air}$ value calculated for each spectrum. Spectra are from Fewell *et al.* (1981) and Birch *et al.* (1979).

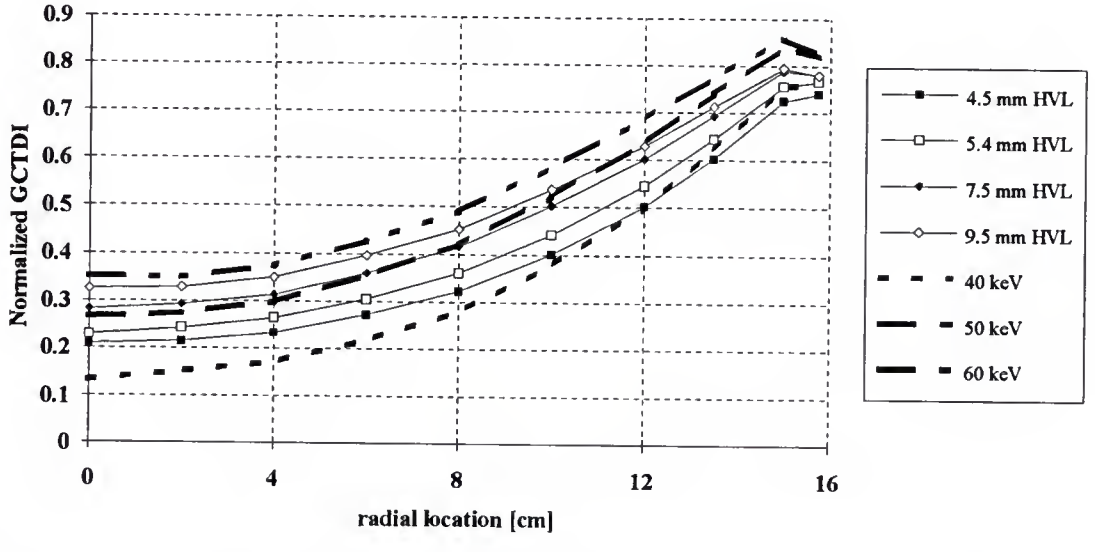

Figure 6-17: $\mathfrak{C}(r,L/2)$ as a function of radial location for four spectra for 5 mm slices in a 16 cm radius acrylic phantom. The data have been normalized to the $CTDI_{air}$ value calculated for each spectrum. Spectra are from Fewell *et al.* (1981) and Birch *et al.* (1979).

Beam Filter Variation

The CTDI data for the no-filter, perfect filter, and GE filter configurations are shown in Figs. 6-18 and 6-19. Figure 6-18 shows the data for the 8 cm radius acrylic phantom at the 50 keV energy and for 5 mm slice thickness. Figure 6-19 shows the data for the 16 cm body phantom for the 50 keV incident energy and a 5 mm slice thickness. All data are normalized to the $CTDI_{air}$ value at 50 keV found with the same filter in the beam.

The value of the $CTDI_{air}$ depends on the beam intensity at the central axis of the fan beam. The intensity at the central axis is expected to change only minimally due to the presence of a beam-shaping filter, because the filter is thinnest at that point. The GE filter is several millimeters thick at the center, and the perfect filter is of zero thickness at the center. The user codes GEINAIR and PERFAIR calculated the dose to a 5 mm diameter acrylic rod in air over the range of energies 40 keV to 140 keV with the GE and perfect filters, respectively. At every energy evaluated, there was less than 1% difference between the no-filter and perfect filter $CTDI_{air}$ values. This was not the case for the GE filter because of its finite thickness at all points.[7] Table 6-3 compares the $CTDI_{air}$ values for the three filters. All the results presented in this section are normalized to the $CTDI_{air}$ value for the appropriate filter.

In the 8 cm radius phantom, the most obvious effects of a beam filter are the overall reduction of the $\mathfrak{C}(r,L/2)$ values and the shape of the GCTDI curves. The $\overline{\mathfrak{C}}$ values, as calculated with (6-8), decrease from 0.918 to 0.766 and 0.575 for the GE and perfect filters, respectively. The three filters produce very different $\mathfrak{C}(r,L/2)$ curves. The GE filter produces the most uniform $\mathfrak{C}(r,L/2)$ distribution as a function of radial location. The no-filter configuration produces a larger $\mathfrak{C}(r,L/2)$ value at the phantom periphery than at the phantom center, whereas the no-filter curve produces a larger value at the phantom

[7] The detailed characteristics of the GE filter are proprietary information, however the filter thickness ranges from several millimeters to several centimeters.

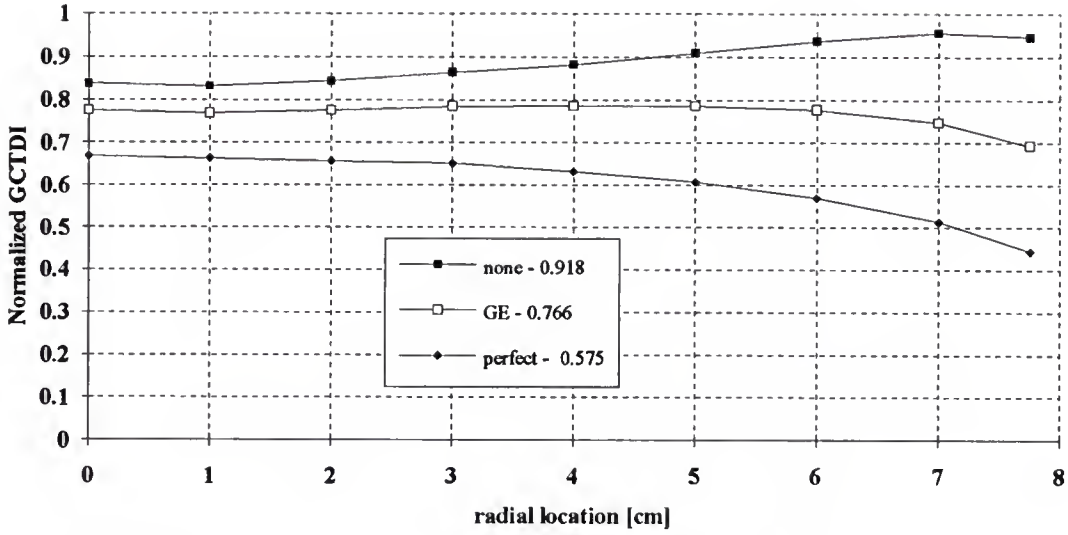

Figure 6-18: $\overline{\mathbb{C}}(r,L/2)$ as a function of radial location in the acrylic 8 cm radius phantom at 50 keV for a 5 mm slice thickness, and the indicated beam filter. The normalized $\overline{\mathbb{C}}$ is given following the filter identification.

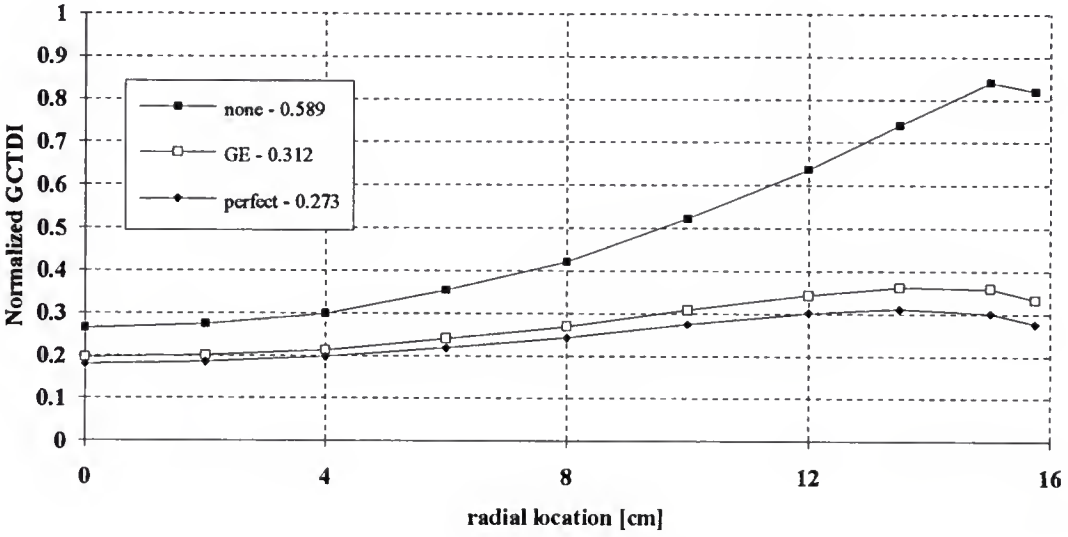

Figure 6-19: $\overline{\mathbb{C}}(r,L/2)$ as a function of radial location in the acrylic 16 cm radius phantom at 50 keV for a 5 mm slice thickness and the indicated beam filter. The normalized $\overline{\mathbb{C}}$ is given following the filter name.

periphery than at the center. This effect is due to the preferential filtering near the phantom edge, that is, the intensity of the beam is reduced near the edge of the fan beam; consequently less energy is deposited there. The differences in the shapes of the $\mathfrak{C}(r,L/2)$ curves are a consequence of the difference between the shapes of the two filters and differences in their attenuating properties, and they may reflect efforts by GE to optimize the filter design for head scans.

The 16 cm radius phantom data also show the mean $\overline{\mathfrak{C}}$ decrease seen in the smaller phantom. The no-filter value of 0.589 is reduced to 0.312 for the GE filter and 0.273 for the perfect filter. The differences between the filters do not make as large a difference in this case, as the $\mathfrak{C}(r,L/2)$ values are almost identical for the two filters. In this phantom, the filters produce $\mathfrak{C}(r,L/2)$ values that show a smaller variation as a function of radial location than the no-filter data. The attenuation of the x-ray beam produces a decrease in the $\mathfrak{C}(r,L/2)$ values from the phantom periphery to the phantom center in the no-filter case. The reduced peripheral intensity of the x-ray beam produces the more moderate decrease in the $\mathfrak{C}(r,L/2)$ values seen in the filtered-beam data.

The beam-filter data above were found using an SAD of 65 cm. However, the SAD of the GE 9800 scanner is actually 63 cm. In order to compare calculated results to measured CTDI ratios, a range of energies was investigated in the body phantom with the GE filter and an SAD of 63 cm. The results are shown in Fig. 6-20. The monoenergetic beams in the range 40 keV to 80 keV are shown. Also, data calculated with the 4.5 mm Al HVL spectrum measured by Fewell *et al.* (1981) and the 5.4 mm Al HVL spectrum from Birch *et al.* (1979) are displayed. These spectra have beam qualities that bracket the 5.0 mm Al HVL value quoted by GE for the 9800 scanner with xenon detectors. The 4.5 mm Al HVL spectrum data are normalized to a $CTDI_{air}$ value of 6.35×10^{-17} Gy/(photon/sr), and the 5.4 mm Al HVL spectrum is normalized to a $CTDI_{air}$ value of 5.93×10^{-17} Gy/(photon/sr). Both of these values were found by modifying the code GEINAIR to use spectra instead of monoenergetic beams. The effect of the filter on the

$CTDI_{air}$ values is shown by the reduction of the $CTDI_{air}$ values of the spectra — the filtered values are 78% and 82% of the non-filtered values for the 4.5 and 5.4 mm Al HVL beams respectively.

The spectrum results shown in Fig. 6-20 are within the range expected from inspection of the no-filter data. The ratio of the central value of the GCTDI to the 1 cm depth (r = 15 cm) is 0.56 for both spectra; this ratio compares favorably with the CTDI values furnished by GE for the 9800 scanners: 0.55 for the xenon detector model and 0.54 for the solid state detector model for 1 cm slice thicknesses (see Table 2-3). The $\mathfrak{C}(r,L/2)$ curve for both spectra lie between the curves for the 40 keV and 50 keV monoenergetic beams. These results are consistent with the results obtained for the spectra with no beam filter and indicate that the mean energy of a spectrum is not an accurate indication of its energy deposition characteristics.

Slice Thickness Variation

Figure 6-21 shows the $\mathfrak{C}(r,L/2)$ as a function of slice thickness in the 8 cm radius head phantom for 50 keV incident photons. Again, these data are normalized to the $CTDI_{air}$ at 50 keV. The data show that $\mathfrak{C}(r,L/2)$ is essentially independent of slice thickness. This result is explained by the fact that, in the model used, (i.e., point sources with perfect collimation), large slice thicknesses may be seen as the sum of a series of smaller slice thicknesses. That is, the 10 mm slice thickness is equivalent to ten contiguous 1 mm slices. The dose at any point (r,z) outside the primary beam in the phantom is directly proportional to the slice thickness, e.g., the dose at a point from a 10 mm slice is twice that from a 5 mm slice and ten times that of a 1 mm slice. The corresponding line integrals are accordingly proportional to the slice thickness. The GCTDI as defined above is the quotient of the line integral and the nominal slice thickness; because both the numerator and denominator are directly proportional to slice thickness, the quotient (the GCTDI) is independent of slice thickness.

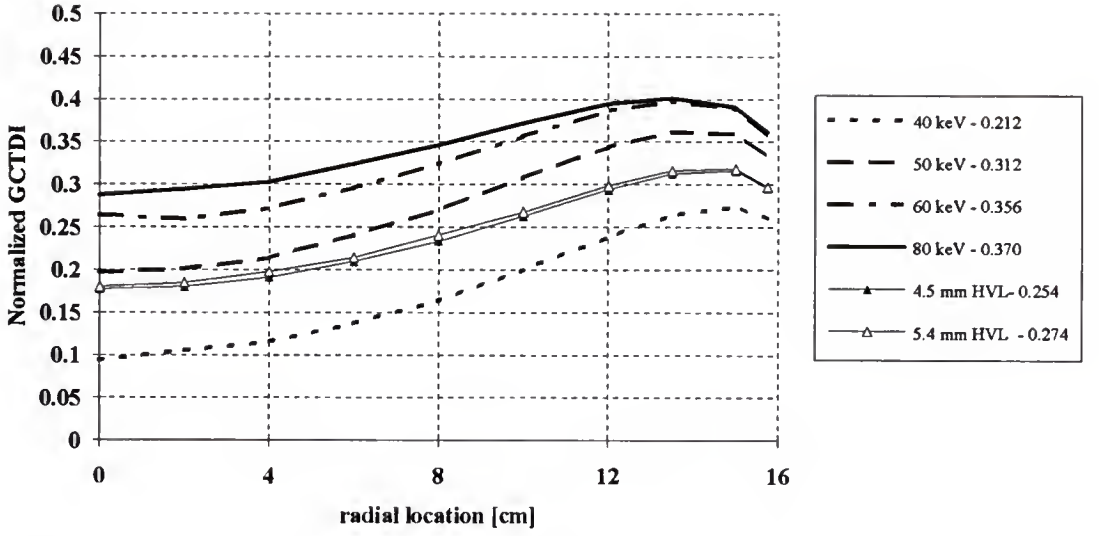

Figure 6-20: $\mathfrak{C}(r,L/2)$ as a function of radial location for the GE filter in a 16 cm acrylic phantom at 63 cm SAD for a 5 mm slice thickness, and various incident beams The $\overline{\mathfrak{C}}$ values are given in the legend along with the incident beam identification.

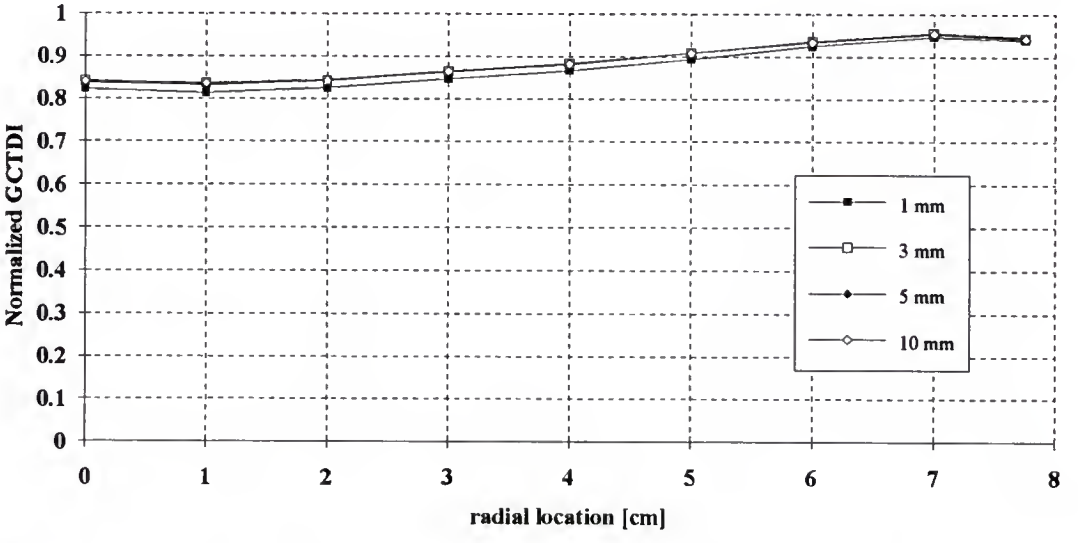

Figure 6-21: $\mathfrak{C}(r,L/2)$ as a function of radial location in an 8 cm radius acrylic phantom at 50 keV, for various slice thicknesses.

The independence of the GCTDI on slice thickness should also be independent of energy. The lower photon energies produce less scatter than the higher energies, but the effect of the summation of small slices is the same for all energies. (The independence of the GCTDI with respect to slice thickness was also shown to apply for 80 keV incident monoenergetic x rays.) This situation may not always apply clinically because of the penumbra produced from the finite size of the focal spots and the imperfect collimation. Published values of the CTDI are found using the seven-slice-thickness limit discussed above and do not show slice thickness independence. This topic is discussed further in Chapter 8.

Phantom Size Variation

The data in Fig. 6-22 illustrate the variation of $\mathfrak{C}(r,L/2)$ with the size of the phantom. The data are calculated with a 5 mm slice thickness at 50 keV. The effect of attenuation is clearly seen from the large decrease in the $\mathfrak{C}(r,L/2)$ from the periphery to the center as the radius increases. The $\overline{\mathfrak{C}}$ values change from approximately 1.0 for the 6 cm radius phantom to 0.5 for the 20 cm radius phantom.

Phantom Material Variation

Various phantom materials were evaluated to determine their effects on the GCTDI. These materials were listed in Table 1-1 and are acrylic, water, bone, fat, lung, and muscle. The composition of the tissues used was taken from ICRU Report No. 44 (ICRU 1989). Note that the lung tissue is assumed to be inflated lung (density = 0.26 g/cm^3), and the bone tissue is cortical bone (density = 1.92 g/cm^3). The density of fat is 0.95 g/cm^3 and that of muscle is 1.05 g/cm^3. The effects of these phantom materials on $\mathfrak{C}(r,L/2)$ values when each is constructed into an 8 cm radius phantom are shown in Fig. 6-23. Figure 6-24 shows similar data for a 16 cm radius phantom.

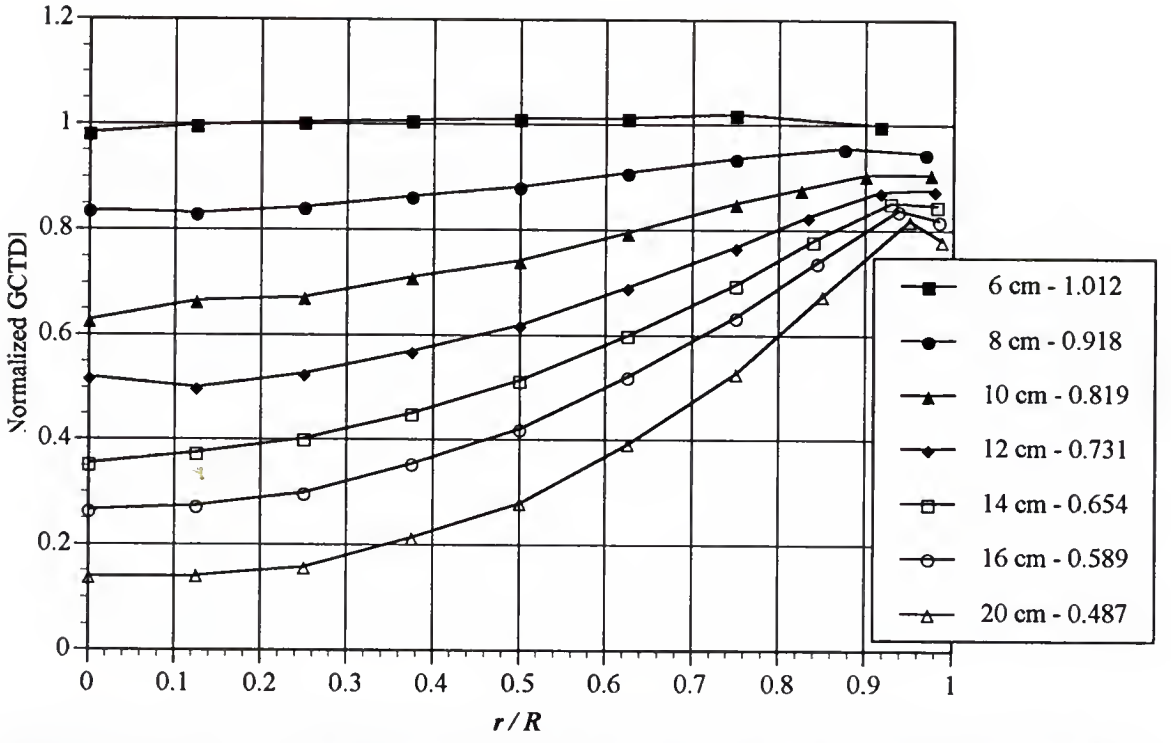

Figure 6-22: $\mathfrak{C}(r,L/2)$ plotted against relative distance from the center of the phantom for various values of phantom radius R. The data are for a 5 mm slice thickness at 50 keV, a 5 mm slice thickness and without beam filtration. $\overline{\mathfrak{C}}$ values are given in the legend for each value of R.

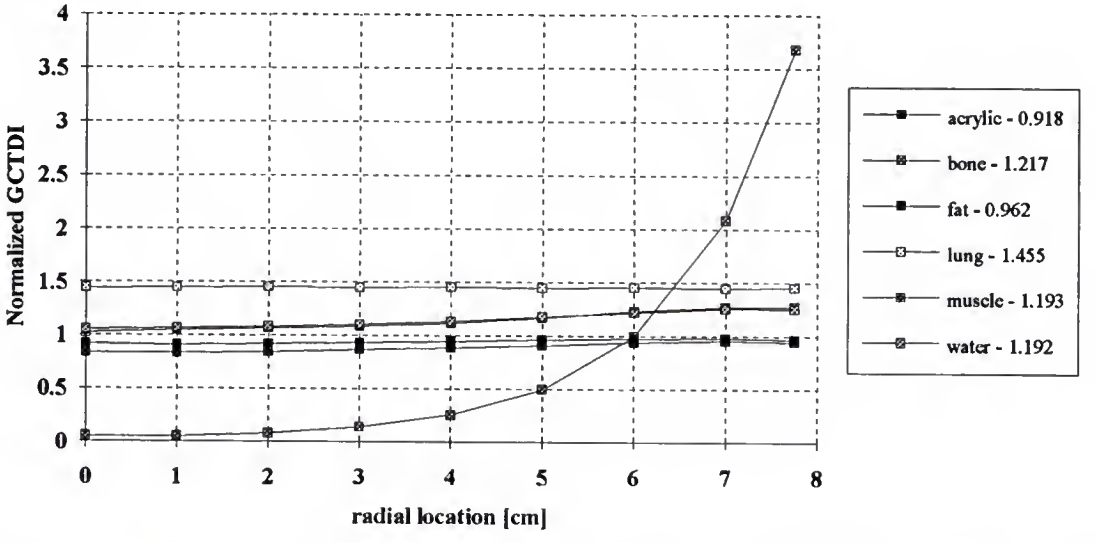

Figure 6-23: $\mathfrak{C}(r,L/2)$ plotted against radial location for various phantom materials in an 8 cm radius phantom for 50 keV photons and 5 mm slice thickness. Normalized $\overline{\mathfrak{C}}$ values are given in the legend.

The results in the 8 cm radius phantom show that, with the exception of bone and lung, all the materials have very similar distributions and all have a $\overline{\mathfrak{C}}$ of approximately 1.0 (i.e., 0.9 to 1.2). Bone, of course, has a greater density and larger mean atomic number than the other materials and therefore is expected to produce greater attenuation. Inflated lung has such a small density that very little photon attenuation occurs; the $\mathfrak{C}(r,L/2)$ curve is extremely uniform and reflects this fact.

In the larger phantom, both bone and lung show markedly different characteristics than the other materials. The bone data shows the expected large attenuation of the incident beam. Because of its low density, lung provides only a small amount of attenuation and is expected to have a more uniform dose distribution than the other tissues. This effect is demonstrated by the flat curve of the $\mathfrak{C}(r,L/2)$. Although there is a decrease in $\mathfrak{C}(r,L/2)$ from periphery to center for the lung data, the distribution is more uniform than in the other tissues. All the other soft tissues are attenuated by approximately 50% from the edge of the phantom to the center, and all the curves have approximately the same shape. The differences among the soft tissue data are most likely due to differences in the densities of the tissues, because the media all have similar mass attenuation and mass absorption coefficients (ICRU 1989). It is interesting to note that the $\overline{\mathfrak{C}}$ value for both water and all the tissues (except lung) are approximately in the same range, despite the wide variation in the $\mathfrak{C}(r,L/2)$ curves.

SAD Variation

The effect of varying the SAD is shown in Fig. 6-25. The data were calculated for an acrylic phantom 8 cm in radius and for a 5 mm slice thickness. These data are normalized to the value of $CTDI_{air}$ as measured at the corresponding SAD at 80 keV. The data show essentially no differences in the value of the normalized $\mathfrak{C}(r,L/2)$ as a function of the SAD at any radial location. Data generated at 80 keV show the same behavior.

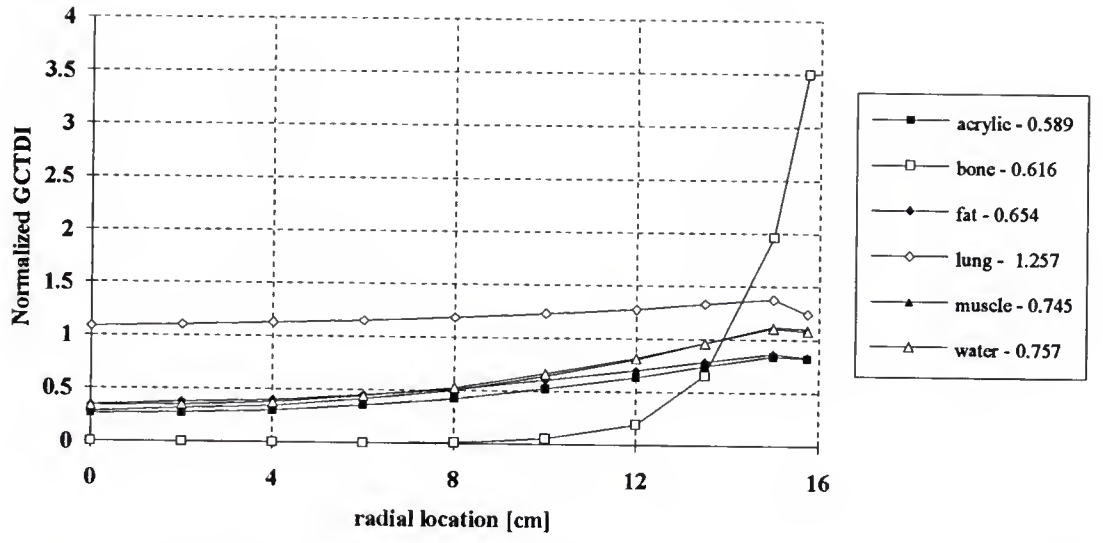

Figure 6-24: $\mathfrak{C}(r,L/2)$ plotted against radial location for various phantom materials in a 16 cm radius phantom for 50 keV photons and 5 mm slice thickness. Normalized $\overline{\mathfrak{C}}$ values are given in the legend.

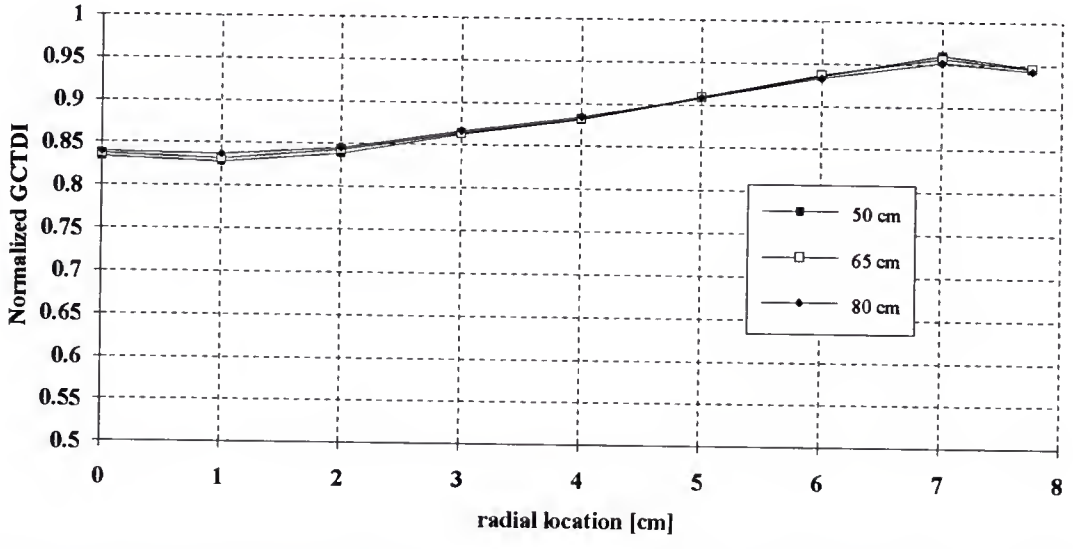

Figure 6-25: $\mathfrak{C}(r,L/2)$ plotted against radial location for various SAD values for a 5 mm slice thickness and 50 keV photons.

Summary

To summarize the results of this chapter, a new concept, the GCDTI, is defined. The GCDTI is a direct function of the dose distribution within a CTDI phantom and can be used to estimate the total energy imparted to a CTDI phantom. The differences between the GCTDI and the CTDI are demonstrated by varying the integration limits used in the GCTDI calculation. At 50 keV, these differences range from 6% to 65 %, dependent on slice thickness and measurement location. These discrepancies can lead to underestimates of the energy imparted by up to 50%. In the head phantom, the differences between the GCTDI and the CTDI do not appear to be very energy dependent, as shown by the similarity between the monoenergetic and spectrum results. This is not the case for the body phantom, as there are distinct differences between the monoenergetic and spectrum data.

The dependence of the GCTDI on incident energy is demonstrated in both the CTDI head and body phantoms. In the smaller phantom, there is relative energy independence at energies greater than 50 keV. In the body phantom, the GCTDI is nearly energy independent at 60 keV and above. When typical x-ray spectra are used in place of monoenergetic incident x rays, the GCTDI curves fall in the range near the 40 keV and 50 keV monoenergetic data. There does not seem to be any simple relationship between the mean energy of the beam and the resulting $\mathbb{C}(r,L/2)$ or $\overline{\mathbb{C}}$ data.

Beam-shaping filters both change the shape of the $\mathbb{C}(r,L/2)$ curves and reduce the $\overline{\mathbb{C}}$ values at 50 keV. In the CTDI head phantom, with no beam-shaping filter present, there is a decrease in $\mathbb{C}(r,L/2)$ from the periphery to the center of the phantom. The perfect filter produces a greater variation in $\mathbb{C}(r,L/2)$ than does the GE filter, and both filters produce a small decrease in the $\mathbb{C}(r,L/2)$ from center to periphery. In the CTDI body phantom, GCTDI values for the filtered x-ray beams are much more uniform than that of the no-filter data. When typical x-ray spectra, filtered by the GE filter, are incident on the

CTDI body phantom, the resulting $\mathfrak{C}(r,L/2)$ data fall between the 40 keV and 50 keV monoenergetic beam values. These data are consistent with the spectra data in the no-filter configuration presented above and show that the mean energy of a spectrum is not an accurate indicator of the $\mathfrak{C}(r,L/2)$ associated with that spectrum.

The results presented above show that, in this model, the GCTDI is independent of slice-thickness dependent and SAD.

The values of $\mathfrak{C}(r,L/2)$ are shown to be highly dependent on the size of the phantom. The larger the phantom, the greater the attenuation of the incident beam, and the greater the variation of $\mathfrak{C}(r,L/2)$ for a given phantom size.

Phantom material is shown to affect $\mathfrak{C}(r,L/2)$ values at 50 keV greatly. The data for the materials with similar density are very similar in both phantoms. The $\mathfrak{C}(r,L/2)$ data for inflated lung tissue show very uniform distributions in both phantoms, reflecting the fact that little attenuation occurs in this tissue. The data for cortical bone shows a large decrease of $\mathfrak{C}(r,L/2)$ values from periphery to center in both phantoms. This decrease is consistent with the greater attenuative properties of bone. For the soft tissues, including water and excluding lung, the values of $\overline{\mathfrak{C}}$ are all in the range of 0.92 to 1.2 for the head phantom and 0.58 to 0.76 for the body phantom.

CHAPTER 7

ENERGY IMPARTED RESULTS

Introduction

The previous chapter presented results involving dose distributions from EGS simulations with various configurations. The final energy dispositions for each run were recorded separately in the following categories (with the indicated abbreviations):

- Total energy incident on the phantom (Total incident),
- Total energy imparted in the phantom (Total imparted),
- Scattered energy deposited in the phantom (Scattered imparted),
- Primary energy deposited in the phantom (Primary imparted),
- Total energy leaving the phantom (Total out),
- Scattered energy leaving the phantom (Scattered out), and
- Primary energy leaving the phantom (Primary out).

The results below are tabulated in terms of the absolute values and percentages of each energy category. In all cases, the uncertainty associated with each quantity is less than 1%. All data are normalized to the appropriate $CTDI_{air}$ value. The results quantitatively demonstrate how the variation of the parameters affect the final energy dispositions, and specifically, which factors are most critical in determining the total energy imparted to phantoms.

Photon Energy Variation

The results illustrating the variation of the energy dispositions with incident energy changes are shown in Table 7-1 and Figure 7-1 for the 8 cm radius acrylic phantom. The data for the 16 cm radius acrylic phantom are shown in Table 7-2 and Figure 7-2. The

data indicate that the energy imparted is relatively independent of incident energy in both phantoms, except at the lower energies. For the 8 cm radius phantom in the energy range 40 keV to 140 keV, the energy imparted ranges between a minimum of 91 mJ/Gy at 40

Table 7-1: Energy dispositions for an 8 cm acrylic phantom with no beam filter and a 5 mm slice thickness.

Normalized energy dispositions [mJ/Gy]							
Disposition	**40 keV**	**50 keV**	**60 keV**	**80 keV**	**100 keV**	**120 keV**	**140 keV**
Total incident	173.4	258.7	312.7	344.2	336.6	320.8	307.7
Scattered imparted	35.8	49.3	55.4	56.6	53.8	50.7	48.3
Primary imparted	55.4	58.7	56.7	51.6	49.4	48.8	49.2
Total imparted	91.2	108.0	112.1	108.2	103.2	99.5	97.5
Scattered out	73.1	132.7	174.6	201.2	194.7	180.4	167.6
Primary out	9.1	18.0	26.0	34.8	38.7	40.9	42.6
Total out	82.2	150.7	200.6	236.0	233.4	221.3	210.2

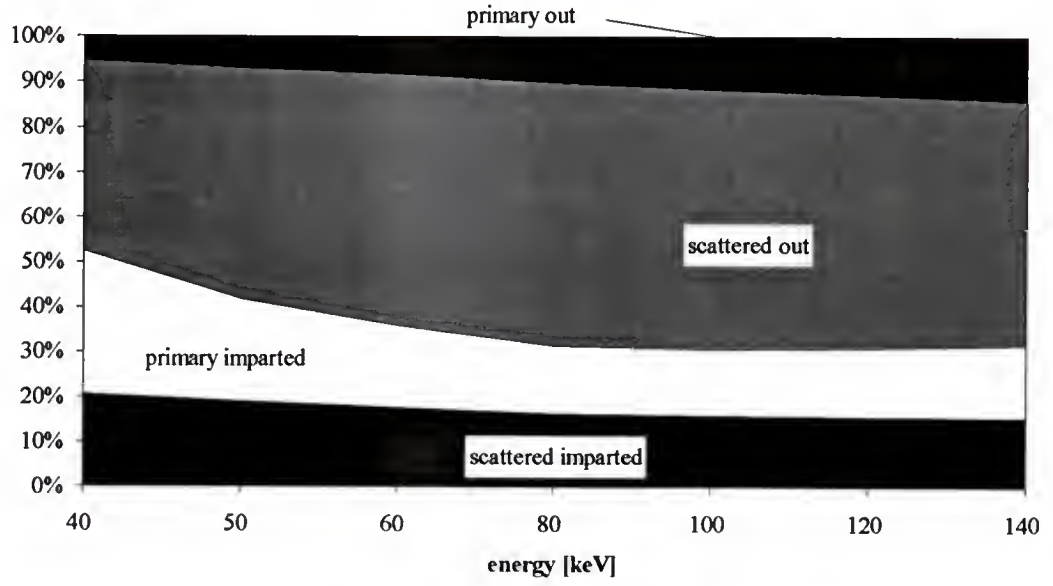

Figure 7-1: Percentage energy dispositions for an 8 cm acrylic phantom with no beam filter and a 5 mm slice thickness.

Table 7-2: Energy dispositions for a 16 cm acrylic phantom with no beam filter and a 5 mm slice thickness.

Normalized energy dispositions [mJ/Gy]							
Disposition	**40 keV**	**50 keV**	**60 keV**	**80 keV**	**100 keV**	**120 keV**	**140 keV**
Total incident	346.7	517.4	625.5	688.4	673.2	641.4	613.6
Scattered imparted	90.3	133.7	158.0	169.5	165.4	158.4	152.5
Primary imparted	128.4	143.4	142.4	129.8	122.0	118.7	118.2
Total imparted	218.7	277.1	300.4	299.3	287.4	277.1	270.7
Scattered out	125.9	235.5	317.5	377.6	371.9	348.9	325.9
Primary out	2.1	4.8	7.6	11.5	13.9	15.4	17.0
Total out	128.0	240.3	325.1	389.1	385.8	364.4	342.9

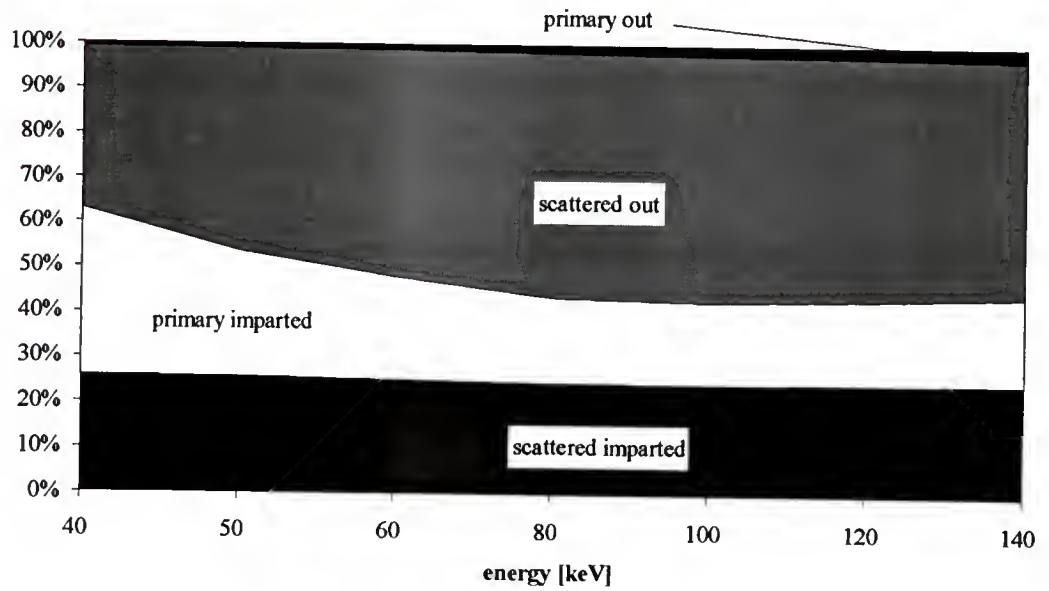

Figure 7-2: Percentage energy dispositions for an 16 cm acrylic phantom with no beam filter and a 5 mm slice thickness.

Table 7-3: Energy dispositions for an 8 cm acrylic phantom with no beam filter and 5 mm slice thickness for four spectra.

Normalized energy dispositions [mJ/Gy]				
Disposition	**120 kVp 4.5 mm Al HVL**	**120 kVp 5.4 mm Al HVL**	**120 kVp 7.5 mm Al HVL**	**120 kVp 9.5 mm Al HVL**
Total incident	214.2	235.7	271.2	296.9
Scattered imparted	38.8	42.5	47.8	50.7
Primary imparted	49.3	51.2	52.2	52.2
Total imparted	88.1	93.7	100.0	102.9
Scattered out	109.3	122.7	147.4	166.2
Primary out	16.8	19.2	23.8	27.8
Total out	126.1	142.0	171.2	194.0

Table 7-4: Percentage energy dispositions for an 8 cm acrylic phantom with no beam filter and 5 mm slice thickness for four spectra.

Energy dispositions (percentage)				
Disposition	**120 kVp 4.5 mm Al HVL**	**120 kVp 5.4 mm Al HVL**	**120 kVp 7.5 mm Al HVL**	**120 kVp 9.5 mm Al HVL**
Total incident	100.0%	100.0%	100.0%	100.0%
Scattered imparted	18.1%	18.1%	17.6%	17.1%
Primary imparted	23.0%	21.7%	19.3%	17.6%
Total imparted	41.1%	39.8%	36.9%	34.7%
Scattered out	51.0%	52.1%	54.3%	56.0%
Primary out	7.9%	8.2%	8.8%	9.4%
Total out	58.9%	60.2%	63.1%	65.3%

Table 7-5: Energy dispositions in an 16 cm acrylic phantom with no beam filter and 5 mm slice thickness for four spectra.

Normalized energy dispositions [mJ/Gy]				
Disposition	**120 kVp 4.5 mm Al HVL**	**120 kVp 5.4 mm Al HVL**	**120 kVp 7.5 mm Al HVL**	**120 kVp 9.5 mm Al HVL**
Total incident	428.6	471.8	543.2	593.7
Scattered imparted	107.3	118.4	136.5	148.6
Primary imparted	117.2	123.6	129.2	129.4
Total imparted	224.5	242.0	265.6	278.0
Scattered out	199.2	223.9	270.1	306.6
Primary out	5.0	6.0	7.6	9.2
Total out	204.2	229.8	277.6	315.8

Table 7-6: Percentage energy disposition for four spectra in a 16 cm radius acrylic phantom with no beam filter.

Energy dispositions (percentage)				
Disposition	**120 kVp 4.5 mm Al HVL**	**120 kVp 5.4 mm Al HVL**	**120 kVp 7.5 mm Al HVL**	**120 kVp 9.5 mm Al HVL**
Total incident	100.0%	100.0%	100.0%	100.0%
Scattered imparted	25.0%	25.1%	25.1%	25.0%
Primary imparted	27.3%	26.2%	23.8%	21.8%
Total imparted	52.4%	51.3%	48.9%	46.8%
Scattered out	46.5%	47.4%	49.7%	51.6%
Primary out	1.2%	1.3%	1.4%	1.6%
Total out	47.6%	48.7%	51.1%	53.2%

keV to a maximum of 112 mJ/Gy at 60 keV. Above 50 keV in the small phantom, the percentage of incident energy imparted is relatively constant at approximately 33%. This value increases to 42% at 50 keV and 53% at 40 keV.

In the CTDI body phantom, the energy imparted ranges from a minimum of 219 mJ/Gy at 40 keV to a maximum of 300 mJ/Gy at 60 keV. Approximately 45% of the incident energy is deposited in the large phantom at energies above 50 keV. At 50 keV, 54% is deposited, and at 40 keV 63% of the incident energy is deposited.

In addition to the monoenergetic results, data for four typical x-ray spectra incident on the 8 cm and 16 cm radii acrylic phantoms were generated and are presented in Tables 7-3 through 7-6. The data in Tables 7-3 and 7-5 are the normalized energy dispositions in units of mJ/Gy, and Tables 7-4 and 7-6 present the data in percentage form. No x-ray beam filter is used. The spectra used are from Birch *et al.* (1979) and Fewell *et al.* (1981) and were described in the previous chapter. These data are consistent with the GCTDI data presented in the previous chapter.

In the CTDI head phantom, the energy imparted values from the spectra range from 88 to 103 mJ/Gy, and represent percentages from 41% to 35%. These values lie near the 40 keV to 50 keV monoenergetic beam values (91 to 108 mJ/Gy).

In the CTDI body phantom, the energy imparted values from the spectra range from 225 mJ/Gy to 278 mJ/Gy and represent percentages from 52% to 47%. As in the head phantom, these values lie in the range near the 40 keV and 50 keV monoenergetic values (219 to 277 mJ/Gy). The mean energies of the spectra vary from 50 keV to 70 keV. Thus in both phantoms, the use of the mean energy of a particular spectrum to estimate the energy imparted would produce an inaccurate estimate of the energy imparted in a CTDI phantom from that spectrum.

Beam Filter Variation

The variations of the energy dispositions in the head phantom are shown in Tables 7-7 and 7-8 for 50 keV incident photons and 5 mm slice thicknesses. All data are normalized to the $CTDI_{air}$ value at 50 keV. The $CTDI_{air}$ value used for normalization was found with the appropriate beam-shaping filter.

The data indicate that the presence of a beam-shaping filter changes the incident photon fluence, but the percentage of the incident energy that is deposited in the phantom is relatively constant at the energies considered here. At 50 keV, the GE filter reduces the incident fluence by 25% in the smaller phantom and by 50% in the larger phantom. The perfect filter reduces the incident fluence by 57% in the small phantom and by 43% in the body phantom. Another effect of the beam shaping filter is the decrease in the amount of primary energy leaving the phantom — a fraction of the primary energy is attenuated before it reaches the phantom and so cannot be transmitted through the phantom.

Comparing the percentage energy deposited values in the no-filter configuration to those for filtered x-ray beams, it is seen that all the values for the head phantom range from 42% to 48%, and for the body phantom, 54% to 58%. The presence of a beam-shaping filter, by reducing the incident photon fluence, has the effect of changing only the absolute values of the disposition categories, because the relative values are all very similar.

Tables 7-9 and 7-10 show data comparing the monoenergetic data to those generated with typical CT spectra. The 4.5 mm Al HVL spectrum was obtained from Fewell *et al.* (1979) and the 5.4 mm Al HVL was obtained from Birch *et al.* (1981). The mean energies of the beams are 50 and 52 keV, respectively. The data are for a 5 mm slice and the CTDI body phantom with the GE beam-shaping filter. The spectra data for the energy imparted are between the 40 keV and 50 keV values, as would be expected

from the GCTDI data presented in the previous chapter. These data are also consistent with the non-filtered spectra data presented in the previous section.

Table 7-7: Energy dispositions at 50 keV for 8 cm and 16 cm radii acrylic phantoms for a 5 mm slice thickness, for three filter configurations.

Normalized energy dispositions [mJ/Gy] at 50 keV						
	8 cm			16 cm		
Dispositions	**No filter**	**GE filter**	**Perfect**	**No filter**	**GE**	**Perfect**
Total incident	258.7	207.0	147.8	517.4	257.6	223.2
Scattered imparted	49.3	41.7	31.7	133.7	72.2	63.5
Primary imparted	58.7	48.5	35.9	143.4	74.6	65.1
Total imparted	108.0	90.1	67.6	277.1	146.8	128.6
Scattered out	132.7	106.0	75.4	235.5	110.2	94.4
Primary out	18.0	10.9	4.9	4.8	0.6	0.2
Total out	150.7	116.8	80.3	240.3	110.8	94.6

Table 7-8: Percentage energy dispositions at 50 keV for 8 cm and 16 cm radii acrylic phantoms for a 5 mm slice thickness, for three filter configurations.

Energy dispositions (percentage) at 50 keV						
	8 cm			16 cm		
Dispositions	**No filter**	**GE filter**	**Perfect**	**No filter**	**GE**	**Perfect**
Total incident	100.0%	100.0%	100.0%	100.0%	100.0%	100.0%
Scattered imparted	19.1%	20.1%	21.4%	25.8%	28.0%	28.4%
Primary imparted	22.7%	23.4%	24.3%	27.7%	29.0%	29.2%
Total imparted	41.8%	43.6%	45.7%	53.6%	57.0%	57.6%
Scattered out	51.3%	51.2%	51.0%	45.5%	42.8%	42.3%
Primary out	7.0%	5.3%	3.3%	0.9%	0.2%	0.1%
Total out	58.2%	56.4%	54.3%	46.4%	43.0%	42.4%

Table 7-9: Comparison of energy disposition categories of monoenergetic beams with two typical CT spectra on a 16 cm acrylic phantom with the GE beam filter (Fewell *et al.*, 1979, and Birch *et al.*, 1981).

Normalized energy dispositions [mJ/Gy]							
	Incident beam energy						
Dispositions	**40 keV**	**50 keV**	**60 keV**	**80 keV**	**100 keV**	**4.5 mm HVL**	**5.4 mm HVL**
Total incident	149.3	257.6	327.4	376.7	379.2	223.5	245.1
Scattered imparted	42.1	72.2	89.7	100.3	100.6	60.8	66.6
Primary imparted	57.7	74.6	77.8	73.7	70.9	58.7	62.7
Total imparted	99.8	146.8	167.5	174.0	171.5	119.5	129.3
Scattered out	49.4	110.2	158.8	200.3	204.4	103.1	114.8
Primary out	0.1	0.6	1.2	2.4	3.3	0.9	1.1
Total out	49.5	110.8	160.0	202.7	207.7	104.0	115.9

Table 7-10: Percentage comparison of energy disposition categories of monoenergetic beams with two typical CT spectra on a 16 cm acrylic phantom with the GE beam filter (Fewell *et al.*, 1979, and Birch *et al.*, 1981).

Energy dispositions (percentage)							
	Incident beam energy						
Dispositions	**40 keV**	**50 keV**	**60 keV**	**80 keV**	**100 keV**	**4.5 mm HVL**	**5.4 mm HVL**
Total incident	100.0%	100.0%	100.0%	100.0%	100.0%	100.0%	100.0%
Scattered imparted	28.2%	28.0%	27.4%	26.6%	26.5%	27.2%	27.2%
Primary imparted	38.6%	29.0%	23.8%	19.6%	18.7%	26.3%	25.6%
Total imparted	66.8%	57.0%	51.1%	46.2%	45.2%	53.5%	52.7%
Scattered out	33.1%	42.8%	48.5%	53.2%	53.9%	46.1%	46.8%
Primary out	0.1%	0.2%	0.4%	0.6%	0.9%	0.4%	0.4%
Total out	33.2%	43.0%	48.9%	53.8%	54.8%	46.5%	47.3%

Slice Thickness Variation

The data illustrating the variation of energy dispositions with slice thickness are listed in Table 7-11. The energy imparted varies from 22 mJ/Gy in the 1 mm slice to 216 mJ/Gy in the 10 mm slice at 50 keV. These results show that the various energy dispositions are directly proportional to the slice width. This is to be expected because of the nature of the calculational geometry, i.e., a point source with perfect collimation. The energy deposited from, say, a 10 mm slice is thus double that from a 5 mm slice, and two 5 mm slices impart the same quantity of energy as one 10 mm slice. This result is expected and corresponds to the GCTDI data presented previously in Chapter 6.

Phantom Size Variation

The variations of energy dispositions with phantom radius are shown in Table 7-12 and Fig. 7-3. These data are calculated for 50 keV incident photons and a 5 mm slice thickness. As expected, the energy deposited in the phantom increases with increasing phantom size. The values range from 67 mJ/Gy to 358 mJ/Gy for the phantoms ranging in size from 6 cm radius to 20 cm radius. In terms of percentages, the values range from a minimum of 35% in the 6 cm radius phantom to 58% in the 20 cm radius phantom.

Phantom Material Variation

The data generated at 50 keV for different phantom materials are shown in Tables 7-13 and 7-14 and Figs. 7-4 and 7-5. As stated previously, ICRU Report No. 44 (ICRU 1989) was used to determine the composition of the materials used. The lung tissue data are for inflated lung, the muscle tissue data are for smooth muscle, and the bone tissue are for cortical bone. The data were all normalized to the $CTDI_{air}$ measured in acrylic.

Table 7-11: Effect of slice thickness on energy dispositions for 50 keV incident photons on an 8 cm radius acrylic phantom with no filter.

Normalized energy dispositions [mJ/Gy]				
Dispositions	**1 mm**	**3 mm**	**5 mm**	**10 mm**
Total incident	51.7	155.2	258.7	517.4
Scatter imparted	9.9	29.5	49.3	98.4
Primary imparted	11.7	35.2	58.7	117.4
Total imparted	21.6	64.7	108.0	215.8
Scattered out	26.5	79.7	132.7	265.5
Primary out	3.6	10.8	18.0	36.1
Total out	30.1	90.5	150.7	301.6

Table 7-12: Energy dispositions for acrylic phantoms with indicated radii for 50 keV incident photons and 5 mm slice thickness.

Normalized Energy dispositions [mJ/Gy]							
Dispositions	**6 cm**	**8 cm**	**10 cm**	**12 cm**	**14 cm**	**16 cm**	**20 cm**
Total incident	194.0	258.7	323.4	388.0	452.7	517.4	646.7
Scatter imparted	28.7	49.3	70.7	92.2	113.1	133.7	173.7
Primary imparted	38.2	58.7	79.8	101.3	122.5	143.4	184.2
Total imparted	66.9	108.0	150.5	193.4	235.6	277.1	357.9
Scattered out	103.1	132.7	159.4	184.9	210.2	235.5	286.6
Primary out	24.0	18.0	13.4	9.7	6.9	4.8	2.2
Total out	127.1	150.7	172.8	194.6	217.1	240.3	288.8

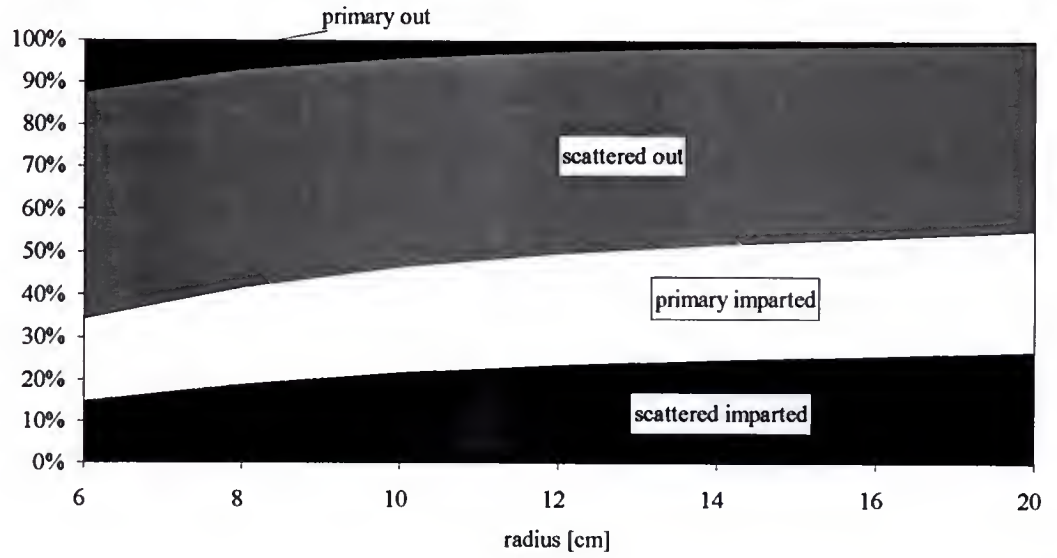

Figure 7-3: Percentage energy dispositions for acrylic phantoms with indicated radii for 50 keV incident photons and 5 mm slice thickness.

Table 7-13: Variations of the energy dispositions with phantom material in an 8 cm radius phantom. All data are normalized to the $CTDI_{air}$ in acrylic at 50 keV. Data are for a 5 mm slice thickness.

Normalized energy dispositions [mJ/Gy]						
Energy dispositions	**Lung**	**Fat**	**Water**	**Muscle**	**Acrylic**	**Bone**
Total incident	258.7	258.7	258.7	258.7	258.7	258.7
Scatter imparted	6.2	40.5	48.1	50.7	49.3	44.4
Primary imparted	31.8	51.3	71.8	75.2	58.7	190.5
Total imparted	38.0	91.9	119.9	125.9	108.0	234.9
Scattered out	97.8	140.5	118.1	113.9	132.7	22.9
Primary out	122.8	26.4	20.8	18.8	18.0	0.8
Total out	220.7	166.8	138.8	132.8	150.7	23.7

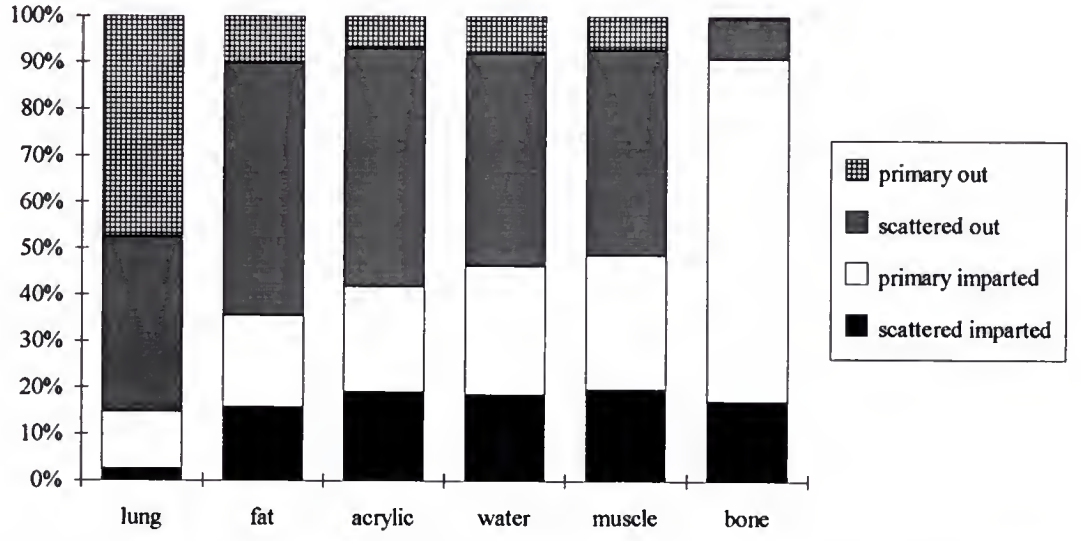

Figure 7-4: Percentage variations with phantom material. Data are for an 8 cm radius phantom and 5 mm slice thickness at 50 keV.

Table 7-14: Variations of energy dispositions with phantom material in a 16 cm radius phantom. All data are normalized to $CTDI_{air}$ in acrylic. Data are for a 5 mm slice thickness at 50 keV

Normalized energy dispositions [mJ/Gy]						
Energy dispositions	**Lung**	**Fat**	**Water**	**Muscle**	**Acrylic**	**Bone**
Total incident	517.4	517.4	517.4	517.4	517.4	517.4
Scatter imparted	31.5	120.5	131.6	136.2	133.7	91.5
Primary imparted	99.9	129.5	172.9	178.4	143.4	383.9
Total imparted	131.4	250.0	304.5	314.6	277.1	475.4
Scattered out	263.9	258.6	206.9	197.7	235.5	42.0
Primary out	122.1	8.8	6.0	5.1	4.8	0.0
Total out	386.0	267.4	212.9	202.8	240.3	42.0

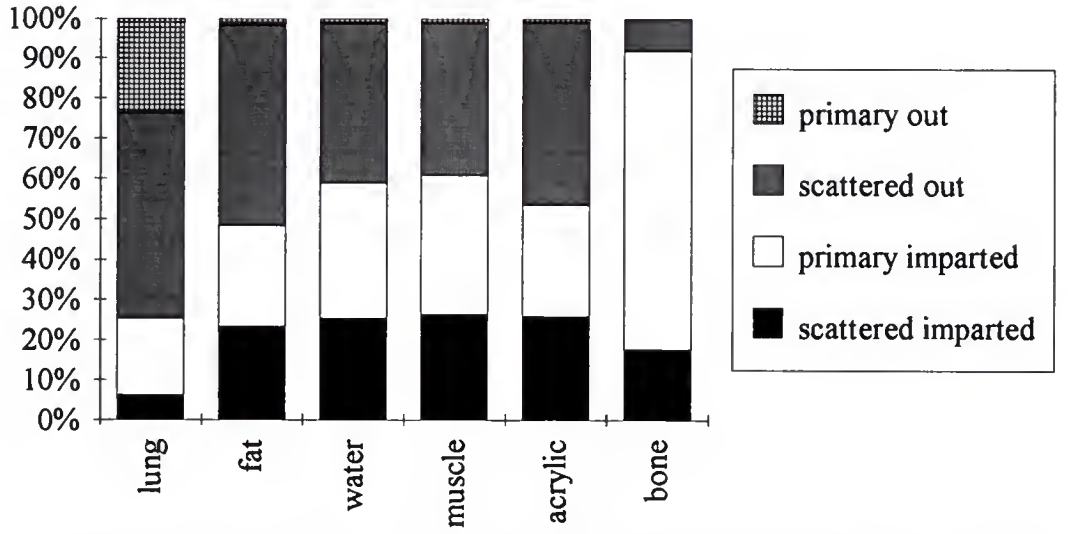

Figure 7-5: Percentage variations with phantom material. Data are for the 16 cm radius phantom and 5 mm slice thickness at 50 keV.

Excluding lung, the mean value for the soft tissues equivalent materials (water, fat, acrylic and muscle) is 111 ± 13 mJ/Gy in the 8 cm radius phantom. The value for lung is approximately one-third less (≈38 mJ/Gy), and that for bone is approximately 2.5 times (≈ 270 mJ/Gy) greater.

In the 16 cm radius phantom, the mean value of the soft tissues is 287 ± 25 mJ/Gy. The value for lung is approximately one-half less, and the bone is approximately 50% as large. These overall results are not surprising, given the similar densities and compositions of the soft tissues, the small density of lung, and the high density and mean atomic number of bone.

SAD Variation

Changes in the various energy disposition categories as a function of SAD are shown in Table 7-15. These values are calculated for 50 keV photons, 5 mm slice thickness, and the 8 cm radius acrylic phantom. Three SAD values were examined: 50, 65, and 80 cm. These SAD values generally cover the range found in commercial scanners as indicated in Chapter 2. Again, all the values were normalized to $CTDI_{air}$ at 50 keV, but in this case, the $CTDI_{air}$ was found at the same SAD used for the measurement with the larger phantom, i.e., 50 cm, 65 cm, and 80 cm. No beam shaping filter was included in the calculations.

The results indicate that there is essentially no SAD dependence on the energy imparted to the phantom, which is as expected because of the method of normalization used. The value of $CTDI_{air}$ measured at the isocenter of a scanner, as well as the doses and energies imparted, are all normalized to the photon fluence per steradian. The photon fluence, when stated per unit solid angle, is independent of the SAD, so the results simply indicate that the same number of photons produces the same energy deposition patterns, irrespective of the source distance.

Table 7-15: Variation of energy dispositions with change in the SAD for 50 keV incident photons and a 5 mm slice thickness.

Normalized energy dispositions [mJ/Gy]			
	SAD		
Energy dispositions	**50 cm**	**65 cm**	**80 cm**
Total incident	258.7	258.7	258.7
Scatter imparted	49.2	49.3	49.2
Primary imparted	58.7	58.7	58.7
Total imparted	107.9	108.0	107.9
Scattered out	133.1	132.7	132.6
Primary out	17.7	18.0	18.2
Total out	150.8	150.7	150.8

Phantom Composition and Shape Variation

To compare the absolute values of energy imparted in cylindrical phantoms to more realistic, anthropomorphic-type phantoms, Monte Carlo simulations were performed on the phantoms described in Chapter 4. The simulations were run over a range of monoenergetic beams from 40 keV to 140 keV with two filter configurations: no filter, and the GE filter. Also, data using four x-ray spectra were used for comparison with the no-filter monoenergetic data.

Monoenergetic X Rays

The following section describes the results found by simulating beams of mono-energetic x-rays incident on anthropomorphic-type phantoms.

Anthropomorphic Head Phantom — No filter

The energy dispositions are tabulated in Table 7-16 and shown graphically as percentages in Fig. 7-6. The energies imparted range from a minimum of 147 mJ/Gy at 140 keV to a maximum of 229 mJ/Gy at 60 keV. Above 80 keV, the percentage of the

incident energy deposited is relatively constant at approximately 40%. At 40 keV, 82% is imparted, 69% at 50 keV, and 58% at 60 keV. These values are larger than the corresponding values in the CTDI head phantom and are due to the increased size and higher attenuating properties of the materials in the anthropomorphic phantom.

At energies less than 80 keV, the anthropomorphic phantom absorbs almost exactly twice as much energy as does the CTDI phantom. Above 80 keV, the anthropomorphic phantom absorbs approximately 65% more energy than the CTDI phantom.

Anthropomorphic Head Phantom — GE filter

The results for the anthropomorphic head phantom with the GE beam filter are given in Table 7-17 and Fig. 7-7. The energy imparted values range from 110 mJ/Gy at 140 keV to 179 mJ/Gy at 60 keV. The effect of the beam filter seen in the CTDI-phantom results is also seen here, i.e., the incident fluence is substantially reduced, but the percentages of the energy dispositions are not greatly affected.

The anthropomorphic phantom also absorbs more energy than the CTDI phantom in this configuration. Comparing the results using the anthropomorphic phantom to those using the CTDI head phantom with the GE filter, there is an increase of approximately 88% in the energy imparted in the anthropomorphic phantom at 60 keV. At 80 keV the anthropomorphic phantom absorbs 73% more, and 59% more at 100 keV.

Anthropomorphic Body Phantom — No filter

The various energy dispositions in the anthropomorphic body phantom with no beam filter are shown in Table 7-18 and Fig. 7-8. The energy imparted values range from 316 mJ/Gy at 40 keV to 451 mJ/Gy at 60 keV. These values are 27% to 57% larger than those for the CTDI body phantom at the same energies.

The percentage of the incident energy deposited is again relatively constant above 80 keV, with approximately 50% imparted. These values increase to approximately 70% at 40 keV, 60% at 50 keV, and 55% at 60 keV.

Table 7-16: Energy dispositions in the anthropomorphic head phantom for the indicated incident energies with no beam filter.

Normalized energy dispositions [mJ/Gy]							
Dispositions	**40 keV**	**50 keV**	**60 keV**	**80 keV**	**100 keV**	**120 keV**	**140 keV**
Total incident	219.18	326.88	395.60	435.31	425.28	405.64	387.46
Scattered imparted	48.25	80.27	96.76	97.96	90.50	82.03	75.58
Primary imparted	131.83	144.72	132.10	101.05	82.97	74.82	71.20
Total imparted	180.08	225.00	228.86	199.01	173.47	156.86	146.78
Scattered out	35.80	91.51	147.07	203.85	213.60	206.35	196.64
Primary out	3.16	10.43	19.35	32.17	38.27	42.11	44.37
Total out	38.96	101.94	166.42	236.01	251.87	248.45	241.01

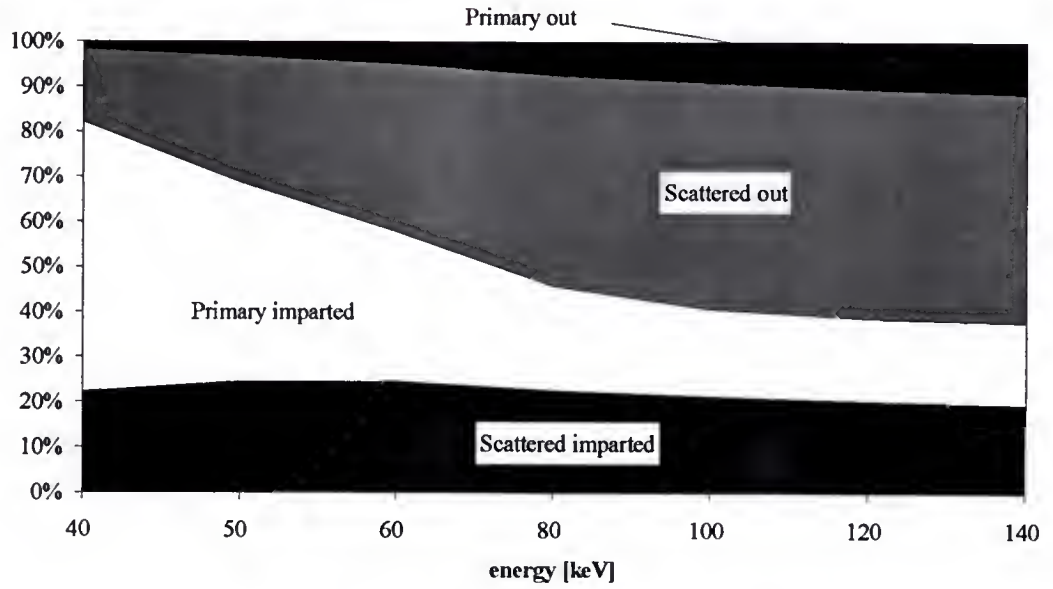

Figure 7-6: Percentage energy disposition for the anthropomorphic head phantom for a 5 mm slice and no beam filter.

Table 7-17: Energy dispositions in the anthropomorphic head phantom with the GE filter for the indicated incident energies.

Normalized energy dispositions [mJ/Gy]							
Dispositions	**40 keV**	**50 keV**	**60 keV**	**80 keV**	**100 keV**	**120 keV**	**140 keV**
Total incident	149.57	244.55	303.37	339.16	336.60	302.22	280.58
Scattered imparted	35.23	63.46	78.31	80.25	75.16	64.14	57.24
Primary imparted	89.22	107.66	100.92	79.34	66.45	56.63	52.35
Total imparted	124.45	171.13	179.23	159.60	141.62	120.77	109.59
Scattered out	23.87	67.88	112.93	159.56	170.05	155.15	143.58
Primary out	1.25	5.54	11.21	20.00	24.94	26.29	27.41
Total out	25.12	73.42	124.14	179.56	194.98	181.45	170.99

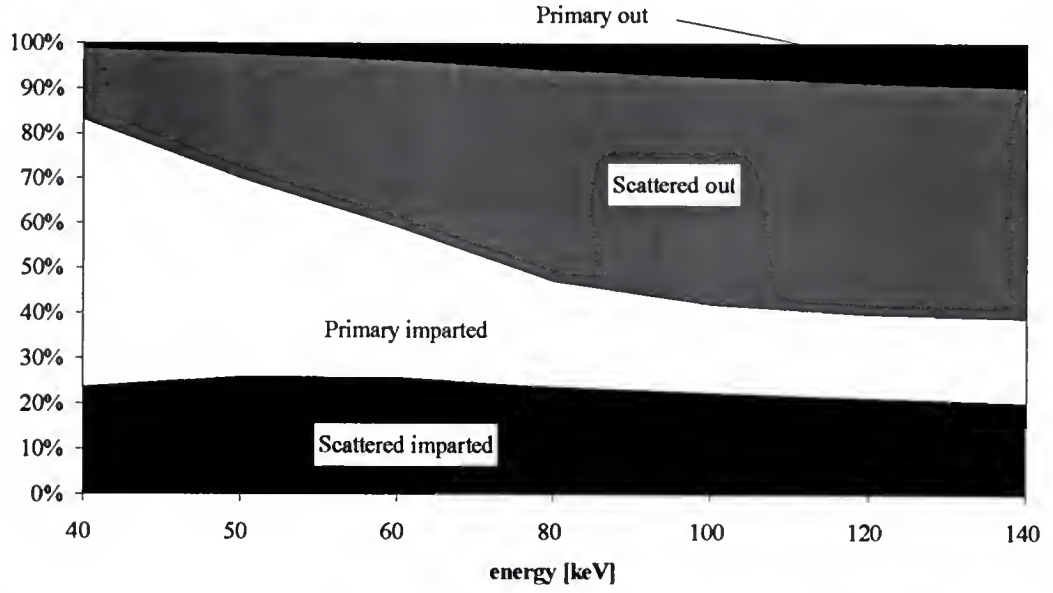

Figure 7-7: Percentage energy disposition for the anthropomorphic head phantom for a 5 mm slice and the GE beam filter.

Table 7-18: Energy dispositions in the anthropomorphic body phantom for the indicated incident energies and no beam filter.

Normalized energy dispositions [mJ/Gy]							
Dispositions	**40 keV**	**50 keV**	**60 keV**	**80 keV**	**100 keV**	**120 keV**	**140 keV**
Total incident	455.45	679.27	822.07	904.58	883.74	842.93	805.15
Scattered imparted	116.57	183.84	226.62	244.89	236.34	224.20	213.17
Primary imparted	199.31	227.95	224.77	197.10	176.59	165.69	160.54
Total imparted	315.87	411.79	451.39	441.99	412.93	389.88	373.70
Scattered out	128.07	244.00	335.74	413.82	416.93	394.66	372.39
Primary out	11.20	23.57	34.27	48.16	54.00	57.70	59.74
Total out	139.27	267.57	370.01	461.98	470.94	452.36	432.14

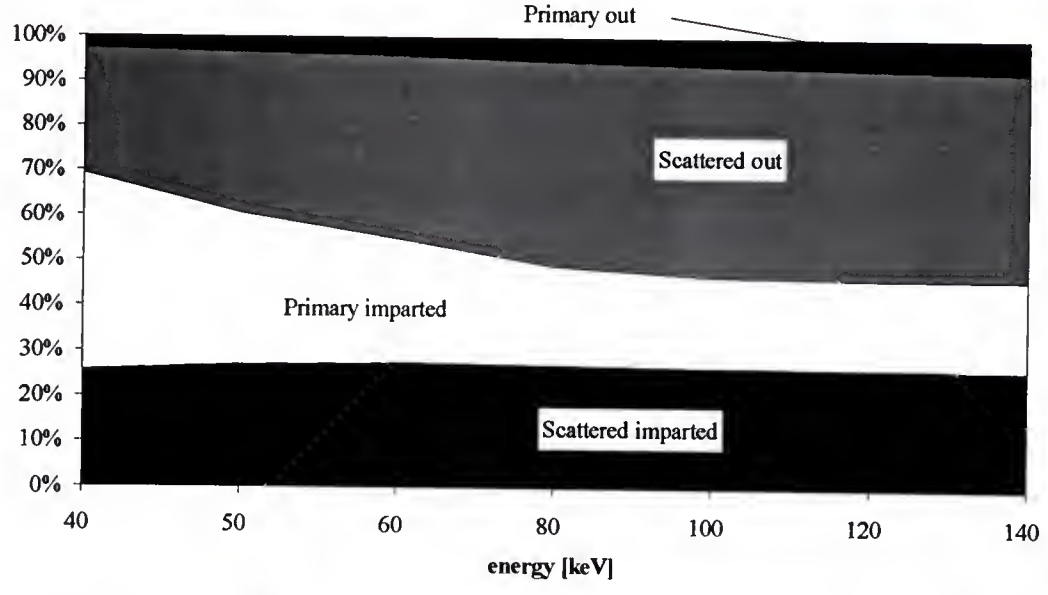

Figure 7-8 Percentage energy disposition for the anthropomorphic body phantom for a 5 mm slice and no beam filter.

Table 7-19: Energy dispositions in the anthropomorphic body phantom for the indicated incident energies with the GE filter.

Normalized energy dispositions [mJ/Gy]							
Dispositions	**40 keV**	**50 keV**	**60 keV**	**80 keV**	**100 keV**	**120 keV**	**140 keV**
Total incident	201.93	345.55	438.20	500.37	425.43	459.03	430.28
Scattered imparted	56.50	103.42	134.06	151.25	127.35	135.98	126.50
Primary imparted	93.42	124.49	128.98	117.49	90.68	95.90	90.53
Total imparted	149.92	227.91	263.04	268.74	218.03	231.88	217.03
Scattered out	51.37	114.72	169.50	221.25	196.12	212.02	196.83
Primary out	0.64	2.88	5.63	10.42	11.27	15.12	16.43
Total out	52.00	117.60	175.13	231.68	207.39	227.13	213.25

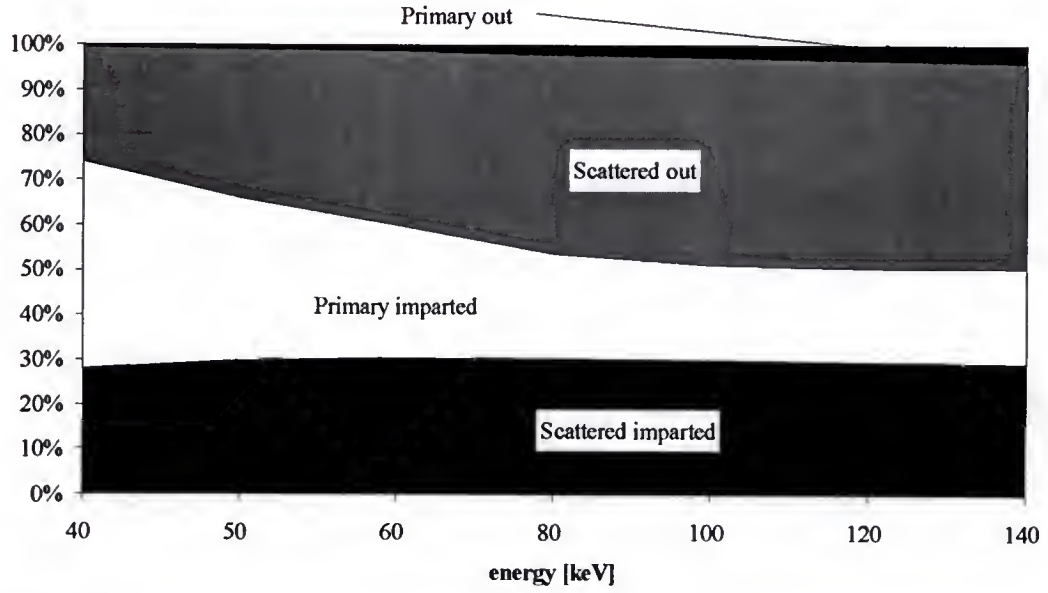

Figure 7-9: Percentage energy disposition for the anthropomorphic body phantom for a 5 mm slice and the GE beam filter.

Anthropomorphic Body Phantom — GE filter

The results for the anthropomorphic body phantom with the GE filter are shown in Table 7-19 and Figure 7-9. Again, the beam-shaping filter reduces the incident fluence but has only a small effect on the percentage of energy imparted. In this case, the energy imparted values range from 150 mJ/Gy at 40 keV to 268 mJ/Gy at 80 keV. These values

are larger than the corresponding ones for the CTDI body phantom: at 60 keV, the anthropomorphic phantom absorbs 57% more than the CTDI phantom; 55% more at 80 keV, and 28% more at 100 keV.

X-Ray Spectra

Data were generated using typical x-ray spectra incident on the anthropomorphic phantoms for comparison with the monoenergetic data. The four spectra from Birch *et al.* (1979) and Fewell *et al.* (1981) described previously were used: 120 kVp, with a 4.5 mm Al HVL, 120 kVp, with a 5.4 mm HVL, 120 kVp, with a 7.5 mm HVL, and 125 kVp, with a 9.5 mm HVL. Tables 7-20 and 7-21 show the results obtained with the spectra incident on the anthropomorphic-type phantoms.

The spectra data in Tables 7-20 and 7-21 may be compared to the monoenergetic data in Table 7-16 for the anthropomorphic head phantom and Table 7-18 for the anthropomorphic body phantom. In the head phantom, the energy imparted data for the spectra again fall in the general range of the 40 keV and 50 keV monoenergetic data (168 to 197 mJ/Gy). In the body phantom, the spectra data also lie near or between the 40 keV and 50 keV monoenergetic data. These results are the same as those for the CTDI phantom spectral data, i.e., the spectra data fall in the general range of the 40 keV to 50 keV data.

The spectra data from the anthropomorphic phantom may also be compared to the spectra data from the CTDI phantoms in Tables 7-3 to 7-6. For all three spectra, the energy imparted to the anthropomorphic head phantom is approximately 90% greater than that deposited in the CTDI head phantom. The energy imparted in the anthropomorphic body phantom is approximately 50% greater than that deposited in the CTDI body phantom for all three spectra. This finding may result from the fact that the larger anthropomorphic phantom absorbs more of the higher energy photons that escape the CTDI phantom.

Table 7-20: Energy dispositions for four x-ray spectra on anthropomorphic-type phantoms with no filter.

Normalized energy dispositions [mJ/Gy]								
	Head phantom				Body phantom			
Dispositions	**4.5 mm HVL**	**5.4 mm HVL**	**7.5 mm HVL**	**9.5 mm HVL**	**4.5 mm HVL**	**5.4 mm HVL**	**7.5 mm HVL**	**9.5 mm HVL**
Total incident	271.0	297.8	343.6	376.6	563.0	623.8	712.7	781.7
Scattered imparted	60.9	65.5	79.3	84.9	147.3	161.6	191.6	209.8
Primary imparted	107.3	114.0	115.3	111.7	181.1	193.4	199.7	203.5
Total imparted	168.1	179.5	194.6	196.6	328.4	354.9	391.4	413.3
Scattered out	90.2	103.8	130.1	155.7	212.1	245.9	290.4	334.3
Primary out	12.7	14.5	18.9	24.3	22.5	23.0	31.0	34.2
Total out	102.9	118.3	149.0	180.0	234.5	268.9	321.4	368.4

Table 7-21: Percentage energy disposition for four x-ray spectra incident on anthropomorphic-type phantoms.

Energy dispositions [percentage]								
	Head phantom				Body phantom			
Dispositions	**4.5 mm HVL**	**5.4 mm HVL**	**7.5 mm HVL**	**9.5 mm HVL**	**4.5 mm HVL**	**5.4 mm HVL**	**7.5 mm HVL**	**9.5 mm HVL**
Total incident	100.0%	100.0%	100.0%	100.0%	100.0%	100.0%	100.0%	100.0%
Scattered imparted	22.5%	22.0%	23.1%	22.5%	26.2%	25.9%	26.9%	26.8%
Primary imparted	39.6%	38.3%	33.6%	29.7%	32.2%	31.0%	28.0%	26.0%
Total imparted	62.0%	60.3%	56.6%	52.2%	58.3%	56.9%	54.9%	52.9%
Scattered out	33.3%	34.9%	37.9%	41.4%	37.7%	39.4%	40.7%	42.8%
Primary out	4.7%	4.9%	5.5%	6.4%	4.0%	3.7%	4.3%	4.4%
Total out	38.0%	39.7%	43.4%	47.8%	41.7%	43.1%	45.1%	47.1%

Summary

The results presented in this chapter quantitatively demonstrate the effects of variation of irradiation parameters on the energy imparted in phantoms. These parameters include the incident photon energy, the beam filter, the slice thickness, the phantom radius, the phantom material, the SAD, and the type of phantom (CTDI or anthropomorphic).

The dependence of the energy imparted on the incident energy is shown for both CTDI phantoms and anthropomorphic-type phantoms. In CTDI phantoms, the energy imparted is relatively constant for energies greater than 80 keV in both phantoms. At energies less than 80 keV, the energy imparted is highly dependent on the incident energy. The energy imparted from x-ray spectra incident on CTDI phantoms fall in the general range between the 40 keV and 50 keV monoenergetic data. This is true for both phantoms and indicates that use of the mean energy of a spectrum is not an accurate indicator of the energy imparted in CTDI phantoms, since the mean energy of these spectra are in the range of 50 keV to 70 keV.

Beam-shaping filters reduce the incident fluence and therefore reduce the energy imparted to CTDI phantoms. However, in terms of percentages, the filters have very little effect on the various energy disposition categories. When spectra similar to those from GE9800 CT x-ray tubes are incident on the phantom and filtered by the GE filter, the resulting energy imparted values fall near the range of the 40 keV and 50 keV monoenergetic values. This result is consistent with the non-filtered spectral data.

The energy imparted in a CTDI phantom is directly proportional to the slice thickness. This result is expected because of the "perfect" nature of the model used.

The energy imparted is also a function of the radius of the phantom. Again, this result is expected, because in the bigger phantoms the larger path lengths provide photons with a smaller chance of escaping.

The phantom material also determines the quantity of energy absorbed in cylindrical phantoms. The soft tissues (including acrylic) all have similar characteristics because of their similar densities and compositions. Inflated lung tissue, because of its low density, attenuates 50 keV x rays less than soft tissues, while bone, because of its large density and higher mean atomic number, attenuates x rays much more than soft tissues.

Variation of the SAD has virtually no effect on the energy imparted in CTDI phantoms when the results are normalized to $CTDI_{air}$ at the appropriate SAD.

The comparison between the CTDI phantom and anthropomorphic-type phantom shows that, for non-filtered monoenergetic incident x rays, the anthropomorphic head phantom absorbs twice as much energy as does the CTDI head phantom below 80 keV. Above 80 keV, the anthropomorphic head phantom absorbs approximately 65% more energy than does the CTDI head phantom. Comparing the spectral results in the anthropomorphic phantom to the spectral results for the CTDI head phantom, the anthropomorphic phantom absorbs approximately 90% more energy than does the CTDI phantom. This percentage increase is due to the highly attenuating layer of skeletal tissue on the periphery of the anthropomorphic head phantom.

The monoenergetic results for the anthropomorphic body phantom show that it absorbs 27% more energy above 80 keV than the CTDI body phantom, and 55% more below 80 keV. The anthropomorphic body phantom absorbs approximately 50% more energy than does the CTDI body phantom for all four spectra considered. In contrast to the head phantom, this percentage increase is probably due to the large size of the phantom, the amount of skeletal tissue in the body phantom is minimal. (The mass of skeletal tissue makes up 32% of the total mass of the anthropomorphic head phantom, while skeletal tissue makes up approximately 2% of the total mass of the anthropomorphic body phantom.)

CHAPTER 8

DISCUSSION AND CONCLUSIONS

The subject of this research is the study of the patterns of energy deposition in CT dosimetry phantoms resulting from a single 360° CT scan. A review of the literature has shown that the energy imparted to patients and phantoms can be used as an index of stochastic risk. The specific goal of this work is the provision of the fundamental knowledge necessary for the development of a method of estimating the energy imparted to CTDI phantoms and anthropomorphic-type phantoms. The information obtained in this work is based on a Monte Carlo model of a CT scanner. The model in turn is based on the attributes of actual CT scanners. The characteristics of the model are such that individual parameters can be varied to study the consequences of each variation.

The findings of this research quantitatively demonstrate the relationships between energy deposition patterns and several specific factors affecting them. In CTDI phantoms, dose profiles, integrals of the dose profiles, and total energy deposited are all functions of the energy of the incident photons, the type of beam-shaping filter present, the slice thickness, and the size of the phantom. The energy imparted to anthropomorphic-type phantoms is also shown to be a function of the incident energy, the filtration present and the size and composition of the phantom.

The integral of the dose profile divided by the nominal slice thickness, the CTDI, was originally intended as an index of the radiation dose to a plastic phantom. The CTDI provides a convenient way to summarize dose profile data. In this work, a superset of the CTDI, the GCTDI, is introduced. The GCTDI, designated by $\mathfrak{C}(r,L/2)$, is the dose profile at radius r integrated between the limits $\pm L/2$, where L is the length of the phantom. The

GCTDI can be measured in the same manner as the CTDI, however the dosimeter used must measure the dose profile along the entire length of the phantom. The GCTDI can be used to estimate the total energy imparted to a CTDI phantom. A mean value of $\mathfrak{C}(r,L/2)$, $\overline{\mathfrak{C}}$, can be found by integrating $\mathfrak{C}(r,L/2)$ from the center of the phantom to the periphery of the phantom and applying equation (6-7). Alternatively, one could estimate $\overline{\mathfrak{C}}$ from the arithmetic average of the central and peripheral GCTDI values. The product of $\overline{\mathfrak{C}}$ and the mass of the directly irradiated slice is equal to the energy imparted to the phantom from a single slice.

The normalized GCTDI shows little energy dependence at energies greater than 60 keV in both the CTDI head phantom and body phantom. In the smaller phantom, normalized $\mathfrak{C}(r,L/2)$ values range from (approximately) 0.8 at the center of the phantom to 0.9 near the periphery for energies above 60 keV. In the larger phantom, the values range from 0.4 near the center to 0.8 near the periphery for the energies greater than 60 keV. The normalized $\mathfrak{C}(r,L/2)$ and $\overline{\mathfrak{C}}$ values for the typical x-ray spectra used in this study *all* fall near or below the value for 50 keV monoenergetic x rays. This is true for both CTDI phantoms and for filtered x-ray beams. Thus, the use of a mean or effective energy of a spectrum for estimation of dosimetric quantities may produce inaccurate data for this spectrum.

Quantitative values of the energy imparted to the CTDI phantoms as a function of energy vary from 91 mJ/Gy to 112 mJ/Gy over the range 40 keV to 140 keV for the CTDI head phantom. In the CTDI body phantom, the energy imparted values range from 219 mJ/Gy to 300 mJ/Gy over the same energy range. The energy imparted data for incident spectra range from 88 mJ/Gy to 103 mJ/Gy in the small phantom and from 225 mJ/Gy to 278 mJ/Gy in the large phantom. These values fall in the general range between the 40 keV and the 50 keV monoenergetic data.

A comparison of the values of the normalized $\mathfrak{C}(r,L/2)$ and the normalized mean GCTDI, $\overline{\mathfrak{C}}$, as a function of energy shows that it is possible to estimate $\overline{\mathfrak{C}}$ from the

Table 8-1: Comparison of the arithmetic average of the central value and 1 cm depth value of the normalized $\mathfrak{C}(r,L/2)$ ("average") and the normalized mean GCTDI ($\overline{\mathfrak{C}}$) for monoenergies and spectra, calculated with no beam filter.

Monoenergy: [keV]	CTDI head phantom			CTDI body phantom		
	average	$\overline{\mathfrak{C}}$	difference	average	$\overline{\mathfrak{C}}$	difference
40	0.739	0.775	4.6%	0.444	0.465	4.5%
50	0.879	0.918	4.2%	0.553	0.589	6.1%
60	0.915	0.953	4.0%	0.605	0.639	5.3%
80	0.890	0.920	3.3%	0.602	0.636	5.3%
100	0.855	0.877	2.5%	0.585	0.611	4.3%
120	0.827	0.845	2.1%	0.565	0.589	4.1%
140	0.806	0.829	2.8%	0.556	0.576	3.5%
Spectra: HVL [mm Al]						
4.5	0.714	0.749	4.7%	0.468	0.477	1.9%
5.4	0.765	0.797	4.0%	0.493	0.514	4.1%
7.5	0.837	0.850	1.5%	0.536	0.565	5.1%
9.5	0.863	0.875	1.4%	0.561	0.591	5.1%

$\mathfrak{C}(0,L/2)$ (i.e., the center) and $\mathfrak{C}(R_{max}\text{-}1,L/2)$ (i.e., the 1 cm depth) values. These two locations are the radii specified by the FDA for CTDI measurements. The arithmetic average of these two values is compared to the mean GCTDI in Table 8-1 for both phantoms and the range of incident energies considered in this work.

The agreement between the two sets of values is very good. Thus by using the GCTDI obtained at the two standard locations, the total energy imparted to the phantom may be estimated through use of the method outlined in Chapter 6. When CTDI measurements are used in place of GCTDI measurements, the energy imparted to the phantom is underestimated. As mentioned in Chapter 6, at 50 keV the energy imparted would be underestimated by 50% for the 1 mm slice thickness, 18% for the 5 mm slice thickness, and 4% for the 10 mm slice thickness in an 8 cm radius acrylic phantom. In the 16 cm radius phantom at 50 keV, the energy imparted would be underestimated by 65 % for the 1 mm slice, 13% for the 5 mm slice, and 4% for the 10 mm slice.

The reason why the CTDI underestimates the GCTDI is clear — the GCTDI accounts for dose deposition outside the integration limits used in the CTDI calculation. In the data presented above, the underestimation of the GCTDI is consistent for given slice thickness and incident beam energies. However, consideration must be given to the fact that this consistency is seen in an idealized, mathematical model. Actual CT scanners have finite-sized focal spots (which produce penumbral effects), and produce scattered radiation from collimators and filters. This scattered radiation may be deposited anywhere in the phantom, and the deposition locations may be outside the limits covered by CTDI. The fact that the GCTDI can account for *all* the energy deposited in a phantom makes it the logical quantity for use as a risk index in actual CT scanners.

Beam-shaping or bow-tie filters reduce the mean GCTDI and change the pattern of dose distribution in CTDI phantoms at 50 keV. In the CTDI head phantom, both filters tested reduce the mean GCTDI. The GE filter produces the most uniform dose distribution. The perfect filter produces a radial distribution different from that of the no-filter configuration: the $\mathfrak{C}(r,L/2)$ values increase from the phantom periphery to the phantom center with the perfect filter. The $\mathfrak{C}(r,L/2)$ values decrease from periphery to center when no filter is present. This effect is due to the preferential filtering of the beam near the phantom periphery.

The $\mathfrak{C}(r,L/2)$ distributions in the CTDI body phantom for the filtered beams show more uniformity than the no-filter distribution. The overall reduction in $\overline{\mathfrak{C}}$ is seen in the body phantom as well, and the two filters produce $\mathfrak{C}(r,L/2)$ curves that are almost identical. The reduction effect is presumably due to the overall reduction of the photon fluence by the filter, especially near the phantom periphery. This reduction produces fewer photons scattered towards the center of the phantom, thereby reducing the energy deposition.

Comparison of $\overline{\mathfrak{C}}$ values and the average of the central and peripheral values of the GCTDI for the filtered cases show differences in the 8 cm radius phantom of 0.5% for the

GE filter and 2.7% for the perfect filter at 50 keV. In the body phantom at 50 keV the differences are 10.9% for the GE and 12.1% for the perfect filter. At other energies, the differences between the mean value and the average value range from 13% at 40 keV to 6.9% at 100 keV in the body phantom with the GE filter. When spectra filtered by the GE filter are incident on the 16 cm radius acrylic phantom, the discrepancy between the $\overline{\mathbb{C}}$ and the average of the peripheral and central GCTDI values are 2.8% for the 4.5 mm Al HVL beam and 9.1% for the 5.4 mm Al HVL beam.

Variation of slice thickness has a minimal effect on the GCTDI, as expected, because, in the calculational model used in this work, a point x-ray source and perfect collimation are assumed. Each individual slice acts like a series of contiguous smaller slices. As an example, a 10 mm slice can be thought of as 10 contiguous 1 mm slices. The dose profile of the 10 mm slice at any radial location, integrated between any limits, is ten times greater than the 1 mm slice. However, by definition, the GCTDI is the quotient of the line integral of the dose and the slice thickness. The slice thickness dependence is simply divided out, and the GCTDI therefore is independent of it.

The effects of increasing phantom radius on $\mathbb{C}(r,L/2)$ and $\overline{\mathbb{C}}$ are demonstrated. The $\mathbb{C}(r,L/2)$ curves are nearly flat for the smaller radius (6 and 8 cm radius) phantoms. As the phantom radius increases, the curves show the effects of the increasing attenuation. The differences between $\overline{\mathbb{C}}$ and the average of the central value and the peripheral GCTDI values range from 0.6% for the 6 cm radius phantom to 15.5% in the 20 cm radius phantom.

The energy dispositions vary with phantom size as well. The larger the phantoms absorb more energy than do the smaller phantoms, and the smaller phantoms allow more primary energy to escape. At 50 keV, the energy imparted ranges from 67 mJ/Gy (34.5% of the incident) in the 6 cm radius phantom to 358 mJ/Gy (to 55.3% of the incident) in the 20 cm radius phantom. These results are not surprising. The larger sizes absorb more energy than smaller phantoms presumably because they present a larger target to the

incident beam and have surfaces closer to the source. In addition, more of the incident energy is absorbed in large phantoms because of the increased path length required to escape the larger phantom. It should be noted that the FDA specifies only a ***minimum*** phantom length of 14 cm for CTDI measurements; longer phantoms would produce larger CTDI values.

The type of material present in the phantom greatly affects both the GCTDI distribution and the energy imparted values. For water and soft tissues, excluding lung, the data indicate that in an 8 cm radius phantom there is only a small difference in $\mathfrak{C}(r,L/2)$ with radial location in the phantom, as a result of the relatively small differences in the composition of the tissues. Bone and lung are both exceptions: bone, which is both of higher density and higher mean atomic number, is more highly absorbing; inflated lung has a small density compared to the other tissues, and shows almost no absorption. At 50 keV there is only a small amount of absorption through the phantom by soft tissues, while bone demonstrates a much greater absorption as a result of the high number of photoelectric interactions.

In the 16 cm radius phantom, there is a larger variation in the values of $\mathfrak{C}(r,L/2)$ as a function of medium at 50 keV. The two media that cause the largest variations are lung and bone. The bone quickly attenuates the $\mathfrak{C}(r,L/2)$ curve, in comparison with the other tissues. For bone, almost all of the energy is deposited in the outer 4 cm of the phantom. The flat curve for lung tissue shows that very little attenuation occurs, due to the low density of inflated lung.

Variation of the source-to-axis-distance has virtually no effect on either $\mathfrak{C}(r,L/2)$ values or the energy imparted, because the normalizing $CTDI_{air}$ value is based on the fluence at the corresponding SAD. The maximum variation in $\mathfrak{C}(r,L/2)$ for any r is approximately 0.5%, which occurs between the 50 cm SAD and the 80 cm SAD results. The maximum difference in the energy imparted values is 0.6%, between 50 cm SAD and

80 cm SAD. These small differences are on the order of the uncertainty of the calculations.

The independence of the energy imparted and the $\mathfrak{C}(r,L/2)$ value on SAD is not expected to apply for filtered x-ray beams. For any given filter, the size of the beam striking the phantom is a function of the SAD, i.e., the closer the phantom, the larger target it presents to the beam. At extended SADs, the angle subtended by the fan beam is small, and the x rays thus pass through only the central part of the filter, which provides only minimal filtration. For smaller values of SAD, the angle subtended by the fan beam is large, thus, more of the beam strikes the thicker, more attenuating parts of the filter. In such a case, one expects a larger variation in the $\mathfrak{C}(r,L/2)$ values due to filtration affects. However, because one would expect a beam compensating filter to be designed only for a specific SAD, and because all the SADs used by the manufacturers are very similar (see Chapter 2), the variation of $\mathfrak{C}(r,L/2)$ with SAD and beam filter was not investigated.

In comparing the energies imparted to CTDI phantoms with the energies imparted to anthropomorphic phantoms, significantly more energy is deposited in the anthropomorphic phantoms. This effect is presumably due to two main reasons: the anthropomorphic phantoms are larger than the CTDI phantoms, and the anthropomorphic phantoms contain more highly absorbing materials.[1] The presence of a beam shaping filter has a similar effect on the energy dispositions in the anthropomorphic phantom as it does with the CTDI phantom, i.e., the filter reduces the overall fluence incident on the phantom but does not greatly alter the percentages in the energy disposition categories.

Comparing the energy imparted in the CTDI head phantom to that in the anthropomorphic phantom, we see that in the no-filter configuration the anthropomorphic phantom absorbs between 50% more (at 140 keV) to 108% more (at 60 keV) energy. In the case where the beam passes through the GE filter, the anthropomorphic head phantom

---

[1]The effective atomic number $\overline{Z}$ for bone is 12.3, for "soft tissue" is 7.36, and is 6.56 for acrylic (Johns and Cunningham 1983).

absorbs 90% more energy than does the CTDI head phantom at 50 keV. When x-ray spectra are incident on the anthropomorphic head phantom, the energy deposited is, on the average, 92% greater than that deposited in the CTDI head phantom for the same spectrum for the four spectra examined.

The anthropomorphic body phantom, without a beam filter in place, absorbs between 57% more (at 60 keV) and 38% more (at 140 keV) than the CTDI body phantom. With the GE filter, the anthropomorphic body phantom absorbs 55% more energy at 50 keV than does the CTDI body phantom. The anthropomorphic body phantom absorbs on the average 46% more energy than does the CTDI body phantom for all the spectra considered.

The data from the simulation of x-ray spectra on both CTDI and anthropomorphic phantoms are unexpected. The spectra used in this study cover a large range, in terms of beam quality (4.5 to 9.5 mm Al HVL); based on the manufacturer-supplied data and recommended techniques, the spectra cover the general range of kVps and HVLs used clinically. What is surprising is the fact that, despite the wide range of beam qualities considered, the GCTDI and energy imparted are all quite similar. Each spectrum produces $\mathfrak{C}(r,L/2)$ and $\overline{\mathfrak{C}}$ values that are near the 40 keV to 50 keV monoenergetic data; similarly, the energy imparted values fall in the same range. This situation is true in both CTDI phantoms and anthropomorphic-type phantoms.

These results are probably due in part to the fact that the quantities GCTDI and energy imparted are both the results of integrations. Spectra with smaller HVLs have more photons in the energy range where the photoelectric effect dominates, whereas "harder" spectra have more photons in the energy range where incoherent scattering comprises a much larger fraction of the interactions that occur. The photons undergoing photoelectric interactions would deposit their energy at the point of interaction, i.e., in the directly irradiated region, producing a narrow, straight-sided dose profile. Photons undergoing incoherent scattering would tend to deposit their energy in a larger volume,

producing a wider and more bell-shaped profile. However, when the dose profile is integrated, the differences between the deposition locations become inconsequential. The results show that the integrated values of the dose profiles are all similar.

While these data suggest that the energy imparted in CT examinations is only minimally dependent on the x-ray beam quality, they do not take into account differences in how the CT scanner is used in order to produce diagnostic-quality images. Ultimately, the total energy imparted is a function the tube current and exposure time, as well as the beam quality. It is beyond the scope of this work to try to evaluate the energy imparted in terms of image quality, however, the results presented in this work must be viewed in this light.

The results of this research allow the following conclusions.

- The CTDI as presently defined significantly underestimates point doses for thin slices. The CTDI would also underestimate the energy imparted to the phantom if used in place of the GCTDI.
- The energy imparted to CTDI phantoms is primarily a function of the type of beam filtration, the x-ray beam energy, and the slice thickness. (In actual CT scanners, this statement assumes fixed exposure times and tube currents.)
- The beam quality of incident spectra appears to have only minimal importance with regard to GCTDI and energy imparted values, when normalized to the $CTDI_{air}$.
- The presence of a beam-shaping filter significantly reduces the photon fluence incident on an object but does not greatly affect the energy dispositions on a percentage basis.
- The average value of the centrally-determined and peripherally-determined values of $\mathfrak{C}(r,L/2)$ is typically within 5% of the mean GCTDI ($\overline{\mathfrak{C}}$) and in no case worse than 15%.

- The mean GCTDI ($\overline{\mathbb{C}}$) may be used to estimate the total energy imparted to the CTDI phantom.
- The energy imparted to an anthropomorphic-type head phantom is approximately 90% greater than that imparted to a CTDI head phantom in the energy range of clinical interest.
- The energy imparted to an anthropomorphic-type body phantom is approximately 50% greater than that imparted to a CTDI body phantom in the energy range of clinical interest.

The method of estimating energy imparted to CT phantoms may be useful where no data exist for providing risk estimates of radiation exposures. Although the recent NRPB reports (Shrimpton *et al.* 1991, Jones and Shrimpton 1991) provide H_E and E estimates for standard CT examinations, the scope of machines and exam types provided in the reports are limited. The NRPB reports do not include every type of CT scanner in clinical use, nor do they provide estimates of dose for non-standard or new types of exams such as helical or spiral CT scanning.

The energy imparted to the CTDI phantom can be used as an index of stochastic risk for comparisons between scanners or techniques. Also, using the method outlined in this work, generating a value of the energy imparted to a patient for any type of exam is straightforward. Using a CTDI phantom, measurements of the GCTDI are made at the central and peripheral positions.[2] The two GCTDI measurements are then averaged and used to estimate the quantity $\overline{\mathbb{C}}$, which is then used compute an energy imparted to the CTDI phantom. The energy imparted value is likely to be 50% to 90% less (depending on the type of phantom used, head or body) than that in the anthropomorphic phantom used in this study. The energy imparted to the anthropomorphic phantom can then be

[2] Of course, one requires a dosimeter or series of dosimeters capable of measuring the dose profile along the total length of the CTDI phantom. Alternatively, one can use the data in Table 6-1 to estimate the GCTDI based on the CTDI.

estimated, and the energy imparted per slice can be found. Summing the energy imparted per slice for the total number of scans, the total energy imparted for the exam can be estimated.

Once the energy imparted per exam is determined, it can be used as a basis of comparison with other diagnostic modalities or techniques for optimization purposes. The energy imparted per exam could also be used to estimate the effective dose equivalent per joule imparted, as shown in Table 1-1. Analysis of the NRPB reports could provide more exact values of E/ε or H_E/ε for various anatomic regions.[3] Alternatively, the energy imparted could be combined with the risk estimate of 2×10^{-4} J^{-1} from Bengtsson *et al.* (1978) to estimate the patient risk directly.

Although the method described in this research produces only rough estimates, it is nonetheless a viable way of estimating the energy imparted to CT dosimetry phantoms. As mentioned previously, the energy imparted has been found to be correlated with the stochastic risk to the patient. The energy imparted in CTDI phantoms, which is correlated with the energy imparted in anthropomorphic-type phantoms, is thus a useful index of patient risk in CT. Risk estimates have been heretofore quoted only for a limited range of very specific exam types and CT scanners, and it is hoped that this work will provide clinical physicists with a relatively convenient method of making quantitative estimates of patient risk for any CT examination on any CT scanner.

---

[3] A complete set of the NRPB data became available on software in July 1993 (Jones and Shrimpton, 1993).

APPENDIX A

CT MANUFACTURER SURVEY FORM

The survey form that was sent to the major CT manufacturers is reproduced on the following pages. Information was requested from General Electric, Elscint, Picker, Philips, and Siemens.

INFORMATION NEEDED FOR EACH MODEL OF CT SCANNER

MANUFACTURER_____CT MODEL NUMBER_____

FORM FILLED OUT BY _____
PHONE_____

. RADIOLOGIC SETTINGS

kVp's available

mA's available

scan times available information

. GENERATOR

Generator type
med/high freq, 3 phase (6/12 pulse), etc.

Is kVp pulsed to tube? YES_____ NO_____.

IF SO FREQUENCY IS_____

. TUBE CHARACTERISTICS

Focal spot size_____mm.

Anode angle_____°.

Anode material(s)

Approximate X ray output in air at 1 m & 100 kVp = _____ mR/mAs

. GEOMETRIC CHARACTERISTICS

slice thicknesses available

(specified at isocenter?) YES____NO_____If not where_____

Fan beam size(s) in degrees

Source-isocenter-distance

Isocenter-detector distance

Scanner generation

scan angles available:(360°, 180°)_____°

typical value=_____°

Orientation of tube with respect to scan plane -- heel effect in scan plane?
_____YES_____NO.

Range of gantry angles

. FILTRATION

Inherent filtration = _____ mm of Al at _____kVp

DOES THE UNIT HAVE A SHAPED OR "BOWTIE" FILTER?
_____YES _____NO

IF NO BOWTIE FILTER, THICKNESS OF ADDED FILTRATION = _____ mm
MATERIAL = _____.

IF BOWTIE FILTER PRESENT, DOES UNIT HAVE FIXED FLAT FILTRATION ALSO?
_____YES _____NO

IF YES, THICKNESS AND MATERIAL = _____

IF BOWTIE FILTER IS PRESENT, LIST MATERIAL, SHAPE, AND DIMENSIONS:

IF POSSIBLE PLEASE INCLUDE A DIAGRAM OF THE FILTER WITH MATERIALS AND DIMENSIONS INDICATED.

If filter changes with technique please include information on all filters provided in the scanner and techniques used with them.

. IMAGE RECONSTRUCTION

Image matrix sizes available

Fields of view (FOV's) available

Reconstruction circle size(s)

Recommended techniques for typical exams: (Please include kVp, mA, time, slice thickness, FOV, matrix size, reconstruction algorithm, for common procedures.

. OTHER

Measured dose data: CTDI, max. entrance, etc. and parameters with which obtained.

Attenuation by patient couch_____

THANK YOU FOR YOUR COOPERATION AND PATIENCE.

APPENDIX B

PRIMARY X RAY TRANSMISSION THROUGH A CYLINDER

Consider a right cylinder of radius R centered at the origin of a cartesian coordinate system with its long axis centered on the z-axis. A source of monoenergetic radiation is located a distance S away on the x-axis (see Figure B1). The source emissions are constrained to lie in a fan beam that intersects the cylinder. The fan beam is highly collimated in the z-axis such that the beam may be considered to be mono-planar. A ray whose origin is located at the source and intersects the cylinder can be described by the angle φ it makes with the x-axis and its two intersection points with the cylinder, (x_{in}, y_{in}) and (x_{out}, y_{out}).

The distance L between (x_{in}, y_{in}) and (x_{out}, y_{out}) is given by

$$L = \sqrt{(x_{in} - x_{out})^2 + (y_{in} - y_{out})^2} \,. \tag{B1}$$

The equation of the line connecting the source, (x_{in}, y_{in}) and (x_{out}, y_{out}) is

$$y = mx + b \tag{B2}$$

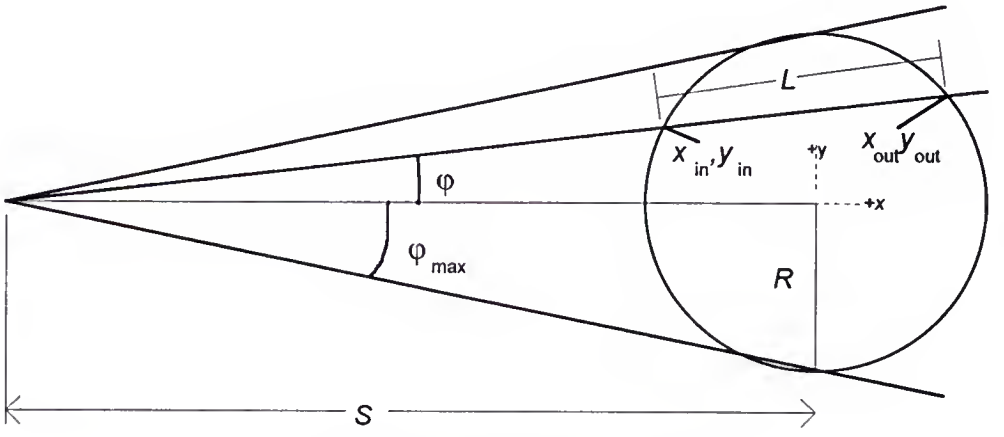

Figure B1: Source-phantom geometry.

where $m = \tan\varphi$ and $b = S\tan\varphi$. The equation of surface of the cylinder in the x-y plane is

$$R^2 = x^2 + y^2. \tag{B3}$$

Substituting (x_{in}, y_{in}) and (x_{out}, y_{out}) in (B2), we find

$$y_{in} = mx_{in} + b \quad \text{and} \quad y_{out} = mx_{out} + b,$$

subtracting these two equations,

$$(y_{in} - y_{out}) = (x_{in} - x_{out})\tan\varphi. \tag{B4}$$

Substituting (B4) in (B1), we find

$$\begin{aligned} L &= \sqrt{(x_{in} - x_{out})^2 + (x_{in} - x_{out})^2 \tan^2\varphi} \\ L &= \sqrt{(x_{in} - x_{out})^2 (1 + \tan^2\varphi)}. \end{aligned} \tag{B5}$$

Next, consider that the two points of intersection of the ray and the cylinder must be

$$y^2 = R^2 - x^2 = (mx + b)^2 = m^2x^2 + 2mbx + b^2. \tag{B6}$$

This quadratic equation has the two solutions:

$$x_{out} = \frac{-mb - \sqrt{m^2R^2 + R^2 - b^2}}{m^2 + 1}$$

and

$$x_{in} = \frac{-mb + \sqrt{m^2R^2 + R^2 - b^2}}{m^2 + 1}$$

Solving for $(x_{in} - x_{out})$ we find

$$x_{in} - x_{out} = \frac{2\sqrt{m^2R^2 + R^2 - b^2}}{m^2 + 1}. \tag{B7}$$

Substituting $m = \tan\varphi$ and $b = S\tan\varphi$ into (B7) we get

$$x_{in} - x_{out} = \frac{2\sqrt{R^2\tan^2\varphi + R^2 - S^2\tan^2\varphi}}{\tan^2\varphi + 1}. \tag{B8}$$

Substituting (B8) into (B5),

$$L(\varphi) = \sqrt{\frac{4\left[R^2\left(1 + \tan^2\varphi\right) - S^2\tan^2\varphi\right]}{1 + \tan^2\varphi}},$$

which can be simplified to

$$L(\varphi) = 2\sqrt{R^2 - \frac{S^2 \tan^2 \varphi}{1+\tan^2 \varphi}}. \tag{B9}$$

Thus the transmission $T(\varphi)$ of monoenergetic radiation through the points (x_{in}, y_{in}) and (x_{out}, y_{out}) is given by

$$T(\varphi) = \exp[-\mu(E)L(\varphi)] \tag{B10}$$

where $\mu(E)$ is the linear attenuation coefficient of the medium at energy E. The mean value of this function $\overline{T}$ can be found from

$$\overline{T} = \frac{1}{\varphi_{max} - (-\varphi_{max})} \int_{-\varphi_{max}}^{\varphi_{max}} T(\varphi) d\varphi = \frac{1}{\varphi_{max}} \int_{0}^{\phi_{max}} T(\varphi) d\varphi \tag{B11}$$

where $\varphi_{max} = \tan^{-1}(R/S)$.

APPENDIX C

DESCRIPTION OF MACRO $ELLCYL

In order to simulate radiation transport in and around elliptical cylinders, the MORTRAN3 macro $ELLCYL was written for inclusion in subroutine HOWFAR. $ELLCYL was based on the $CYL series of macros for right circular cylinders. The treatment below follows that of Nelson and Jenkins (1988).

The position and trajectory of a particle is described by the vectors

$$\vec{\mathbf{X}} = x\hat{\mathbf{i}} + y\hat{\mathbf{j}} + z\hat{\mathbf{k}} \qquad \text{(C1)}$$

and

$$\hat{\mathbf{U}} = u\hat{\mathbf{i}} + v\hat{\mathbf{j}} + w\hat{\mathbf{k}} \qquad \text{(C2)}$$

where *(x,y,z)* are the coordinates of the particle at point P, and *(u,v,y)* are its direction cosines. The geometry is illustrated in Figure C1.

The point of intersection P' is located by the vector $\vec{\mathbf{X}}'$, where

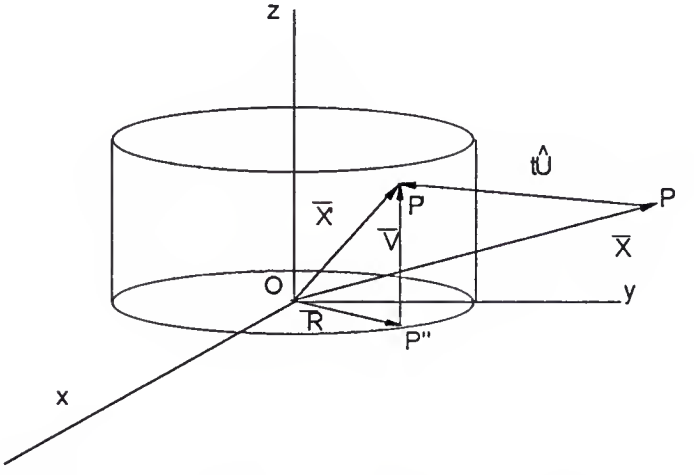

Figure C1: Geometry of intersection of a vector and an elliptical cylinder.

$$\vec{\mathbf{X}}' = \vec{\mathbf{X}} + t\hat{\mathbf{U}} \text{ and } \vec{\mathbf{X}}' = \vec{\mathbf{R}} + \vec{\mathbf{V}}$$

and t is the distance between points P and P'. The vertical vector $\vec{\mathbf{V}}$ is defined by

$$\vec{\mathbf{V}} = (z + tw)\hat{\mathbf{k}}. \tag{C3}$$

The radial vector $\vec{\mathbf{R}}$ can be found from

$$\vec{\mathbf{R}} = \vec{\mathbf{X}}' - \vec{\mathbf{V}} = (x + tu)\hat{\mathbf{i}} + (y + tv)\hat{\mathbf{j}}. \tag{C4}$$

The vector $\vec{\mathbf{R}}$ can also be found from

$$\vec{\mathbf{R}} = x'\hat{\mathbf{i}} + y'\hat{\mathbf{j}} \tag{C5}$$

where x' and y' are found in the equation for the ellipse,

$$\frac{x'^2}{a^2} + \frac{y'^2}{b^2} = 1, \tag{C6}$$

a and b being the semi-major and semi-minor axes, respectively. Thus we may write

$$\begin{aligned} x' &= x + tu \\ y' &= y + tv \end{aligned} \tag{C7}$$

and so substituting in C7 into C6 we get the quadratic equation

$$\frac{(x + tu)^2}{a^2} + \frac{(y + tv)^2}{b^2} = 1. \tag{C8}$$

The solution to equation C8 is given by

$$t = \frac{-\beta \pm \sqrt{\beta^2 - \alpha\gamma}}{\alpha} \tag{C9}$$

where

$$\begin{aligned} \alpha &= u^2 + v^2 \\ \beta &= \frac{xu}{a^2} + \frac{vy}{b^2} \\ \gamma &= \frac{x^2}{a^2} + \frac{y^2}{b^2} - 1 \end{aligned} \tag{C10}$$

The solutions to equation C9 correspond to the possibilities of particle location and trajectory (see Fig. C2). The solution that gives $\alpha = 0$ implies $w = 1$, so the particle is traveling parallel to the z-axis and will never strike the cylinder.

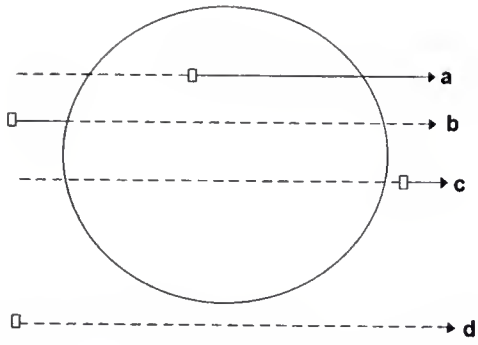

Figure C2: Geometric possibilities of particle intersecting an elliptical cylinder.

When $\gamma < 0$, the particle is inside the cylinder (case **a** in Fig. C2), and there are two real solutions, one positive and one negative. The positive solution is the desired one, i.e., the distance to the intersection point along the line of motion of the particle. When $\gamma > 0$, the particle is outside the cylinder, and several possibilities exist. If $\beta^2 \leq \alpha\gamma$, the solution corresponds to the particle missing the cylinder (case **d**) or just tangent to (or grazing) the cylinder. When $\beta^2 > \alpha\gamma$ there are two possible sets of solutions: either both are negative (case **c**), or both are positive (case **b**). In case **c**, both solutions indicate that the particle is moving away from the cylinder, and are of no interest. In case **b**, the smaller positive solution is the desired distance to the intersection point.

When the $ELLCYL routine is used in HOWFAR, the distance to the possible intersection point of the particle's trajectory and the elliptical cylinder is found using the algorithm outlined above. If the distance is less than the proposed particle step size, the particle is transported to the point of intersection, and a new step size is sampled.

The algorithm used in $ELLCYL is also used to pick the initial particle parameters for each photon. The symmetry of the geometry in the circular cylinder simulations allows the use of only one source location. (Note that only 360° scans are simulated.) In the elliptical cylinder case, cylindrical symmetry is not maintained, and a range of source locations must be used. The symmetry of the ellipse about the *x* and *y* axes dictate that the source must be randomly located in one quadrant and trajectories for emitted photons be randomly sampled within the fan beam. The method for sampling source locations and

initial particle parameters is described below, and the geometry is shown in Figure C3. The algorithm is based on the "pick-point-in-rectangle" method used in DOSRZ and is modified to change the box size as a function of the source angle. The size of the box is defined by the slice thickness (in the z-plane), and the projected size of the cylinder from the beam's eye view. In the x-y plane, the length of the box is given by L_a+L_b. The method used to find these two lengths is described below.

The position of the focal spot, (x_{fs},y_{fs}), is found from

$$x_{fs} = S\sin\delta$$

and

$$y_{fs} = S\cos\delta \quad ,$$

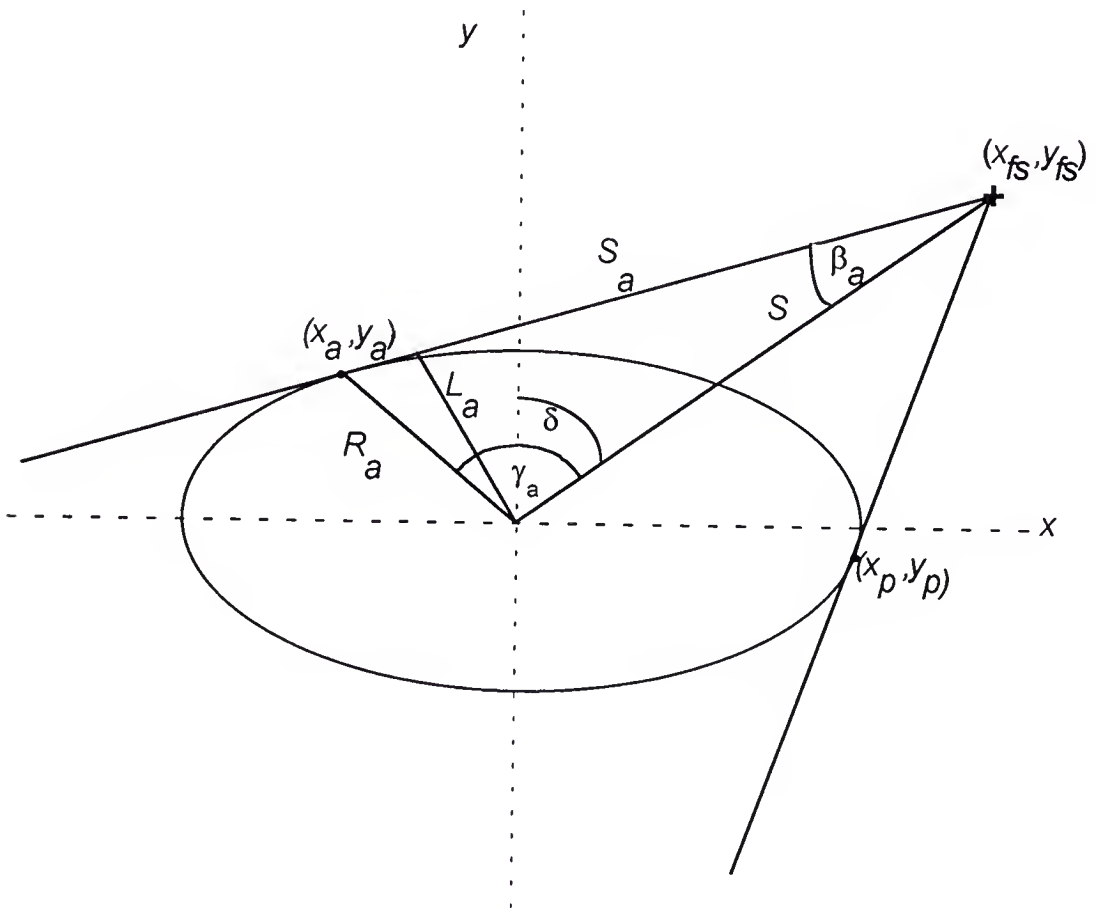

Figure C3: Geometry used to pick incident particle parameters. For simplicity, only the quantities associated with x_a,y_a are shown.

where S is the source-to-axis-distance (SAD), and δ is the angle between the y-axis and the ray between the focal spot. The equation of the line from the focal spot to the tangent point (x_a,y_a) is

$$\frac{x_{fs}x_a}{a^2}+\frac{y_{fs}y_a}{b^2}=1, \tag{C11}$$

and the equation of the line from the source to the tangent point (x_p,y_p) is similar. The points (x_a,y_a) and (x_p,y_p) must lie on the ellipse defined by (C6). Combining and solving (C6) and (C11) results in a quadratic equation, with the two solutions

$$x_a=\frac{-\mathrm{B}-\sqrt{\mathrm{B}^2-4\mathrm{A}\Gamma}}{2\mathrm{A}} \quad , \quad y_a=\frac{b^2}{y_{fs}}\left[1-\frac{x_a x_{fs}}{a^2}\right] \tag{C12}$$

$$x_a=\frac{-\mathrm{B}+\sqrt{\mathrm{B}^2-4\mathrm{A}\Gamma}}{2\mathrm{A}} \quad , \quad y_p=\frac{b^2}{y_{fs}}\left[1-\frac{x_p x_{fs}}{a^2}\right] \tag{C13}$$

where

$$\begin{aligned}\mathrm{A}&=a^2y_{fs}^2+b^2x_{fs}^2\\ \mathrm{B}&=-2a^2b^2x_{fs}\\ \Gamma&=a^4\left(b^2-y_{fs}^2\right).\end{aligned} \tag{C14}$$

The two solutions (C12) and (C13) correspond to the points that lie on rays that are tangent to the ellipse and that intersect the point (x_{fs},y_{fs}). Next, the distances from the tangent points to the origin, R_a and R_p, are found from

$$R_a=\sqrt{x_a^2+y_a^2} \text{ and } R_p=\sqrt{x_p^2+y_p^2}\,. \tag{C15}$$

The distance from the two tangent points to the focal spot, S_a and S_p, are

$$S_a=\sqrt{\left(x_{fs}-x_a\right)^2+\left(y_{fs}-y_a\right)^2} \text{ and } S_p=\sqrt{\left(x_{fs}-x_p\right)^2+\left(y_{fs}-y_p\right)^2}\,. \tag{C16}$$

The angles γ_a and γ_p are found using the law of cosines:

$$\gamma_a=\cos^{-1}\left[\frac{R_a^2+S^2-S_a^2}{2R_aS}\right] \tag{C17a}$$

$$\gamma_p = \cos^{-1}\left[\frac{R_p^2 + S^2 - S_p^2}{2R_p S}\right] \tag{C17b}$$

The angles β_a and β_p are found from the law of sines:

$$\beta_a = \sin^{-1}\left[\frac{R_a}{S_a}\sin\gamma_a\right],\ \beta_p = \sin^{-1}\left[\frac{R_p}{S_p}\sin\gamma_p\right]. \tag{C18}$$

Finally, the distances L_a and L_p are found from

$$L_a = S\tan\beta_a \tag{C19a}$$

and

$$L_p = S\tan\beta_p\,. \tag{C19b}$$

The larger value of the two is assigned as L_{max} for the angle δ. A lookup table is then created which lists L_a and L_p as well as L_{max} for each value of δ. This entire procedure is performed in the "Initialization for HOWFAR" part of the User Code, where a lookup table is created with increments of one degree in δ.

Once all initializations have been performed, the simulation is begun. The source location is sampled first. Based on the source location, the size of the rectangle (the slice thickness and phantom diameter) that the photons will strike is found. The photon trajectory is sampled in the source reference frame, which is rotated -δ from the gantry (reference) frame. Once an acceptable photon trajectory is found, the trajectory is rotated into the gantry frame, and the history commences.

The angle between the y-axis and the ray between the focal spot (the source) and the origin is randomly sampled from

$$\delta = \frac{\pi}{2}\zeta_1 \tag{C20}$$

where ζ_1 is random number. This sampling method assures that random source points in the first quadrant in the gantry frame of reference are found. Next, the direction within the fan beam must be found. This direction is sampled in the source frame of reference.

Once δ is found, particles are emitted so as to strike the rectangle that is $2L_{max}$ cm by s cm, where s is the slice thickness, and is S cm away. The algorithm is as follows:

1. First, pick the possible x coordinate within the rectangle, x^*:

$$x^* = (1-2\zeta_2)L_{max}(\delta)$$

2. If ($x^* > -L_a$) and ($x^* < L_p$), then x^* is accepted, else go to step 1.

3. Pick z^* : $z^* = \frac{s}{2}(1-2\zeta_3)$, and $y^* = 0$.

4. Rotate from the source frame of reference to the gantry frame:

$$x_{int} = x^*\cos\delta + y^*\sin\delta = x^*\cos\delta$$

$$y_{int} = y^*\cos\delta - x^*\sin\delta = -x^*\sin\delta$$

$$z_{int} = z^* .$$

Now we have the *(x,y,z)* location that the photon is being "aimed" at in the gantry frame of reference. The direction cosines *(u,v,w)* are found from:

$$D = \sqrt{(x_{fs} - x_{int})^2 + (y_{fs} - y_{int})^2 + (z_{fs} - z_{int})^2} \qquad \text{(C21)}$$

$$u_{in} = \frac{x_{int} - x_{fs}}{D}$$

$$v_{in} = \frac{y_{int} - y_{fs}}{D} \qquad \text{(C22)}$$

$$w_{in} = \frac{z_{int} - z_{fs}}{D} .$$

Equations (C9) and (C10) are used to find the distance t from the source to the point of intersection with the cylinder:

$$x_{in} = x_{fs} + ut \qquad y_{in} = y_{fs} + vt \qquad z_{in} = y_{fs} + wt .$$

Source Code Listing

The MORTRAN3 source code is listed for below for the macro $ELLCYL.

```
" Macro ELLCYL"
REPLACE {$ELLCYL(#,#,#,#);} WITH {
```

```
  {P3}=1;
  {P4}=0.0;
  U2=U(NP)*U(NP);
  V2=V(NP)*V(NP);
IF((U2+V2).EQ.0.0D+0)[{P3}=0;]  "CHECKS IF PARALLEL TO Z AXIS"
ELSEIF({P2}.EQ.1)[                    "INSIDE"
 ALPHIN=U2/ECYLA2({P1})+V2/ECYLB2({P1});    "ALPHA"
 BETAIN=X(NP)*U(NP)/ECYLA2({P1})+Y(NP)*V(NP)/ECYLB2({P1}); "BETA"
 GAMMIN=X(NP)*X(NP)/ECYLA2({P1})+Y(NP)*Y(NP)/ECYLB2({P1}) -
1.0;"GAMMA"
  IF(GAMMIN.LT.1.0D-5.AND.{P2}.NE.1)[OUTPUT;(1X,'GAMMA<0AND P2<>1 IN
HOWFAR');  STOP;]
 QUAN2=BETAIN*BETAIN-ALPHIN*GAMMIN;
 IF(QUAN2.LT.0.0D0)[QUAN2=0.0D0;]   "THIS WILL REDUCE ROUNDOFF
ERROR PRBS"
 T1IN=-BETAIN/ALPHIN+DSQRT(QUAN2)/ALPHIN;
 T2IN=-BETAIN/ALPHIN-DSQRT(QUAN2)/ALPHIN;
 {P3}=1;{P4}=DMAX1(T1IN,T2IN);]
ELSEIF({P2}.EQ.0)[              "OUTSIDE"
 ALPHOU=U2/ECYLA2({P1})+V2/ECYLB2({P1});    "ALPHA"
 BETAOU=X(NP)*U(NP)/ECYLA2({P1})+Y(NP)*V(NP)/ECYLB2({P1}); "BETA"
 GAMMOU=X(NP)*X(NP)/ECYLA2({P1})+Y(NP)*Y(NP)/ECYLB2({P1}) -
1.0;"GAMMA"
  IF(GAMMOU.GT.0.0D+0.AND.{P2}.NE.0)[OUTPUT;(1X,'GAMMA>0AND
P2<>0');STOP;]
ELSEIF(BETAOU*BETAOU.LE.ALPHOU*GAMMOU.OR.BETAOU.GE.0.0)[{P3}=0
;]
  ELSEIF(BETAOU.LT.0.0)[
   T1OU=-BETAOU/ALPHOU+DSQRT(BETAOU*BETAOU-
ALPHOU*GAMMOU)/ALPHOU;
   T2OU=-BETAOU/ALPHOU-DSQRT(BETAOU*BETAOU-
ALPHOU*GAMMOU)/ALPHOU;
   {P3}=1;{P4}=DMIN1(T1OU,T2OU);]
  ELSE[OUTPUT;(1X,'SHOULDNT BE HERE');]
  ]
ELSE[OUTPUT;(1X,'SHOULDNT BE HERE');]
}
"NOTE:   EVERYWHERE $ELLCYL IS USED ONE MUST INCLUDE
COMIN/ELCYDT,STACK/"
```

APPENDIX D

LISTING OF PERFMON1.MOR

This EGS4 user code simulates monoenergetic photons in a fan beam filtered with a "perfect" bowtie filter.

```
%L
%E
%C80
!INDENT M 4;  "INDENT MORTRAN LISTING 4 PER NESTING LEVEL"
!INDENT F 2;  "INDENT FORTRAN OUTPUT 2 PER NESTING LEVEL"
"*************************************************************************"
"                                                "
"              **************                    "
"              *          *                      "
"              * perfmon1.MOR *                   "
"              *          *                      "
"              **************                    "
"  NAME=perfect filter,  MONoenergy photons version 1"
"                                                "
" An EGS4 user code which scores the energy deposited in          "
" a cylindrical water phantom divided into planes and CONCENTRIC CYLINDERS"
" when a FAN beam of MONOENERGETIC PHOTONS is incident     "
" on the central slice; the cylinderS are parallel to the z axis"

"  perfect BOWTIE FILTER (see next statement) <<<<<<<<<<<<<<<<<"

" WEIGHTS ARE THE TRANSMISSION PROBABILTIES THRU BOWTIE"

"  see SUBROUTINE HOWFAR for a more complete description"
" PHOTONS WILL BE TRAVELLING NORMAL TO Z AXIS IN A FAN BEAM IN
XY PLANE"
" PLANES ARE PERPENDICULAR TO Z AXIS"
" SUBROUTINE HOWFAR FROM DOSRZ.MOR FROM EGS4 package"

"  THIS VERSION USES A POINT SOURCE, WITH NO SCATTER FROM THE
FILTER"
```

```
" NOTE THAT THE ANGLE THETA WILL BE SMALL-NO CORRECTION TO
DISTANCE"
" THRU THE FILTER"

" JVA 04 MAR 1992"
" 17 MAR 1992-FAN BEAM 10 MM THICK"
" 19 mar 1992-change medium to pmma "
" 20 MAR 92- CHANGE TO POINT SOURCE"
" 3 May 92 - change HOWFAR for more detailed spatial resolution "
" 21 MAY 92 CHANGE TO GEmono NRG FOR INVESTIGATIONS"
" 17 JUNE 92 change to GEFLAT for sensititivity test for spectra"
" 23 JUNE 92 - IN AIR FOR NORMALIZATION"
" 29 June 92- changed plane spacing for better integeration"
" 30 JULY 92 ADDED NEW LATCH"
" 4 AUG 92 inair to nogemon & STATS FOR NRG'S AND DOUBLE PRECESION"
" 8 AUG 92 CHANGED NUMBER AND ARRANGEMENT OF PLANES"
" 24 SEP 92 ADDED 6 CM MAXIMUM RADIUS OPTION"
" 27 Sep 92 version perfmon1 for perfect filter-DROP WT/UNWT DIFFER"
"*****************************************************************"
PROGRAM PERFMON1;
"---------------------------------------------------------------"
"STEP 1: USER-OVERRIDE-OF-EGS4-MACROS "
"---------------------------------------------------------------"
REPLACE {$MXMED} WITH {1} "only 1 medium in the problem(default 10)"
REPLACE {$MXREG} WITH {601} "601= 1+geometric regions=1+10*61"
" NOTE THAT FOR $MXREG-ADD 1 FOR STARTING ZONE-MAKE VACUUM"
REPLACE {$MXSTACK} WITH {30}"less than X particles on stack at once"
REPLACE {$MAXZPLANE} WITH {61} "61 planes in this problem"
REPLACE {$MAXRADII} WITH {10}
REPLACE {$MXPLANS} WITH {61} " 61 PLANES"

"replacing with 1 entry arrays for mono problems"
"REPLACE {$INVDIM} WITH {1000} GRID FOR SPECTRUM SAMPLING"
"REPLACE {$NENSRC} WITH {150} PLACE HOLDER FOR BINS IN SPECTRUM"
REPLACE {$INVDIM} WITH {1} "GRID FOR SPECTRUM SAMPLING"
REPLACE {$NENSRC} WITH {1} "PLACE HOLDER FOR BINS IN SPECTRUM"

REPLACE {;COMIN/SPECTR/;} WITH
{;
COMMON/SPECTR/
CDFINV($INVDIM,2),ENSRCD($NENSRC),SRCPDF($NENSRC),SRCCDF($NENSR
C),NENSRC;
}

"DEFINE A COMMON FOR SCORING IN AUSGAB"
```

```
REPLACE {;COMIN/SCORE/;} WITH {;

COMMON/SCORE/
ENTOT(10,$MXREG),
PENTOT(10,$MXREG),
SENTOT(10,$MXREG),
TEOUT(10),
SEOUT(10),
PEOUT(10),

"double precsion"
$ENERGY PRECISION
ENTOT,PENTOT,SENTOT,TEOUT,SEOUT,PEOUT,PDIRIR,SDIRIR,TOTINC;

}
"declare result accumulators"
"ENTOT(I,J) SCORES ENERGY DEP  FOR BATCH I, REGION NUMBER J     "
"PENTOT(I,J) SCORE PRIMARY ENERGY DEP"
"SENTOT(I,J) SCORES SCATTERED ENRGYDEP"
"TEOUT=TOTAL ENERGY SCATTERED OUT OF PHANTOM"
"SEOUT=SCATTERED ENERGY SCATTERED OUT OF PHANTOM"
"PEOUT=PRIMARY ENERGY EMERGING FROM PHANTOM"


" Now add variables that will only be used in MAIN for outputting results"
" and the corresponding statistics"
" The variables above in the common statements are the accumulators"
" that must be AUSGAB. These below are for the SUms, AVerages,"
" DiFferences, and Standard Errors for each category"
" 4 AUGUST THESE ARE FOR UNWEIGHTED VARIABLES"
" 27 SEPT - FOR PERFMON1 CHANGE TO ONLY SCORE WEIGHTED AND
DONT"
"  DIFFERENTIATE"

$ENERGY PRECISION

TTOT(10),PTOT(10),STOT(10), "Energy imparted bin totals"

PTOTSU,STOTSU,TTOTSU, "Enrgy imparted sums"
POUTSU,SOUTSU,TOUTSU, "NRG OUT SUMS"

PTOTAV,STOTAV,TTOTAV, "Enrgy imparted AVGS"
POUTAV,SOUTAV,TOUTAV, "NRG OUT AVG"
PDIRAV,SDIRAV, "Direclty irradiated slab AVG"
```

```
PTOTDF,STOTDF,TTOTDF, "Enrgy imparted DIFFERENCEs"
POUTDF,SOUTDF,TOUTDF, "NRG OUT DIFFERENCES"

PTOTSE,STOTSE,TTOTSE, "Enrgy imparted sTND ERROS"
POUTSE,SOUTSE,TOUTSE, "NRG OUT STD ERROS"


"THE FOLLOWING TWO MACROS WILL IMPLEMENT THE LATCH FEATURE
IN WHICH THE"
"VALUES OF THE PARAMETER LATCH ARE PASSED TO ALL SUCCEEDING
GENERATIONS"
"OF PARTICLES. THUS, FOR EXAMPLE, IF LATCH IS SET FOR A PARTICULAR
"
"INCIDENT ELECTRON WHICH GENERATES A PHOTON WHICH CREATES AN
ELECTRON  "
"WHICH THEN CREATES A KNOCK-ON ELECTRON, THE FINAL ELECTRON
(AND ALL  "
"OTHER DESCENDANTS OF THE INITIAL PARTICLE) WILL HAVE THE SAME
VALUE OF"
"LATCH                                    "

REPLACE {;COMIN/STACK/;} WITH
{;COMMON/STACK/$LGN(E,X,Y,Z,U,V,W,DNEAR,WT,
IQ,IR,LATCH($MXSTACK)),LATCHI,NP; $ENERGY PRECISION E;}
"NOTE THIS MACRO ADDS THE VARIABLE ARRAY LATCH AND ITS INITIAL"
" VALUE LATCHI  TO THE COMMON STACK IN EVERY ROUTINE IN EGS4  "
REPLACE {$TRANSFER PROPERTIES TO # FROM#;} WITH
{X{P1}=X{P2};Y{P1}=Y{P2};Z{P1}=Z{P2};IR{P1}=IR{P2};WT{P1}=WT{P2};
  DNEAR{P1}=DNEAR{P2};LATCH{P1}=LATCH{P2};}


"MACRO THAT GETS GEOMETRICAL ZONES FROM THE REGION NUMBER"
REPLACE {$GET-IX-IZ(#);} WITH {;IX=({P1}-2)/NZ+1; IZ={P1}-1-NZ*(IX-1);}

"MACRO THAT GETS REGION NUMBER FROM THE PLANAR AND RADIAL
ZONES"
"NOTE ORDER-USE IRL(IZ,IX)"
;REPLACE {$GET-IRL(#,#);} WITH {;IRL={P1}+NZ*({P2}-1)+1;}

"GEOMETRICAL INFORMATION"
REPLACE {;COMIN/GEOM/;} WITH
{;
COMMON/GEOM/ZPLANE($MAXZPLANE),RCYL(0:$MAXRADII),
CYRAD2($MAXRADII+1),CYLDTA,NZ,NR,NREG,NPLANE;}
```

```
"this common will allow ENSRC to pass EIN back to MAIN w/o too much fuss"
COMMON/IODAT2/EIN;

;COMIN/BOUNDS,GEOM,EPCONT,PLADTA,MEDIA,MISC,SCORE,STACK,THRE
SH,RANDOM/;

"      THE ABOVE EXPANDS INTO A SERIES OF COMMON STATEMENTS"

"NEXT COMMON TO PASS BATCH INDEX TO AUSGAB FOR SCORING"
"ALSO LARGEST Z IN DIRECTLY IRRADIATED SLAB"
COMMON/PASSIT/KI,I,ZDIR;

"THIS DECLARE THE TWO BOWTIE TRANSMISSION ARRAYS"
"EMU (10-150)=ENERGY,,MU AND,BANG(0-250))BANG=Beam ANGle "
"WILL BE IN LOOKED UP AS KEV, AND ANGLE WILL BE BY TENTH'S"
"I.E. WILL COVER 0 TO 25 DEGREES"
REAL EMU(10:150);
REAL BANG(0:250);

"NOW DEFINE AN ARRAY TO COUNT THE SELECTED BEAM ANGLES"
REAL SLECTBA(0:250);
"AND INITIALIZE"
DO IM=10,150[EMU(IM)=0.0;]
DO IKJ=0,250[BANG(IKJ)=0.0;SLECTBA(IKJ)=0.0;]

"Now declare scoring array for calculating the CTDI"
REAL CTDI(10,$MAXRADII); "UNWEIGHTED"

"NOW MAKE CALL TO RNG INITIALZATION SUBROUTINE"
$RNG-INITIALIZATION;

"OPEN STATEMENTS FOR ENSRC IN/OUTPUTS"
"****************** CHANGE FOR NEW SPECTRA INPUTS
****<<<<**********"
OPEN (UNIT=5,FILE='SPEC\MONO.INP',STATUS='OLD');
OPEN (UNIT=7,FILE='SPEC\MONO.OUT',STATUS='OLD');

"NOW MAKE CALL TO SPECTRA-HANDLING/SAMPLING SUBROUTINES"
CALL ENSRC(IEOF);
"CALL ENSRC1; NOT FOR MONO"

%E
"-------------------------------------------------------------"
"STEP 2 PRE-HATCH-CALL-INITIALIZATION                        "
"-------------------------------------------------------------"
```

```
"IF WANT TO CHANGE MEDIUM DO IT HERE"

$TYPE MEDARR(24) /$S'PMMA',20*' '/; "PLACE MEDIUM NAME IN AN ARRAY"
DO I=1,24[MEDIA(I,1)=MEDARR(I);]"THIS IS TO AVOID A DATA STATEMENT
FOR"
"                          A VARIABLE IN COMMON"
"NMED AND DUNIT DEFAULT TO 1, I.E. ONE MEDIUM AND WE WORK IN CM"

DO I=1,24[OUTPUT MEDARR(I);
('+',A);]

MED(1)=0; "REGION 1 IS VACUUM, REST ARE H2O"
DO J=2,$MXREG[
MED(J)=1;
ECUT(J)=1.0;"    TERMINATE ELECTRON HISTORIES AT 1.0 MEV IN THE
PHANTOM"
PCUT(J)=0.010;"  TERMINATE  PHOTON HISTORIES AT 0.01 MEV IN THE
PHANTOM"
IRAYLR(J)=1;]  "TURN ON RAYLEIGH SCATTERING"

"NOTE, ABOVE THREE PARAMETERS NEED TO BE SET FOR ALL REGIONS IN
WHICH "
"THERE IS PARTICLE TRANSPORT     "

"-------------------------------------------------------------"
"STEP 3   HATCH-CALL                                          "
"-------------------------------------------------------------"
CALL HATCH;"   PICK UP CROSS SECTION DATA FOR MEDIUM"
"            DATA FILE MUST BE ASSIGNED TO UNIT 12"

"-------------------------------------------------------------"
"STEP 4  INITIALIZATION-FOR-HOWFAR                            "
"-------------------------------------------------------------"
PI=3.141593;

"SAD=SOURCE-ISOCENTER DISTANCE"
"NOW READ IN SAD"
OPEN (UNIT=17,FILE='SAD.INP',STATUS='OLD');
READ(17,*) SAD;
CLOSE(UNIT=17);
OUTPUT SAD;
(1X,'SAD IN CM = ',F8.4);
```

```
"RADII OF CYLINDRICAL REGIONS"

"NOW READ IN MAXIMUM RADIUS"
OPEN (UNIT=17,FILE='MAXRAD.INP',STATUS='OLD');
READ(17,*) RMAX;
CLOSE(UNIT=17);

OUTPUT RMAX;
(1X,'PHANTOM RADIUS = ',F10.5,' CM');

"Check max radius-if 8 must adjust radii & NR"
"if <8 cant do with this geometry"

IF(RMAX.GT.8.00)[
NR=10;
RCYL(1)=0.5;  "CENTRAL CORE"
RCYL(2)=0.25*RMAX-0.5; "2 & 3 ARE 0.25 Rmax BOUNDRIES"
RCYL(3)=RCYL(2)+1.;
RCYL(4)=0.5*RMAX-0.5;   "4,5 ARE .5 Rmax BOUNDS"
RCYL(5)=RCYL(4)+1.;
RCYL(6)=0.75*RMAX-0.5;  "6,7 ARE .75 Rmax BOUNDS"
RCYL(7)=RCYL(6)+1.;
RCYL(8)=RMAX-1.5;       "8 AND 9 ARE AT 1 CM DEPTH"
RCYL(9)=RMAX-0.5;
RCYL(NR)=RMAX;]

ELSEIF(RMAX.EQ.8.000)[
NR=9;
RCYL(1)=0.5;  "CENTRAL CORE"
RCYL(2)=1.5; "2 & 3 ARE 0.25 Rmax BOUNDRIES"
RCYL(3)=2.5;
RCYL(4)=3.5;   "4,5 ARE .5 Rmax BOUNDS"
RCYL(5)=4.5;
RCYL(6)=5.5;  "6,7 ARE .75 Rmax BOUNDS"
RCYL(7)=6.5;
RCYL(8)=7.5;      "8 AND 9 ARE 1 CM DEPTH BOUNDARIES"
RCYL(9)=RMAX;]

ELSEIF(RMAX.EQ.6.000)[
NR=8;
RCYL(1)=0.5;  "CENTRAL CORE"
RCYL(2)=1.0; "2 & 3 ARE 0.25 Rmax BOUNDRIES"
RCYL(3)=2.0;
RCYL(4)=2.5;   "4,5 ARE .5 Rmax BOUNDS"
RCYL(5)=3.5;
```

```
RCYL(6)=4.0;  "6,7 ARE .75 Rmax BOUNDS"
RCYL(7)=5.0;
RCYL(8)=RMAX;] " 7 AND 8 ARE 0.5 CM DEPTH BOUNDARIES"


ELSEIF(RMAX.LT.6.00)[
OUTPUT;
(1X, 'THIS CONFIGURATION CANNOT SUPPORT RMAXS LESS THAN 6 CM');
STOP;]

ELSE[ "SHOULDNT BE HERE"
STOP;]

DO I=1,NR[
 CYRAD2(I)=RCYL(I)*RCYL(I);]


NZ=60; "NUMBER OF PLANAR ZONES"
NREG=1+NR*NZ; "NUMBER OF GEOMETRICAL & DOSE SCORING REGIONS"
NPLANE=NZ+1;"number of planes"


"NOW READ IN SLICE WIDTH"
OPEN (UNIT=17,FILE='SLICE.INP',STATUS='OLD');
READ(17,*) SLWDTH; "SLice WiDTH"
CLOSE(UNIT=17);

OUTPUT SLWDTH;
(1X,'SLICE WIDTH IN CM = ',F8.4);

"now calulate the largest z-value that is in the directly-irradiated"
"slab in the phantom - will score separately REMEMBER TO PUT IN A COMIN!"

ZDIR=SLWDTH*(SAD+RCYL(NR))/SAD;

"now declare variables for initial photon trajectory--"
"the rectangular outline of the cylinder as seen from the focal spot"
"will be the outer limits-pick a point within that rectangle"
"and calc cosines based on them--see SRCRZ.MOR"
ZSIDE=SLWDTH/2.0;
XSIDE=RCYL(NR);

"now set up planes -- will be symmetric about zero"

ZPLANE(1)=-8.00;
```

```
 ZPLANE(2)=-7.00;
 ZPLANE(3)=-6.00;
 ZPLANE(4)=-5.50;
 ZPLANE(5)=-5.00;
 ZPLANE(6)=-4.50;
 ZPLANE(7)=-4.00;
 ZPLANE(8)=-3.50;
 ZPLANE(9)=-3.00;
 ZPLANE(10)=-2.50;
 ZPLANE(11)=-2.00;
 ZPLANE(12)=-1.75;
 ZPLANE(13)=-1.50;
 ZPLANE(14)=-1.25;
 ZPLANE(15)=-1.00;
 ZPLANE(16)=-0.80;
 ZPLANE(17)=-0.60;
 ZPLANE(18)=-0.50;
 ZPLANE(19)=-0.45;
 ZPLANE(20)=-0.40;
 ZPLANE(21)=-0.35;
 ZPLANE(22)=-0.30;
 ZPLANE(23)=-0.25;
 ZPLANE(24)=-0.20;
 ZPLANE(25)=-0.15;
 ZPLANE(26)=-0.10;
 ZPLANE(27)=-0.08;
 ZPLANE(28)=-0.06;
 ZPLANE(29)=-0.04;
 ZPLANE(30)=-0.02;
 ZPLANE(31)= 0.00;
 DO IZ=1,30[
  IZPLUS=62-IZ;
  ZPLANE(IZPLUS)=-ZPLANE(IZ);]

 "-----------------------------------------------------------------"
 "STEP 5  INITIALIZATION-FOR-AUSGAB                              "
 "-----------------------------------------------------------------"
 TOTINC=0.0; "VARIABLE TO ACCUMULATE TOTAL UNWEIGHT NRG
 INCIDENT ON PHANTOM"


 " ZERO SCORING ARRAYS AT START -include weighted/unweighted"
 DO JI=1,10[/TEOUT(JI),PEOUT(JI),SEOUT(JI),SDIRIR(JI),PDIRIR(JI),
 TTOT(JI),STOT(JI),PTOT(JI),/=0.0;
```

```
 DO I=1,$MXREG[/ENTOT(JI,I),PENTOT(JI,I),SENTOT(JI,I)/=0.0;]]

" NOTE THAT IN ENTOT(JI,I), JI IS BATCH NUMBER AND I IS REGION INDEX
"

"now initialize the CTDI array"
DO J=1,10[
 DO K=1,$MAXRADII[
  CTDI(J,K)=0.0;]]

"TURN OFF THE FOLLOWING FLAGS- WILL DECREASE # OF CALLS TO
AUSGAB"
/IAUSFL(1),IAUSFL(6)/=0;

"TURN ON THE FOLLOWING FLAG TO ALLOW CALLS TO AUSGAB TO
SCORE"
"SCATTERING EVENTS"
IAUSFL(24)=1; " A RAYLEIGH EVENT IS TO OCCUR"
IAUSFL(18)=1; " A COMPTON EVENT IS TO OCCUR"

"the following section intializes and calculates values for the"
"arrays BANG & EMU, which is the transmission thru the bowtie filter"
"as a function of photon energy(EMU) and angle(BANG) within the fan beam"
"This is done in AUSGAB initialization since the transmitted"
"fraction will be taken to be the WEIGHT of the photon"

"Declare Energy Fitting Constants"

">>>>>>>>>>THESE ARE FOR ACRYLIC"
AC0=-30.6482;
AC1=+57.7297;
AC2=-36.6898;
AC3=+10.5775;
AC4=-1.44422;
AC5=+0.0760889;
"NOW LOOP OVER ENERGIES AND ANGLES"
DO IKEV=10,150[
 ELN=LOG(REAL(IKEV)); "FIT WITH LOG OF ENERGY IN KEV"
 ELN2=ELN*ELN;
 ELN3=ELN2*ELN;
 ELN4=ELN3*ELN;
 ELN5=ELN4*ELN;

"EMU IS THE LINEAR ATTEN COEF IN INVERSE CM"
```

```
EMU(IKEV)=1.17*EXP(AC0+AC1*ELN+AC2*ELN2+AC3*ELN3+AC4*ELN4+AC5
*ELN5);
 ]

 "BANG IS THE FILTER THICKNESS IN CM"
 "CALCULATES RAY FROM FOCAL SPOT THRU CYL PHANTOM THICKNESS"
  "AND SUBTRACTS THAT FROM 2*RMAX TO GET FILTER THICKNESS"

 ANGMAX= REAL(NINT(10.* (180./3.141593)*ATAN(RMAX/SAD))/10.);
   "ABOVE CALCS MAX ANGLE, AND ROUNDS OFF TO NEARTEST TENTH OF
ANGLE"

 DO BAG=0.0, (ANGMAX - 0.1), 0.1[     "ANGLES IN DEGREES to max (-0.1 )"

 .TANAN=TAN(BAG*3.141593/180.0);    "TAN OF ANG"
  TANAN2=TANAN*TANAN;              "TAN **2 OF ANGLE"
  THK=2.*SQRT(RMAX*RMAX-(SAD*SAD*TANAN2)/(1+TANAN2));
"THICKNESS THRU PHAN"
  BANG(NINT(10.0*BAG))=2.*RMAX-THK;] "THIS FILLS UP ARRAY TO
ANGMAX"

 DO BAG=ANGMAX, 25.0, 0.1[   "THIS FILLS UP RESTOF ARRAY"
  BANG(NINT(10.*BAG))=2.*RMAX;]

"-----------------------------------------------------------------"
"STEP 6   DETERMINATION-OF-INICIDENT-PARTICLE-PARAMETERS          "
"-----------------------------------------------------------------"
"DEFINE INITIAL VARIABLES FOR spectrum OF PHOTONS INCIDENT"
"IN A FAN BEAM PERPENDICULAR TO THE Z AXIS WITH POINT SOURCE"

IQIN=0;"             INCIDENT PHOTONS"

"NOW READ IN NCASE"
OPEN (UNIT=17,FILE='NCASE.INP',STATUS='OLD');
READ(17,*) NCASE; "SLice WiDTH"
CLOSE(UNIT=17);

"WEIGHT WILL BE LOOKED UP BELOW-- FUNCTION OF ENERYG AND
ANGLE"
"WEIGHT WILL BE THE TRANSMISSION THRU THE BOWTIE"

%E
"-----------------------------------------------------------------"
"STEP 7   SHOWER-CALL                                            "
```

```
"-----------------------------------------------------------------"
"USE 10 STATISTICAL BATCHES"

"NCASE IS READ IN ABOVE"
"NCASE=  ;  INITIATE THE SHOWER NCASE TIMES"

ISTAT=10;
OUTPUT NCASE;
('  NCASE= ',I12);
JCASE=NCASE/ISTAT;

DO KI=1,ISTAT[
DO I=1,JCASE[
"OUTPUT KI,I;       "
"(I5,I5,'=IK,I');  "

"SET LATCH"
LATCHI=0;

"NOW GET HISTORY-SPECIFIC PARTICLE PARAMETERS"

"CALL ENSRCH(EIN); CALLS SPECTRUM-SAMPLING SUBROUTINE"

"pick new uin,vin,WIN"
"will be from POINT source "

" This 'macro' used to be $CHOOSE-POINT-IN-RECTANGLE"
"recall XBEAM is the half width of the box inwhich to choose point"
"  '    ZBEAM  '  '    ' height '   ... "
$RANDOMSET XINT;XINT=(2.0*XINT-1.0)*XSIDE;
$RANDOMSET ZINT;ZINT=(2.0*ZINT-1.0)*ZSIDE;

"Now pick intersection point for YINT - recall R**2=X**2+Y**2"
YINT=SQRT((RCYL(NR)-XINT)*(RCYL(NR)+XINT));

D=SQRT(CYRAD2(NR)+SAD**2-2.0*SAD*YINT+ZINT**2);

UIN=XINT/D;"FOCAL SPOT ON X-AXIS--(XINT-0)"
VIN=(YINT-SAD)/D;
WIN=ZINT/D; "SAME AS FOR X-AXIS"

"now we have the direction cosines-now must calculate the actual"
"point of intersection of the ray connecting the focal spot with"
"the point selected in the normal plane where XINT and ZINT are found"
```

```
" Z is easy"
ZIN=ZINT*(SAD-RCYL(NR))/SAD;"MUST SCALE BACK TO ENTRANCE POINT
ON CYL NR"

IF(XINT.NE.0.0)[
 SLOPE=-SAD/XINT;
 BINT=SAD;
 BINT2=SAD**2;
 ONEPLU=(1+SLOPE**2);
 XI1=(+SQRT(CYRAD2(NR)*ONEPLU-BINT2)-SLOPE*BINT)/ONEPLU;
 XI2=(-SQRT(CYRAD2(NR)*ONEPLU-BINT2)-SLOPE*BINT)/ONEPLU;
  IF(ABS(XI1).GT.ABS(XI2))[
   XIN=XI2;]
  ELSE[
   XIN=XI1;]
 ]
ELSE[XIN=XINT;]

"now have XIN, get YIN"
YIN=SQRT((RCYL(NR)-XIN)*(RCYL(NR)+XIN));

"NOW FIND GEOM REGION "
DO IZ=2,NPLANE[IZ1=IZ;
 IF(ZIN.LE.ZPLANE(IZ))EXIT;]
 IRIN=(NR-1)*NZ+IZ1;

"NOW GET WEIGHT"
"GET PHIHAT IN DEGREES FOR LOOKUP TABLE -NEGLECT EXTRA LENGTH"
"THRU FILTER FROM LARGER THETA"
PHIHAT=ATAN(XINT/SAD);
DEGPHI=ABS(PHIHAT*180.0/PI);
WTIN=EXP(-EMU(1000.*EIN)*BANG(NINT(10.*DEGPHI)));

"NOW RECORD TOTAL INCIDENT NRG INCIDENT THRU FILER (WEIGHTED)"
"AND TOTAL UNWEIGHTED (FOR NRG CONSERVATION CHECK)"
TOTINC=TOTINC+DBLE(EIN)*DBLE(WTIN);

"RECORD BEAM ANGLE SELECTED"
SLECTBA(NINT(10.*DEGPHI))=SLECTBA(NINT(10.*DEGPHI))+1.0;

CALL SHOWER(IQIN,EIN,XIN,YIN,ZIN,UIN,VIN,WIN,IRIN,WTIN);
] "END OF LOOP ON CASES"
] "END OF LOOP ON BATCHES "

"-----------------------------------------------------------------"
```

```
"STEP 8   OUTPUT-OF-RESULTS                                    "
"--------------------------------------------------------------------"

"OUTPUT ANGLES SELECTED"
"DO IO=0,20[OUTPUT IO,SLECTBA(IO);(I4,1X,F10.1);]"

RHOMED=1.17; "DENSITY OF PMMA"

"NOW LOOP OVER ALL REGIONS AND SUM ENERGY"

DO IB=1,10[
 DO IX=1,NR[
  DO IZ=1,NZ[
  $GET-IRL(IZ,IX);

 STOT(IB)=SENTOT(IB,IRL)+STOT(IB);
 PTOT(IB)=PENTOT(IB,IRL)+PTOT(IB);
 TTOT(IB)= ENTOT(IB,IRL)+TTOT(IB);

]]]

 "ZERO THESE QUANTITIES BELOW!!!!"
/PTOTSU,STOTSU,TTOTSU,POUTSU,SOUTSU,TOUTSU,
PTOTAV,STOTAV,TTOTAV, POUTAV,SOUTAV,TOUTAV,
PTOTDF,STOTDF,TTOTDF, POUTDF,SOUTDF,TOUTDF,
PTOTSE,STOTSE,TTOTSE, POUTSE,SOUTSE,TOUTSE/=0.0;



"Now loop over bins and get sums"
DO IB=1,10[
 PTOTSU=PTOTSU+PTOT(IB);
 STOTSU=STOTSU+STOT(IB);
 TTOTSU=TTOTSU+TTOT(IB);

 POUTSU=POUTSU+PEOUT(IB);
 SOUTSU=SOUTSU+SEOUT(IB);
 TOUTSU=TOUTSU+TEOUT(IB);

]

"Now get averages from sums"
 PTOTAV=PTOTSU/10.;
 STOTAV=STOTSU/10.;
 TTOTAV=TTOTSU/10.;
```

```
 POUTAV=POUTSU/10.;
 SOUTAV=SOUTSU/10.;
 TOUTAV=TOUTSU/10.;

"Now loop over bins and get differences from averages"
DO IB=1,10[
 PTOTDF=PTOTDF+(PTOTAV-PTOT(IB))**2;
 STOTDF=STOTDF+(STOTAV-STOT(IB))**2;
 TTOTDF=TTOTDF+(TTOTAV-TTOT(IB))**2;

 POUTDF=POUTDF+(POUTAV-PEOUT(IB))**2;
 SOUTDF=SOUTDF+(SOUTAV-SEOUT(IB))**2;
 TOUTDF=TOUTDF+(TOUTAV-TEOUT(IB))**2;

]

"now calculate the standard errors"
 PTOTSE=SQRT(PTOTDF/90.);
 STOTSE=SQRT(STOTDF/90.);
 TTOTSE=SQRT(TTOTDF/90.);

 POUTSE=SQRT(POUTDF/90.);
 SOUTSE=SQRT(SOUTDF/90.);
 TOUTSE=SQRT(TOUTDF/90.);


"NOW OUTPUT TOTAL ENERGIES IN VARIOUS CATEGORIES"

"first print total dose to phantom"
PVOL=PI*CYRAD2(NR)*(ZPLANE(NPLANE)-ZPLANE(1)); "VOLUME OF
PHANTOM"

TDOSE=(TTOTSU*1.602192E-10)/(PVOL*RHOMED); "FROM MEV/G TO J/KG"

OUTPUT TDOSE;
(1X, 'MEAN DOSE TO PHANTOM = ',E20.10,'  Gy');

OUTPUT;
(' THESE ARE IN KEV AND STANDARD ERROR (NOT FRACT S.E.) ')

TOTINC=1000.*TOTINC; "IN KEV"
OUTPUT TOTINC;
('    TOTAL ENERGY INCIDENT [keV]= ',3X,',',D20.14);
OUTPUT STOTSU*1000.,STOTSE;
```

```
(' SCATTERED ENERGY ABSORBED [keV]= ',3X,',',D20.14,3X,',',D20.14);
OUTPUT PTOTSU*1000.,PTOTSE;
('  PRIMARY ENERGY ABSORBED [keV]= ',3X,',',D20.14,3X,',',D20.14);
OUTPUT TTOTSU*1000.,TTOTSE;
('    TOTAL ENERGY ABSORBED [keV]= ',3X,',',D20.14,3X,',',D20.14);
OUTPUT SOUTSU*1000.,SOUTSE;
('     SCATTERED ENERGY OUT [keV]= ',3X,',',D20.14,3X,',',D20.14);
OUTPUT POUTSU*1000.,POUTSE;
('      PRIMARY ENERGY OUT [keV]= ',3X,',',D20.14,3X,',',D20.14);
OUTPUT TOUTSU*1000.,TOUTSE;
('       TOTAL ENERGY OUT [keV]= ',3X,',',D20.14,3X,',',D20.14);

"CARRY ON"

"------------------------------------------------------------"
"---------------------- CALCULATE CTDI'S ----------------------"
"------------------------------------------------------------"


SCTDI=70.0; "NUMBER OF SLICES TO INTEGRATE CTDI OVER"

"OUTPUT SCTDI; "
"(' CTDI VALUES INTEGRATED OVER +/-',F6.2,' SLICE WIDTHS');"

OUTPUT;
(' MEAN RCYL,UNWEIGHTED CTDI,STD ERR-not frac');   ",WEIGHTED CTDI,W-
SD');"

"LOOP OVER RADIAL ZONES"
DO IX=1,NR[

 "CTDI INTEGRATION LIMIT VARIABLES INITIALIZATION"
 IRST=1;
 LAST=(NZ+1);"THESE WILL BE RESET BELOW IF NECESSARY"

 "NOW LOOP OVER STAT BATCHES"
  DO I=1,10[

 "NOW LOOP OVER SLABS TO GET DOSE FROM AND SUM ALL"
   DO IZ=1,NZ[

    IF(ABS(ZPLANE(IZ)).LE.(SCTDI*SLWDTH))[
    "NOW SEE IF SLAB IS FIRST OR LAST FOR INTEGRATION LIMITS"
    IF(ABS(ZPLANE(IZ-1)).GT.SCTDI*SLWDTH)[IRST=(IZ);]
    IF(ZPLANE(IZ+1).GT.SCTDI*SLWDTH)[LAST=(IZ);]
```

```
   $GET-IRL(IZ,IX);

   THICK=ZPLANE(IZ+1)-ZPLANE(IZ); "THICKNESS OF SLAB"

   "GET VOLUME OF IRL"
   IF(IX.EQ.1)[VOLUME=PI*THICK*CYRAD2(IX);]
   ELSE[
   VOLUME=PI*THICK*(CYRAD2(IX)-CYRAD2(IX-1));]

 "now calculate dose"
   DOSE=ENTOT(I,IRL)*1.602192E-10/(VOLUME*RHOMED);
  "CONVERTS FROM keV/g to GRAYS"

 "and integrate for CTDI  "
   IF (IZ.EQ.IRST.OR.IZ.EQ.LAST)[
    CTDI(I,IX)= CTDI(I,IX)+0.5* DOSE*THICK/SLWDTH;]

   ELSE[
    CTDI(I,IX)=CTDI(I,IX)+  DOSE*THICK/SLWDTH;]
   ]
   ]
   ]
   "ZERO AVG CTDI COUNTERS"
   SUMIX=0.0;
 "now have the ctdi at this radius in each batch-get avg"
 DO I=1,10[
  SUMIX= SUMIX+ CTDI(I,IX);]

 AVGIX=SUMIX/10.0;


   CTDIF=0.0;


   DO I=1,10[
    CTDIF= CTDIF+( AVGIX- CTDI(I,IX))**2;]

   "CALC STD DEV"

    SDCT=SQRT(CTDIF/90.);

IF (IX=1)[RMEAN=0.0;]
ELSE[RMEAN=(RCYL(IX)+RCYL(IX-1))/2.0;]
```

```
 "OUTPUT ZPLANE(IRST),ZPLANE(LAST);"
 "(' CTDI LIMITS WERE ',F12.6,',',F12.6,' CM');"
 "CTDI's in Grays"
  OUTPUT RMEAN,SUMIX,SDCT;
   (1X,'CTDI AT ',F8.4,' cm = ',1X,E15.5,1X,'   Gy, ',1X,E12.6);",1X,E15.5,1X,F12.6);"


] "ix closer"

"****************************** OUTPUT RADIAL/SLAB DATA
*************"

"LOOP OVER SLABS AND RADII"
"FIRST INITIALIZE SOME CONSTANTS"

UMAXDO=0.0;"UNWEIGHTED MAXIMUM DOSE"
WMAXDO=0.0;"  WEIGHTED MAXIMUM DOSE"


OUTPUT;
(1X,'SLAB THICK.,SLAB CENTER,MEAN RADIUS, DOSE, STD.ERR.,NRG DEP ');
DO IZ=1,NZ[
 THICK=ZPLANE(IZ+1)-ZPLANE(IZ); "THICKNESS OF SLAB"
 DO IX=1,NR[

  $GET-IRL(IZ,IX);
  "GET VOLUME OF IRL"

  IF(IX.EQ.1)[
   VOLUME=PI*THICK*CYRAD2(IX);]
  ELSE[
   VOLUME=PI*THICK*(CYRAD2(IX)-CYRAD2(IX-1));]

"MUST SEPARATE WEIGHTED & UNWEIGHTED"
 /SUMIX,AVGIX,SUMDIF/=0.0;

 "LOOP OVER STAT BATCHES"
 DO JJJ=1,10[
  "FIRST GET SUM"
   SUMIX=SUMIX+ENTOT(JJJ,IRL);]

   AVGIX= SUMIX/10.0;
```

```
  IF (AVGIX=0.0)[AVGIX=1E6;]


"CALCULATE STANDARD DEVIATION "
 DO JJ=1,10[
 SUMDIF=SUMDIF+(AVGIX-ENTOT(JJ,IRL))**2;]

SDEV=SQRT(SUMDIF/90.0); "STANDARD ERROR"


"DOSE PER INCIDENT ENERGY IN GY"
DOSE=(SUMIX*1.602192E-10)/(VOLUME*RHOMED);


IF(DOSE.GT.UMAXDO)[UMAXDO=DOSE;]


"CALC MEAN RADIUS"
IF (IX=1)[RMEAN=0.0;]
ELSE[RMEAN=(RCYL(IX)+RCYL(IX-1))/2.0;]

"NOW OUTPUT RESULTS"
OUTPUT
THICK,(ZPLANE(IZ+1)+ZPLANE(IZ))/2.0,RMEAN,DOSE,SDEV/AVGIX,SUMIX;
(1X,F8.4,'CM',1X,F8.4,'CM',1X,F8.4,'  CM',1X,E15.5,' GY',1X,F15.5,E15.8,' MEV');
]
]



STOP;END;"END OF MAIN ROUTINE"
%E
"*************************************************************************"
"                                                                         "
SUBROUTINE AUSGAB(IARG);

"17JUNE92 CHANGED TO DUAL-SCORING SYSTEM, UNWEIGHTED AND
WEIGHTED"

" SCORE ANYTHING IN OR EMERGING FROM PHANTOM "

COMIN/EPCONT,SCORE,STACK/;
COMMON/PASSIT/KI,I,ZDIR;
```

```
"THE RETURN IF IARG=0 OR 5 AREN'T NECESARRY SINCE HAVE TURNED "
"OFF THE CORRESPONDING IAUSFL FLAGS"


" 30 JULY 92 -  CHANGES"
" PREVIOUSLY, LATCH WAS SET TO 1 BEFORE ANY SCATTERING
INTERACTION,"
"  SO ONLY THE PHOTOELECTRONS FROM PRIMARY INTERACTIONS WERE
SCORED"
" AS PRIMARY ENERGY DEPOSITION EVENTS. THIS EXCLUDES THE
COMPTON-"
" ELECTRONS FROM PRIMARY COMPTON EVENTS. MADE THE FOLLWOING
CHANGES:"
" BEFORE A COMPTON EVENT, AUSGAB IS CALLED"
" LATCH IS CHECKED: 3 POSSIBILTIES 0,1,OR 10"
" IF LATCH IS 0 ( A PRIMARY) THEN LATCH IS SET TO 10"
" IF LATCH IS 10 IT IS RESET TO 1"
" IF LATCH IS 1 IT IS LEFT AS 1"
" WHEN ENERGY DEPOSITION IS TO BE MADE, CHECK FOR LATCH-"
" IF PARTICLE DEPOSITING IS A PHOTON AND LATCH NOT EQUAL 0, THEN"
" CLEARLY SCATTERED PHOTON ENERGY"
" IF PARTICLE DEPOSITING HAS A LATCH OF 0 - PHOTOELECTRON -
PRIMRAYR"
" IF PARTICLE DEPOSITING HAS LATCH OF 10 - COMPTON ELECTRON FROM"
" PRIMARY INTERACTION - PRIMARY BIN"
" IF PARTICLE HAS LATCH OF 1 - FROM PREVIOUS SCATTERING EVENTS -
SCATTER"
" THE RAYLEIGH-SCATTERING CALLS WILL BE LEFT ALONE"


IF(IARG.EQ.23)[LATCH(NP)=1+LATCH(NP);RETURN;] "COHERENT SCATTER
TO OCCUR-OK"

IF(IARG.EQ.17)[  "COMPTON TO OCCUR"
 IF(LATCH(NP)=1)[RETURN;] "ALREADY SCATTERED"
 IF(LATCH(NP)=0)[LATCH(NP)=10;RETURN;] " A PRIMARY INTERACTION"
 IF(LATCH(NP)=10)[LATCH(NP)=1;RETURN;] "SECOND SCATTER"
 ]


"CHECKS FOR SCAT-COMP OR RAYLEIGH NOTE THAT THIS STEP SETS THE"
"FLAG BEFORE THE EVENT OCCURS -- IF A PRIMARY HAS A COMPTON
EVENT"
"THE RESULTING ENERGY-DEPOSITING ELECTRON IS SCORED AS IN THE "
"SCATTERED ENERGY BIN - CAN CHANGE IS SET FLAGS AFTER THE EVENT"
```

```
IF(IARG.EQ.3)[ "USER-REQUESTED DISCARD-MUST BE LEAVING PHANTOM"

"NOTE - ELECTRONS WILL NEVER LEAVE PHANTOM SO DONT HAVE TO "
"DIFFERENTIATE ON LATCH HERE"

 IF(LATCH(NP).EQ.0)[ " A PRIMARY PHOTON"
   PEOUT(KI)= PEOUT(KI)+EDEP*WT(NP);]
 ELSE[             " A SCATTERED PHOTON"
   SEOUT(KI)= SEOUT(KI)+EDEP*WT(NP);]

  "TOTALS"
  TEOUT(KI)= TEOUT(KI)+EDEP*WT(NP);

 RETURN;]

IF(EDEP.EQ.0.0)[RETURN;]

"Score by EDEP and Weight since will weight photons by chance of "
"absorption in Bowtie"


IRL=IR(NP); "pick up current region number"
 ENTOT(KI,IRL)= ENTOT(KI,IRL)+EDEP*WT(NP);



"NOW CHECK LATCH FOR SCATTER/PRIMARY"
"30 JULY CHANGE - SINCE ALL DOSE SCORING CALLS COME THRU HERE"
" PICK UP WHETHER THE DOSE IS FROM AN COMPT-ELECTRON FROM A "
" PRIMARY INTERACTION."

"CHECK WHETHER ELECTRON OR PHOTON"
IF(IQ(NP).EQ.0)[ "A PHOTON"

 IF (LATCH(NP).EQ.0)[
 "IF 0 THEN NO SCATTERING HAS OCCURED- ADD TO PRIMARY"

  PENTOT(KI,IRL)=PENTOT(KI,IRL)+EDEP*WT(NP);]

 ELSE[
  SENTOT(KI,IRL)=SENTOT(KI,IRL)+EDEP*WT(NP);]

]
```

```
ELSE[ "AN ELECTRON"

 IF (LATCH(NP).NE.1)[
  "IF 0 THEN NO SCATTERING HAS OCCURED- ADD TO PRIMARY"
  "IF 10 THEN ONLY 1 SCATTER - ADD TO PRIMARY"

   PENTOT(KI,IRL)=PENTOT(KI,IRL)+EDEP*WT(NP);]


  ELSE[
   SENTOT(KI,IRL)=SENTOT(KI,IRL)+EDEP*WT(NP);]

]




"NOW CHECK TO SEE IF IN DIRECTLY-IRRADIATED SLAB"
IF(ABS(Z(NP)).GT.ZDIR)[ "NOT IN DIRECT IRRAD SLAB"RETURN;]

ELSE[

"IN DIRECT DIRECT IRRAD SLAB-SCORE IF PRIM OR SCAT"
  IF(IQ(NP).EQ.0)["APHOTON"

  IF (LATCH(NP).EQ.0)[
   PDIRIR(KI)=PDIRIR(KI)+EDEP*WT(NP);]

   ELSE[
   SDIRIR(KI)=SDIRIR(KI)+EDEP*WT(NP);]


   ]

   ELSE[
   IF(LATCH(NP).NE.1)[
   PDIRIR(KI)=PDIRIR(KI)+EDEP*WT(NP);]

   ELSE[
   SDIRIR(KI)=SDIRIR(KI)+EDEP*WT(NP);]

   ]
   ] "IF IN SLAB ELSE CLOSER
```

```
RETURN;
END;"END OF AUSGAB"
"*************************************************************************"

%Q1
%C80
%I2
%E
;
"*************************************************************************
********
"
"                    **********
"                    *        *
"                    * HOWFAR *
"                    *        *
"                    **********
"
"      A GENERAL PURPOSE CYLINDRICAL GEOMETRY ROUTINE FOR USE
WITH THE EGS4
"      CODE SYSTEM ADAPTED FOR USE WITH DOSRZ.
"
"      FOR PARTICLE NP ON THE STACK IN REGION IR(NP), THIS ROUTINE
"      DETERMINES IF THE PARTICLE CAN GO A DISTANCE USTEP WITHOUT
CHANGING
"      ZONES. IF USTEP CAUSES A ZONE CROSSING, IT IS REDUCED TO PLACE
IT ON
"      THE BOUNDRY AND IRNEW IS SET TO THE ZONE NUMBER ON THE FAR
SIDE OF
"      THE BOUNDARY. IF IR(NP) IS 1 THEN THE PARTICLE HAS ESCAPED THE
REGION
"      OF INTEREST AND THE HISTORY IS TERMINATED.(IDISC IS SET TO 1.)
"
"
"
"
"      SOME VARIABLES
"      ==============
;
"OUTEND =       .TRUE.  =>      PARTICLE MAY TRANSMIT OR BACKSCATTER
OUT ENDS
"      =       .FALSE. =>      PARTICLE STAYS WITHIN THE END BOUNDARIES
"OUTSID =       .TRUE.  =>      PARTICLE MAY TRANSMIT OUT THE SIDES
```

```
"     =     .FALSE. =>     PARTICLE STAYS WITHIN THE SIDE BOUNDARY
"IRL   =      STARTING REGION NUMBER THE PARTICLE IS IN
"IZ    =      STARTING PLANAR ZONE NUMBER THE PARTICLE IS IN.
"            THE PARTICLE IS BETWEEN ZPLANE(IZ) AND ZPLANE(IZ+1).
"IX    =      STARTING CYLINDRICAL ZONE NUMBER THE PARTICLE IS IN.
"            THE PARTICLE IS BETWEEN RCYL(IX-1) AND RCYL(IX).
"
"     COMMON/GEOM/
"          ZPLANE(IZ)     Z VALUES OF PLANES
"                    1<=IZ<=NZ+1
"          RCYL(IRR)      RADII OF CYLINDERS
"                    1<=IRR<=NR
"          CYRAD2(IRR)    =RCYL(IRR)**2
"          NZ             # PLANAR GEOMETRICAL ZONES (NPLANE-1)
"                    ZONE(I) IS BETWEEN ZPLANE(I) AND ZPLANE(I+1)
"          NR             # CYLINDRICAL GEOMETRICAL ZONES
"                    ZONE(I) IS BETWEEN RCYL(I-1) AND RCYL(I)
"          NREG           TOTAL # GEOMETRICAL ZONES =NR*NZ +1
"                          +1 FOR VACUUM ENVELOPE
;
%E   "DOSRZ.MORTRAN"
"     DEFINITIONS OF REGION NUMBER, PLANAR ZONE, CYLINDRICAL
ZONE
"     ================================================================
"          Z AXIS RUNS ACROSS PAGE SHOWN AS .....
"
"
"                         1
"
"
"     ------------------------------------------------- RCYL(NR)
"     |(NR-1) |(NR-1) |(NR-1) |   . . . .   | NR*NZ | NR*NZ |   IX=NR
"     | *NZ+2 | *NZ+3 | *NZ+4 |             |       |  +1   |
"     ------------------------------------------------- RCYL(NR-1)
"     |  .  |  .  |  .  |                   |  .  |  .  |
"     |  .  |  .  |  .  |                   |  .  |  .  |
"     |  .  |  .  |  .  |                   |  .  |  .  |
"     ------------------------------------------------- RCYL(2)
"     | NZ+2 | NZ+3 | NZ+4 |   . . . .   | 2NZ  | 2NZ+1 |   IX=2
"     ------------------------------------------------- RCYL(1)
"..1....|...2...|...3...|...4...|.............|...NZ..|..NZ+1.|....IX=1..1..
;"     ---------------------------------------------
"     |     |     |     | . . . .  |     |     |
"     ---------------------------------------------
"     |  .  |  .  |  .  |          |  .  |  .  |
```

```
"    | . | . | . |         | . | . |
"    | . | . | . |         | . | . |
"    -----------------------------------------------------
"    |   |   |   |  . . .  |   |   |
"    |   |   |   |         |   |   |
"    -----------------------------------------------------
"     IZ=1  IZ=2  IZ=3              IZ=NZ-1  IZ=NZ
"
"                       1
"
"
"
"    VERSION 1     ADAPTED FROM CAVITY HOWFAR        06/84  ERIC FOX
"    VERSION 2     THE SUBROUTINE CALLS TO PLANES AND  10/87  AFB
"                  CYLINDER HAVE BEEN REPLACED BY MACROS
"                  TO SPEED THINGS UP
"
"
"*************************************************************************
*******
;
%E    "DOSRZ.MORTRAN"
"THE MACRO REPLACING THE CALL TO CYLND
"*************************************************************************
******
"
"                  ***********
"                  *         *
"                  * $CYLND  *
"                  *         *
"                  ***********
"
"MACRO TO BE CALLED BY SUBROUTINE HOWFAR IN THE EGS CODE
SYSTEM
"A FULLY DOCUMENTED SUBROUTINE VERSION IS CONTAINED IN
NRCCAUX.MOR, PART
"OF THE STANDARD NRCC DISTRIBUTION
"
"FOR A PARTICLE TRAVELLING INSIDE TWO CONCENTRIC, INFINITE, RIGHT
CYLINDERS,
"THIS SUBROUTINE DETERMINES THE MINIMUM DISTANCE IT MUST GO TO
HIT A CYLINDER.
"THE CYLINDERS ARE ASSUMED TO BE ALIGNED AND CENTERED ALONG
THE Z-AXIS.
"
```

```
"      SOME VARIABLES
"      ==============
"
"{P1} = ICYL  = THE NUMBER OF THE OUTER CYLINDER
"{P2} = IHITC = 1 => PARTICLE HITS THE OUTER SURFACE
"           = 0 => PARTICLE MISSES THE SURFACES
"           =-1 => PARTICLE HITS THE INNER SURFACE
"{P3} = TCYL  = DISTANCE TO SURFACE IF IT HITS
"CYRAD2(ICYL) = RADIUS**2 OF THE OUTER CYLINDER
"
"THIS CODE IS OPTIMIZED FOR SPEED, NOT SIZE.
"
"FOR PARTICLES NEAR THE SURFACE, A FIRST ORDER APPROXIMATION IS
MADE
"FOR EXPRESSIONS LIKE X-SQRT(X**2+EPSILON), WHICH SOMETIMES SETS
TCYL=0.
"
"MACRO VERSION 1          A.F.BIELAJEW NRCC          87/10
"
"
"*************************************************************************
*******
"
REPLACE {$CYLND(#,#,#);} WITH {
;
U1=U(NP);V1=V(NP);A=U1*U1+V1*V1;
IF(A.EQ.0.0)[{P2}=0;{P3}=1.0E30;]
ELSE[
  X1=X(NP);Y1=Y(NP);B=X1*U1+Y1*V1;B2=B*B;
  C=X1*X1+Y1*Y1;
  COUT=C-CYRAD2({P1});
  IF(COUT.GT.0.0)[
    IF(IWATCH.GT.0)[OUTPUT COUT;(' COUT=',E11.3);]
    COUT=0.0;
    ]
  IF(B.GT.0.0)[{P2}=1;
    IF(COUT/B2.GT.-1.0E-3)[{P3}=-0.5*COUT/B;]
    ELSE[{P3}=-COUT/(SQRT(B2-A*COUT)+B);]
    ]
  ELSEIF(B.LT.0.0)[{P2}=1;
    IF(COUT/B2.GT.-1.0E-3)[{P3}=-2.*B/A*(1.-0.25*A*COUT/B2);]
    ELSE[{P3}=(SQRT(B2-A*COUT)-B)/A;]
    IF({P1}.NE.1)[
      CIN=C-CYRAD2({P1}-1);
      IF(CIN.LT.0.0)[
```

```
          IF(IWATCH.GT.0)[OUTPUT CIN;(' CIN=',E11.3);]
          CIN=0.0;
          ]
        RAD=B2-A*CIN;
        IF(RAD.GE.0.0)[
          {P2}=-1;
          IF(CIN/B2.LT.1.0E-3)[{P3}=-0.5*CIN/B;]
          ELSE[{P3}=CIN/(SQRT(RAD)-B);]
          ]
        ]
      ]
    ELSE[
      {P2}=1;
      {P3}=SQRT(-COUT/A);
      ]
    ]
;
}

"THE MACRO REPLACING THE CALL TO PLANES
"**************************************************************************
*******
"
"                    ***********
"                    *         *
"                    * $PLANES *
"                    *         *
"                    ***********
"
"PROGRAM TO BE CALLED BY HOWFAR IN THE EGS CODE SYSTEM
"A FULLY DOCUMENTED SUBROUTINE VERSION IS CONTAINED IN
NRCCAUX.MOR, PART
"OF THE STANDARD NRCC DISTRIBUTION
"
"FOR A PARTICLE TRAVELLING INSIDE TWO PARALLEL, INFINITE PLANES
WITH NORMALS
"ALIGNED ALONG THE Z-AXIS, THIS ROUTINE CALCULATES THE STRAIGHT
LINES DISTANCE
"IT MUST GO TO HIT ONE OF THE PLANES
"
"     SOME VARIABLES
"     ==============
"
"{P1}          =      THE NUMBER OF THE INNER PLANE (LESSER Z-
COORDINATE)
```

```
"                  IT MUST BE .GE. 1
"{P2}        =     THE NUMBER OF THE OUTER PLANE (GREATER Z-
COORDINATE)
"                  IT MUST BE .GE. 2
"{P3} = IHITP  =      1  => PARTICLE HITS THE OUTER PLANE
"              =      0  => PARTICLE MISSES BOTH PLANES
"              =     -1 => PARTICLE HITS THE INNER PLANE
"{P4} = TPLANE =     DISTANCE TO THE PLANE THAT IT HITS
"ZPLANE(IPLANE) =    Z-COORDINATE OF THE OUTER PLANE
"
"MACRO VERSION 1          A.F.BIELAJEW NRCC          87/10
"
"
"*************************************************************************
*******
"
REPLACE {$PLANES(#,#,#,#);} WITH {
;
WL=W(NP);
IF (WL.GT.0.0) [{P3}=1;{P4}=(ZPLANE({P2})-Z(NP))/WL;]
ELSEIF (WL.LT.0.0) [{P3}=-1;{P4}=(ZPLANE({P1})-Z(NP))/WL;]
ELSE[{P3}=0;{P4}=1.0E30;]
;
}

%E    "DOSRZ.MORTRAN"
%Q0

SUBROUTINE HOWFAR;

;
"MACRO USED LOCALLY TO CHANGE REGIONS, ADJUST USTEP, AND EXIT"
REPLACE {$SET NEW REGION(#,#);} WITH
"     ======================="
{;
IF({P1}.LE.USTEP)[
  USTEP={P1};IRNEW={P2};IMSOFF=0;NEWNRC=NWNRCL;
  ]
RETURN
;}

;COMIN/EPCONT,GEOM,MISC,SCORE,STACK/;
COMMON/PASSIT/KI,I,ZDIR;
LOGICAL OUTEND,OUTSID;
```

```
"DISCARD ZERO WEIGHT PARTICLES"
IF(WT(NP).EQ.0.0)[IDISC=1;RETURN;]

OUTEND=.FALSE.;OUTSID=.FALSE.;"INITIALLY ASSUME PARTICLE STAYS IN
THE TARGET"

IQL=IQ(NP);IRL=IR(NP); "LOCAL VARIABLES"

"DISCARD IF PARTICLE WANTS TO LEAVE THE GEOMETRY OR OF THE
REGION IS TOTALLY"
"ABSORBING"
"IF ((IRL.EQ.1).OR.(CABSRB(IRL).EQ.ACHAR))[IDISC=1;RETURN;]"
IF (IRL.EQ.1)[IDISC=1;RETURN;]


$GET-IX-IZ(IRL); "GET PLANAR AND CYLINDRICAL ZONES NUMBERS"

$PLANES(IZ,IZ+1,IHITP,TPLANE);"GET DISTANCE TO PLANE"
      "IHITP  =  1 => HITS GREATER Z PLANE"
      "       =  0 => MISSES BOTH PLANES"
      "       = -1 => HITS LESSER Z PLANE"

$CYLND(IX,IHITC,TCYL);"GET DISTANCE TO CYLINDER"
"     IHITC   =  1 => HITS OUTER CYLINDER"
"             =  0 => MISSES BOTH CYLINDERS"
"             = -1 => HITS INNER CYLINDER"

IZNEW=IZ+IHITP;                          "GET NEW PLANAR REGION"
IF((IZNEW.LT.1).OR.(IZNEW.GT.NZ)) OUTEND=.TRUE.; "FLAG IF LEAVES BY
THE ENDS"

IXNEW=IX+IHITC;              "GET NEW CYLINDRICAL REGION"
IF(IXNEW.GT.NR) OUTSID=.TRUE.; "FLAG IF LEAVES BY THE SIDES"

"DO MOST PROBABLE CASE FIRST WHERE A PLANE AND A CYLINDER CAN
BE HIT"
IF((IHITP.NE.0).AND.(IHITC.NE.0))[
  IF(TPLANE.LT.TCYL)["HITS PLANE FIRST"
    IF(OUTEND)[NWNRCL=0;$SET NEW REGION(TPLANE,1);]
    ELSE[NWNRCL=20-10*IHITP;$SET NEW REGION(TPLANE,IRL+IHITP);]
    ]
  ELSEIF(TCYL.LT.TPLANE)["HITS CYLINDER FIRST"
    IF(OUTSID)[NWNRCL=0;$SET NEW REGION(TCYL,1);]
    ELSE[NWNRCL=30+10*IHITC;$SET NEW REGION(TCYL,IRL+NZ*IHITC);]
    ]
```

```
   ELSE["ODD CASE TCYL=TPLANE:HITS PLANE AND CYLINDER
TOGETHER"
      IF(OUTEND.OR.OUTSID)[NWNRCL=0;$SET NEW REGION(TCYL,1);]
      ELSE[NWNRCL=20-10*IHITP;$SET NEW
REGION(TCYL,IRL+IHITP+NZ*IHITC);]
      ]
   ]

"DO ODD CASE-PARTICLE CAN HIT PLANE BUT NOT CYLINDER"
ELSEIF(IHITP.NE.0)[
   IF(OUTEND)[NWNRCL=0;$SET NEW REGION(TPLANE,1);]
   ELSE[NWNRCL=20-10*IHITP;$SET NEW REGION(TPLANE,IRL+IHITP);]
   ]

"DO ODD CASE-PARTICLE CAN HIT CYLINDER BUT NOT PLANE"
ELSE[
   IF(OUTSID)[NWNRCL=0;$SET NEW REGION(TCYL,1);]
   ELSE[NWNRCL=30+10*IHITC;$SET NEW REGION(TCYL,IRL+NZ*IHITC);]
   ]

"AT THIS STAGE ALL GEOMETRICAL POSSIBILITIES HAVE BEEN CHECKED
AND CONTROL"
"HAS ALREADY BEEN TRANSFERRED TO EGS"

END; "END OF SUBROUTINE HOWFAR"
```

REFERENCES

American Association of Physicists in Medicine 1983 A Protocol for the Determination of Absorbed Dose from High-Energy Photon and Electron Beams *Med. Phys.* **10** 741

Alm Carlsson G and Carlsson CA 1986 Relations between effective dose equivalent and mean absorbed dose (energy imparted) to patients in diagnostic radiology *Phys. Med. Biol.* **31** 911-21

Andreo P 1991 Monte Carlo techniques in medical radiation physics *Phys. Med. Biol* **36** 861-920

Attix FH 1986 *Introduction to Radiological Physics and Radiation Dosimetry* (Wiley: New York) 266

Beck JW, Dunn WL, and O'Foghludha F 1983 Monte Carlo model for absorbed dose calculations in computed tomography *Med. Phys.* **10** 314-20

Bengtsson G, Blomgren PG, Bergman K, and Åberg L 1978 Patient exposures and radiation risks in Swedish diagnotstic radiology *Acta. Radiol. Oncol. Rad. Phys. Biol.* **17** 81-105

Berger MJ and Seltzer SM 1983 *Stopping Powers and Ranges of Electrons and Positrons,* 2nd ed, (US Department of Commerce, National Bureau of Standards: Washington DC)

Birch R, Marshall M, and Ardran GM 1979 *Catalogue of Spectral Data for Diagnostic X-rays* Hospital Physicists' Association Scientific Report Series - 30, (Hospital Physicists' Association: London)

Bunge RE and Herman CL 1987 Usage of Diagnostic Imaging Procedures: A Nationwide Hospital Study *Radiol.* **163** 569-73

Butcher JC and Messel H 1960 Electron Number Distribution in Electron-Photon Showers in Air and Aluminum Absorbers *Nucl. Phys.* **20** 15

Carlsson CA and Alm Carlsson G 1990 Dosimetry in Diagnostic Radiology and Computerized Tomography in *The Dosimetry of Ionizing Radiation* Volume III Kase K R, Bjärngard, and Attix F H, eds (Academic: New York) 163-257

Carter LL and Cashwell ED 1975 *Particle-Transport Simulation with the Monte Carlo Method* TID-26607 (National Technical Information Service: Springfield, VA)

Cashwell ED and Everett CJ 1959 *A Practical Manual on the Monte Carlo Method for Random Walk Problems* (Pergamon: New York)

Chan HP 1981 *Investigation of Physical Characteristics of Scattered Radiation and Performance of Antiscatter Grids in Diagnostic Radiology: Monte Carlo simulation studies,* Ph.D. Dissertation (University of Chicago)

Chilton AB, Shultis JK, and Faw RE 1984 *Principles of Radiation Shielding* (Prentice Hall: Englewood Cliffs NJ) 310-365

Christy TM 1980 *Mathematical Phantoms Representing Children of Various Ages for use in Estimates of Internal Dose* Oak Ridge National Laboratory, NUREG/CR-1159, ORNL/NUREG/TM-367

Christy TM and Eckerman KF 1987 *Specific Absorbed Fractions of Energy at Various Ages from Internal Photon Sources: I. Methods* Oak Ridge National Laboratory ORNL/TM-8381/V1

Cygler J, Szanto J, Soubra M and Rogers DWO 1990 Effects of gold and silver backings on the dose rate around ^{125}I seeds *Med. Phys.* **17** 172-8

Dance DR 1984 The Monte Carlo calculation of integral radiation dose in xeromammography *Phys. Med. Biol.* **29** 237

Dio K and Chan HP 1980 Evaluation of Absorbed Dose in Mammography: Monte Carlo SSimulation Studies *Radiol.* **135** 199

Dixon RL and Ekstrand KE 1978 A Film Dosimetry System for Use in Computed Tomography *Radiol.* **127** 255-8

Drexler TG, Panzer W, Widenmann L, Williams G, Zankl J 1985 *The Calculation of Dose from External Photon Exposures using Reference Human Phantoms and Monte Carlo methods. Part III. Organ doses in X-ray diagnosis* GSF-Bericht, S-1026, Gesellschaft fur Strahlen-Und Umwelttorschung, Munich 1985

Ehrman JR 1981 *The Care and Feeding of Random Numbers* SLAC VM Note Book Module 18 (SLAC Computer Services: Menlo Park, CA)

Evans RD 1955 *The Atomic Nucleus* (McGraw-Hill: NewYork) 672-745

Faulkner K and Moores BM 1987 Radiation dose and somatic risk from computed tomography *Acta Radiologica* **28** 483-8

Fearon T and Vucich J 1985 Pediatric Patient Exposures from CT Examinations: GE CT/T 9800 Scanner *AJR* **144** 805-9

Felmlee JP, Gray JE, Leetzow ML, and Price JC 1990 Estimated Fetal Radiation Dose from Multislice CT Studies *AJR* **154** 185-190

Fewell TR, Shuping RE, and Hawkins KR, Jr 1981 *Handbook of Computed Tomography X-Ray Spectra* Bureau of Radiological Health, HHS Publication (FDA) 81-8162

Food and Drug Administration 1985 21 CFR Ch. 1 (4-1-85) Edition, FDA, HHS §1020.33

Gibbs SJ, Pujol A, Chen TS, Malcolm AW, and James AE, 1984 Patient risk from interproximal radiography *Oral Surg.* **58** 347

Greening JR 1986 Instability of radiation protection quantities *Phys. Med. Biol.* **31** 191

Guidozzi F, Anderson J, and Moore R 1987 Experimental estimation of intrauterine fetal irradiation dosage in computed tomography using a Rando Phantom *Brit. J. Obs. Gyn.* **94** 35-37

Hammersley JM and Handscom DC 1964 *Monte Carlo Methods* (Methuen & Co.: London)

Harrison, RM 1983 A re-evaluation of the 'saturated scatter' method for estimating the energy imparted to patients during diagnostic radiology examinations *Phys. Med. Biol.* **28** 701-707

Herbold G, Hartmann G, Treuer H, and Lorenz W 1988 Monte Carlo calculation of energy buildup factors in the range from 15 to 100 keV, with special reference to the dosimetry of ^{125}I seeds *Phys. Med. Biol* **33** 1037-53

Horsley RJ and Peters VG 1976 Radiation exposure from EMI scanner -- multiple scans *Brit. J. Radiol.* **49** 810.

Houndsfield GN 1973 Computerized transverse axial scanning (tomography) *Brit. J. Radiol.* **46** 1016

Hubbell JH and Overbø I 1979 Relativistic Atomic Form Factors and Photon Coherent Scattering Cross Sections *J Phys. Chem. Ref. Data* **9** 69

Huda W 1984 Is energy imparted a good measure of the radiation risk associated with CT examinations? *Phys. Med. Biol.* **29** 1137-42

Huda W 1992 Should the CTDI definition be changed? presentation, AAPM National meeting, Calgary, August 1992

Huda W and Sandison GA 1985 CT dosimetry and risk estimates *Radiat. Prot. Dos.* **12** 241-9

— 1986 The use of the effective dose equivalent, H_E, as a risk parameter in computed tomography *Brit. J. Radiol.* **59** 1236-8

Huda W, Sandison GA, and Lee TY 1989 Patient doses from computed tomography in Manitoba from 1977 to 1987 *Brit. J. Radiol.* **62** 138-144

ICRP 1977 *Recommedations of the ICRP*, International Commission on Radiological Protection Publication 26 (Pergamon: Oxford)

ICRP 1986 *Developmental effects of irradiation on the brain of the embryo and fetus* ICRP 16 Publication 42 (Pergamon: Oxford)

ICRP 1990 *Recommedations of the ICRP*, International Commission on Radiological Protection Publication 60 (Pergamon: Oxford)

ICRU 1989 *Tissue Substitutes in Radiation Dosimetry and Measurement*, International Commision on Radiation Units and Measurements Report 44 (ICRU: Washington, DC)

Ito A 1988 Three-Dimensional Dose Calculation for Total Body Irradiation in *Monte Carlo Transport of Electrons and Photons Below 50 MeV* Jenkins TM, Nelson WR Rindi A, Nahum AE, Rogers DWO, eds (Plenum: New York) 573-598

James LO and Arnason AN 1973 A true random number generator for the IBM 360 machine in *Proc. 4th Southeastern Conf. on Combinatories, Graph Theory, and Computing* Hoffman F, ed. (Utilitas Mathematica Publishing: University of Manitoba)

Johns H E and Cunningham J R 1983 *The Physics of Radiology* 4th ed (Thomas: Springfield, IL)

Johns HE and Yaffe MJ 1983 Coherent Scatter in Diagnostic Radiology *Med. Phys.* **10** 40

Jones D G and Shrimpton P C 1991 *Survey of CT practice in the UK Part 3: Normalized Organ Doses Calculated using Monte Carlo Techniques*, National Radiation Protection Board NRPB-R250 (HMSO: London)

— 1993 *Normalized Organ Doses for X-ray Computed Tomography Calculated using Monte Carlo Techniques,* National Radiation Protection Board NRPB-SR250 (HMSO: London)

Jones DG and Wall BF 1985 *Organ Doses from Medical X Ray Examinations Calculated using Monte Carlo Techniques,* National Radiation Protection Board NRPB-R186, (HMSO:London)

Kahn H 1950 Random sampling techniques in neutron attenuation problem, I *Nucleonics* **6** 27

Knuth DE 1969 Random Numbers, in *The Art of Computer Programming Vol.2 Semi-numerical Algorithms* 2nd ed. (Addison-Wesley: Reading MA)

Koblinger L and Zaràndi P 1983 Monte Carlo Calculations on Chest X ray Examinations for the Determination of the Absorbed Dose and Image Quality *Phys. Med. Biol.* **18** 518

Kramer R, Zankl M, Williams G, and Drexler G 1982 *The Calculation of Dose from External Photon Exposures using Reference Human Phantoms and Monte Carlo methods. Part I: The male (ADAM) and female (EVA) adult mathematical Phantoms* GSF-Bericht S-885 (Gesellschaft fur Strahlen-Und Umwelttorschung: Munich)

Laws PW and Rosenstein M 1978 A somatic dose index for diagnostic radiology *Health Phys.* **35** 629-42

Le Heron JC 1992 Estimation of effective dose to the patient during medical x-ray examinations from measurements of the dose-area product *Phys. Med. Biol.* **37** 2117-2126

Lehmer DH 1951 Mathematical methods in large-scale computing units *Harv. Univ. Comput. Ann.* **26** 141

Mach H and Rogers DWO 1984 A Measurement of Absorbed Dose to Water Per Unit Incident 7 MeV Photon Fluence *Phys. Med. Biol.* **29** 1555

McCrohan JL, Patterson BS, Gagne RM, and Goldstein HA 1987 Average Radiation Doses in a Standard Head Examination for 250 CT Systems *Radiol.* **163** 263-268

McCullough EC and Payne JT 1978 Patient Dosage in Computed Tomography *Radiol.* **129** 457

Mohan R, Chui C, and Lidofsky L 1986 Differential pencil beam dose computation mdoel for photons *Med. Phys.* **13** 64-73.

Mooney MJ and Speller RD 1992 Photon absorption measurements of bone density in the presence of scattered radiation *Phys. Med. Biol.* **37** 1873-82

Morin RL 1980 *The Use of Monte Carlo Simulation and Pattern Recognition in Computed Tomography for the Removal of Foreign Object Artifact*, Ph.D. Dissertation, University of Oklahoma

Morin RL, Raeside DE, Goin JE, and Widman JC 1988 Random number generation and testing in *Monte Carlo Simulation in the Radiological Sciences*, Morin RL, ed. (CRC: Boca Raton, FL)

Murray D 1990 Using EGS4 Monte Carlo in medical radiation physics, *Australas-Phys-Eng-Sci-Med.* **13**(3) 132

Nelson W R 1992 What and why is Monte Carlo? *Electron and Photon Transport using the EGS4 Monte Carlo System Course* 9-12 March 1992, Institute of Applied Physiology and Medicine, Seattle, Washington

Nelson W R, Hirayama H, and Rogers D W O 1985 *The EGS4 Code System*, Stanford Linear Accelerator Center report SLAC-265 (Stanford University: Stanford, CA)

Nelson WR and Jenkins TM 1987 *Writing* SUBROUTINE HOWFAR *for* EGS4 Stanford Linear Accelerator Center Report SLAC TN-87-4 (Stanford University: Stanford, CA)

Nelson WR and Jenkins TM 1988 Geometry Methods and Packages, *Monte Carlo Transport of Electrons and Photons*, Jenkins TM, Nelson WR and Rindi A eds (Plenum: New York)

Nishizawa K, Maruyama T, Takayama M, Okada M, Hachiya J, and Furuya Y 1991 Determinations of organ doses and effective dose equivalents from computed tomographic examination *Brit. J. Radiol.* **64** 20-8

Panzer W, Scheurer C and Zankl M 1989 Dose to Patients in Computed Tomographic Examinations: Results and Consequences from a Field Study in the Federal Republic of Germany *BIR Report 20: Optimization of Image Quality and Patient Exposure in Diagnostic Radiology* Moores BM, Wall BF, Eriskat H, and Schibilla H, eds (British Institute of Radiology: London) 185-8

Pujol TA and S.J. Gibbs SJ 1982 A Monte Carlo method for patient dosimetry from dental x ray *Dentomaxillofac. Radiol.* **11** 25

Raeside DE 1976 Monte Carlo Principles and Applications *Phys. Med. Biol.* **21** 181-197

Rand Corporation 1955 *A Million Random Digits with 100,000 Normal Deviates* (Free Press: Glencoe IL)

Rogers DWO 1982 More Realistic Monte Carlo Calculations of Photon Detector Response Functions *Nucl. Instr. Meth.* **A199** 531

Rogers DWO and Bielajew AF 1989 Experimental Benchmarks of EGS, in *Monte Carlo Transport of Electrons and Photons Below 50 MeV* Jenkins TM, Nelson WR Rindi A, Nahum AE, Rogers DWO, eds (Plenum: New York) 307-321

Rogers DWO and Bielajew AF 1990 Monte Carlo Tecniques of Electron and Photon Transport for Radiation Dosimtery in *The Dosimetry of Ionizing Radiation* Volume III Kase K R, Bjärngard, and Attix F H, eds (Academic: New York) 427-539

Rogers DWO, Ewart GM, Bielajew AF 1985 *Calculation of Contamination of the ^{60}Co Beam from an AECL Therapy Source* NRCC report PXNR-2710 National Research Council of Canada

Rosenstein M 1976 *Organ Doses in Diagnostic Radiology* HEW Publication (FDA) 76-8030 (Bureau of Radiological Health:Rockville, MD)

— 1982 *Int. J. Appl. Radiat. Isot.* **33** 1051-60

Scarbrough EC, Sandborn GE, Anderson JA, Nguyen PD, Niederkron JY, and Antich PP 1990 Dose Distribution around a 3.0-mm type 6702 ^{125}I seed *Med. Phys.* **17** 460-3

Shope TB, Gagne RM, and Johnson GC 1981 A method for describing the doses delivered by transmission x-ray computed tomography *Med. Phys.* **8** 488-95

Shope TB, Morgan TJ, Showalter CK, Pentlow KS, Rothenberg LN, White DR, Speller RD 1982 Radiation dosimetry of computed tomography systems from ten manufacturers *Brit. J. Radiol.* **55** 60-69

Shrimpton PC 1985 Energy imparted as a measure of radiological hazard to patients from x-ray examinations *J. Int. Fed. Med. Biol. Eng.* **23** Suppl. Part 2 1135-6

Shrimpton PC, Jones DG, Hillier MC, Wall BF, LeHeron JC, and Faulkner K 1991 *Survey of CT practice in the UK Part 2: Dosimetric Aspects* National Radiation Protection Board NRPB-R249 (HMSO: London)

Southon FC 1980 CT scanner comparison *Med. Phys.* **8** 62-75

Spanier J and Gelbard EM 1969 *Monte Carlo Principles and Neutron Transport Problems* (Addison-Wesley: Reading, MA) 26-28

Spokas JJ 1982 Dose descriptors for computed tomography *Med. Phys.* **9** 288-292

Stentström B, Henrikson CO, Karlsson L and Sarby B 1986 Energy imparted from intraoral radiography *Swed. Dent. J.* **10** 125-136

Storrs BB and Byrd SE 1988 Radiation Exposure to the Ocular Lens during CT Scanning *Pediatr. Neurosci.* **14** 254-257

Tibbett LHC 1927 *Random Sampling Numbers* (Cambridge University Press: New York)

Wagner LK, Archer BR, and Zeck OF 1986 Conceptus Dose from Two State-of-the-Art CT Scanners *Radiol.* **159** 787-792

Wall BF, Harrison RM, and Spiers FW 1988 *Patient Dosimetric Techniques in Diagnostic Radiology,* The Institute of Physical Sciences in Medicine Report No. 53 (ISPM: York)

Williamson, JF 1988 Monte Carlo Simulation of Photon Transport Phenomena: Sampling Techniques in *Monte Carlo Simulation in the Radiological Sciences*, Morin RL, ed (CRC: Boca Raton, FL) 53-101

BIOGRAPHICAL SKETCH

James Vincent Atherton was born in the Borough of Queens in the City of New York in November 1957. He was educated in the New York City Public School system and graduated from the Bronx High School of Science in 1975. After attending Hunter College of the City University of New York for one year, he transferred to Wake Forest University in Winston-Salem, North Carolina. He received a Bachelor of Science in 1980 and a Master of Science in 1982, both from Wake Forest and both in physics.

In 1982 the author was hired as the Junior Radiation Safety Officer at Downstate Medical Center of the State University of New York at Brooklyn. He has subsequently worked as a staff physicist at the Northeast Center for Radiological Physics at Memorial Sloan-Kettering Cancer Center, and at the Columbia University College of Physicians and Surgeons as an Instructor in Clinical Radiology. In June of 1988 he was certified in Diagnostic Radiological Physics by the American Board of Radiology, and in August 1988 he began work on his doctoral degree at the University of Florida. From August 1988 to March 1991 he worked as a graduate assistant in the Departments of Nuclear Engineering Sciences and Radiology at the University of Florida. His work was funded in part by a contract from the Center for Devices and Radiological Health, U.S. Department of Health and Human Services. In April 1991 he accepted employment as the Chief Physicist at the CancerCare Center in Gainesville, Florida, and as Deputy Radiation Safety Officer at Alachua General Hospital, also in Gainesville.

In August of 1988 the author married the former Margaret Louise Cole of Charlotte, North Carolina. They presently live in Gainesville where Margaret is employed at the University of Florida Foundation as Director of Annual Giving. They have one daughter, Grace Suzanne, who was born in November 1992.

I certify that I have read this study and that in my opinion it conforms to acceptable standards of scholarly presentation and is fully adequate, in scope and quality, as a dissertation of the degree of Doctor of Philosophy.

William S. Properzio, Chair
Associate Professor of
Environmental Engineering Sciences

I certify that I have read this study and that in my opinion it conforms to acceptable standards of scholarly presentation and is fully adequate, in scope and quality, as a dissertation of the degree of Doctor of Philosophy.

Libby F. Brateman, Cochair
Associate Professor of
Nuclear Engineering Sciences

I certify that I have read this study and that in my opinion it conforms to acceptable standards of scholarly presentation and is fully adequate, in scope and quality, as a dissertation of the degree of Doctor of Philosophy.

David Hintenlang
Assistant Professor of
Nuclear Engineering Sciences

I certify that I have read this study and that in my opinion it conforms to acceptable standards of scholarly presentation and is fully adequate, in scope and quality, as a dissertation of the degree of Doctor of Philosophy.

Janice C. Honeyman
Assistant Professor of
Radiology

I certify that I have read this study and that in my opinion it conforms to acceptable standards of scholarly presentation and is fully adequate, in scope and quality, as a dissertation of the degree of Doctor of Philosophy.

Charles E. Roessler
Professor of Environmental
Engineering Sciences

This dissertation was submitted to the Graduate Faculty of the College of Engineering and to the Graduate School and was accepted as partial fulfillment of the requirements for the degree of Doctor of Philosophy.

August 1993

Winfred M. Phillips
Dean, College of Engineering

Dean, Graduate School

UNIVERSITY OF FLORIDA
3 1262 08556 9712